Numerical Simulation of Hydraulic Fracturing in Tight Gas Shale Reservoirs

Michael Robert Hudson

February 2017

Submitted in accordance with the requirements for the degree of Doctor of Philosophy

The University of Leeds

School of Earth and Environment

Declaration

The candidate confirms that the work submitted is his/her own and that appropriate credit has been given where reference has been made to the work of others.

This copy has been supplied on the understanding that it is copyright material and that no quotation from the thesis may be published without proper acknowledgment.

Acknowledgments

Dedication

This work, what there is of it, is dedicated to my immediate family in New Zealand - Mum, Dad, Little Sis, Nephew and Nana, my adoptive and imminently legal Welsh family, and most especially the ever tolerant, supportive and continually amazing Jenny.

Abstract

Hydraulic fracturing of tight gas shales is a relatively new method of producing economically from extremely low permeability reservoirs. Due to the low permeability, it is crucial that fracturing treatments are able to efficiently create regions of enhanced permeability in the reservoir. The mechanical properties of prospective shale mean that stress interactions between adjacent fractures can be of real consequence to the efficiency of the treatment, and alternative treatments to mitigate these effects have been designed.

The aim of this research is to conduct numerical simulation of alternative treatment designs, and objectively evaluate critical parameters. In particular, key aspects of the so-called Texas Two Step method are simulated. This treatment aims to create zones of altered stress anisotropy between pressurised fractures. This study examines the behaviour of said zones as the distance between the fractures is altered, in parallel with literature describing the method. Explanations for unusual fracture curvature behaviour are provided.

Further studies examine fracture reorientation within a modified stress field such as that created by the treatment. Rates of reorientation are measured under varying levels of stress anisotropy, initial fracture length and orientation to the stress field.

The influence of pre existing natural fractures on the path of a hydraulic fracture is investigated through further simulations. The effects of natural fracture permeability and interface properties are studied. The impact of shear stress caused by a propagating fracture is also examined, and the possible implications for interpretation of microseismic data discussed.

Finally, a new treatment for simultaneous fracturing with reduced stress shadowing is proposed and simulated.

Contents

List of Figures

6

Chapter 1

Introduction

1.1 Background to project

Natural gas has been produced from shales since the early 19th Century. However, the extremely low permeability of tight shales has meant that gas flow rates were so low that the total gas produced was negligible. Over the last decade, advanced technology such has horizontal drilling and hydraulic fracturing has meant that there has been a rapid increase in the amount of gas that is now produced from shales. In particular, shale reservoirs now supply around 47% of gas produced in the US. This "shale gas revolution" has now started to spread to other parts of the world with exploration and appraisal now occurring throughout the world. Despite this huge interest, the economics of shale gas production remain marginal. For example, even in the USA, where a production-line approach has allowed companies to dramatically reduce drilling and completion costs, the low gas price combined with the low gas flow rates means that only a small number of shale resource plays are profitable (Baihly et al., 2010).

It is clear that further technological advances are needed to allow gas production from shales to compete with conventional gas resources such as those found within Russia and the Middle East. Hydraulic fracturing, where artificial fractures are created by increasing the fluid pressure in a borehole beyond the fracture pressure, have been the key game changer regarding the ability of industry to extract gas from shales. It is probably fair to say that key developments within this area have generally been made on a trial-and-error basis. Techniques that prove successful in one area spread by word of mouth and are adopted elsewhere without regard for differences in the reservoirs (e.g. mineralogy, geomechanical properties, stress etc.).

1.1.1 Aims and Objectives

The key aim of this research project is to conduct finite element based geomechanical modelling to provide a more scientific basis for the development of new techniques for hydraulically fracturing shales.

Specifically, the project aims to increase knowledge around issues of stress field modifications induced by hydraulic fractures. Examining fracturing treatments which aim to increase fracture complexity raises further questions about the way in which fractures propagate under modified in-situ stresses.

Fracturing treatments designed to increase fracture complexity will be modelled, and the influence of propagated fractures on the surrounding stress field studied. Fracture path deviation due to interactions between these stresses is expected. Similar numerical simulations of such fracture treatments have shown intriguing fracture path deviations, and explaining these behaviours is a primary objective. Metrics to quantify the effectiveness of such treatments will be studied.

Fracture curvature will be studied using numerical simulation of fracture propagation under various conditions. It is hoped that insight can be gained regarding the dependence of fracture curvature on relative principal stress magnitudes, opening pressure, and initial fracture orientation. These studies could be considered applicable both to propagating hydraulic fractures, and (re)activated natural fractures.

Natural fractures are expected to play an important role in fracturing treatments. Information gained from studies conducted in homogeneous materials will be compared to similar studies conducted in the presence of natural fractures.

1.2 Hydraulic Fracturing Primer

Conventional recovery of oil or gas involves drilling a well into a reservoir which contains the target oil or gas. These hydrocarbons are contained within the pores of a reservoir rock which has high permeability, allowing the fluid within to move reasonably freely. The hydrocarbons are constrained from reaching the surface by a layer of impermeable rock, or other natural barrier. A well placed in the reservoir provides a conduit for the hydrocarbons and the differential between the surface pressure and reservoir pressure drives the hydrocarbons through the well, up to the operator.

Tight gas shales are natural gas bearing mudstones with extremely low permeabilities. The permeabilities are so low that they are often the rocks constraining other hydrocarbons from reaching the surface (cap rocks). They can also act as source rocks for reservoirs, generating hydrocarbons internally. Drilling into such a low permeability rock will allow a very limited amount of gas to escape into the well - a pore pressure reduction of a few MPa into an exposed shale can take years. Hence, shale gas recovery has simply not been an economically viable option until relatively recently. The advent of horizontal drilling has allowed a long horizontal well to be placed inside a layer of shale. From this horizontal well, fracturing treatments are able to create fractures into the shale at regular intervals. First, perforation guns are fired through the well into the shale. These create starter or seed fractures, orthogonal to the well. Blocking the end of the well and pumping it full of fracturing fluid increases the pressure in the well until the starter fractures start to grow into the shale, again generally at right angles to the well. This dramatically increases the surface area of the shale exposed to the well, and may make contact with natural occurring fractures in the shale that can also add to the amount of gas that can be recovered.

During the fracturing treatment, small hard particles known as proppant are added to the fracturing fluid in increasing concentrations. Once the required amount of fracturing has occurred, the fluid is allowed to flow back into the well in such a way as to leave the proppant in place, which hold the fractures open. The increased surface area of the stimulated region should produce gas at a much higher rate than a single vertical well.

1.3   Layout of Thesis

This thesis consists of 8 chapters. This chapter provides the background to the project and a very brief explanation of the basics of hydraulic fracturing. The subsequent chapters are summarised below:

Chapter 2   presents a review of the literature regarding the fracturing medium, shale which is focused on in this work. The nature of some well studied and productive fields are examined. A review of the prevalence and nature of natural fractures in shales is conducted, and a summary of current numerical simulation techniques is provided.

Chapter 3   gives an overview of the numerical simulation framework used throughout this work. This is a fully coupled mechanical-fluid system with discrete fracturing, and localised adaptive remeshing. Constitutive equations used for mechanical, porous flow and network flow through fractures are summarised.

Chapter 4   focuses on simulation of a treatment for creating enhanced complexity. This uses the interaction between fractures to alter the stress state between them, and a third fracture is initiated in the zone between them. The simulations consider the effects of spacing the fractures at varying distances, and a metric for evaluating the effectiveness of the treatment is developed and compared with literature. Two methods of manipulating the stress field are identified.

Chapter 5   models a domain which has been altered by a treatment such as that examined in chapter 4. The behaviour of a fracture propagating through a stress field to which it is not preferentially aligned is examined, under varied levels of stress anisotropy. The fracture's initial length and orientation to the stress field are also varied.

Chapter 6   provides an examination of structured natural fractures interacting with a propagating hydraulic fracture. Natural fracture permeability and interface properties are considered. Later, stochastically generated fractures are used to model the trajectory of a fracture in conditions from chapter 5. The effect of the natural fractures on the trajectory are evaluated. A final simulation evaluates the effect of shear stress due to a propagating hydraulic fracture on surrounding natural fractures.

Chapter 7   simulates a well inclined to the principal stress directions, stimulating multiple fractures simultaneously. The primary aim is to reinforce the shear stresses around each fracture and reduce the impact of stress shadowing.

Chapter 8   presents a summary of the findings in each chapter, noting original findings and possible topics for publication. Possible topics of further study are suggested where applicable.

Chapter 2

Literature Review

2.1 Hydraulic Fracturing

The permeability of gas shale reservoirs is so low that drilling a single or even network of wells does not provide enough surface area for gas to flow at rates that are economical given the cost to drill each well. A solution to this problem is to stimulate fractures extending from the well surface into the matrix, increasing the effective surface area of the well such that enough gas can be recovered to justify the expense of the well and fracture stimulation.

This is accomplished by pumping fluid at high pressure into sealed off sections of wellbore, which have usually been given "starter" fractures using an explosive treatment. The fluid moves into the starter fractures and the pressure (not the rate) of the fluid application causes the matrix to fracture in a number of possible configurations. In higher permeability reservoirs, the aim is to provide maximum fracture width in order to maximise flow rates to the well. However, in very low permeability scenarios, fracture conductivity is so much better than the matrix even at very low fracture widths, so the priority is to maximise fracture *length* (Economides and Martin, 2007), or as Warpinski et al. (2009) describe, creating a complex fracture network (Figure 2.1.1) rather than a simple planar fracture.

Generally speaking, some form of *proppant* is mixed with the fracturing fluid, the aim of which is to keep the fractures propped open after the fracturing fluid is flushed away.

2.1.1 Stimulated Reservoir Volume

The stimulated reservoir volume (SRV) is the reservoir volume affected by stimulation, and is commonly estimated using stimulated reservoir area (SRA), in turn estimated using microseismic data, and estimates of fracture height. Within the SRV, fracture density

can vary depending on a number of factors including the type of fracturing induced, the spacing of initial fractures and the effect of pre-existing natural fractures. The percentage of gas recovery from within the SRV is highly dependent on fracture density when permeabilities are as low as those found in shale reservoirs. In figure 2.1.2, Warpinski et al. (2009) show this percentage plotted for a simulated tight sandstone reservoir with a permeability of 1μD and two shale reservoirs with permeabilities of 100 nD and 10 nD each. The sandstone reservoir is modelled with parallel planar fractures, and the shale with an orthogonal network of fractures, all at 300 ft spacings. The sandstone will eventually recover 80-90% within 15 years, whereas the for the tighter shales, only 25-50% is estimated to be recoverable.

(Mayerhofer et al., 2010) illustrate the effects of reducing fracture spacing in a fixed SRV of approximately 2000×10^6 ft^3 , shown in figure 2.1.3. For a fracture network of equally spaced orthogonal fractures, they note the total fracture length L_{total} for the entire SRV is

$$L_{total} = \frac{4x_f x_n}{\Delta x_s} + 2x_f + x_n \qquad (2.1.1)$$

where x_f is the SRV half length, x_n the SRV width, and Δx_s the spacing between fractures. By reducing the spacing from 300 to 50ft a more than five-fold increase in L_{total} is observed, which they estimate would accelerate the 3 year cumulative gas recovery by the same factor.
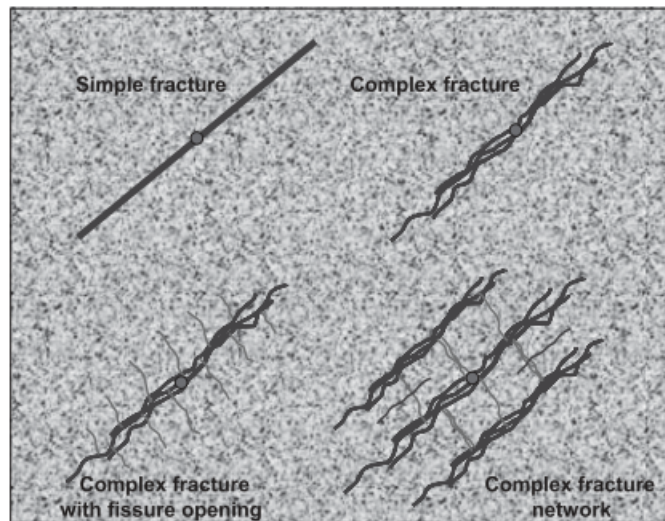
Figure 2.1.1: Types of fracture growth (Mayerhofer et al., 2010)
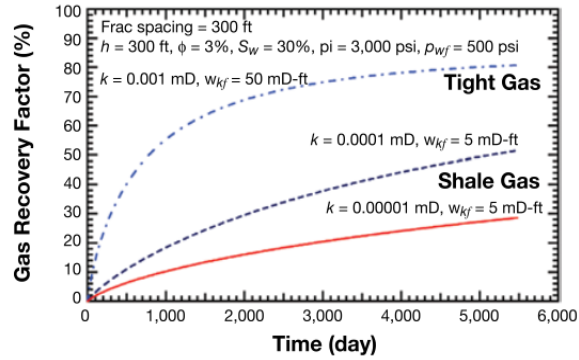
Figure 2.1.2: Gas recovery factors for example shale and tight gas reservoir performance (Mayerhofer et al., 2010)
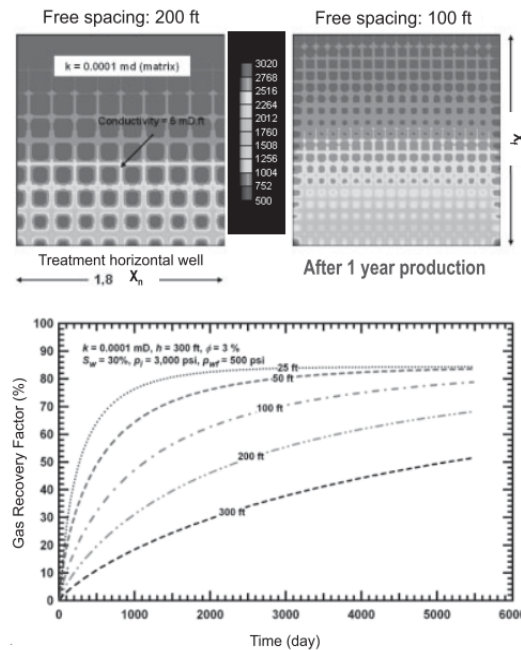
Figure 2.1.3: Effect of fracture spacing (Δx_s) on recovery factor (Mayerhofer et al., 2010)

Studies such as Mayerhofer et al. (2010) have shown that for some generalised fracture networks:

- Gas shales need to be fractured in blocks that are less than 330 m (100 ft) wide to enable recovery of the majority of the gas-in-place.

- Increased fracture conductivity within realistically achievable bounds increases the cumulative gas production. Although high conductivity is unlikely to be achieved throughout the entire network, higher near-wellbore conductivity should, however, add value.

16

- Increasing the stimulated reservoir volume (SRV) increases the total production. The development of the SRV is influenced by shale thickness, the stress field, the open and sealed natural fracture network, rock brittleness and large geological features; e.g. faults.

- Fracture skin damage is predicted to be insignificant unless the damage is greater than a 95% loss in permeability.

- Stimulation strategies which result in unstimulated regions are likely reduce production by the equivalent volume of the unstimulated region.

Unstimulated regions may be the result of stress shadow effects induced by the fracture stimulation process (Fisher et al. (2004),Warpinski et al. (2009)). When a hydraulic fracture is opened, the compressive stress normal to the fracture faces is increased above the initial in-situ stress (σ_{Hmin}) by an amount equal to the net fracturing pressure. This stress elevation is a maximum at the fracture face, but the perturbation of the stress field radiates out into the reservoir, increasing the fracturing pressure necessary to fracture the adjacent formation. The rate of stress perturbation declines with distance from the fracture face, and is mainly controlled by the smallest areal fracture dimension (height or length). In the Barnett Shale fracture heights control the stress shadow, with the stress shadow becoming quite small at an offset distance equal to about 1.5 times the fracture height. In the core area of the Barnett fracture heights are typically around 300 to 400 ft, hence the stress shadow dissipates around 500 ft away from a fracture opening.

Maximising SRV and reducing fracture spacing in multi-stage stimulations is a subject of ongoing research, and current strategies are designed by considering (Mayerhofer et al., 2010):

- Lateral length and orientation of the well relative to the natural fracture and stress orientations.

- Treatment sizes.

- Number of stimulation stages.

- The number and spacing of perforation clusters.

- Diversion techniques and/or openhole packer completion systems for multiple stage completions.

2.1.2 Fracturing Fluids

Rickman et al. (2008) suggest using brittleness to determine fracturing fluid, which in the case of brittle shales, slick water (water containing additives to reduce viscosity and

control capillary pressure effects) is appropriate, with more ductile materials requiring higher viscosity fluids. They propose that with increased ductility the fracture type tends towards planar, and conversely complex fracture networks are more readily achieved with brittle materials (figure 2.1.4). Slickwater fracturing is also known as "waterfracing".

Fluid System Recommendations Based on the Brittleness Calculation

Brittleness	Fluid System	Fracture Geometry	Fracture Width Closure Profile	Proppant Concentration	Fluid Volume	Proppant Volume
70%	Slick Water			Low	High	Low
60%	Slick Water					
50%	Hybrid					
40%	Linear					
30%	Foam					
20%	X-Linked					
10%	X-Linked			High	Low	High

Figure 2.1.4: Fluid recommendations via brittleness (Rickman et al., 2008)

Warpinski et al. (2009) discuss the departures that unconventional gas and shale gas reservoirs make from previous industry rules of thumb and experience, including with respect to the use of higher viscosity gels as fracturing fluids, which are more difficult to recover from complex fracture networks, reducing conductivity of the resulting fracture network. They also suggest that low permeability slickwaters are able to penetrate into pre-existing natural fractures and reopen them. Warpinski et al. (2005) compared stimulation using slick water and higher viscosity cross-linked gel systems on wells with similar conditions, and showed that stimulations using cross-linked gel resulted in a more limited fracture network. Crucial to the success of waterfracing is the ultra low permeability of the shale-gas formations, as this limits leak-off of the low-viscosity waterfrac fluid into the formation, facilitating the overpressuring of the fracture relative to the formation. For higher permeability formations or for formulations with open joints, waterfracs may not generate sufficient pressure to open natural fractures due to leak-off into the formation and/or along open fractures.

One concern with waterfracs is that typically only 10-20% of the injected fluid can be recovered during the process of flowback for cleanup of loaded fluid. The influence of this water on production is dependent on various mechanisms, such as (i) imbibition dominated by capillary pressure; (ii) relative permeability; (iii) gravity segregation; and (iv) stress-sensitive fracture conductivities, etc. Retained water if imbibed rapidly into the formation may not necessarily adversely affect gas production.

2.1.3 Fracture conductivity - proppants

During stimulation the interconnected fracture network has very high permeability, but the fractures will subsequently close unless supported by proppant or by shear offset

(surface roughness). Shear offset is a natural part of the stimulation process and the microseismic activity observed in Barnett stimulations suggest that considerable large-scale movement occurs. How much permeability/conductivity can be generated by shear offset alone is not however well quantified (Warpinski et al., 2009). Consequently, proppant, often graded sand, is generally injected in suspension in the fracturing fluid. For water-frac shale-gas completions the proppant concentrations are generally quite low and the settling of proppant particles is quite rapid due to the low viscosity of the water (which is generally "slickened" using a linear gel).

Warpinski et al. (2009) also question whether the conductivity of the secondary fractures that are oriented orthogonal to the primary hydraulic fracture azimuth is maintained mostly by shear offset during fracturing or by proppant. Fluid transport analysis (Warpinski et al., 2009) for field observations (Fisher et al., 2004) shows that during stimulation the combined influence of the orthogonal fractures results in a network-permeability of the order of tens to hundreds of Darcies. Although many methods exist for estimating the permeability of rough natural fractures and the effect of variable closure stress as the reservoir depletes, the amount of conductivity that is retained is unclear, primarily because of the unknown condition of the fracture walls. The impact of proppant size on prop efficiency for these fractures is also unknown, for example Warpinski et al. (2009) suggests that small diameter (100-mesh) sand could potentially increase fracture intensity by bridging across some fractures forcing new fractures to propagate.

Kassis and Sondergeld (2010) measure the hydraulic conductivity of a rock fracture in Barnett shale as a function of effective stress, proppant, proppant distribution and fracture offset. The fractures were created by axial splitting specimens by loading in uniaxial compression. The permeability of the samples were then measured for matched fractures with no proppant, offset fractures with no proppant and with Ottawa sand or ceramic proppant with either sparse or dense distributions (figure 2.1.6). The principal findings of the study are:

- Fracture offset is as effective as propping a fracture; both increase initial permeabilities more than 1000 fold over initial fracture values. Initial permeability was measured at a normal stress of 800 psi (5.5 MPa) as 48md for matched fractures rising to 220-4805 mD for fractures offset by 0.004-0.020" (0.1-0.5mm).

- Initial fracture permeability is dependent on surface roughness, quantified as root mean square asperity heights.

- The pressure dependence of the propped fracture is stronger, i.e. the permeability is reduced more per increment of pressure than the offset fractures.

- The flow in unpropped or propped does not obey the simple cubic pressure dependence law proposed by Walsh (1981).

- A simple sparse monolayer of proppant is as effective as a fairway distribution of proppant in enhancing permeability.

- Ceramic proppant offers no significant advantage over Ottawa sand, even at pressures as high as 6000 psi (41.4 MPa) effective stress. SEM images showed that sand fractured while ceramic proppant became embedded into the fracture walls. Failure of sand grains induces more microfractures in the substrate, thus potentially increasing permeability effect.
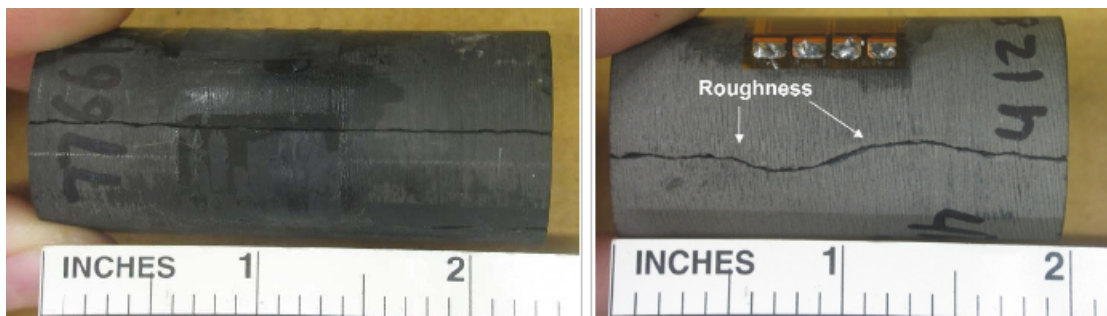
Figure 2.1.5: Two fractured Barnett cores (Kassis and Sondergeld, 2010)

(Left) Sparse monolayer and (right) centralized fairway distribution

Figure 2.1.6: Proppant distribution (Kassis and Sondergeld, 2010)

2.2 Mineralogy

A wide range of mineralogical properties can be seen across the most productive U.S shale plays.

Vitrinite reflectance is one measure of the thermal maturity of organic matter. Vitrinite is the major component in coal but also appears as grains in shale (and other organic source

sedimentary rocks). As vitrinite undergoes maturation due to the temperature and pressure of burial, its reflectance increases. The reflectance is defined as the the proportion of normal incident light reflected by a plane polished surface of vitrinite, and accurately establishes the effective maximum paleotemperature and its duration at any stage in geological time (Mukhopadhyay, 1994). This value increases with the number of planar aromatic sheets in the kerogen. Killops and Killops (2004) give the reflectance values associated with the production of oil and gas types, shown here in Table 2.1. King (2010) state that a value of 1.4% or less indicates the possible presence of liquid hydrocarbons and associated permeability issues.

Vitrinite Reflectance	Hydrocarbon Produced
0.65-1.3%	oil
1.3-2%	wet gas
> 2%	dry gas

Table 2.1: Vitrinite Reflectance

Clay content appears to be an important indicator of the viability of a shale play. Britt and Schoeffler (2009) state that a clay content over 35-40% is too high to be considered widely prospective, and summarise the mineralogy of samples from 8 shale gas formations in Figure 2.2.1. Values to the left of the dotted line (with less than 40% clay) make up the majority of the samples they studied, and of the samples to the right, they note that the significant samples come from two shales which although gas producing are not currently economically viable.
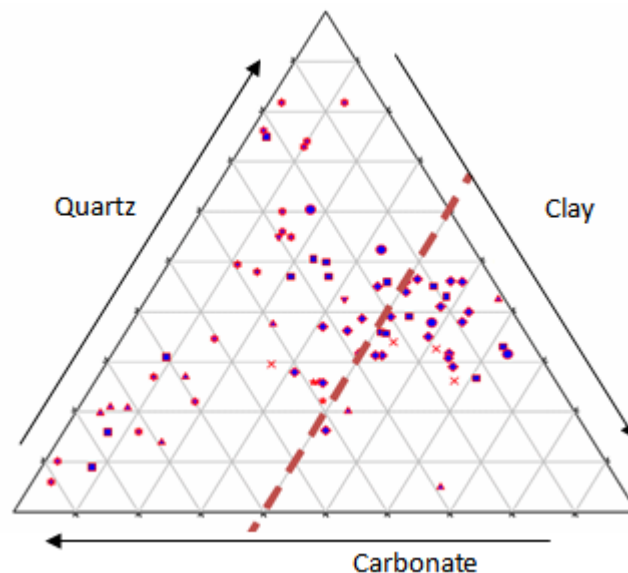
Figure 2.2.1: Ternary Diagram of the Mineralogy of Shales(Britt and Schoeffler, 2009)

2.3 Mechanical properties

Basic geomechanical properties useful in describing (and modelling) their behaviour include the static and dynamic Young's moduli (E_s, E_d), Poisson's ratio (ν_s, ν_d), the subcritical crack index and associated values, and the Biot parameter.

Measurement of mechanical properties often involves the use of core samples taken from the field to find correlations between important mechanical parameters. Values which can be more readily gathered in the field can then be used to determine those which are difficult or impossible to test on site. Barree et al. (2009) discuss numerous sources of complication in applying correlation techniques designed for conventional resources to unconventional reservoirs such as gas shale. They also point out several processes associated with obtaining, transporting and processing core samples which can result in the core becoming an inaccurate representation of the in-situ stress state.

2.3.1 Young's moduli and Poisson ratios

These give an indication of the brittleness of the shale, which appears to be an important indicator of prospectivity. Brittle rock is easier to fracture due to its lower Poisson ratio, and is also able to maintain fracture conductivity due to its stiffness. Grieser and Bray (2007) plot E_s against ν_s in Table 2.3.1, indicating brittle and ductile regions.

Barree et al. (2009) find that for samples with moderate permeability, Young's modulus can either be tested with constant internal pore pressure (drained tests) or with pore fluid trapped (undrained tests). They postulate that the extremely low permeability of shale prevents pore pressure from dissipating in response to external loads during the timescale of hydraulic fracture treatments. This may result in the undrained test being more appropriate for determining the Young's modulus. Poisson's ratio is similarly affected.

Britt and Schoeffler (2009) note the relationship between previously tested clastic rocks (Morales and Marcinew, 1993) and their data from prospective shales is consistent. They illustrate this relationship in Figure 2.3.2. Several non-prospective plays are also plotted which all exhibit E_s modulus below 4 Mpsi (27 GPa). The non prospective samples all had a very high clay content and were considered "true shales", in comparison to the Barnett which is actually a laminated siliceous mudrock.

Britt and Schoeffler (2009) also conducted a series of laboratory experiments to determine the ability of cores with unpropped fractures (both induced and natural) to maintain gas flow, and found clay content and mechanical properties likely to play a role in the ability of samples to maintain fracture permeability with increasing stress.
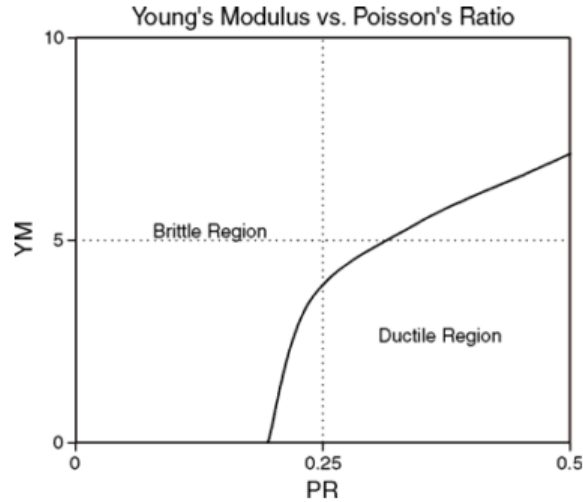
Figure 2.3.1: Poisson's ratio vs Young's modulus (Mpsi) (Grieser and Bray, 2007)

When determining dynamic Young's modulus using ultrasonic velocity testing, they were able to gather shear travel time information both perpendicular and parallel to the core axis. They found that many of the prospective shales with E_s above 3.5 MPsi (24.1 GPa) could be considered isotropic. Samples with this level of stiffness or above averaged 6% in comparison to nearly four times this for samples with E_s below 3.5 MPsi. These shales exhibited visible laminations, possibly suggestive of (anisotropic) fissile behaviour.
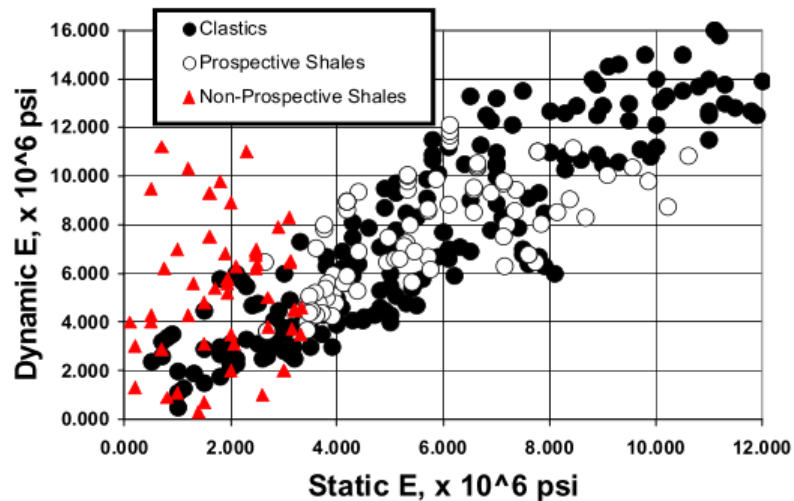
Figure 2.3.2: Dynamic to Static Young's Modulus Correlation (Britt and Schoeffler, 2009)

Ranges of Poisson's ratio and Young's modulus for 4 major fields are compiled in Table 2.2. These assume isotropic moduli, however authors such as Prioul et al. (2011) stress the importance of considering material property anisotropy.

Sondergeld et al. (2010) describe a range of Young's moduli anisotropy of between 0 and 65% in measured Devonian shales. Distinguishing horizontal (E_h) and vertical (E_v) Young's moduli, they use an example of a sample from the Floyd shale to show that $E_h = 2.2E_v$. They give a modified calculation for closure stress which takes into account anisotropy in both Young's modulus and Poisson's ratio:

$$\sigma_h = \frac{E_h}{E_v}\left(\frac{\nu_{zx}}{1 - \nu_{xy}}\right)\sigma_V \qquad (2.3.1)$$

They point out that since E_h and ν_{zx} are typically larger than E_v and ν_{xy}, closure stresses in these anisotropic shales will be greater than those calculated from the isotropic equation. They also plot $\frac{\nu_{xy}}{\nu_{zx}}$ against $\frac{E_h}{E_v}$ for Floyd and Barnett shales, finding a trend suggesting that Poisson ratios increase with stiffness anisotropy.

Prioul et al. (2011) discuss the effect of anisotropic material properties on fracture initiation pressure, first noting that most shales can be well approximated as transversely isotropic; that is they can be considered isotropic within the bedding plane and different normal to the bedding plane. They give elastic parameters for two rocks; a siliceous mudstone (rock C) and an argillaceous/calcerous shale (rock F). Young's moduli and Poisson parameters from these samples are presented in Table 2.3, in which the subscript v denotes normal to the bedding plane and subscript h within the bedding plane. Although the Young's moduli are not consistent with previously discussed rocks[1], the ratio of Young's moduli in rock C is similar to that of the Floyd shale in Sondergeld et al. (2010).

	Barnett	Haynesville	Woodford	Marcellus
E min Mpsi (GPa)	4.8 (8.3)	1.2 (8.27)	1.57 (10.82)	3.3 (22.75)
E max Mpsi (GPa)	4.8 (33)	8.3 (57.2)	1.62 (11.17)	3.36 (23.17)
ν min	0.2	0.15	0.33	0.187
ν max	0.33	0.25	0.33	0.249

Table 2.2: Comparison of Geomechanical Properties of U.S Gas Shales(Gale et al., 2007; Jacot et al., 2010)

Sondergeld et al. (2010) compare a brittleness index calculated using relative proportions of Quartz, Carbonates and Clays proposed by Rickman et al. (2008), with one proposed by Grieser and Bray (2007), which is based on Young's modulus and Poisson ratio measurements. They find both methods produce similar results, indicating a relationship between mineralogy and mechanical properties.

Horsrud et al. (1998) characterised several North Sea shales petrophysically and me-

---

[1]These psi values are very low - did the authors intend 2.817×10^6psi?

	Siliceous Mudstone (C)	Argillaceous/Calcereous Shale (F)
E_v psi	2817	1360
E_h psi	5690	5155
$\frac{E_h}{E_v}$	2.02	3.79
ν_v	0.197	0.115
ν_h	0.252	0.145
$\frac{\nu_h}{\nu_v}$	1.28	1.26

Table 2.3: Transverse Anisotropy in two Shales(Prioul et al., 2011)

chanically. These samples were from a wide range of depths, and mechanically exhibited trends including increasing strength and stiffness with depth. Heating shale was observed to significantly reduce its strength and stiffness, with the implication that laboratory testing should either aim to replicate downhole temperature or correct it.

2.3.2 The subcritical fracture index

The subcritical fracture index is the exponent n in the relationship

$$V = A \cdot K_I^n \tag{2.3.2}$$

where V is the propagation velocity and K_I is the mode I stress intensity (from Holder et al. (2001a)). This relationship describes the stable growth of fractures at stresses below the fracture toughness of the material, which is a cause of natural fracture growth in geologic materials. It can also be thought of as a measure of brittleness, with a high value indicating a rapid transition from zero propagation to almost rupture-crack velocity for small load increases.

The constant A as well as n can be measured in the laboratory, and Holder et al. (2001b) describe a methodology specific to (problematic) sedimentary rocks. Olson et al. (2002) illustrate the effect of this parameter on fracture patterns in Figure 2.3.3. With increasing n, fracture density decreases and clustering occurs at values 40 and 80.

Gale and Holder (2008) measure the subcritical crack index for a number of samples taken from two cores obtained from the Barnett shale. Although they note the difficulty of measuring mudstone samples, they measured consistently high values between 92 and 378. These values are comparable to those for dolostones and chalk (Gale et al., 2007), but are high relative to those for sandstones, which have means of approximately 55 (Rijken, 2005). They conclude that large fractures in the Barnett are likely to be highly clustered, with the distance between clusters being dependent on the thickness of the layer, and in Gale et al. (2007) predict a spacing of several hundred feet between these clusters.
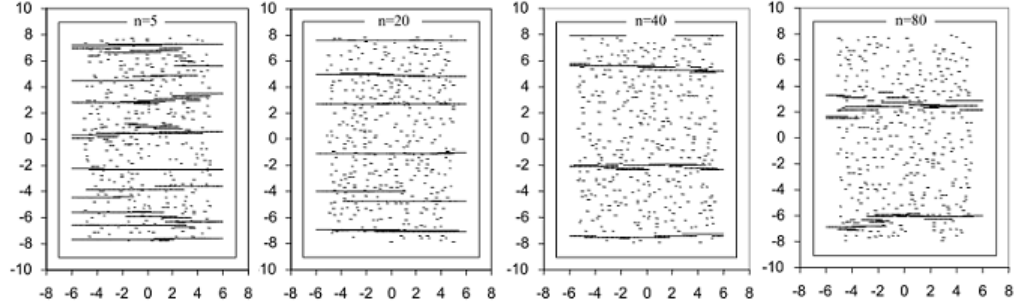
Figure 2.3.3: Numerical simulation of subcritical fracture growth with varying n (Olson et al., 2002)

2.3.3 Biot Parameter

The Biot parameter α describes the effect pore pressure P_p has on effective stress $\bar{\sigma}_i$, as in equation 2.3.3 where σ_i are the diagonal components of the stress tensor (since P_p can have no effect on shear stress)

$$\bar{\sigma}_i = \sigma_i + \alpha P_p \tag{2.3.3}$$

It is related to the bulk modulus (K_d) of the drained rock, and the undrained bulk modulus stiffness of the individual rock grains K_g. Both bulk moduli are measures of the stiffness of the material in hydrostatic compression (i.e. Young's modulus E is the bulk modulus of a sample in an unconfined uniaxial compression test), and are determined experimentally in a triaxial (compression) test. The drained modulus is measured by allowing the pore fluid to escape (i.e the sample is at constant pore pressure) as the sample is compressed.

$$\alpha = 1 - \frac{K_d}{K_g} \tag{2.3.4}$$

The bulk modulus can also be written

$$K = \frac{E}{3(1 - 2\nu)} \tag{2.3.5}$$

and therefore α can also be expressed purely as a function of E and ν:

$$\alpha = 1 - \frac{E_d(1 - 2\nu_g)}{E_g(1 - 2\nu_d)} \tag{2.3.6}$$

For highly porous and compliant materials such as uncemented sandstone, α approaches 1 and pore pressure changes have maximum influence on effective stress. Conversely for a stiffer and/or less porous material (such as shale) the effect of P_p drops to zero as the material becomes completely solid or unconnected in terms of fluid flow.

Miskimins et al. (2004) evaluated the economic importance of the elastic properties E_d, E_g, ν_d and ν_g which comprise α, using three models of varying stiffness reservoir. Their hard rock model, although representing an oil reservoir, was the most sensitive to changes in α and they caution against the assumption that $\alpha = 1$ for stiffer rocks, noting that in their hard rock model replacing the calculated value of 0.27 with a value of 1 (a common assumption) resulted in a reserve recovery estimate that was out by 16%.

Lothe et al. (2004) modelled a North Sea reservoir, paying particular attention to Biot's constant as they varied Poisson's ratio with depth using a low, medium and high depth dependence of ν in the shale cap rock. They illustrated the associated depth dependence of α to in Figure 2.3.4, using data from Horsrud et al. (1998). Their model showed a reduction in α as Poisson's ratio drops, with between 10-20% reduction (from 1) at a depth of 6 km.

It should be noted, however, that these shales had a *minimum* clay content of 30% and average of 57%, which as discussed in 2.2, puts these samples outside the range of prospective shales, and is an indicator of a lower stiffness than in the prospective shales. Indeed, the measured Young's modulus of these samples ranged from 0.8-12.2 GPa and averaged just 2.91 GPa (cf. Table 2.2). The implication of this is that the values for α reported are likely to be higher, in particular at shallower depths, than those of a stiffer shale.
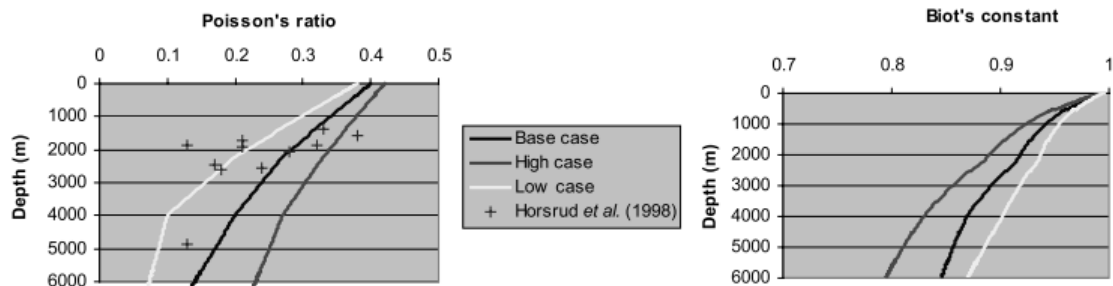
Figure 2.3.4: Depth dependence of Biot's parameter Lothe et al. (2004); Horsrud et al. (1998)

Vincke et al. (1998) evaluated shale samples from a depth of about 450 m in an undisclosed location. Although the Biot parameter is often described using a scalar value, they assume anisotropy and measure core samples taken perpendicular and parallel to the bedding planes in the shale. The samples they used had a Young's modulus of 2.2 GPa (0.3 Mpsi), which is also considerably less stiff than most of the prospective shales in Table 2.2. They measured the response both to decreasing total stress in a uniaxial strain setup, as well as increasing the pore pressure and also found a a change in the Biot parameter with loading. They found no evidence of strong anisotropy in the Biot parameter

27

and concluded that using a scalar (stress dependent) value is sufficient.

Both the above examples found a stress dependence of the Biot parameter in shales with relatively low Young's moduli. The Biot parameter is a function of E and ν (2.3.5) which are themselves stress dependent.

Tran et al. (2010) develop an analytic model of near-wellbore fracture initiation due to thermal differentials and calculate values for Barnett shale based on the material stiffness. They use values ranging between 0.632 and 0.87 for different case studies.

Abousleiman et al. (2007) used a Ultrasonic Pulse Velocity tests to determine mechanical properties for samples from the Woodford shale. The results are tabulated in Figure 2.4. They measured in the direction parallel to the bedding planes (subscripted 1) and perpendicular (subscripted 3). At this depth range α_1 averaged 0.69 and α_3 0.62.

Core	E_1 (GPa)	E_3 (GPa)	ν_1	ν_3	G (GPa)	α_1	α_3
131-0	17.91	10.46	0.11	0.29	5.17	0.69	0.74
154-12	21.63	12.27	0.11	0.24	6.52	0.69	0.75
166-0	19.47	10.87	0.11	0.26	5.32	0.70	0.76
175-10	23.47	13.37	0.15	0.23	5.62	0.65	0.73
185-10	16.47	9.25	0.10	0.29	4.94	0.72	0.76

Table 2.4: Mechanical properties by UPV: Woodford Shale (Abousleiman et al., 2007)

2.4 In-situ Stress

In-situ stress regimes can be described by relating the magnitudes of the greatest, intermediate and least principle stresses (σ_{11},σ_{22}, σ_{33}) to the vertical, maximum horizontal and minimum horizontal stresses (σ_V,σ_{Hmax}, σ_{hmin}), as in Table 2.5. In a normal faulting regime, the vertical stress is the maximum principle stress ($\sigma_V = \sigma_{11}$). In the context of hydraulic fracturing, mode I (tensile) fractures propagate perpendicular to σ_{33}, this results in fracture growth vertically and in the direction of σ_{Hmax}.

Regime	Stress		
	σ_{11}	σ_{22}	σ_3
Normal	σ_V	σ_{Hmax}	σ_{hmin}
Strike-slip	σ_{Hmax}	σ_V	σ_{hmin}
Reverse	σ_{Hmax}	σ_{hmin}	σ_V

Table 2.5: Relative stress magnitudes and faulting regimes (Zoback, 2007)

Principle stresses vary with depth as a consequence of the increasing load above and around the rock with depth. Variation at a given depth in each direction can occur throughout the stress field for many different reasons. These are primarily tectonic or gravitational, the first being driven by forces acting on the tectonic plates of the earth's crust, and the second due to material density. More localised effects can be seen due to fault interaction, subsidence, vertical uplift, structural effects such as arching, to name but a few. Reservoir depletion, fluid injection, and other human factors can also introduce important changes.

Prioul et al. (2011) tabulate stress to depth ratios for the principle stresses and pore pressure (P_p) of four major fields (Table 2.6). Clearly the different stress gradients of σ_H and σ_h will result in strong differences in the horizontal stress field. It is apparent that all four of these fields are in a normal faulting regime since the first principle stress is always the vertical stress.

Field	σ_V	σ_H	σ_h	P_p	Depth
	(psi/ft)	(psi/ft)	(psi/ft)	(psi/ft)	ft
Barnett	1.13	0.6-0.8	0.55-0.75	0.43-0.55	4000-8000
Haynesville	1.11	1.0-1.1	0.95-1.05	0.80-0.90	10500-13500
Marcellus	1.13	0.85-1.05	0.75-1.0	0.55-0.80	4000-8500
Fayetteville	1.13	0.95-1.0	0.85-0.95	0.40-0.45	2000-7000

Table 2.6: Stress gradients of four U.S gas shales (Prioul et al., 2011)

Barree et al. (2009) discuss the difficulty of obtaining accurate pore pressure measurements in unconventional reservoirs with such low permeabilities. They also note that pore pressure can vary by a large amount when the reservoir rock is also the source (and may still be producing). They recommend that for unconventional resources core samples are used to provide qualitative information about small-scale anisotropy, but should be extended to large-scale estimates of stress and deformation with great caution. They strongly encourage the use of synthetic sonic logs and elastic moduli derived from standard wire-line tests as described in Mullen et al. (2007).

2.4.1 Stress changes with production

Zoback (2007) discusses stress paths in depleting reservoirs, beginning by showing the relationship between P_p and σ_H. Assuming an infinite isotropic, porous and elastic reservoir with instantaneously applied gravitational loading being the only source of horizontal compressive stress:

$$\sigma_H = \left(\frac{\nu}{1-\nu}\right)\sigma_V + \alpha P_p \left(1 - \frac{\nu}{1-\nu}\right) \qquad (2.4.1)$$

29

In 2.4.1 σ_H refers to both σ_H and σ_h, since isotropy is assumed. Differentiating with respect to P_p gives

$$\Delta\sigma_{Hor} = \alpha\frac{(1-2\nu)}{(1-\nu)}\Delta P_p \tag{2.4.2}$$

For example, if $\alpha = 1$ and $\nu = 0.25$, $\Delta\sigma_{Hor} \sim \frac{2}{3}\Delta P_p$.

Segall and Fitzgerald (1998) have shown that for reservoirs with a length:width ratio of 1:10 or greater, equation 2.4.2 is nearly exactly correct. It follows that in depletion of such reservoirs, the horizontal stresses will in general decrease with depletion, while the vertical stress remains essentially constant (Zoback, 2007).

Segura et al. (2011) perform numerical studies on 3D reservoirs, coupling mechanical stress simulations with an external reservoir flow simulator to characterize stress path behaviour. In particular, they look at stress path behaviour as stress arching occurs. This is the transferal of overburden stress to the sideburden as the reservoir compacts. They examine the effect of 3D geometry on the effect of reservoir stresses, and the results of these simulations are used to improve the accuracy of standalone fluid simulations. This is achieved by enabling the effect of the stress path changes to effect pore volume multiplier tables (PVM), which are then used by standard production simulation software.

2.5 Permeability and Porosity

2.5.1 Permeability

Permeability is a measure of the ability of a porous material to allow fluid to pass through it. In relation to Darcy's law:

$$v = \frac{k}{\mu}\frac{\Delta P}{\Delta x} \tag{2.5.1}$$

where v is fluid velocity, μ is fluid viscosity, ΔP is an applied pressure gradient and Δx is the thickness of the material, k is the permeability. Permeability is measured using constant flow, constant head, transient pulse decay (TPD) and pore pressure oscillation techniques. Constant flow and constant head tests are steady state tests, and more suited to permeabilities above $10^{-15}m^2$. TPD is used by Javadpour et al. (2007) to measure 152 shale samples from 9 reservoirs, where they found a mode permeability of 54 nD. The cumulative frequency plot of this data (Figure 2.5.1) shows that over 90% of the measured permeabilities were less than 150 nD.

Horsrud et al. (1998) use a pressure transient method to measure permeability of 7 North Sea shales, with a mean permeability of $58.85 \times 10^{-21}m^2$ (approx 58.85 nD). They also

present data obtained from the consolidation part of triaxial tests. All transient test samples where measured perpendicular to the bedding plane, and while it would be reasonable to see higher permeabilities in the bedding plane direction, these higher permeabilities should have dominated their triaxial permeability data, which it did not. Attempts to measure in the bedding plane direction with the transient method were hampered by high sample failure rates and pre-existing cracks. These cracks are to be expected when unloading samples from effective stresses of around 50 MPa, and may not necessarily close fully when repressurised.
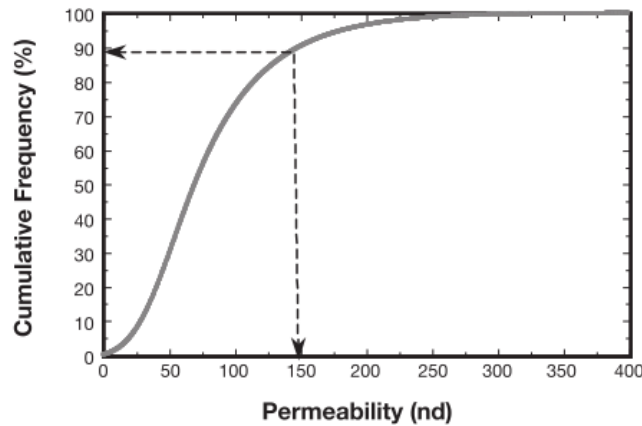
Figure 2.5.1: Cumulative Frequency of permeability measurements (Javadpour et al., 2007)

Yang and Aplin (2007) give an overview of their TPD setup and test 30 shale samples at a range of effective stresses (2.5 to 60 MPa). These results are presented in Figure 2.5.2. They comment that the effective stress/permeability curve can be used to estimate the maximum effective stress to which the the sample has been subjected, the break in slope of such a curve (on a log-log scale) representing this stress. The vertical permeability results range from 2.4×10^{-22} to 1.6×10^{-19} m^2, with horizontal permeabilities being in general higher, with a range 3.9×10^{-21} to 9.5×10^{-19} m^2.

2.5.2 Porosity

Porosity is the amount of void space in the material, expressed as a percentage of volume. Pore sizes in shales are highly significant when regarding flow regimes, since pore diameters are often at a similar scale as fluid molecular diameters. For instance, the molecular diameter of methane is estimated to average 0.381 nm over 3 studies in Sondergeld et al. (2010).

Several authors (Horsrud et al. (1998) ,Javadpour et al. (2007), Yang and Aplin (2007)) measure porosity and pore size distribution using high pressure mercury injection (mer-

Permeability vs Effective Confining Stress
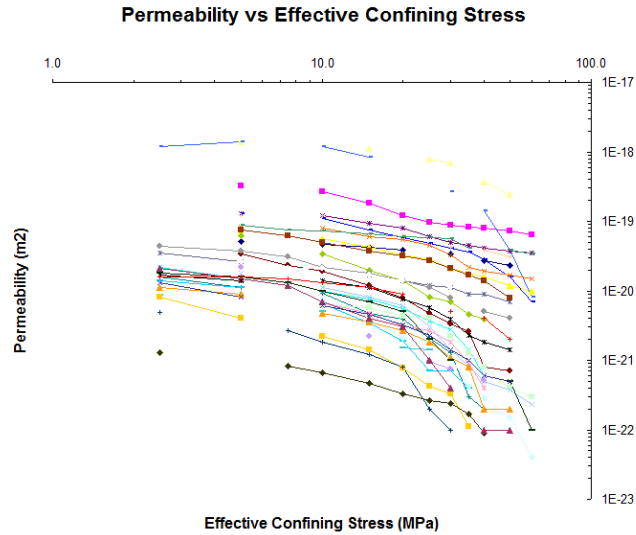
Figure 2.5.2: Permeability vs Effective Stress, 30 Shale samples

cury porosimetry). Shale samples are dried and the volume of mercury injected is recorded against injection pressure. Injection pressure is related to the pore radius in the Young-Laplace equation:

$$P = \frac{2\gamma \cos\theta}{r} \tag{2.5.2}$$

Where P is pressure, r the pore radius, γ the interfacial tension and θ the contact angle between the solid and liquid. Use of this equation assumes cylindrical pore channels. This experiment yields both pore size distribution due to the stepped application of pressure, as well as the final injected volume which establishes the porosity. Javadpour et al. (2007) measure pore sizes ranging between 4 and 200 nm over 3 shale samples.

Horsrud et al. (1998) summarize pore size distributions in Table 2.7. The notation indicates that 5% of the pore volume is made up of radii below r_5 , 20% below r_{20}, etc. They attribute the larger pore sizes in sample K, which is the deepest sample at 4870 m, to damage associated with pressure unloading from such a depth (as also mentioned with regards to permeability). They comment on the significant capillary pressure such low pore sizes can effect, and caution against evaluating shale-fluid interaction effects when samples are not fully saturated. As an example, a capillary pressure of 4.85 MPa is generated for water by a 15 nm pore size.

Yang and Aplin (2007) correct for microfracturing caused by unloading and (the physical process of) sampling, finding the point at which the porosity cumulative frequency curve vs pore radius becomes a minimum, and removing pores with radii larger than this value from the data set (Figure 2.5.3). They calculate mean pore throat radius from the relative pore size distribution, and plot cumulative porosity graphs for all 30 samples, a sample of

Shale	r_5	r_{20}	r_{50}	r_{80}	r_{95}
B	4	6	8	11	115
E	6	12	20	32	90
F	5	10	16	19	33
I	5	7	12	30	195
K	4	7	20	157	1360

Table 2.7: Pore size (nm) distribution in 5 North Sea shale samples (from Horsrud et al. (1998))

which are repeated in Figure 2.5.4.
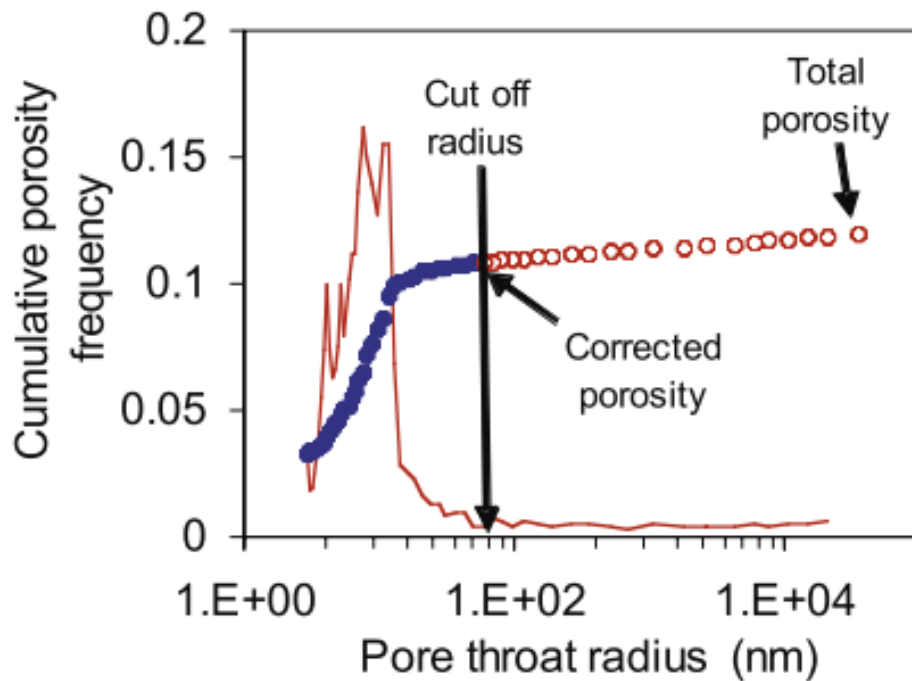
Figure 2.5.3: Correcting for microfractures (Yang and Aplin, 2007)

Horsrud et al. (1998) test porosity using both drying of the sample (to estimate free water content) and by He injection, and see a difference in the results which they propose is due to the compaction of samples during the drying phase.

Schieber (2010) examined several shale successions using Transmission and Scanning Electron Microscopy (TEM and SEM) of samples prepared using ion milling, a technique enabling sufficiently thin samples to be prepared without causing damage. The samples had a range of thermal maturity between immature and supermature, and over this range 3 distinct pore types were observed. These are classified by the author as:
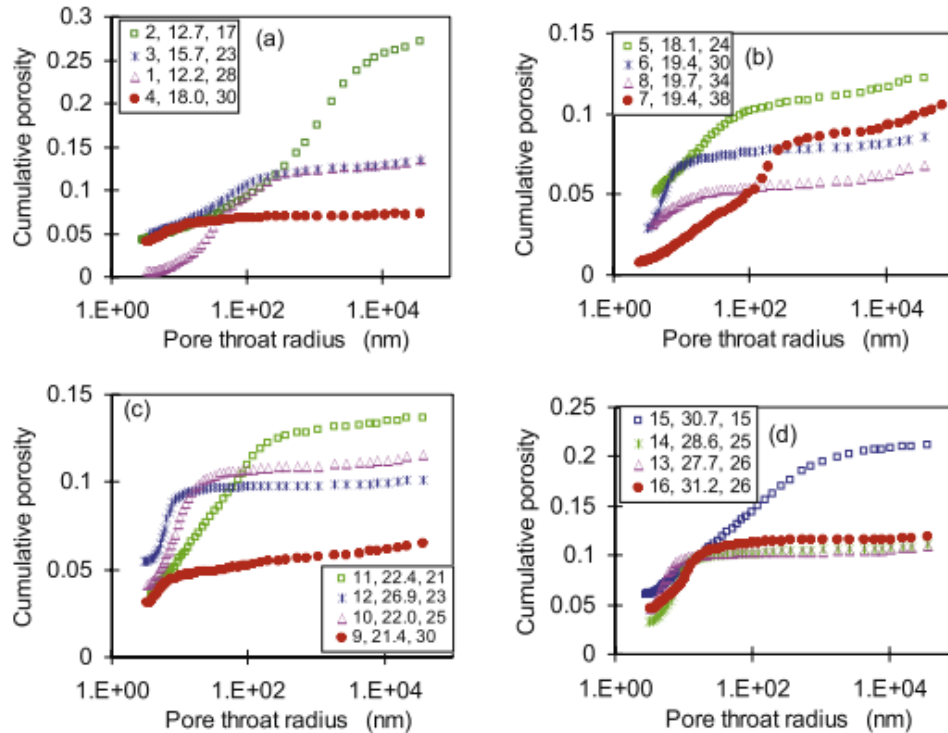
Figure 2.5.4: Cumulative porosity for 16 of 30 samples(Yang and Aplin, 2007)

- PF - Phyllosilicate framework.

- CD - Carbonate dissolution

- OM - Organic matter

PF pores are the most widespread in all samples and consist of *triangular* openings in a lattice of randomly oriented clay mineral platelets. Pores range from a few nm to over a micron. Although randomly oriented, the pores lie within a largely planar setting, and are shown to form in pressure shadows around larger compaction resistant grains such as silt, sand and fossil debris, and the spaces between these grains. Larger pores can be supported by diagenetic mineral growth which cements the ends of larger clay flakes, preventing pore collapse. Figure 2.5.5 shows SEM images of PF pores at increasing resolution.

Shale	He	Drying
B	0.30	0.41
D	0.28	0.34
E	0.26	0.31
F	0.25	0.29
I	0.15	0.17
K	0.01	0.03

Table 2.8: Porosity by He-injection and Sample drying (Horsrud et al., 1998)
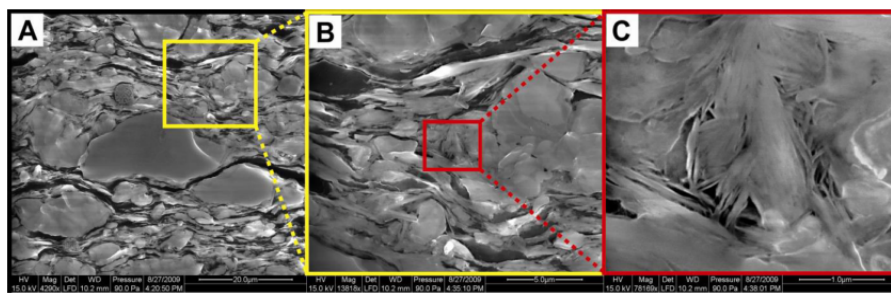
Figure 2.5.5: Phyllosilicate pores(Schieber, 2010)

CD pores are formed by the partial dissolution of carbonate grains, most commonly dolomite and calcite. Rather than the entire grain being removed, it is more commonly observed that the grain margins are eroded. This results in seams of pore space that are irregular or which retain the rectangular outline of the carbonate substrate. Neither collapse into these pores nor filling by secondary materials was observed in these pore spaces, which range in width from a few tens to several hundred nanometers. Figure 2.5.6 shows images of calcite (top) and dolomite (bottom) dissolution pores (black arrows).

OM pores (Figure 2.5.7) are voids left behind due to the maturation of organic material, and in immature shales are present as kerogen blebs, which in mature shale become voids varying in size from a few nm to over a micron.

Schieber (2010) comments that porosity measured in this petrographic manner may not match values calculated from method driven techniques, such as mercury porosimetry. These often contain simplifications (such as equation 2.5.2 assuming cylindrical pores) that do not do justice to the complex nature of the pore space in fine grained sediments.
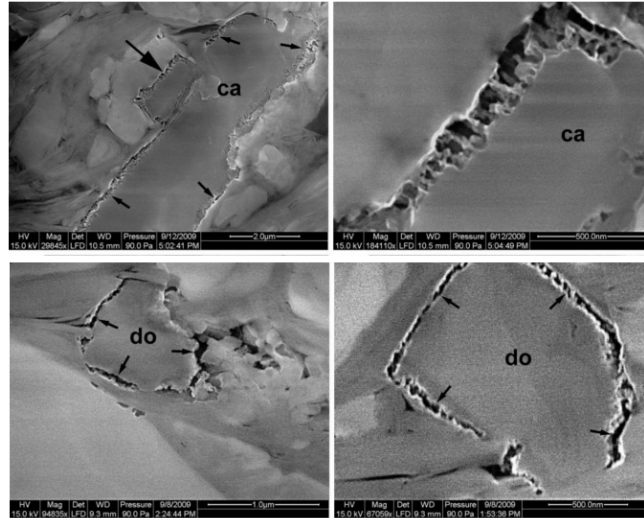
Figure 2.5.6: Carbonate Dissolution pores (Schieber, 2010)
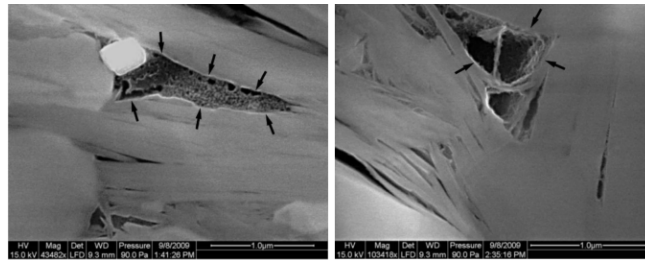
Figure 2.5.7: Organic Matter pores (Schieber, 2010)
On the left, porous kerogen blebs from a mature shale. On the right, empty pore space left by migrated material.

2.6 Natural Fractures

Most rocks at depth are fractured or damaged to some extent, due to any of a large number of potential causes of deformation. In shales, fractures are readily observed in exposed outcrops and subsurface through core samples, as well as being visible in wireline logs. In the context of hydraulic fracturing, it is important to understand the role these fractures can have in affecting hydraulic fracture growth.

The nature of, abundance, and connectivity of natural fractures in the reservoir are all able to affect growth of a hydraulically induced fracture. A natural fracture network may cause a hydraulic fracture to create a more complex network of stimulated fractures. This could be to the advantage of the operator, providing connectivity to a larger region of reservoir per unit volume/area, whilst conversely this could be a mechanism for fracturing fluid loss and ultimately reduced productivity.

2.6.1 Formation

Natural fractures can occur via any of the standard three fracture propagation modes, illustrated in 2.6.1, as well as combinations of the three. Mode I fractures propagate due to failure in tension, while mode II and III are shearing failures.

Mode I: Mode II: Mode III:
Opening   In-plane shear   Out-of-plane shear
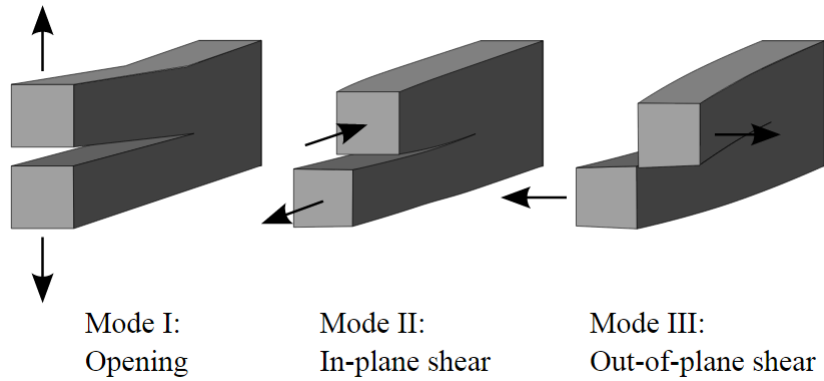
Figure 2.6.1: Fracture Opening Modes

Figure 2.6.2 from Gale et al. (2014) shows mode III and mode I fractures in an outcrop in northwest Argentina. Mixed mode fracturing is shown in sandstone and limestone in Figure 2.6.3, where a) shows mode I in sandstone, b) mixed mode I-II fractures in sandstone and c) mixed mode I-III parent and en-echelon fringe cracks in limestone. (Olson et al. (2009)).
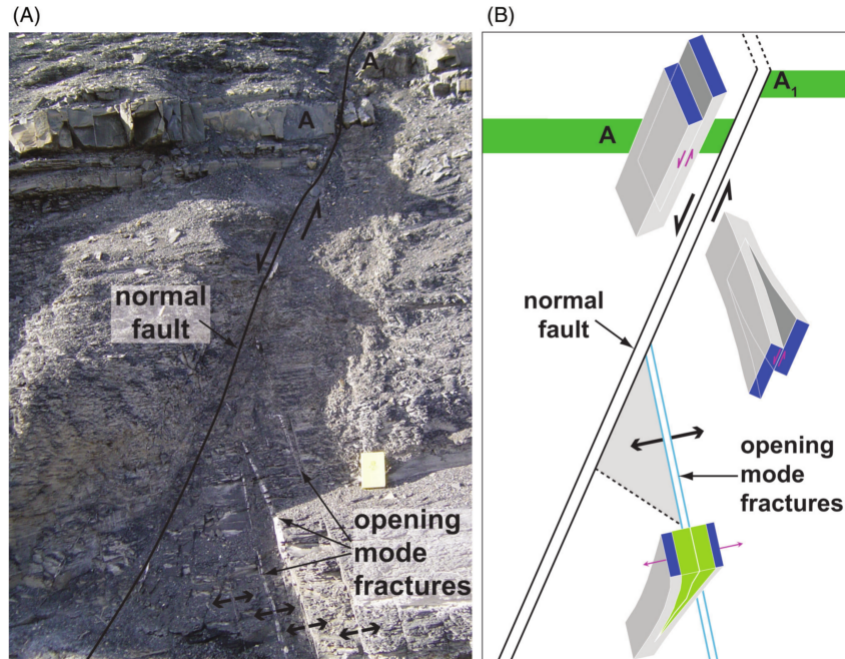
Figure 2.6.2: Normal fault (Mode III) and Opening (Mode I) fractures in the Vaca Muerta Formation, Rio Molichinco, Neuquén, northwest Argentina.
(A): Field book scale = 19 × 12 cm (B): Interpretative diagram showing sense of displacement for different fractures in A. (taken from Gale et al. (2014))
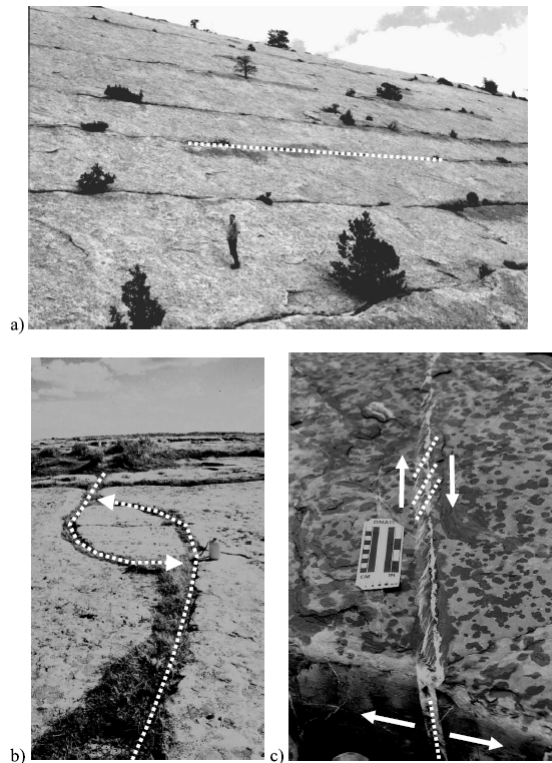
Figure 2.6.3: Mode I and mixed mode natural fractures. Dotted lines indicate representative fracture planes, solid arrows inferred loading conditions. (from Olson et al., 2009)

Generally speaking, rock is much weaker in tension than shear, so much so that their tensile strength is commonly approximated as zero (Zoback, 2007), and mode I fractures are consequently more commonly observed in those rocks which support them. Reservoir shales in particular can have high variations of clay content, and those with higher levels of clay are more susceptible to visco-plastic deformation, rather than brittle tensile failure (Sone and Zoback, 2011)

Mechanisms for mode I fracturing are prevalent in many geological processes. Over time, strata can be bent or folded, which can cause tensile fracture on the outside of a bend. Lateral extensional forces can cause tensile failure. When strata of differing stiffnesses are subjected to the same tectonic stress, the differing strain responses can also result in tensile failure.

Natural hydraulic fracturing via an increase in pore pressure is another possible mechanism. Should the pore pressure increase, effective stress will be reduced, potentially to the point of becoming tensile. Equally, should the lateral total stress decrease due to uplift, tectonic movement or erosion, an unchanged pore pressure reduces the effective stress in the same manner.

Lorenz et al. (1991) focused on the generation of regional (large scale) fractures at significant depth, arguing against this mechanism acting to create natural hydraulic fractures. The importance of Poisson's ratio is significant, since a uniform increase in pore pressure will not result in a uniform change in effective stresses. They derive the relationship:

$$\sigma_h = \sigma_V \left(\frac{\nu}{1-\nu} \right) + \alpha p \left(1 - \frac{\nu}{1-\nu} \right) \tag{2.6.1}$$

assuming isotropic horizontal stresses (σ_h). Given a Poisson's ratio ν of 0.2, Biot parameter α of 1, σ_h will increase around 75% of any pore pressure increase. The equation below can be solved for effective horizontal stress $\sigma_h^{'}$ becoming zero:

$$\sigma_h^{'} = \left(\frac{\nu}{1-\nu} \right) (\sigma_V - \alpha p) \tag{2.6.2}$$

resulting in:

$$p = \frac{\sigma_V}{\alpha} \tag{2.6.3}$$

Which is to say that under isotropic horizontal stress conditions, the pore pressure p needs to either reach or exceed the overburden stress to reduce the horizontal stress to zero, depending on the value of the Biot parameter. If this is the case, then it would be unlikely to see natural hydraulic fractures as long, straight fractures, since the effective stress in every

direction is tensile, which should result in random, explosive type fractures. Significant rock material anisotropy could mitigate this unoriented fracturing.

At low confining stresses, relatively low differential stresses have been observed in laboratories to generate extensional fractures. Increasing pore pressure at depth can reduce the effective stresses to the point that the differential in horizontal stresses can cause the same extensional fractures on a regional scale. However, the pore pressure is not required to exceed the minimum principal stress, as local tensile stresses around flaws in the rock can initiate microfractures which coalesce and remain held open, not by pore pressure but the compressional stresses in the rock. These fractures can remain open long enough to become mineralised (Lorenz et al., 1991).

In contrast, Engelder et al. (2009) investigated the marine Middle and Upper Devonian section of the Appalachian Basin, which includes the Marcellus shale, and found two regional joint sets which were observed in outcrop, core, and borehole images. The joints were formed close to or at, peak burial depth, attributed to natural hydraulic fracturing induced by overpressures generated by gas production during burial (Lash and Engelder, 2005).

2.6.2 Scale and Orientation

In shales, a wide range of fracture sizes and spacings can be observed. Spacings can be centimeter scale to several meters (Laubach et al., 1998, Lorenz et al., 1991, Gale et al., 2014). In some cases relationships between strata thickness and subvertical fracture spacing can be demonstrated, although not consistently (Lorenz et al., 1991, Gale et al., 2014).

Regional fractures are commonly composed of two orthogonal sets, typically an older set which are longer and parallel with a newer set that is shorter and less planar, terminating against the older set (Engelder et al., 2009 , Lorenz et al., 1991, Gale et al., 2014). Detailed studies are typically performed on outcrops, sedimentary strata which are currently exposed at the surface. These studies must account for the outcrop being exposed, namely by recognising fracturing brought about by stress relief associated with the outcrop arriving at the surface, as well as changes to fractures at depth being modified by the same. Figure 2.6.4 illustrates the scale of fractures observed in tertiary sandstone in the Wasatch Formation on northwestern Colorado (in Lorenz et al., 1991) - showing longer, earlier fractures running left to right and shorter, more irregular cross fractures.
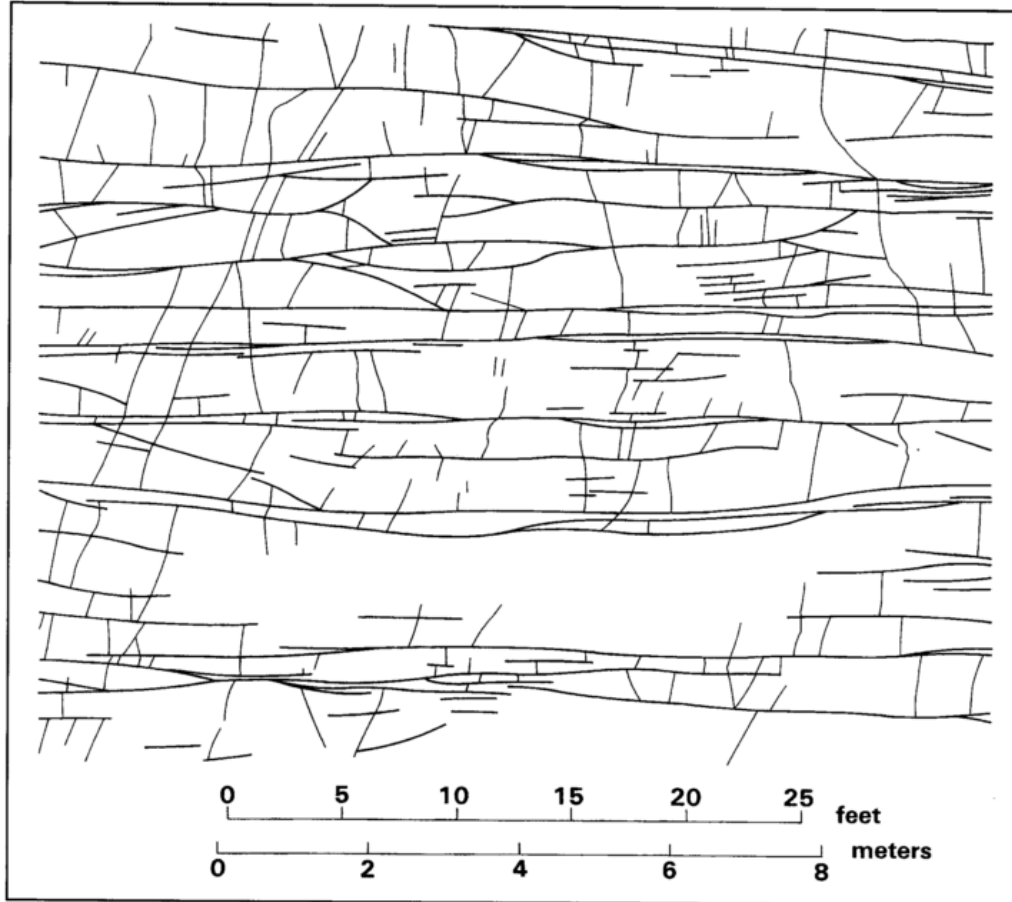
Figure 2.6.4: Regional Fracture Scale
Plan view pattern of fractures in sandstone, Wasatch Formation (Tertiary age), Piceance basin, northwestern Colorado. Tracing from a photo mosaic. Note two sets of fractures: a set of smooth, subparallel fractures trending left to right, and a more irregular set of cross fractures. Fractures of the first set commonly parallel each other at very closely spaced intervals; fractures of the second set commonly terminate against members of the first set (from Lorenz et al., 1991).

Gale et al. (2014) examined natural fractures in 18 shale deposits, via outcrops and core samples. They could categorise three types of fractures; those at a high angle to bedding (subvertical), bedding parallel, and compacted fractures.

Subvertical fractures were the most common type of fracture observed, and are also the least likely to be encountered by vertical core samples. Figure 2.6.5 shows some of their samples exhibiting various characteristics:

Figure 2.6.5: Subvertical Fracture Characteristics (Gale et al. (2014))

A)   Inclined Fractures

B)   Termination (at T) of steeply dipping fracture against another dipping steeply
        in the opposite direction. In this example the core has broken along the ce-
        ment, and was not open in situ

C)   Composite fracture, stepping downward to the right and left ((R) and (L),
        respectively), with gradually tapering terminations. Lorenz et al. (1991) at-
        tributes gradual tapering in regional fractures to growth at subcritical/quasi-
        static rates.

D)   Offset, partially open fractures

E)   Image log showing the fractures in D, indicating they were open at depth

F)   Vuggy pores in fractures with calcite and quartz filling

Bedding parallel fractures can be up to 15cm thick and tens of meters long. Observed cements were most commonly calcite, but barite and gypsum have been observed. Examples of compacted fractures are shown in Figure 2.6.6 . These are unlikely to contribute to production or be volumetrically significant.
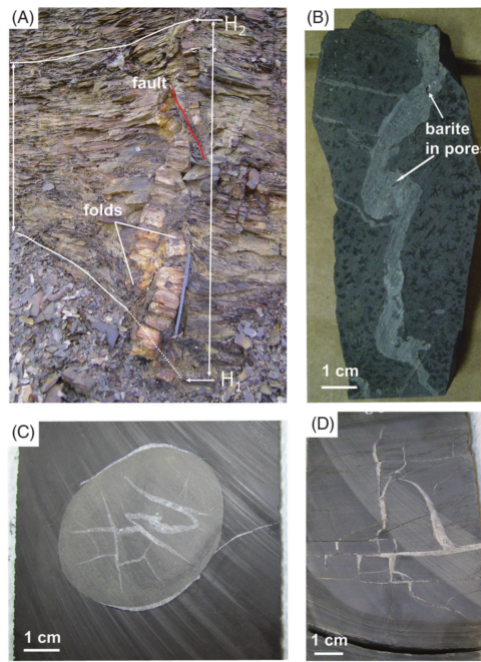
Figure 2.6.6: Compacted Fractures (Gale et al. (2014))

Aperture The kinematic aperture of a fracture is the distance between fracture walls, including cement and pores, or opening displacement. This is recognised as a practical measure of fracture size, since core samples, for example, may not capture the full length or height of a fracture. In fact, given the prevalence of subvertical fractures being sampled by vertical cores, it is unlikely that a fracture longer than a few inches in length will be visible to its full extent in more than one dimension. Gale et al. (2014) observed that in shales, kinematic apertures are mostly in the range of 30 μm-1 mm. A histogram of the measured apertures in their samples is shown in Figure 2.6.7 to this effect.

2.6.3 Cementation

Shales are typically diagenetically reactive, making fractures likely seal to via mineralisation. In subvertical fractures, these are comprised of several minerals. The textures of minerals filling the fractures can aid in determining the fracturing process. For example, some fractures are filled with fibrous cements which can show evidence of mixed mode
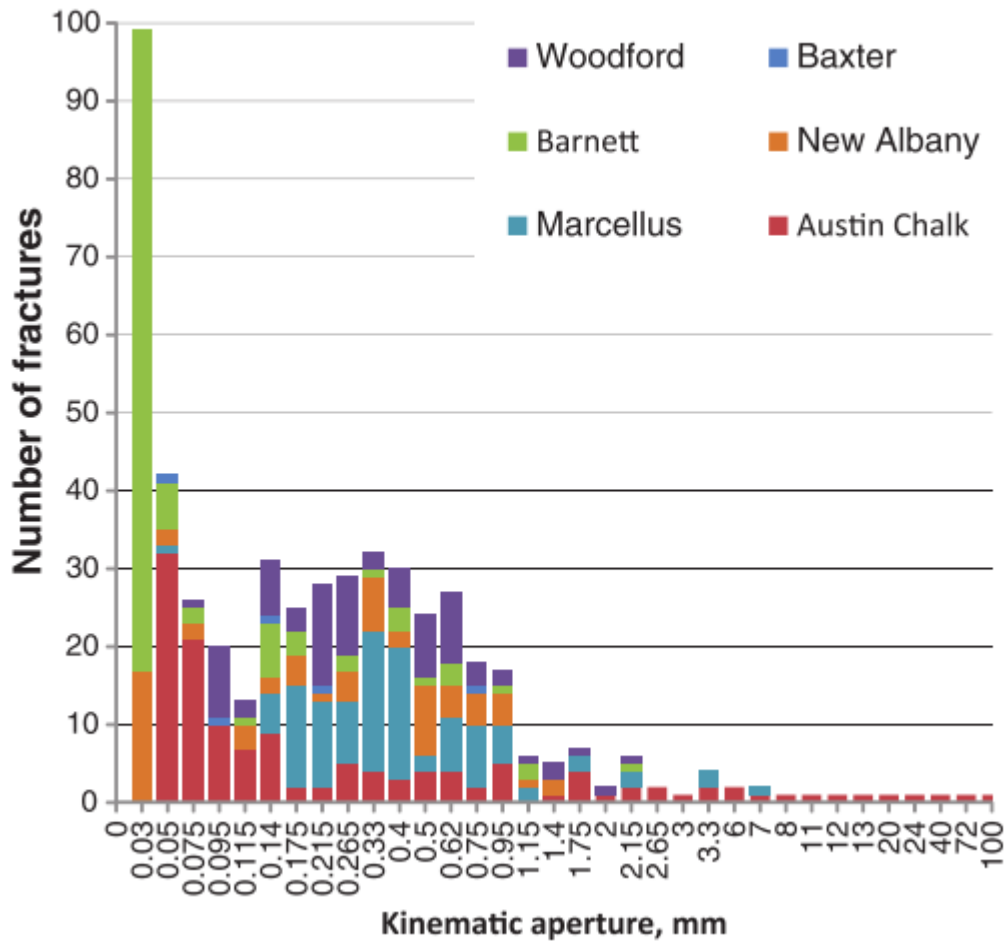
Figure 2.6.7: Kinematic aperture histogram, from Gale et al. (2014)

opening where fibre directions change. Other fractures contain host rock inclusions within the cement, evidence of the crack seal mechanism operating as the fracture continues to open. The most common cement in shales is calcite, found in all samples in Gale et al. (2014). Other minerals observed in shale cementations include quartz, barite, dolomite, and pyrite.

Cementation is important when considering interaction with hydraulic fractures, since it can affect the strength of the natural fracture, and affect its permeability. Gale and Holder (2008) found that a fracture sealed with calcite had half the tensile strength of the host rock, acting as a plane of weakness during fracturing. However, a cemented fracture is also quite likely to be stronger than an uncemented fracture, providing additional shear and tensile strength, affecting the mechanical interaction with a hydraulic fracture.

Fracture size and rate of growth can affect the amount of cementation that occurs within the fracture. Slower growing fractures are more likely to be completely filled, as are nar-

rower apertures (Lander and Laubach (2014)). Other factors include thermal exposure, the geochemical environment, and the reactivity of the fracture wall rock.

2.6.4 Permeability

While it is commonly assumed that fully sealed fractures are unlikely to contribute to reservoir permeability (Gale et al. (2007)), Landry et al. (2014) examined calcite filled fracture with a width of 200 μm using a scanning electron microscope, finding well connected porosity. They determined, via lattice Boltzmann simulations and effective medium upscaling, the cross fracture permeability of the calcite to be between 25 and 100 nD. This is very low, but well within the range of tight gas shales. They concluded that in the direction normal to the fracture, the calcite provides no significant permeability barrier. Permeability in this direction is not particularly relevant to hydraulic/natural fracture interaction (Bahorich et al. (2012)), rather it indicates that cemented fractures would be unlikely to adversely affect production. The permeability which they calculate in the orthogonal direction, i.e. along the natural fracture, is of more interest when considering the behaviour of a propagating hydraulic fracture. They estimate that this could be higher than 10-50 μD, again a low value but higher than shale permeabilities, and enough to provide a conduit for fracturing fluid.

Gutierrez et al. (2000) examined the permeability of closed natural fractures, by dissolving the mineralisation out of the fracture, and subjecting the samples to both normal and shear stresses. They found that despite applying pressures in excess of the unconfined compressive strength of the shale, the fracture permeability remained above that of intact shale, concluding that once opened, natural fractures are difficult to close mechanically. Fractures are therefore likely to remain as pathways for fluid flow unless closed by cementation. The findings of Landry et al. (2014) are thus particularly interesting when considered in this context.

Stochastic Modelling   The assortment of fracturing mechanisms, and resulting fracture properties of natural fractures, result in systems that are very difficult to characterise in the field, and for this reason natural fracture modelling will often take some form of stochastic approach based on core or wire-line log observations, or simplify the problem to regular sets of fractures oriented in a small number of orientations.

2.7 Numerical Modelling

This section discusses the numerical hydromechanical (HM) simulation of fracture stimulation and fluid flow in TGRs.

2.7.1 Formulation Types

For coupled simulations which consider flow from the reservoir, there are mainly 3 approaches that can be used: (i) equivalent continuum, (ii) discrete and (iii) double porosity formulations/multi porosity. This study is primarily concerned with fracturing fluid and mechanical reservoir interactions prior to proppant and or production, and this section considers the first two formulations.

Equivalent continuum formulations

Equivalent continuum formulations consider an equivalent continuum that averages the mechanical and flow properties of both fractures and intact material. Rutqvist and Stephansson (2003) refer to several equivalent continuum models for the HM modelling of fractured media. One of the simplest approaches is to assume three orthogonal sets of fractures in a "sugar cube" medium model, for which simple equations for the fluid flow and elastic properties can be derived. Non-orthogonal fracture sets can be modelled using a multi-laminate model. If fractures are not grouped in sets but rather randomly distributed, the equivalent properties may be calculated by the concept of the fabric or crack tensor.

Classical and more recent references on the derivation of equivalent continuum mechanical properties are highlighted in this paragraph. Singh (1973) studies a rock intersected by a single set of uniformly distributed joints and derives the equivalent elastic modulus of the system. Gerrard (1982) and Fossum (1985) extended this formulation for a rock mass with two or three sets of joints and for a randomly jointed rock mass respectively. Zienkiewicz and Pande (1977) proposed an elasto-viscoplastic multi-laminate model for non-orthogonal jointed rock masses. More recently Huang et al. (1995) proposes a stress-strain model for an assemblage of intact rock blocks separated by joint sets that have different spacing and orientations. The elastic moduli expressions for a rock mass with three intersecting sets of joints are derived explicitly in terms of properties of joints and intact rock. Sridevi and Sitharam (2000) model jointed rock behaviour by using some empirical relations that express the properties of the equivalent jointed medium as a function of a joint factor -dependent on joint orientation, joint frequency and joint strength- and the properties of the intact rock. Hao et al. (2002) review and use anisotropic constitutive models with statistical initial damage to model existing random cracks and joints in

rock. Zhang (2004) revise the relationships between the rock mass elastic modulus (i.e. with joints), the intact rock elastic modulus and the RQD (Rock Quality Designation) index property in rock mechanics on the base that the equivalent continuum approach must use deformation properties of intact rock and of discontinuities obtained through laboratory or in situ tests. They provide several references of works that use the equivalent continuum approach.

Cho et al. (1991) present the equivalent constitutive equations for the mechanical and flow behaviour of saturated porous rock with an arbitrary number of joint sets with specific orientations. The model assumes linear elastic material properties and isotropic permeability for the intact rock. Each joint set is assumed to have linear elastic stiffnesses and isotropic in-plane permeability. A continuum theory is obtained by adding the compliances and fluid flows associated with the intact rock and each of the joint sets. The resulting theory accounts for the anisotropy of mechanical properties due to joint orientation, elastic stiffnesses and spacing and for fluid flow along and fluid exchange between the various flow paths. Phenomena such as joint separation, sliding and dilatancy are not accounted for. Some application examples (e.g. sugar cube model) are analyzed.

Chen et al. (2007) formulate and use an equivalent elastic–perfectly plastic constitutive model with non-associated flow rule and mobilized dilatancy to describe the global non-linear response of a fractured rock mass with one or multiple sets of parallel fractures. A strain-dependent hydraulic conductivity tensor is also formulated which accounts for the normal compressive deformation of the fractures, the effect of material nonlinearity and post-peak shear dilatancy. Numerical simulations are performed to investigate the changes in hydraulic conductivities of a cubic block of fractured rock mass under triaxial compression and shear loading, as well as a circular underground excavation in a real application example.

Osorio et al. (1999) develop a finite difference model based for stress sensitive reservoirs with isotropic properties. The mechanical properties and the permeability are a function of the mean effective stress. A nonlinear elastic representation is used for the mechanical properties of the rock formation.

Grün et al. (1989) present a 2D FEM coupled HM formulation with the permeability dependent on the fluid pressure as well as the over-pressure.

Han (2003) present different formulations for the calculation of stress-dependent porosity and permeability for application to a wellbore producing oil from unconsolidated or weakly consolidated sand. In particular, an expression based on the Carman-Kozeny equation is used for the dependence of the permeability on the porosity.

Yuan and Harrison (2005) present a hydro-mechanical constitutive model that incorporates the degradation of strength and stiffness, a confining pressure-dependent dilatancy,

and a deformation-dependent permeability. In terms of a deformation-dependent permeability they implement a reduction of the permeability during the elastic compaction and an increase during dilation based on the cubic law. A relationship between permeability and strain is preferred to a relationship between permeability and stresses.

Ohman et al. (2005)consider a stochastic component to the deterministic stress-induced component in the determination of the transmissivity of fractured media. The outcome is a tensorial description of fracture transmissivities in an anisotropic stress-regime, where the transmissivity for an arbitrarily oriented fracture in the network is determined by its orientation in relation to the ambient stress-field. These transmissivities are conditioned such that the overall results satisfy a hydraulic packer test data.

Jin and Somerville (2000) present a coupling strategy, using VISAGE and ECLIPSE, where the faults/fractures are represented structurally in VISAGE by smeared multi-laminate joints with a permeability that is strain-path sensitive and its hysteresis may be represented. A single porosity model is used for flow where the permeability is evaluated as the sum of the intact and fracture permeabilities.

Duarte Azevedo et al. (1998) use an equivalent continuum approach based on Zienkiewicz and Pande (1977) multi-laminate model for the HM coupled analysis of fractured materials, coupling also the permeability to the deformation of discontinuities. The model is applied to dam stability analyses.

Liu et al. (1999) propose a model with hydraulic conductivities dependent on the indices RQD (Rock Quality Designation) and RMR (Rock Mass Rating) defining the rock mass structure. The model is applied to an effective stress analysis of conductivity changes in a tunnel subjected to a biaxial stress field.

Discrete formulations

Discrete models describe the flow and mechanical behaviour in detail by discretizing small components of the model individually. The Discrete Element Methodology (DEM) models particle scale (microscopic) interactions to predict macroscopic deformation. In contrast to the Finite Element Method, which applies complicated constitutive equations to macroscopic scale elements, the DEM uses relatively simple equations of motion for very small elements. Tradeoffs for the simpler equations include a vastly increased number of elements to solve for, and extensive experimental validation to verify simulation results (Sheng et al., 2015).

Sheng et al. (2015) conduct a review of several techniques used to model hydraulic fracturing, with an emphasis on discrete formulations. They describe state of the art software packages which use variations of DEM modelling techniques:

- Particle Flow Code (PFC) uses a bonded particulate model (BPM), in which inter-particle bonds are modelled. Breakage of these bonds simulate nucleation of microcracks, which can coalesce to form microcracks. BPM introduces the ability to model micromechanical behaviour of solid rocks to DEM models originally designed to model noncohesive materials such as soils and sands. They provide details of enhancements to PFC such as the smooth-joint contact model (SJM) and synthetic rock mass (SRM), and others, which aim to improve upon disadvantages of earlier versions of the PFC. These included unrealistic ratios between tensile and UCS in the models, and issues related to the roughness of interface surfaces.

- Yade is a recently developed open source package which has the fundamental principals of PFC in common, adding several simulation methods which can be coupled within the same framework (including DEM, FEM and Lattice Geometrical Model (LBM)). It also has the advantage of being immediately alterable by researchers due to its open-source nature. It addresses some of the issues with PFC with alternative techniques, for example ensuring frictional behaviour despite surface roughness rather than using the SJM and SRM models.

- UDEC, or Universal Distinct Element Code, is a package based on the DEM equations, and is targeted at modelling jointed and blocky material. In earlier versions of UDEC, the domain was divided into blocks, with a finite number of intersecting discontinuities, the blocks themselves discretised using a finite difference scheme. It was unable to model the introduction of new fractures, which Sheng et al. (2015) note has been addressed through the introduction of a polygonal block pattern.

- Discontinuous Deformation Analysis (DDA) contains similarities to FEM, although it is based on DEM. It can be used to simulate systems of rock blocks, including interactions such as sliding and detachment. In common with the FEM, the basic structure consists of linear equations which are the result of differentiating and minimising each energy contribution to the system. Recent advances include combination of the DDA with Rock Failure Process Analysis (RFPA) software, looking at large scale deformations of discontinuous rock systems. RFPA is a continuum mechanics based software, which has the ability to capture small scale effects such as crack initiation and propagation, small deformations and coalescence in intact rocks.

Zhang et al. (1996) use DEM (via modified UDEC) to study the effects of stress on the 2-D permeability tensor of natural fracture networks. On the basis of three natural fracture networks sampled around Dounreay, Scotland, numerical modelling examines the dependency of fluid flow on the variations in burial depth, differential stress and loading

direction. A factor, termed the average deviation angle of maximum permeability, is defined to describe the deviation degree of the direction of the major permeability component from the applied major stress direction. For networks whose behaviour is controlled by set(s) of systematic fractures, this angle is significantly greater than zero, whereas those comprised of non-systematic fractures have an angle close to zero.

Zhang et al. (1996) also study the 2D permeability tensor of a network of natural fractures using a discrete element based approach as a function of flow direction and stress conditions for two different models.

Zhang et al. (2009) compare the prediction of effective permeability and elastic properties using effective medium theories of fractured media with numerical simulations using a discrete fracture network (DFN) containing two sets of non-orthogonal vertical fractures. The effect on seismic anisotropy is also studied. Discrepancies between the permeability obtained from the simulations and using effective medium theory are attributed to an oversimplified treatment of fracture interconnectivity in the effective medium theory used. By contrast, the effective elastic compliances obtained from numerical simulation and effective medium theory are in good agreement, even for relatively complicated fracture networks. Although permeability and seismic anisotropy both vary with stress, the relation between them is not simple. The variation in reflection amplitude with offset and azimuth is found to be sensitive to the ratio of the normal to shear compliance of the fractures, whereas permeability is less sensitive to this ratio. For the DFN studied, the permeability rapidly increases at high level of stress due to dilation of the fractures when the in situ stress field is strongly anisotropic.

Min (2003) and Min et al. (2004) use also the distinct element method to study the equivalent mechanical and flow behaviour of 2D samples. Min (2003) propose a methodology to determine the equivalent elastic properties of fractured rock masses using a 2D distinct element program for the numerical representation of stochastic fracture systems, and obtaining an equivalent constitutive model based on the theory of anisotropic elasticity to describe the macroscopic mechanical behaviour of fractured rock masses. The methodology to determine the elastic compliance tensor is verified against known closed-form solutions for regularly fractured rock mass. For the analyses performed, the results show that a REV can be defined and the elastic properties of the fractured rock mass can be represented approximately by the elastic compliance tensor through numerical simulations. The paper provides a good overview of the equivalent continuum approach and related aspects/theories. Min et al. (2004) investigate the effect of different stress states on the permeability of a 2D fractured rock model using the distinct element method and considering the effects of nonlinear normal deformation and shear dilation of fractures. Effects such as stress-induced channelling or permeability anisotropy are captured. A set of empirical equations in closed-form, accounting for both normal closure and shear dilation

of the fractures, is proposed to model the stress-dependent permeability and compared with the numerical results.

Baghbanan and Jing (2008) study the coupling between stress and permeability of a fractured sample using the 2D discrete element method. The intact rock matrix is linear elastic and impermeable, and the fluid flows only through connected fractures obeying the cubic law. Different stress states are studied, as well as the possibility of establishing an equivalent permeability tensor and a representative elementary volume (REV).

Jiang et al. (2009) describe several models to relate transmissivity of single joints to normal stresses. They use Swan's model to get the transmissivity with depth (i.e. geostatic stress), and finally obtain a linear relationship between normal stiffness and depth. Kulhawy's equivalent continuum model (Kulhawy, 1978) is finally used to verify the model.

Mas Ivars (2006) use a 3-D distinct element model for the 3D HM analysis of water inflow into fracture rock excavations. The fractured rock mass is treated as an assemblage of discrete deformable blocks, subjected to mechanical stress and hydraulic pressure boundary conditions, with water flow occurring only along the fractures, i.e., no matrix flow is included. The cubic law is considered and a sensitivity analysis is performed.

Karimi-Fard and Firoozabadi (2001) present the theoretical and finite element formulations of the 2D problem of water injection in discrete fractured media with capillary pressure. They state that dual-porosity models are very powerful for sugar-cube representations in water-wet media, but for a mixed-wet system, the evaluation of the transfer function becomes complicated due to the effect of gravity.

Taleghani (2010) study the effect of natural fractures on stimulated fracture paths, in particular the conditions required to initiate new hydraulic fractures at "kinks" where propagating fractures meet natural fractures. Having joined a natural fracture and traveled some distance along its length, further stimulation may cause a fracture to initiate in the opposite direction, as in Figure 2.7.1. They investigate this process by calculating energy release rates via the Contour Integral Method, which they describe briefly noting that it does not require calculating displacement derivatives or the calculation of stresses. The energy release rate G is calculated from mode I and II (tensile and shearing mode) stress intensity factors K_I and K_{II}: $G = \frac{(K_I^2 - K_{II}^2)}{E^*}$ where $E^* = E$ for plane stress and $E^* = \frac{E}{(1-\nu^2)}$ for plane strain. If $G > G_c$, the fracture will propagate critically (cf. sub-critical crack growth, see 2.3.2). Taleghani (2010) give formulations for the stress intensity factors required to calculate G at a given angle, commenting that crack growth will occur in the direction maximising G.
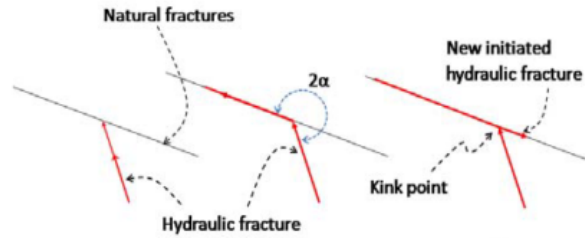
Figure 2.7.1: Fracture re-initiation(Taleghani, 2010)

Fracture growth is simulated using the extended finite element method (XFEM), which is designed to handle discontinuities such as those occurring at fractures. Sets of natural fractures are modelled in 2D at two orientations - 30 and 60 degrees from σ_{Hmax}, finding that the 60 degree case produced new fracture initiation. Adding horizontal stress differences reduced the amount of re-initiation.

Wu et al. (2009) comment that the discrete fracture approach is the more rigorous of the three formulations, but is limited by the computational intensity required and lack of knowledge of fracture and matrix properties and their spatial distributions within reservoirs.

Warpinski et al. (2009) suggests that modelling of fracture treatments in this type of reservoir is complicated by the poor understanding of the processes that occur during the treatment, and the lack of experimentally derived geomechanical and flow data. Proxy information, mainly from sonic logs, are routinely used to compute stress profiles based on usually inappropriate assumptions of rock mass behaviour; i.e. linearly elasticity (even though all rocks are fractured) together with vertical dynamic property measurements along a relatively competent wellbore represent the heterogeneous transverse isotropic response. For the shale-gas formations, the complexity of the hydraulic fracture process makes it very difficult to formulate phenomenological algorithms to describe the fundamental behaviour. Furthermore, the asymmetry observed in many mapping tests suggests that various combinations of rock, stress, and natural fracture features have a major influence on the development of the fracture network. Models therefore need to account for the primary hydraulic fracture that connects to the wellbore and the activation and opening of the network of fractures that are connected to it.

2.8 Summary of Literature Review

A review of studies on shale mechanical properties, mineral makeup, and properties related to fluid flow was presented. Many prospective shales are relatively brittle, as ductile materials do not support the fracturing required to increase production from the ultra low

(nD) permeability medium. A wide range of geomechanical properties can be observed in shales. Brittleness is in part due to a reduced clay content, which in turn has a negative effect on permeability.

The presence of natural fractures in brittle shales in particular is commonplace, and several studies on natural fracture scale, abundance and orientation provide useful background information.

Key findings from the literature review are:

- The term shale is used extremely loosely when applied to "shale gas resource plays". In the past, geologists have tended to regard shales as being extremely fine-grained fissile rocks with high clay contents (i.e. >70%). Most producing shale reservoirs are not fissile and often contain clay contents of less than 30%; their mineralogy is dominated by quartz and/or calcite.

- Until recently, there has been a tendency in industry to treat shale gas reservoirs as linearly elastic isotropic materials. Service companies are now selling wireline logging tools (sonic dipole) that are capable of measuring Young's modulus in the vertical and horizontal plane so these results have now been incorporated into formulations to predict the pressure at which fractures are likely to form. In reality shales are likely to be vertically transverse isotropic (VTI) materials which require five elastic constants to characterise their elastic behaviour.

- Industry has tended to treat the effective stress parameter for volume change (i.e. Biot parameter) as being isotropic and equal to unity. This is unlikely to be the case in shale reservoirs which are both anisotropic and have a framework modulus that is similar to the mineral modulus. The Biot parameter has a fundamental control on horizontal stress – pore pressure coupling and therefore gaining an understanding of its magnitude is important regarding how the propagation of fractures formed in partially depleted shales (i.e. refracing jobs).

- The optimal combination of fracing fluids and proppant size depends on both the fracture complexity and the brittleness of the shale. Predicting shale brittleness and fracture complexity could therefore help optimise fracture treatments.

- A range of modelling techniques can be used to model flow and mechanical deformation within shale reservoirs.

- Most studies seem to agree that there is no single rule for natural fracture properties in shales, and that modelling specific to the particular reservoir is essential. Several difficulties associated with characterisation of natural fractures were discussed.

Much of the literature regarding the modelling of hydraulic fracturing comprises the details of specific approaches, and published simulation results justifiably tend towards isolated examples that demonstrate the strong points of the particular approach. This study will be using a combined technique which marries the strengths of conventional FEM with discrete approaches to modelling fractures. As a commercial product, small scale validation has already been performed as part of rigorous pre-release testing. The software will be applied to investigate complex interactions between multiple fractures, aiming to provide a view of fracturing in shales that is not routinely seen in published works.

Chapter 3

Hydraulic Fracturing Simulation

3.1 Introduction

The simulations in this study have been conducted using "Elfen TGR[1]" which is a state-of-the-art finite and discrete element software that has been specifically designed to address reservoir geomechanics. It is capable of modelling many aspects of hydraulic fracturing, including non-Newtonian fracturing fluids, fluid leakoff, proppant transport, as well as gas production in Darcy and non-Darcy flow regimes. Many of the more advanced features were developed during the course of this study, which has been focused on fracture propagation in shales, with low viscosity Newtonian fluid. The following sections contain details of the theory used in Elfen TGR, omitting discussions of some of the more advanced capabilities that were not applied.

3.2 Overview

Elfen TGR carries out a coupled multi-field finite and discrete element analysis. A geomechanical analysis of the rock matrix is coupled with pore fluid seepage and fracture fluid flow analyses. The combined seepage and network fields are referred to as "seepnet", which is a term simply derived from "seepage" and "network".

The Elfen TGR modelling process is driven by three main sets of equations:

1. Mechanical stresses and fluid pore pressures of the rock formation (mechanical equation)

---

[1]Developed in Swansea, Wales. Elfen is the Welsh word for "Element", TGR is an acronym of **T**ight **G**as **R**eservoirs

2. Porous flow in the rock formation (liquid and gas seepage equations)

3. Fluid flow in the fracture region (liquid and gas network equations)

Two types of solution algorithms are used:

- For the mechanical field, the explicit solution method is used. This approach is conditionally stable and the time step is limited to maintain stability. However, it does not require the inversion of a matrix to update the primary field variable – making it computationally inexpensive - and it can be used where situations such as strain softening of materials make the enforcement of a convergence condition difficult.

- For the seepage and flow fields (both liquid and gas), the implicit solution method is used. This approach is unconditionally stable and allows the use of large time increments. In solving the seepnet field, convergence conditions are generally easily enforced, making the implicit method suitable. However, it does require the inversion of a matrix, which can be computationally costly.

3.2.1 Validation

Rockfield Software have performed extensive in-house validation of the modelling software. The plane strain model used can be validated against a well known 2D fracture model known as the KGD (for Khristianovic-Geertsma-de Klerk). The Elfen TGR model fits the following assumptions made in the KGD model:

- vertical fracture propagating in a straight line from the well

- restricted fracture height

- homogeneous, isotropic, linear elastic rock mass

- purely viscous fluid in laminar flow regime

- geometric fracture-extension patterns are simple

- rectangular vertical cross-section of fracture

- plane strain conditions in the horizontal plane

56
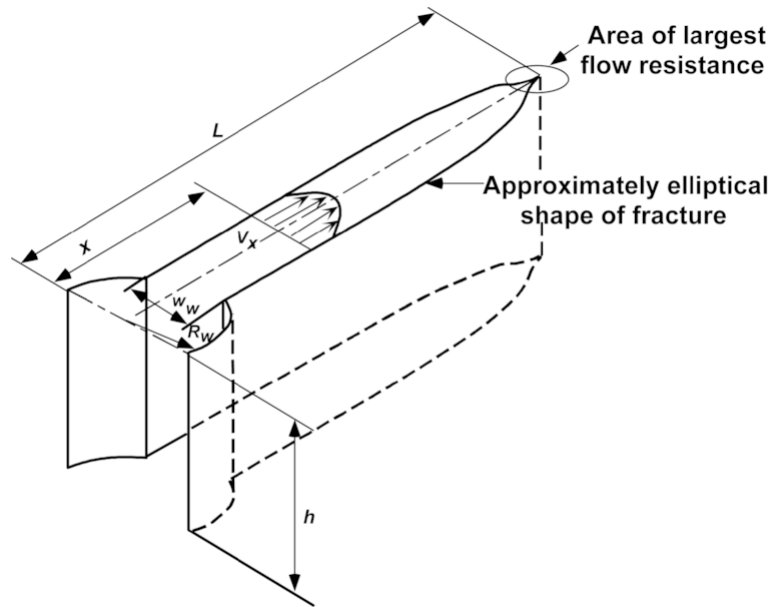
Figure 3.2.1: KGD 2D fracture model

An example of an Elfen TGR validation of fracture length against the analytical KGD is shown in Figure 3.2.2.
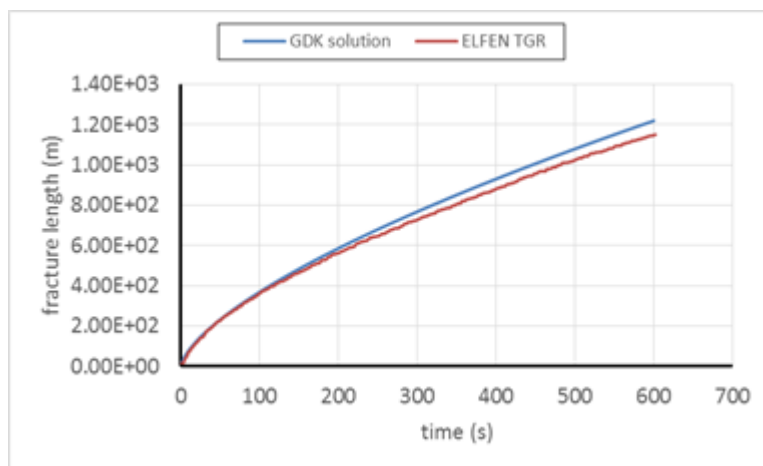
Figure 3.2.2: Elfen TGR analytical model validation

3.3 Governing Equations

The main equations governing the simulations are derived assuming the following conditions:

1. Equilibrium of stresses with an appropriate constitutive model (mechanical analysis)

2. Mass conservation with Darcy's law (liquid seepage analysis) and fracture region liquid flow characteristics (liquid network analysis).

Note that a distinction is made between a pore fluid and its components:

- a pore *fluid* can refer to either a *liquid* or *ga*s body

- *liquid* and *gas* components are specifically referred to as such.

For example, p_f would refer to a fluid pore pressure which could either be liquid or gas, p_l refers to a liquid pore pressure, p_g refers to a gas pore pressure.

In the mechanical equation, the pore pressure could be either liquid or gas, so the pore fluid label, i.e. p_f, is appropriate.

For the seepage and network equations, a distinction must be made between liquid and gas components, since each has separate treatment at the fundamental equation level. For example, in the liquid seepage equation the fluid is assumed to be incompressible, whilst fluid compressibility is permitted in the gas seepage equation. At present, at any part of the simulation, only single phase flow is considered, and interaction between the two phases is not modelled.

Mechanical   The update of the mechanical stresses satisfies the momentum balance equation, with the assumption that the fluid acceleration relative to the solid and the convective terms can be neglected.

$$\mathbf{L}^{\mathbf{T}} \left(\boldsymbol{\sigma}' - \alpha \mathbf{m} p_l \right) + \rho \mathbf{g} = 0 \tag{3.3.1}$$

$$\rho = \rho_l \phi + \rho_s \left(1 - \phi \right) \tag{3.3.2}$$

where:

Symbol	Explanation
$\mathbf{L}$	spatial differential operator
$\boldsymbol{\sigma}'$	effective stress tensor
α	Biot parameter
$\mathbf{m}$	vector which in 2D is of the form $\{1,1,0\}^T$
p_f	pore fluid pressure
ρ	density of the solid/fluid mixture
ρ_l	pore fluid density
ρ_s	density of the solid grains
ϕ	porosity of the porous medium
$\mathbf{g}$	gravity vector

Table 3.1: Nomenclature for equation 3.3.1

Porous Flow The liquid seepage equation combines mass conservation along with Darcy's law and is summarised in equation 3.3.3

$$\nabla \cdot \left(\frac{k}{\mu_l} \left(\nabla p_l - \rho_l \mathbf{g} \right) \right) = \left(\frac{\phi}{K_l} + \frac{\alpha - \phi}{K_s} \right) \frac{\partial p_l}{\partial t} + \alpha \frac{\partial \epsilon_v}{\partial t} \tag{3.3.3}$$

where :

Symbol	Explanation
k	intrinsic or absolute permeability of the porous medium
μ_l	viscosity of the pore liquid
p_l	pore liquid pressure
ρ_l	density of the pore fluid
$\mathbf{g}$	gravity vector
ϕ	porosity of the porous medium
α	Biot coefficient
K_l	bulk stiffness of the pore liquid
K_s	bulk stiffness of the solid grains
ϵ_v	volumetric strain of the porous medium

Table 3.2: Nomenclature for equation 3.3.3

Liquid Flow within Fractures Similar to the liquid seepage equation, the liquid network equation combines mass conservation along with Darcy's law and is summarised in equation 3.3.4.

$$\frac{\partial}{\partial x} \left[k_{fr} \left(\frac{\partial p_l}{\partial x} - \rho_l \mathbf{g} \right) \right] = S_{fr} \frac{\partial p_l}{\partial t} \tag{3.3.4}$$

where:

Symbol	Explanation
k_{fr}	intrinsic or absolute permeability of the fractured region
p_l	pore liquid pressure
ρ_l	density of the pore liquid
g	gravity vector
S_{fr}	storage coefficient of the porous medium

Table 3.3: Nomenclature for equation 3.3.4

The intrinsic permeability k_{fr} and storage coefficient S_{fr} are defined as follows (Elfen TGR provides two network flow definitions; this is the aperture based definition used in the simulations herein):

- $k_{fr} = \frac{e^2}{12\mu_l}$

- $S_{fr} = \left(\frac{1}{K_{fr,n}} + \frac{e}{K_f} \right)$

where:

- e is the fracture equivalent aperture (see equation 3.3.5)

- μ_l is the viscosity of the pore liquid

- $K_{fr,n}$ is the normal stiffness of the fracture

- K_f is the bulk stiffness of the fracturing fluid

The storage term thus reflects the compressibilities of both the fluid and rock. This definition was developed around the concept of parallel plate flow, and was first derived for solid interfaces with smooth walls (parallel fractures) which are only an approximation of reality. In Elfen TGR, the fracture aperture of a wedge-shaped, non-parallel fracture has been taken as an equivalent aperture e with a modification factor F to the mean fracture aperture e_m:

$$e = \frac{e_m}{F} = e_m \sqrt[3]{\frac{16r_e^2}{(1 + r_e^2)^4}} \tag{3.3.5}$$

where r_e is the ratio between the apertures at the ends of the network element, e_a and e_b: $r_e = \frac{e_a}{e_b}$. The mean hydraulic radius e_m is simply $e_m = \frac{e_a + e_b}{2}$.

3.4 Time Integration

The mechanical governing equation is solved explicitly, which means that the time step to advance the solution is conditionally stable and, with the very stiff shales often observed in tight gas reservoirs, can be relatively small.

Conversely, the liquid seepage, liquid network, mass transport and heat flow governing equations (where appropriate) are solved implicitly.

In practice, this mixing of solution schemes results, for a given time interval, in many more time steps in the explicit scheme compared against the implicit scheme. Therefore, some form of interpolation of the field variable, in this instance the liquid seepage and liquid network pore pressures, is required on the explicit side between coupling times.

3.5 Models

3.5.1 Mechanical Model

Elfen TGR has several mechanical models available for use. For the simulations discussed in later chapters, a Mohr-Coulomb with Rankine corner material was used to represent the shale. The Mohr-Coulomb yield criterion is a generalisation of the Coulomb friction failure law and is defined by

$$\tau = c - \sigma_n tan\phi \qquad (3.5.1)$$

where :

- τ is the magnitude of the shear stress

- σ_n is the mean effective stress

- c is the cohesion

- ϕ is the friction angle.

In principal stress space, the yield surface is a six-sided conical shape. The conical nature of the yield surface reflects the influence of pressure on the yield stress and the criterion is applicable to rock, concrete and soil problems. The implementation includes a tension cut-off in the form of a complete Rankine tensile corner, as opposed to a hydrostatic cut-off. The Rankine tensile corner introduces additional yield criteria defined by:

$$\sigma_i - \sigma_t = 0 \quad i = 1, 2, 3 \tag{3.5.2}$$

where

- σ_i refers to each principal stress

- σ_t is the tensile strength

Although at present no explicit softening law is included for the tensile strength, indirect softening does result from the degradation of cohesion according to the following criterion:

$$\sigma_t \leq c \frac{(1 - \sin \phi)}{\cos \phi} \tag{3.5.3}$$

This ensures that a compressive normal stress always exists on the failure shear plane. Figure 3.5.1 illustrates the yield surface according to this model.
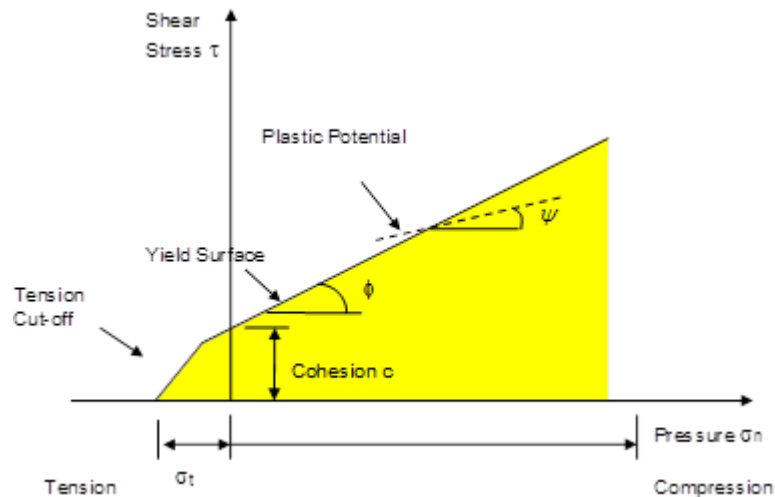
Figure 3.5.1: Yield Surface for the Mohr-Coulomb Model

Figure 3.5.2 shows the yield surface in principal stress space both without (a) and with (b) the Rankine Tensile Corner.

Failure The Mohr-Coulomb model is combined with a Rankine Crack formulation to represent failure in tension and subsequent fracture. Two parameters are required:

- Tensile Strength σ_t
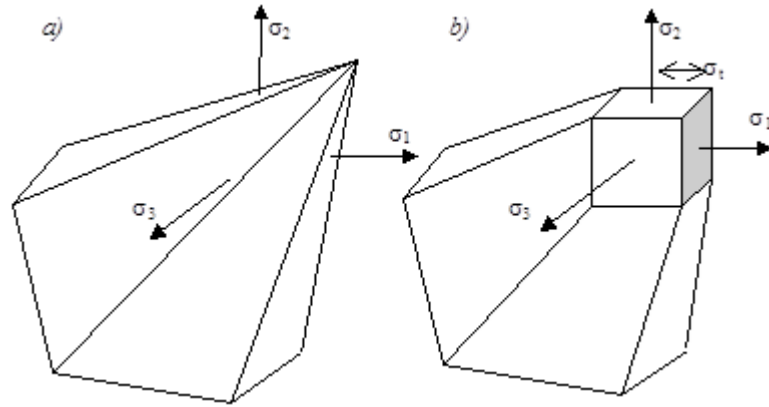
Figure 3.5.2: Yield Surface for the Mohr-Coulomb Model in Principal Stress Space

- Fracture Energy G_f

Once the material has reached its tensile strength, it softens and finally fails once the appropriate amount of fracture energy has been released. This is illustrated in Figure 3.5.3- the softening slope E_T is defined as:

$$E_T = \frac{\sigma_t^2 l_c}{2G_f} \tag{3.5.4}$$

where l_c is the characteristic length scale, and is incorporated into the material model characterisation process. This diagram also shows the softened Young's modulus E_S .
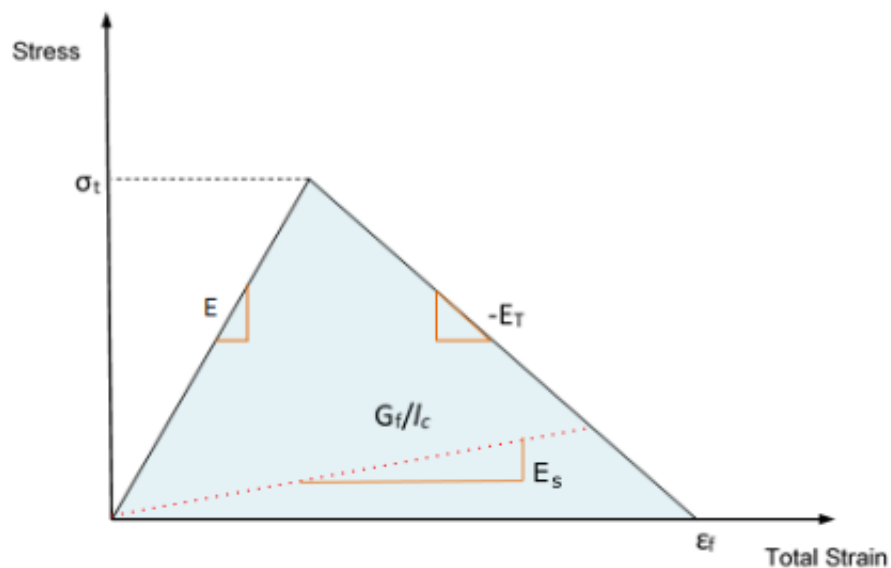
Figure 3.5.3: Failure: General Expression

3.5.2 Liquid Model

Elfen TGR makes available both Newtonian and non-Newtonian fluids. In the following chapters, simulations were restricted to Newtonian, low viscosity fluids.

The following assumptions are made to (proppantless) fluid flow within fractures:

- The fluid is incompressible.

- Flow is locally equivalent to the flow between two smooth, parallel plates.

- Flow is laminar, with a low Reynolds number.

- Gravity is not considered.

Newtonian Fluid   A simple, constant viscosity fluid was used:

$$\tau_f = \mu\gamma \tag{3.5.5}$$

where

- μ is the constant Newtonian viscosity

- γ is the shear rate

- τ_f is the shear stress in the fluid

Although Newtonian fluids are not frequently used in general for hydraulic fracturing operations (Detournay, 2016), a low and constant viscosity fluid is applicable to treatments of brittle shales. More viscous, non Newtonian gels and polymers are often used in higher permeability media.

3.6   Fracturing with Local Remeshing

One of the key difficulties with modelling hydraulic fracturing, in particular when interacting with pre-existing fractures, is the huge range of scale that must be accounted for in the simulation. To correctly capture near-fracture events, element sizes must be small; typically well under 1 m. However, the fracture is likely to travel hundreds of metres in a domain in the order of kilometres in size. Elfen TGR makes extensive use of a local remeshing technique which allows a fine mesh to be maintained at the fracture tip as it travels, while keeping a relatively coarse mesh throughout the rest of the domain.

This method results in much higher quality fracture geometry than other schemes which rely on fracturing along element boundaries. Authors such as Fu et al. (2012) argue that a regular triangular mesh allows a fracture to change direction in increments of 45°, and that multiple direction changes can be summated to achieve any desired fracture path. The motivation behind the development of the following scheme was the mesh dependence which element boundary fracturing schemes enforce.

3.6.1 Fracture Prediction

The insertion of a fracture is based on a failure indicator F^S:

$$F^S = \frac{2F^R - 1}{F^R} \tag{3.6.1}$$

where

$$F^R = \frac{\sigma_t}{\sigma_1 + \sigma_t} \tag{3.6.2}$$

A local nodal failure model defines the local average nodal failure factor for a node F^f as

$$F^f = \max \left(F^S : \text{all adjacent elements} \right) \tag{3.6.3}$$

A non-local nodal failure model is used in Elfen TGR, which is based on the failure path predicted by a patch of damaged adjacent elements. The methodology for evaluating the fracture path direction and length is as follows:

- Monitor nodal failure factors F^f, and when a node's value exceeds 1.0, introduce a failure path.

- Extend the failure path as adjacent elements in the fracture direction fail. Fracture direction is defined as perpendicular to the maximum tensile principle stress.

- When failure path exceeds a specified length all points along path are used to form the fracture. The fracture polyline is smoothed by a linear function.

3.6.2 Fracture Insertion

A requirement of the coupled geomechanical-flow network-seepage analysis is that the nodes on either side of a fracture match with the nodes on the fracture flow network - this is to ensure conservation of the liquid/gas flow into/out of the matrix from the flow network.

To generate a matching matrix/flow network mesh, the fracture surfaces and flow network are first merged to a single geometric line - see Figure 3.6.1.
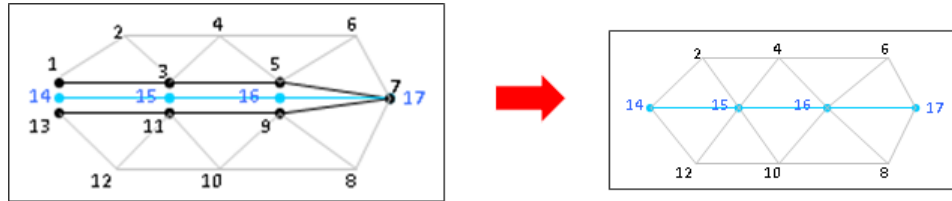
Figure 3.6.1: Mesh collapse prior to insertion

The proposed fracture path polyline is then added to the existing fracture geometry. Elements crossed by the new fracture geometry are identified and marked as "seed elements". A zone of a configurable number of layers of elements around the seed elements becomes the local remesh patch. This is illustrated in Figure 3.6.2. The local remesh patch is able to selectively refine the patch, as well as de-refine regions outside it. This greatly reduces runtime in comparison to performing a remesh of the entire model. Local remeshing also allows a coarser mesh to be used initially, since the refinement around new fracture geometry ensures that there is a fine mesh ahead of the fracture tip. Dere-finement can reduce the effect of continually refining around the propagating fracture; the result is a fine mesh around the current fracture tip, with a slightly coarser mesh along the rest of the fracture.
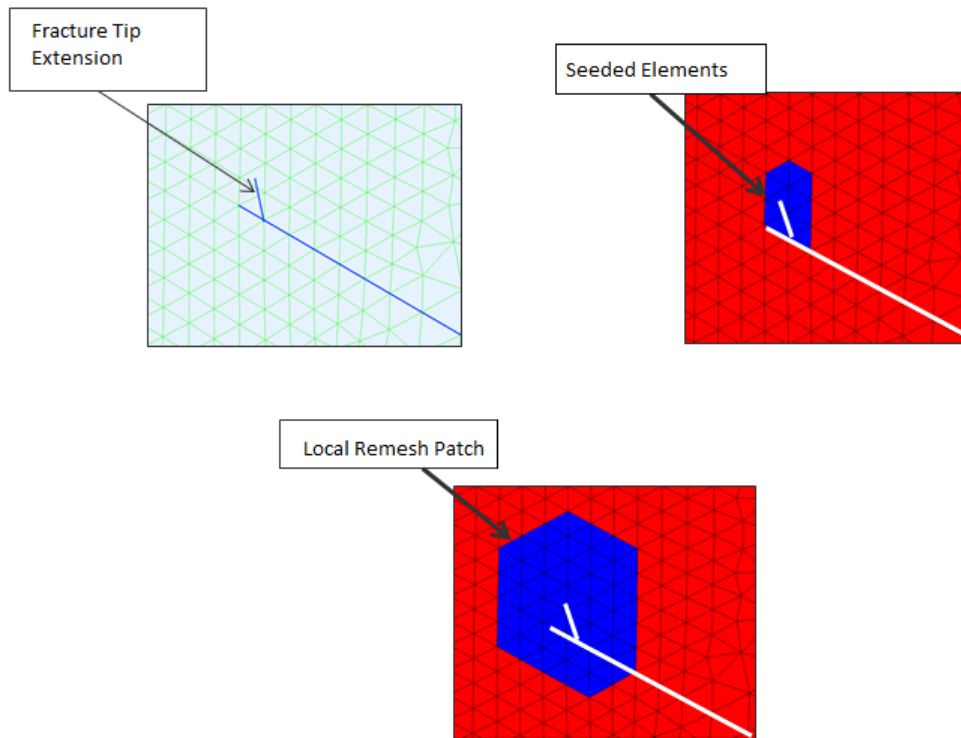
Figure 3.6.2: Local Remesh Patch Identification

Once the local patch has been remeshed, all state variables from the old mesh patch are mapped to the new patch. The fracture is then reinflated, reversing the process illustrated in Figure 3.6.1.

3.7 Results Visualisation

Most of the result visualisation techniques employed in this work will be familiar or intuitive to the reader. Contour plots, which colour the simulation domain according to the magnitude of a scalar variable, are commonplace. Simple 2D tensor visualisations are also used throughout, these show two orthogonal lines at nodal positions which indicate principal stress orientations, and their lengths are scaled according to their magnitudes. The line colours differentiate the tensor components.

A less common technique employed regularly here are Line Integral Convolution (LIC) plots. LIC is an image convolution technique first described in Cabral and Leedom (1993), and is used here to display the principal stress field. The maximum principal stress vector is used as in input to advect a random noise image; for each point in the output, two streamlines are calculated using the stress field components - one forwards and one

backwards. The colours of the noise image lying on the streamlines are combined to arrive at a final value for the output point. The advected noise image replaces the original noise image, and the process is repeated several times to arrive at the final plot. The noise image is greyscale, and colour is introduced to the final output to represent the magnitude of a given value, which for the stress field is a stress intensity ($\sigma_I = \sqrt{\sigma_{11}^2 + \sigma_{22}^2}$). In this work, the colour range is often selected to emphasise the field direction only.

3.8 Conventions

Conventions used to describe relative stress magnitudes in Elfen are not the same as those typically used in geomechanics. In Elfen, tensile stresses are positive, and σ_{11} is the most tensile stress. In the 2D simulations throughout this work, all are in plan view unless otherwise stated, and are plane strain simulations under normal faulting conditions (i.e. $\sigma_V > \sigma_{Hmax}$). Contour keys in screenshots obtained from Elfen will label the horizontal principal stresses as either σ_{11} or σ_{22}, whereas from a geomechanics perspective, σ_V would be σ_{11}.

It should be made clear in any discussion of contour plot screenshots exactly what is being described, however for reference the following Table 3.4 should clarify any doubt. Furthermore, note that typically Elfen displays effective stresses.

Elfen	Geomechanics	Alternative	Description
σ_{11}	σ_{33}	σ_{Hmin}	Most Tensile/Least Compressive Principal Stress
σ_{22}	σ_{22}	σ_{Hmax}	Intermediate Principal Stress
σ_{33}	σ_{11}	σ_V	Least Tensile/Most Compressive Stress

Table 3.4: Elfen vs Geomechanics Notation for Normal Faulting

Chapter 4

Modelling the Texas Two Step Method

4.1 Introduction

One of the simplest forms of fracturing a horizontal well is simultaneous stimulation of transverse fractures. In common with current fracturing treatments, it requires first perforating the well at intervals along its length. Perforation clusters (or intervals in some literature) are created using high energy methods, including shaped charge explosives, resulting in perforations through the well casing and opening starter fractures in the rock. The term opening is used loosely here, as "blasting" or "shattering" may be more appropriate. "Opening", as used in the rest of this work, is a specific mode of fracture propagation caused by fracture walls being pulled apart.

The starter fractures are designed to ensure fracturing initiates at specific intervals along the well. A simultaneous stimulation will isolate a section of the well using a packer, and pump the well full of fracturing fluid, creating multiple parallel fractures transverse to the well. A key decision made in this type of fracturing is the spacing of the perforations, since the stress changes induced by the opening of each fracture can interact with each other and produce a phenomenon known as stress shadowing.

Stress shadowing is a well known and studied issue in hydraulic fracturing (Olson, 2004, Fisher et al., 2004, Soliman et al., 2008, Morrill and Miskimins, 2012). Although each fracture in the scenario described is stimulated at the same time and rate, they experience increased stresses to varying degrees based on their location relative to the other fractures. In a group of 3 or more fractures, the outer fractures see increased lateral stress acting on their walls from one side only, and since the other side is relatively free to move, are easier to propagate. The central group of fractures are usually significantly shorter

69

than the outer fractures due to this phenomenon. It is also common to see the outer fractures bending away from the zone of higher stresses, before realigning with the in-situ stresses once beyond the influence of the central fractures. The amount of increased stress experienced by each fracture decreases with distance, and at a suitable spacing, the fracture lengths will be very similar. The balance for an operator using this method of stimulation is getting the spacing right; too close together and the preferential growth of the outer fractures will render the central fractures relatively unproductive, too far apart and gas recovery rates per length of well will be low.

The Texas Two Step Method (Soliman et al., 2010), abbreviated as TTSM throughout this work, is a fracturing treatment that is sequential, i.e. rather than stimulating a series of fractures at the same time, individual perforation clusters are isolated using movable sleeves and treated individually. The method is named after a country and western dance which allegedly involves taking two steps forward and one step back. For a series of fractures, the first cluster is stimulated and held open, while the third (i.e. two steps forward down the well) is then stimulated. Once the fracture from the third cluster has grown, the injection point is moved back one cluster and the second cluster, now in the space between two open fractures, is stimulated. See Figure 4.1.1 for a schematic of the early stages of a TTSM treatment.
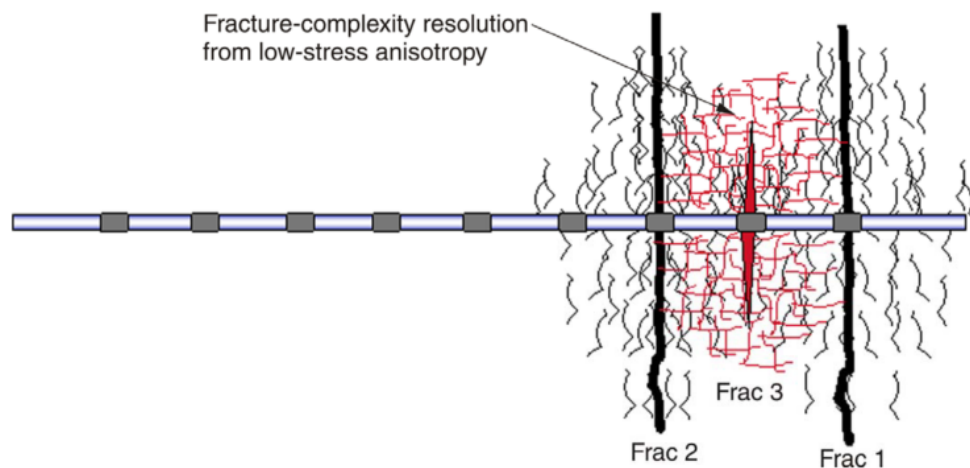
Figure 4.1.1: TTSM schematic (Soliman et al., 2010)

An important property of the stress increases following fracture insertion is that the lateral stresses are increased more than the longitudinal. This is especially important considering that the hydraulic fracture propagates in the direction perpendicular to the minimum stress, and that stress increases from neighbouring fractures can be linearly superimposed. Assuming a certain amount of stress anisotropy, the resulting effect is that the minimum horizontal stress between the first two fractures is increased, and this will result

70

in a reduction of stress anisotropy. Given appropriate conditions, the principal stresses may even become reversed. Soliman et al. (2010) argue that this alteration of the stress field between the two first fractures creates a stress state conducive to increased fracture complexity. This is based on the idea that reducing the stress anisotropy may allow natural fractures to open during stimulation of the third fracture, creating a "swarm" of fractures. Alternatively, if the anisotropy is reversed, they propose that a longitudinal fracture between the first two would be created.

Jo (2012) examined this technique further, using the Boundary Element Method to model the first two fractures propagating sequentially. The effect of fracture spacing on the geometry of the second fracture was examined. Beyond a certain spacing, the second fracture deviated away from the first (a "repulsive" path), and conversely at distances less than this spacing, the second fracture curved towards the first, taking an "attractive" path.

In this chapter, a series of simulations were performed using Elfen TGR to examine various effects associated with the TTSM and look at some of the points raised in Jo (2012). The simulations modelled the propagation of the first two fractures in a TTSM cycle, and consider the effects on the area between them. Later chapters examine issues relevant to the propagation of the third fracture, namely propagation in a modified stress field, and interaction with natural fractures.

4.2   Methodology

A series of simulations using the fully coupled hydro-mechanical analysis technique described in chapter 3 were carried out. The model is driven by a prescribed fluid flux which generates the required pressure to open a starter fracture. The 2D simulation models a plan view, i.e. at a constant depth, of a relatively thin layer of shale in a 1km square domain. Under these circumstances gravitational effects are ignored, and uniform, axis aligned stresses are used to initialise the model, as well as a uniform pore pressure.

Figure 4.2.1, from Bunger et al. (2012) is a schematic of the two fracture problem. In this chapter, the two fractures are denoted F_1 and F_2.

Figure 4.2.2 shows the the simulation model setup. Fractures initiate from injection into vertically oriented starter fractures, the horizontal distance between them being equivalent to H in figure 4.2.1. Boundary conditions on the domain include consist of fixed external boundary lines; the size of the domain in relation to the stimulated region mitigates the effects of these boundaries being unable to move.
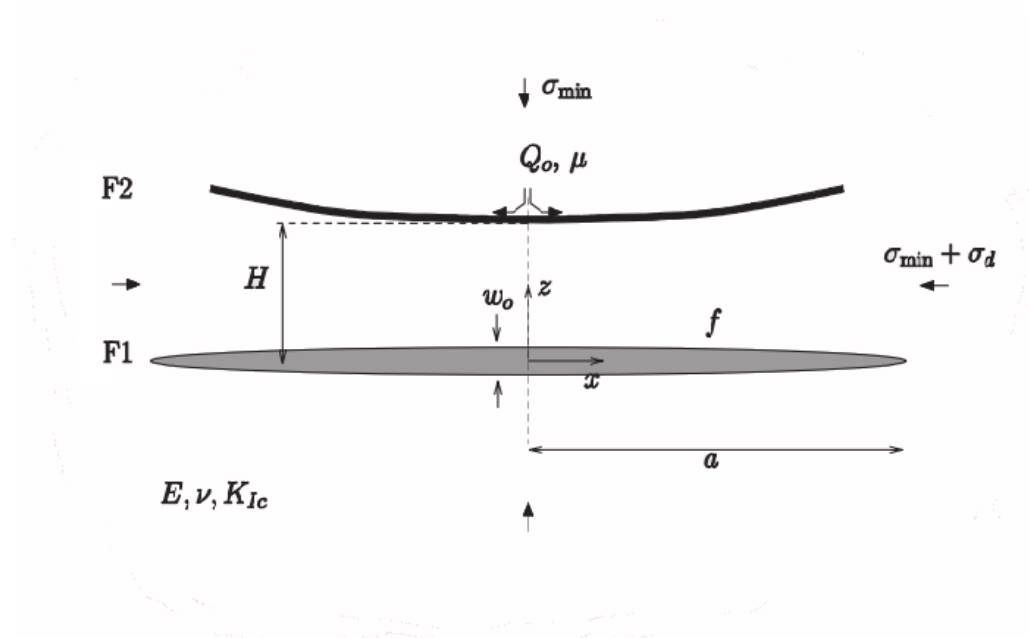
Figure 4.2.1: Outline of the problem in Bunger et al. (2012)
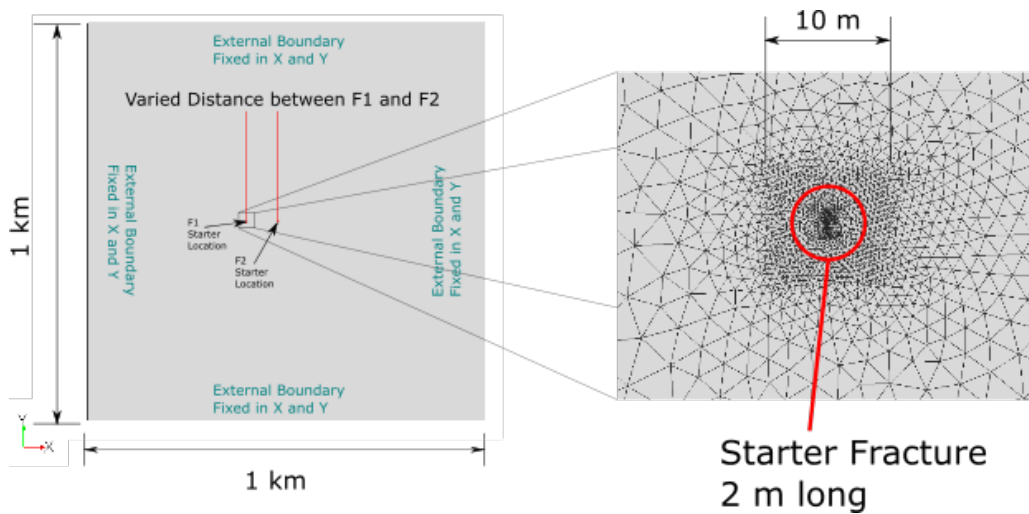
Figure 4.2.2: Simulation Initial Conditions

In a series of simulations, two fractures were opened sequentially, for each fracture pumping a volume of $10 \mathrm{~m}^3$ of slickwater at a rate of $0.1 \frac{\mathrm{m}^3}{\mathrm{s}}$. Table 4.1 lists the parameters used, unless noted otherwise. After the first fracture had taken $10 \mathrm{~m}^3$ of fluid, the flux loading was removed and the fracture isolated from the rest of the system, effectively locking the fluid in the fracture. No leak-off was modelled, to maximise the effect of the first fracture remaining open due to fluid pressure.

Parameter	Value	Unit
Young's Modulus	32	GPa
Poisson's Ratio	0.2	
Reservoir Pore Pressure	20	MPa
Effective Stress XX	10	MPa
Effective Stress YY	12.75	MPa
Effective Stress Ratio Sxx:Syy	0.7843	
Effective Stress ZZ	15	MPa
Porosity	0.01	
Fracture Height (Layer thickness)	10	m
Fluid Volume	10	m^3
Flow Rate	0.1	$\frac{m^3}{s}$
Fluid Viscosity	1.67e-3	Pa.s
Layer Height	10	m

Table 4.1: Indicative Simulation Parameters

4.3 Results

The simulation results are presented in three aspects. The geometry of the two fractures, the change in stress anisotropy between and around them, and the pressure required to open them.

4.3.1 Geometry

The geometry of simulating fractures spaced at 10, 25, 50, 100, 150, 200 and 250 m are shown superimposed upon each other in Figure 4.3.1.

In Figure 4.3.2, the geometry of the upper half-length of F_1 is shown, again with each simulation result superimposed. The plot has been scaled by an order of magnitude in the horizontal direction (x) only, to exaggerate the differences between the runs.
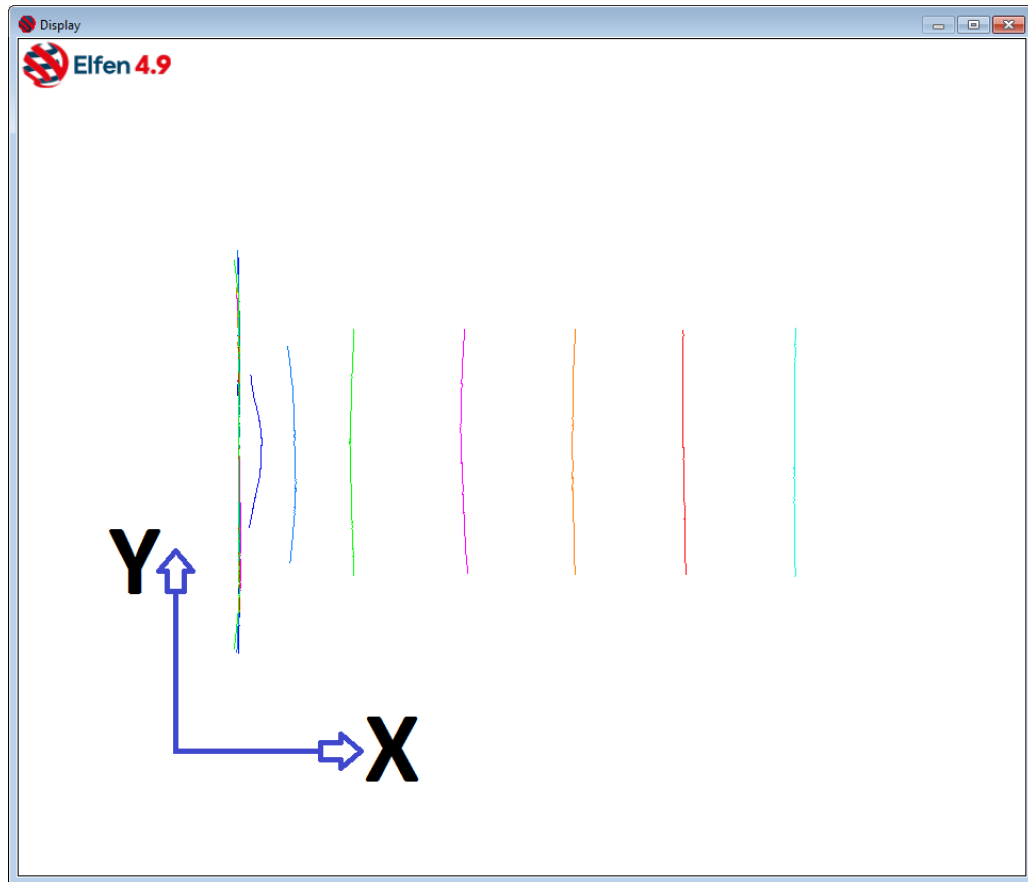
Figure 4.3.1: Fracture Geometry at 10, 25, 50,100, 150, 200 and 250 m spacing
This image shows the results of the simulations superimposed upon each other, with the F_2 fractures at each spacing clearly visible. The F_1 fractures can also be seen superimposed upon each other at the same position, and are the left most set of fractures.
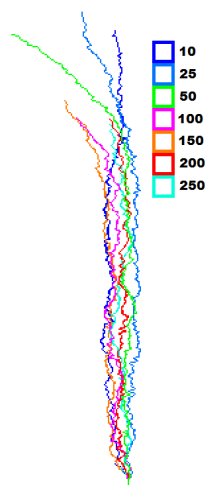
Figure 4.3.2: Half length of F_1, scaled in x by 10

Figure 4.3.3 plots the final length of the first fracture for each simulation, the aperture of F_1 and F_2 vs normalised length are presented in Figure 4.3.4 and 4.3.5 respectively.
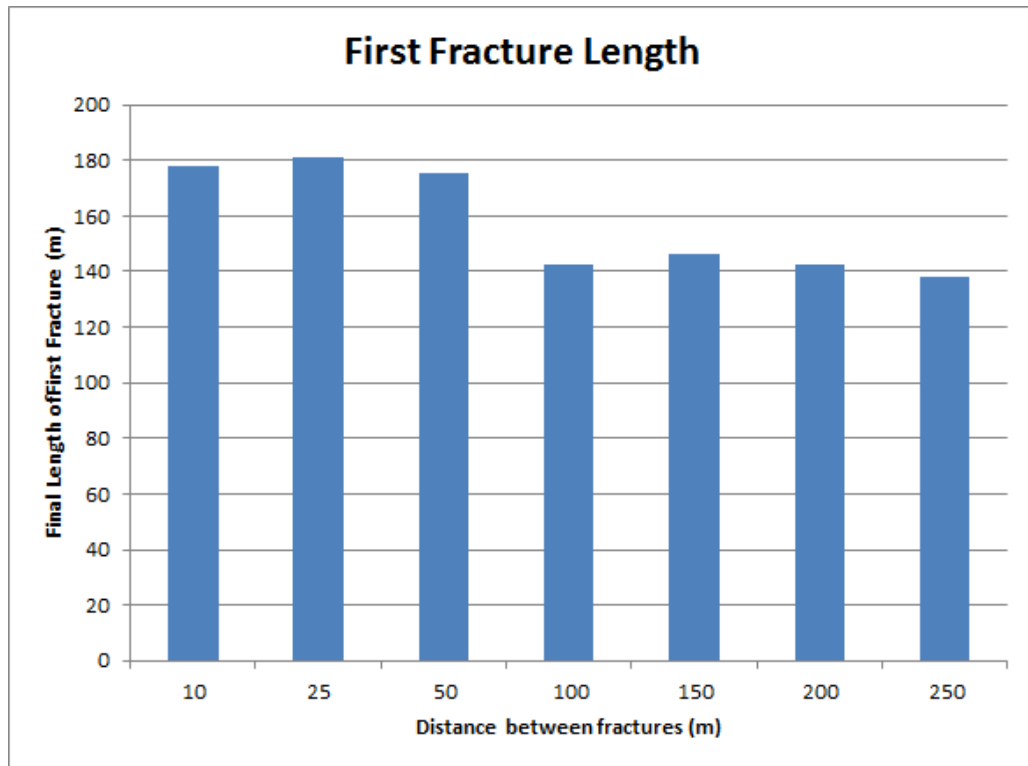
Figure 4.3.3: Final length of first fracture

4.3.2 Pressure

The pressure histories for the two extreme spacings are plotted in 4.3.6. Figure 4.3.7 is a detail of the pressure histories, showing pressure differences at the end of the simulations.
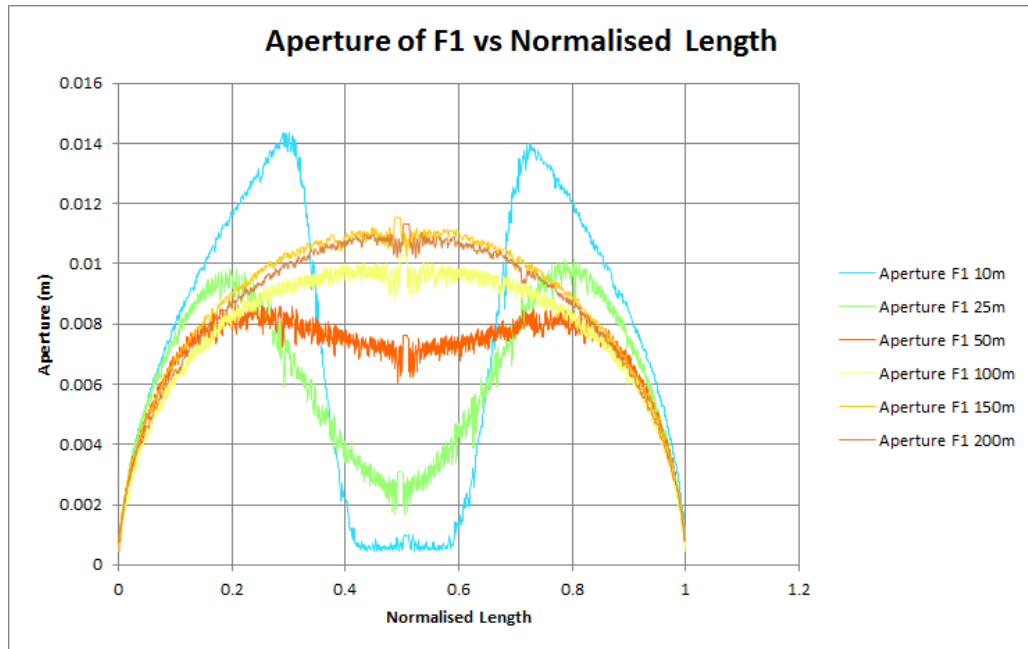
Figure 4.3.4: Aperture of F_1 vs Normalised Length
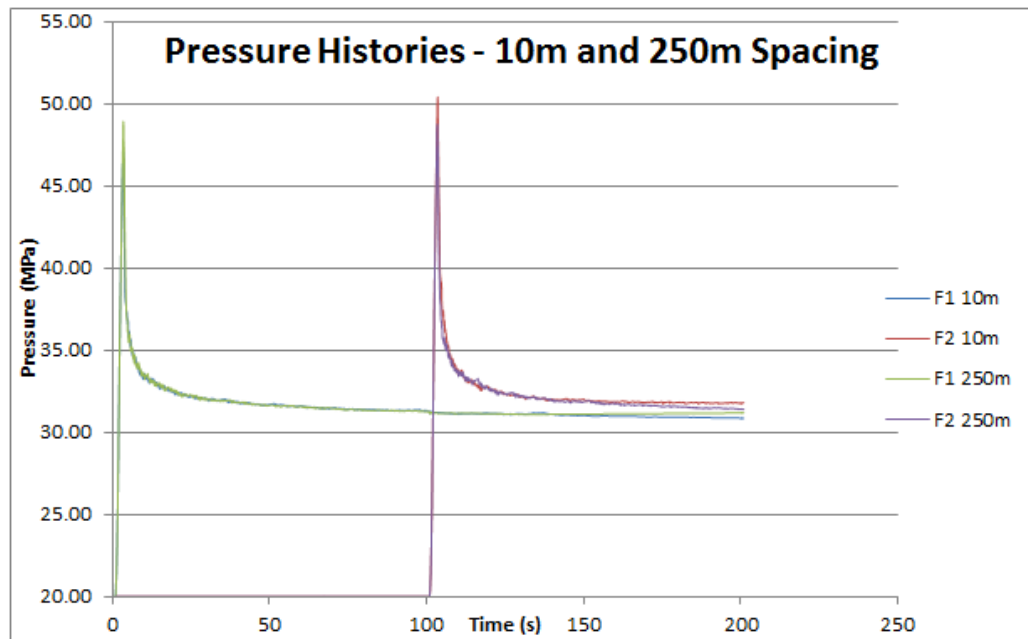
Figure 4.3.6: Pressure Histories 10m and 250m (F_1 and F_2)
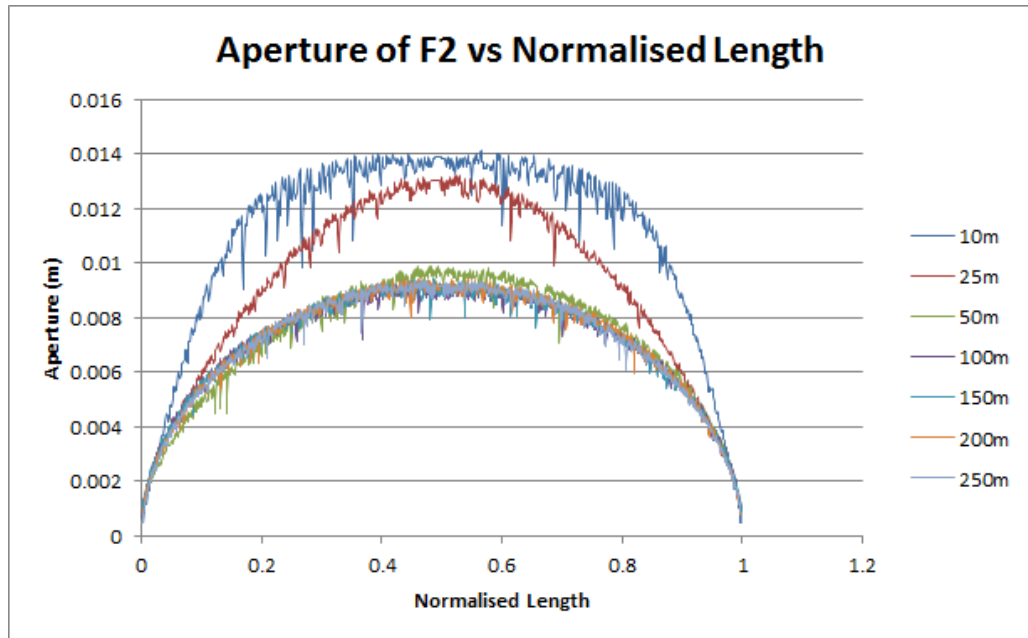
Figure 4.3.5: Aperture of F_2 vs Normalised Length
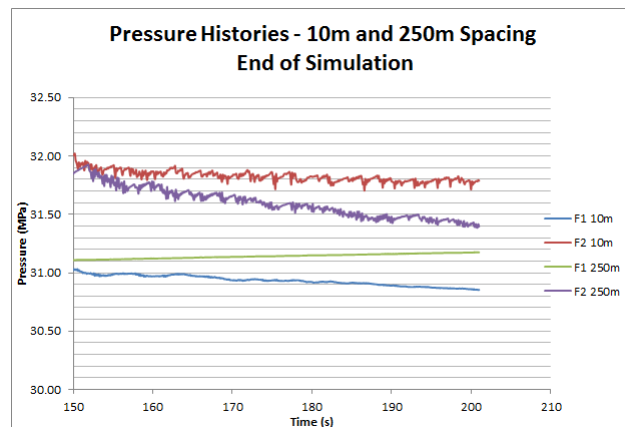
Figure 4.3.7: Pressure Histories 10m and 250m (F_1 and F_2)- End of Simulation

Figure 4.3.8 plots the net opening pressure of F_2 for each distance.
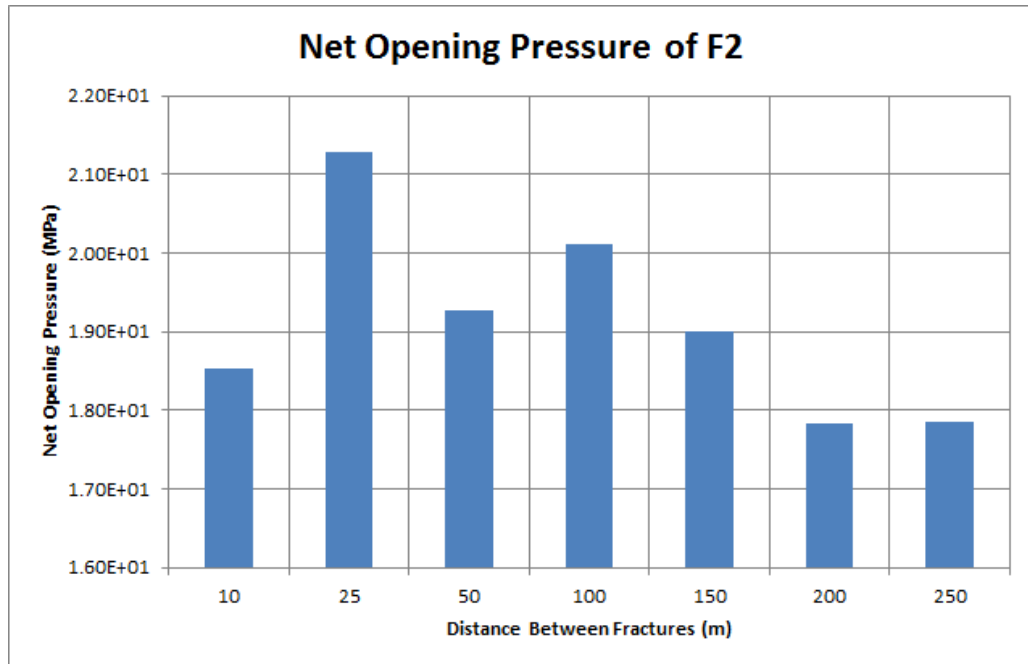
Figure 4.3.8: Net Opening Pressure of F_2

4.3.3 Stress

Soliman et al. (2008) presented the results of Sneddon's (Sneddon (1946)) solution for the stress state around semi-infinite crack, dividing the change in stresses by the net extension pressure, and plotting this against the distance from the fracture divided by the fracture length. This is evaluated along a line perpendicular to the fracture, and the resulting graph is shown in Figure 4.3.9. A similar plot can be obtained from the numerical simulations being discussed. Figure 4.3.10 plots the same change in stress/net extension pressure vs the distance from F_1 at 101s.
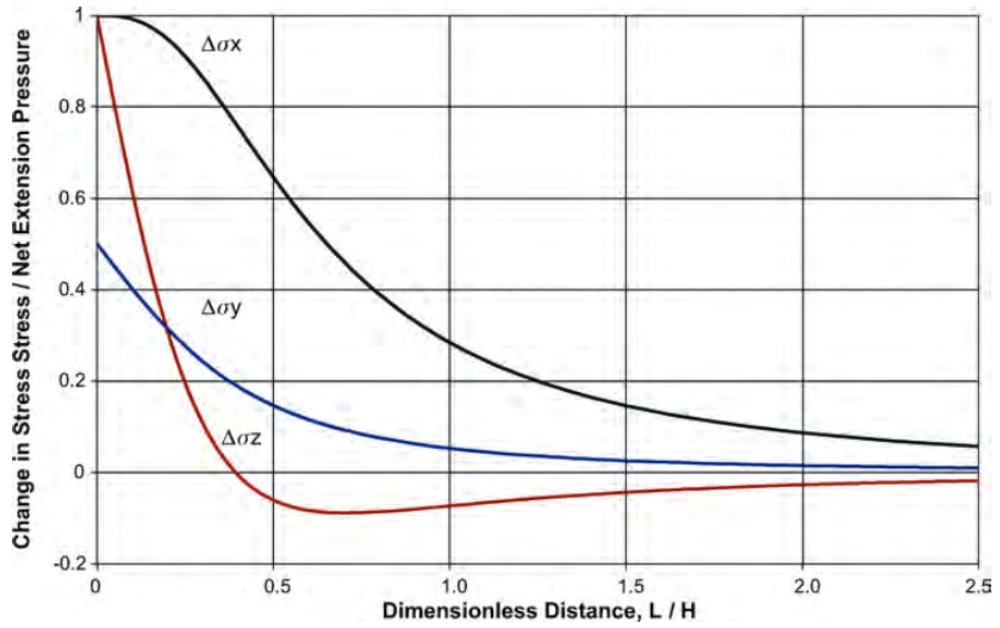
Figure 4.3.9: Dimensionless Stress Change vs Dimensionless Distance, Soliman et al. (2008)
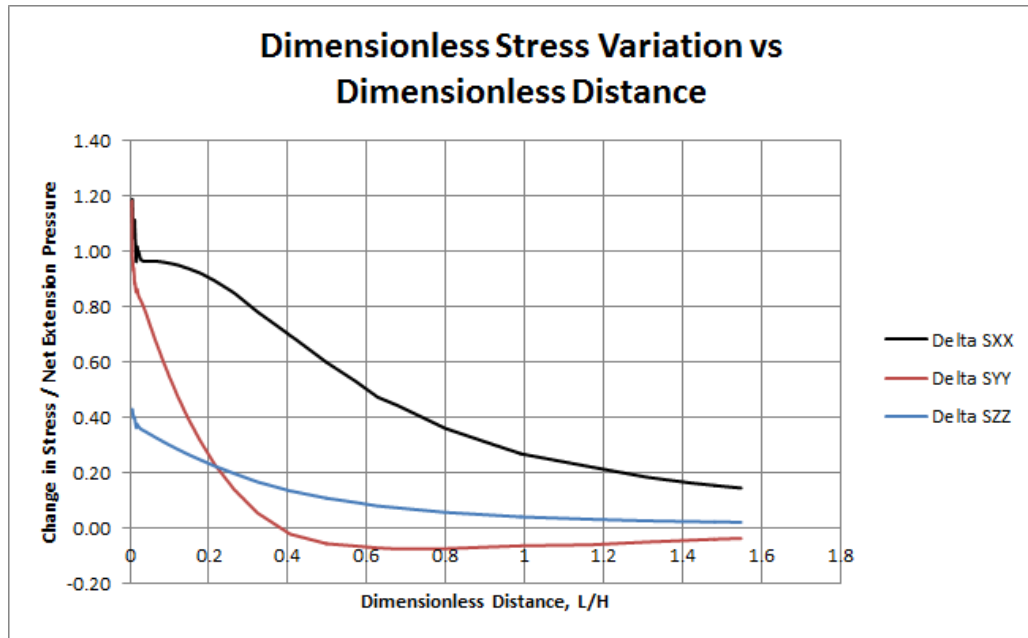
Figure 4.3.10: Dimensionless Stress Change for a Single Fracture - Simulation
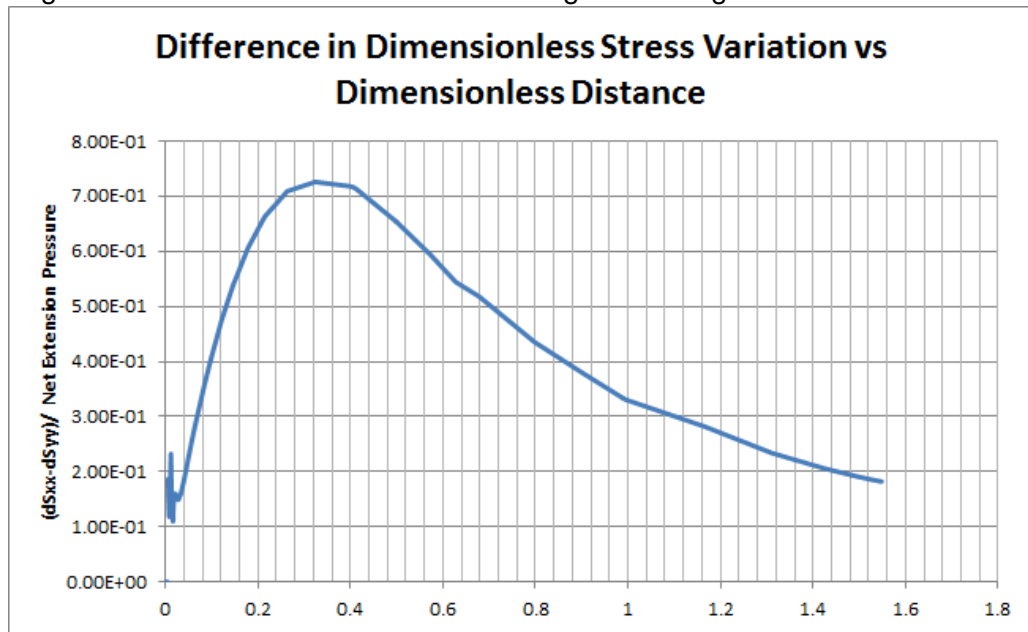
Figure 4.3.11: Difference between Delta SXX and Delta SYY

Figure 4.3.11 plots the difference between the Delta Sxx and Delta Syy values, showing the maximum occurring at a L/H ratio of approximately 0.3.

Figure 4.3.12 shows the ratio of principal stresses between the two fractures at the end of the simulation. Figure 4.3.13 shows the ratio of σ_{xx} vs σ_{yy}, showing stress anisotropy reversal as a value > 1.0.
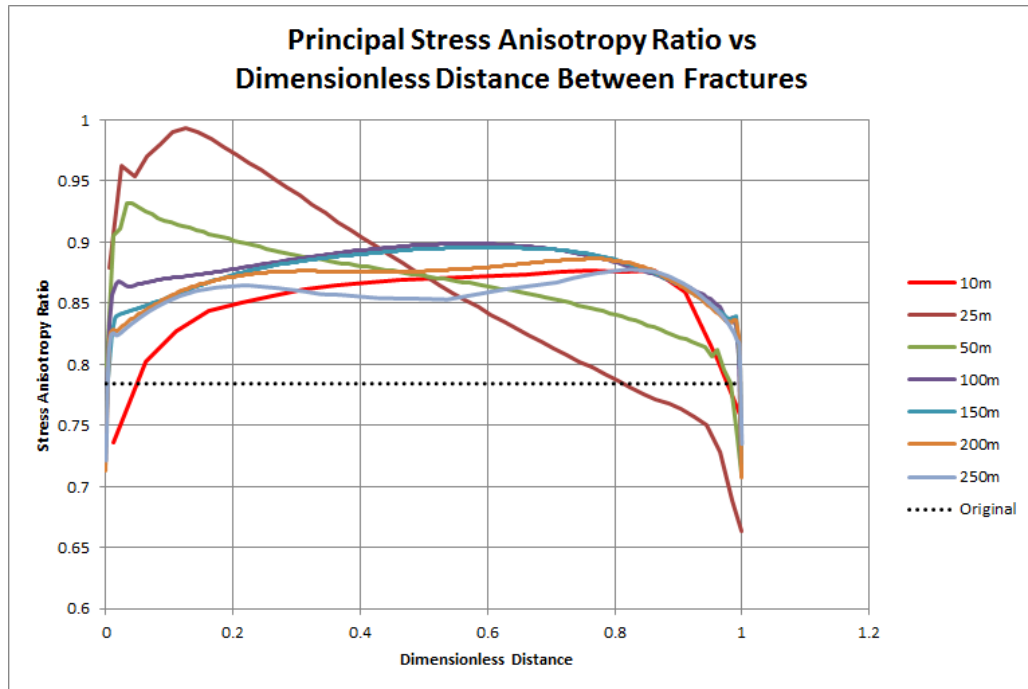
Figure 4.3.12: Stress Anisotropy Factor vs Dimensionless Distance between fractures
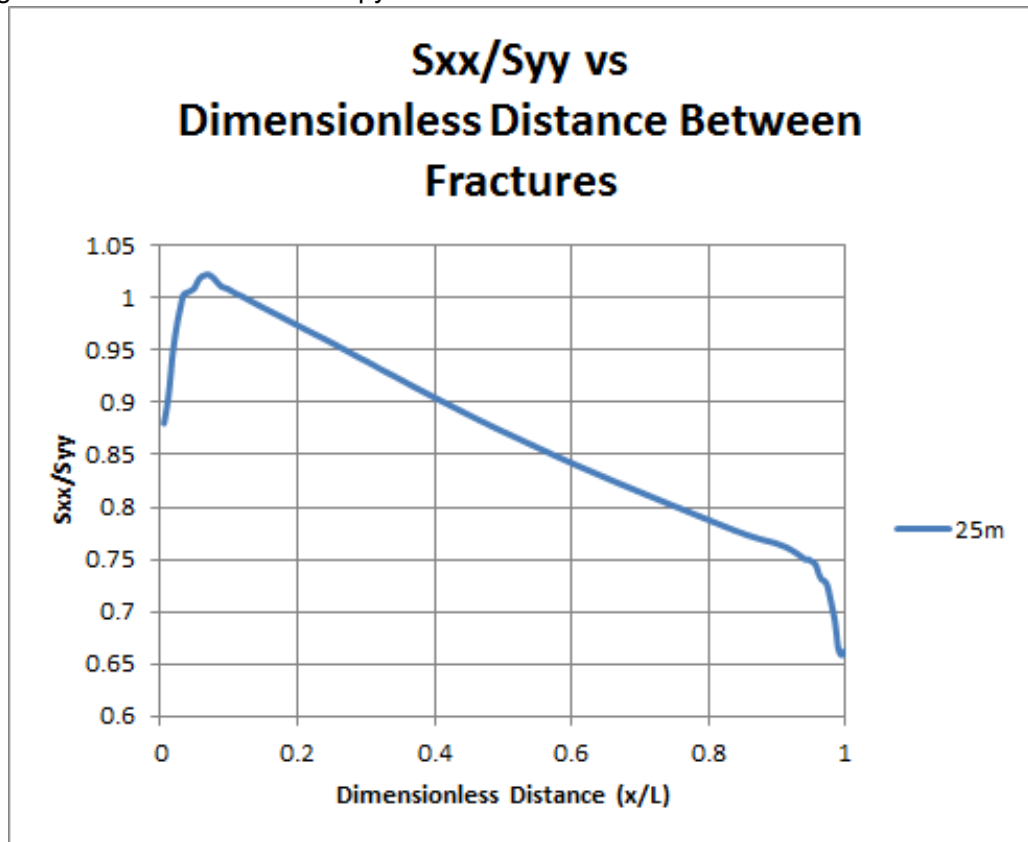
Figure 4.3.13: Sxx/Syy vs Dimensionless Distance at 25m spacing

81

Figure 4.3.14 plots the ratio of principal stresses at the end of each simulation. Values nearer 1 are red, those at zero or less are blue - and the minimum and maximum values are local to each simulation. Figure 4.3.15 plots the anisotropy ratio r (equation 4.3.1) for each case using a common scale of 0.85 to 1.0, for direct comparison (the initial value is 0.78).

$$r = \frac{\sigma_{Hmin}}{\sigma_{Hmax}} \tag{4.3.1}$$
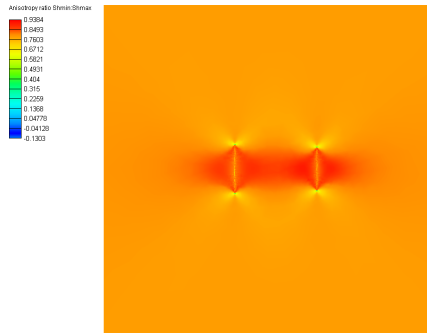
250m Spacing
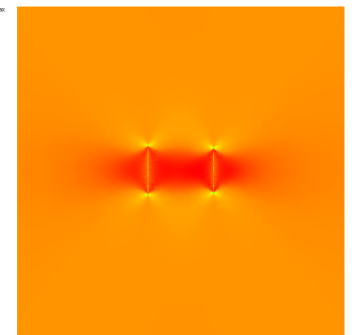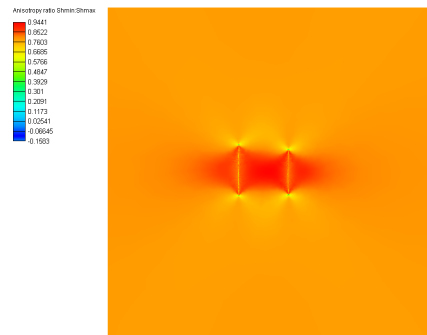
200m Spacing
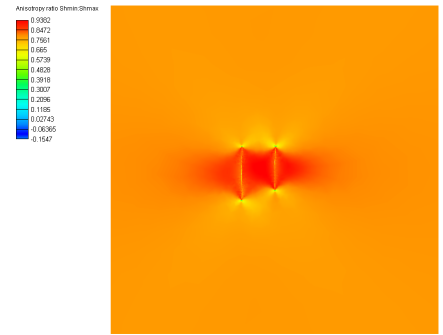
150m Spacing
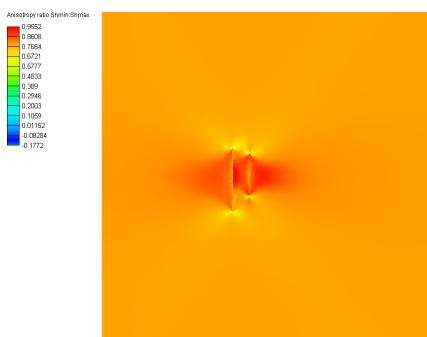
100m Spacing
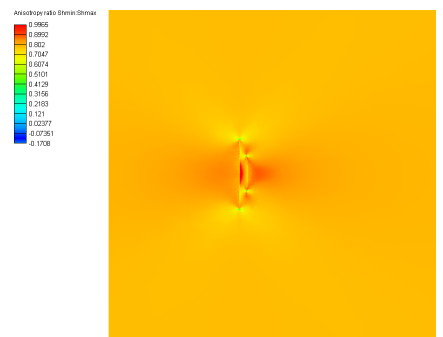
50m Spacing

25m Spacing
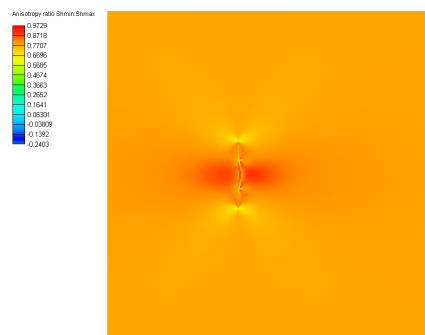
10m Spacing

Figure 4.3.14: Anisotropy 250m-10m, local maxima/minima

Anisotropy ratio Shmin:Shmax

0.9729
0.9627
0.9524
0.9422
0.9319
0.9217
0.9114
0.9012
0.891
0.8807
0.8705
0.8602
0.85

Legend

250m

200m

150m

100m

50m

25m

10m
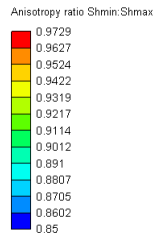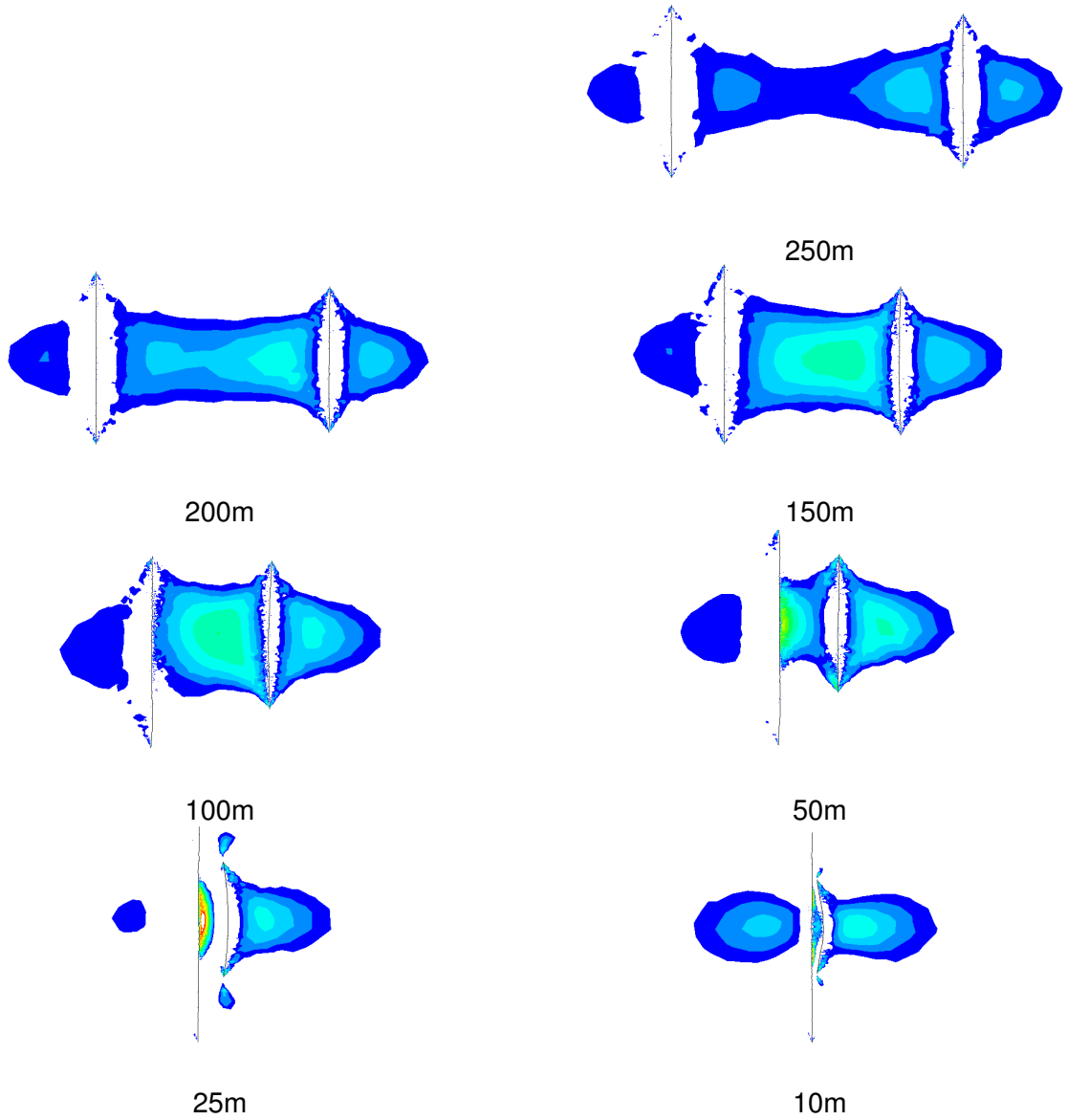
Figure 4.3.15: Anisotropy ratio 0.85-1.0, 250m-10m spacing

4.4 Discussion

4.4.1 Geometry

Several observations can be made regarding Figure 4.3.1. In all cases, F_1, on the left, is considerably longer than F_2. This is due to the residual fluid pressure in F_1 continuing to propagate the fracture as F_2 is formed. Classic stress shadowing effects are seen in the 50, 100 and 150 m F_2 fractures. The principal stress field, as will be seen in the following discussion, is rotated due to F_1 in such a way that the maximum principal stress is oriented away from F_1 at (or just ahead of) the initiation point of F_2. This causes the F_2 fracture to bend away from F_1. The effect is reduced as the fractures are spaced further apart, and the 250 m fracture is essentially unaffected by F_1.

In the 10 and 25 m cases, F_2 behaves in a way that could not be easily predicted by looking at the principal stress field at the time of initiating it. Rather counter-intuitively, F_2 is attracted towards F_1. This behaviour will be studied in more detail in section 4.4.4.

Variation in the shape and length of F_1 can also be seen. Until the initiation of F_2, the simulations are identical (within the limits of mesh dependent effects). For this reason the variation is restricted to the portion growing under residual pressure in F_1.

In Figure 4.3.2, the geometry of the upper half-length of F_1 is shown, again with each simulation result superimposed. The plot has been scaled by an order of magnitude in the horizontal direction (x) only, to exaggerate the differences between the runs. The influence of F_2 on the continuing growth of F_1 can be seen in this plot, and is more intuitive to interpret than the shapes of the F_2 fractures. The furthest spaced F_2 fractures at 200 m and 250 m have little effect on the direction or length of F_1. The F_2 fracture at 10 m spacing appears to increase the length of F_1 without significantly redirecting its direction. An examination of the stress state below will help to explain this further, although Figure 4.3.1 shows that the second fracture is much further from the tip of the first due to its short length, and that this may explain the lack of influence on its curvature.

Figure 4.3.3 plots the final length of the first fracture, which is higher when the fractures are spaced closer together. Plots of the aperture of F_1 vs normalised length (Figure 4.3.4) show the influence of the nearer F_2 fractures. These act to close F_1 near its center. In the 10 and 25m cases, this has the effect of increasing the aperture as the distance from the center increases, before returning to the more familiar elliptic profile.

4.4.2 Pressure

Examining the pressure histories (Figure 4.3.6) for the two extreme spacings shows some divergence towards the end of the simulation in both F_1 and F_2. Looking at this part of the history in more detail (Figure 4.3.7), the difference in final pressures for F_1 is approximately 1.2 MPa, and for F_2 0.8 MPa. These differences are not considered to be of particular consequence.

In Figure 4.3.8, the net opening pressure of F_2 is plotted for each distance. At 25 m, a relatively high opening pressure is observed. This may be due to some stress interference forming a "sweet spot" here, although it will be necessary to examine the stress state for further insight.

4.4.3 Stress

Anisotropy Change

Line of Symmetry The plot of dimensionless stress change - Figure 4.3.9 - can be compared to a similar plot obtained from these numerical simulations. Figure 4.3.10 plots the same change in stress/net extension pressure vs the distance from F_1 at 101s. At this point in time F_2 had not started to open, and there was residual pressure which would allow F_1 to continue propagating, so the analytic solution for the fracture at equilibrium is not expected to match perfectly. Some spikes are visible near the fracture which are numerical artifacts - the effects of damage on the near wellbore surface - but in general, the two sets of curves match well, showing a larger change in the minimum horizontal stress direction, and an overall drop in vertical (z) stress. Figure 4.3.11 plots the difference between the Delta σ_{xx} and Delta σ_{yy} values, showing the maximum occurring at a L/H ratio of approx. 0.3. In this example, the fracture length H is 134.98 m, making the distance ~40 m.

The principal aim of the TTSM is to reduce or reverse stress anisotropy in the zone between F_1 and F_2, to increase fracture complexity when stimulating the third fracture (Soliman et al., 2010). With this aim in mind, Figure 4.3.12 shows the ratio of principal stresses between the two fractures at the end of the simulation. Examining this chart, the most favourable spacing is at 100 or 150 m, since in both cases the ratio of principal stresses increases from an in-situ value of 0.78 to ~0.9, and is maintained at this higher level for a better proportion of the space between the fractures. In the 250 and 200 m cases, the anisotropy increases as the influence of F_1 and F_2 on each another is reduced.

Because the maximum principal stress is always higher than the minimum, the ratio of principal stresses can not exceed a value of 1.0. For this reason that ratio is unable

to show anisotropy reversal (ignoring tensile stresses). However, if these are assumed to remain oriented with the x and y axes, reversal can be shown by plotting σ_{xx} vs σ_{yy}. Figure 4.3.13 does this, and shows the only simulation in this set of results with any anisotropy reversal, in which for a short region σ_{xx} is greater than σ_{yy}. This is at 25 m spacing, and by looking at 4.3.12 it can be seen that the nearest result to anisotropy reversal is in that same region, for the same fracture spacing.
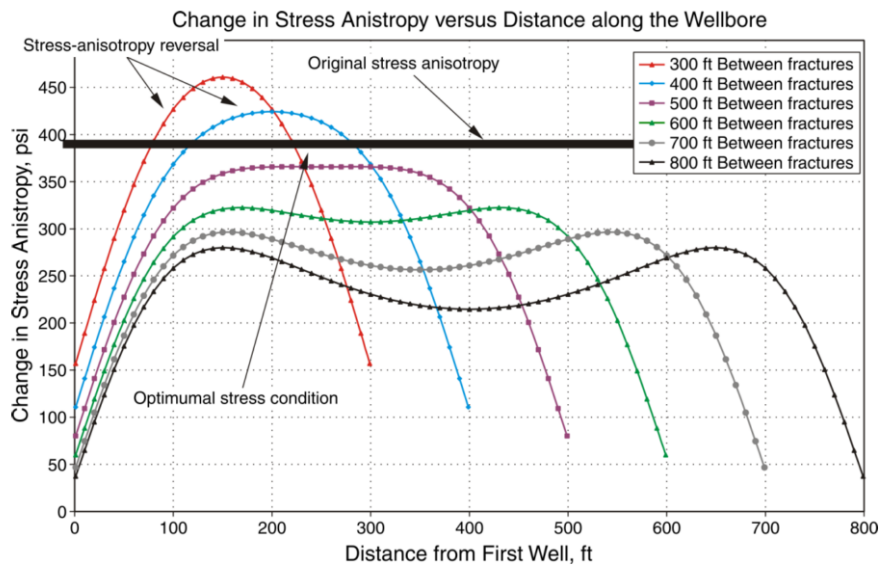
Figure 4.4.1: Change in Stress Anisotropy vs Distance along the Wellbore (Soliman et al. (2010))

In Soliman et al. (2010), similar results are predicted, illustrated in Figure 4.4.1. The simulations were run under the same conditions given in Table 4.1, with the exception of a stiffer Young's modulus (48 MPa vs 32 MPa), and a narrower range of fracture spacings - between 91 m and 244 m vs 10 m and 250 m. The curve is not directly comparable with Figure 4.3.12, since Figure 4.4.1 plots absolute distances and the change in absolute anisotropy, whereas the normalised ranges compress the data in Figure 4.3.12. However, general trends can be compared in both. In Figure 4.4.1 the anisotropy change is an M-shaped curve between the most distant fractures, which flattens as the fractures get closer together, becoming parabolic at the closest spacing. This pattern can also be observed in Figure 4.3.12.

There are also clear differences. The results are notably asymmetric in Figure 4.3.12, and at spacings below 100 m it is difficult to distinguish a clear trend. Anisotropy reversal is apparent in Figure 4.4.1, which does not occur (beyond the small region discussed above) in these results.

Full Field   4.3.14 shows the ratio of principal stresses for each simulation. These plots are contoured using the local maxima and minima. Comparing these maxima over the whole field with those obtained along the line of symmetry in Table 4.2, it appears that the closest ratio to 1.0 is not obtained along the line of symmetry, and in that for every case, higher values are found outside this line.

Fracture Spacing (m)	Maximum Anisotropy Ratio SHmin/SHmax - Full Field	Maximum Anisotropy Ratio - Line of Symmetry
10	0.973	0.877
25	0.997	0.993
50	0.955	0.932
100	0.938	0.899
150	0.944	0.896
200	0.930	0.887
250	0.938	0.877

Table 4.2: Maximum Anisotropy ratio at end of Simulation - full field

It is possible that these high values are single element "hotspots" or numerical artifacts, as previously seen near the fracture surface in 4.3.10. To investigate this, plots of the elements with values between the maximum value along the line of symmetry and the full-field maxima were created. They showed in all cases, isolated elements near the fracture which are distributed sparsely enough so as to be ignored - each have at most two adjacent elements with a similarly high value. When averaged across nodes, the effect of these elements is seen to be negligible.

An example is presented in Figure 4.4.2. This is one of the "worst" - the 250m spacing case, which has some larger elements near F_2 with an anisotropy ratio above the line of symmetry maximum. All elements with an anisotropy ratio below the line of symmetry maximum (0.877) are hidden. The upper image shows the per-element values. When these are viewed averaged onto the mesh nodes, their impact is significantly reduced, and on this basis the values above the line of symmetry maximum are deemed outliers. All values remaining visible are at the lower end of the range.

Figure 4.3.15 plots the anisotropy ratio for each case using a common scale of 0.85 to 1.0, for direct comparison. The ratio of 0.85 has been chosen using Figure 4.3.12, as it represents an area of lower anisotropy than the initial state (a ratio of 0.78), while most of the simulations appear to have a comparable amount of data to evaluate. The area of the simulation domain falling within this range can be considered one metric of performance of a treatment, given that the aim of the treatment is to reduce anisotropy. Consistent with
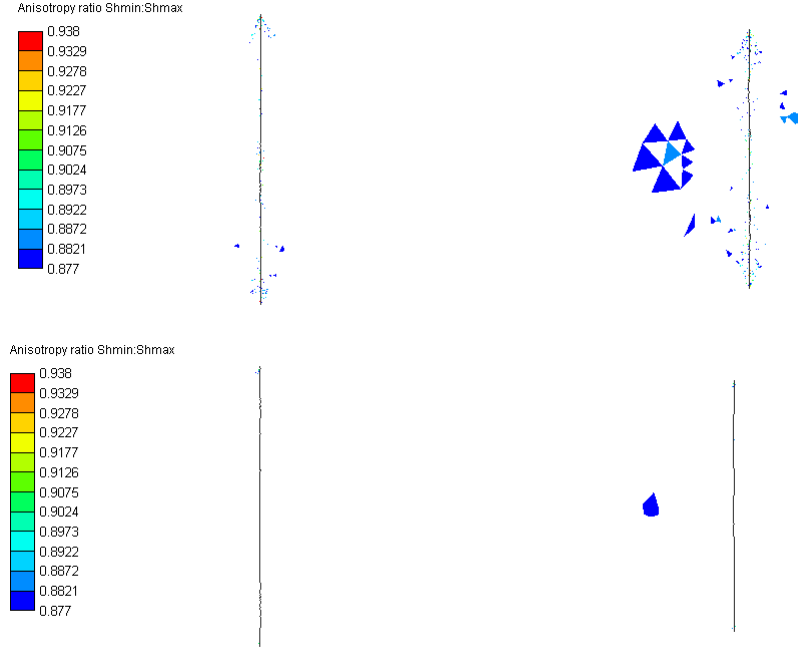
Figure 4.4.2: Anisotropy ratio: Values above the axis of symmetry maximum, 250m spacing.

the line of symmetry results, the plots show large areas within this range at 100m and 150m. To take a more objective look at these contour plots, the total area of elements falling within the range 0.85 to 1.0 for each simulation are presented in three different charts, each representing a particular metric. The first metric, A_T, in Figure 4.4.3, is a straight sum of the areas of elements A_i with an anisotropy ratio r within that range.

$$r = \frac{\sigma_{Hmin}}{\sigma_{Hmax}} \tag{4.4.1}$$

$$\chi_A(r) := \begin{cases} 1 & r \geq 0.85 \\ 0 & r < 0.85 \end{cases} \tag{4.4.2}$$

$$A_T = \sum_i A_i \chi_A(r_i) \tag{4.4.3}$$

This metric puts the 150 m spacing ahead of the 200 m and then 100 m spacings. Perhaps a better metric would only consider the area between the fractures, since that is the region which will be stimulated next. Here the x component of each element's centroid (C_x) is used in conjunction with the x position of F_1 and F_2 at initiation (F_x^1 and F_x^2) as follows:

$$\chi_x\left(C_x\right) := \begin{cases} 1 & F_x^1 \leq C_x \leq F_x^2 \\ 0 & C_x < F_x^1 \\ 0 & C_x > F_x^2 \end{cases} \tag{4.4.4}$$

$$A_I = \sum_i A_i \chi_A\left(r_i\right)\chi_x\left(C_x\right) \tag{4.4.5}$$

This internal area A_I is plotted for each spacing in Figure 4.4.4, and the relative position of the best four spacings does not change. It is not surprising that the closest spaced fractures appear to be far less significant in this plot, given the similar lengths of all the fractures and the reduced capacity for internal area by the very nature of their proximity. For this reason, a third metric, A_N is introduced in equation 4.4.7, in which the internal area values are divided by the fracture spacing. This metric is plotted in Figure 4.4.5, and ranks the 100 m spacing ahead of the others, followed by 150 m, then 50 m and 200 m. Recalling Figure 4.3.8, at 100 m spacing there is a ~1 MPa higher opening pressure for F_2 at 100 m in comparison to the 150 and 50 m spacings. This is a (minor) tradeoff for a 12% and 24% difference in this metric respectively. Whether this metric is an indicator of increased fracture complexity requires further investigation.

$$L = F_x^2 - F_x^1 \tag{4.4.6}$$

$$A_N = \frac{\sum_i A_i \chi_A\left(r_i\right)\chi_x\left(C_x\right)}{L} \tag{4.4.7}$$

Stress State - Rotation

As well as anisotropy reduction, TTSM also aims to go beyond the isotropic stress state and reverse the principal stress directions if possible. There are two mechanisms which can cause this. The first is a pure magnitude shift of σ_{xx} and σ_{yy} until the first is larger than the other. This is the method used to reduce anisotropy along the axis of symmetry in the TTSM - the magnitudes of σ_{xx} and σ_{yy} change at different rates as the fractures open. Alternatively, introduction of shear stress τ_{xy} will rotate the principal stresses. Recall that under the conditions of these simulations, namely an in-situ stress state aligned with the global X and Y axes, a non-zero X/Y shear stress τ_{xy} indicates a rotation of the principal stresses. Figures 4.4.6 and 4.4.7 are cartoons of these two mechanisms; Figure 4.4.6 illustrates a magnitude change that is higher in the X direction, either by addition of σ_{xx}, or reduction of σ_{yy}, or both. Figure 4.4.7 shows the effect of increasing τ_{xy}, which rotates
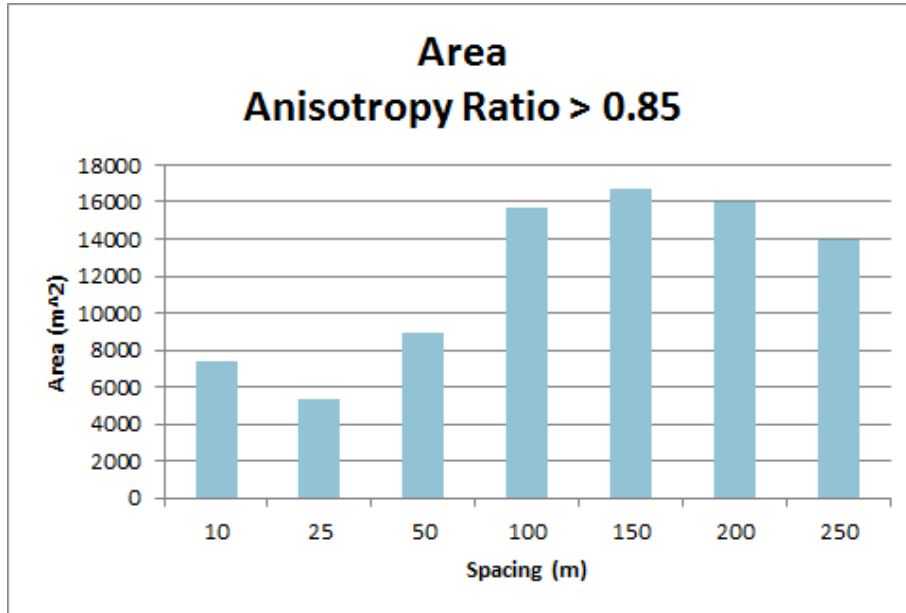
Figure 4.4.3: Total Area with Anisotropy Ratio > 0.85

the the principal stresses until they are 90° from their original orientation. In this cartoon, the arrow heads indicate the direction of the compressional principal stresses.

The angle of rotation of the principal stresses is given by

$$\alpha = \frac{atan2\left(\tau_{xy}, \left(\frac{\sigma_{xx} - \sigma_{yy}}{2}\right)\right)}{2} \qquad (4.4.8)$$

where $atan2$ is the function which returns an angle between $-\pi$ and π for a given x, y pair[1]. A plot of the absolute value of this angle α for $\alpha > 5\breve{r}$, at spacing 150m is presented in Figure 4.4.8. This shows that the area between the two fractures is exposed to low amounts of stress rotation.

Stress rotation will be examined in detail for the more complex cases in 4.4.4 - those which result in attractive growth of F_2. The other examples, 50 - 250 m exhibit behaviour typical of stress shadowing cases and are dealt with here generally.

---

[1]The exact implementation of this function depends on the programming language used, which in this case is C
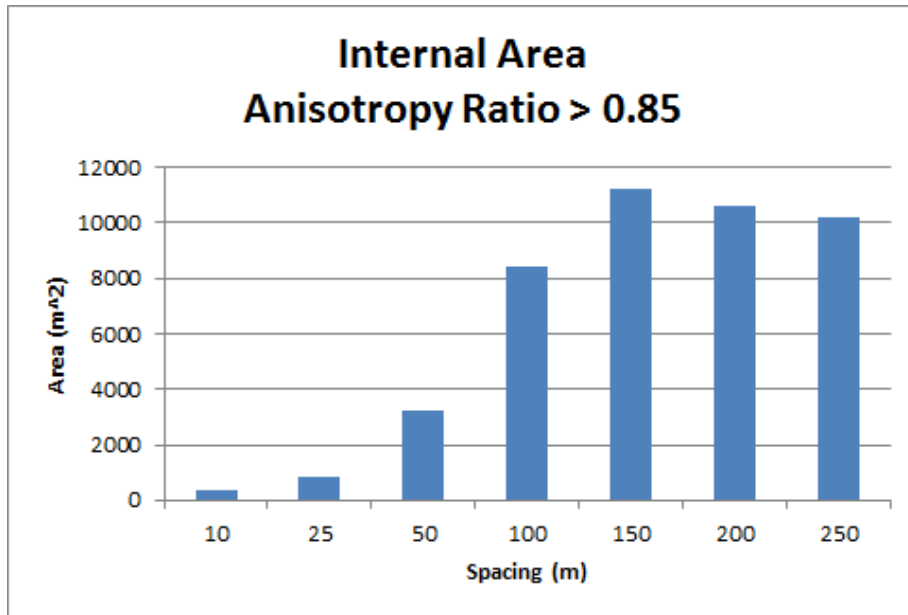
Figure 4.4.4: Total Internal Area with Anisotropy Ratio > 0.85
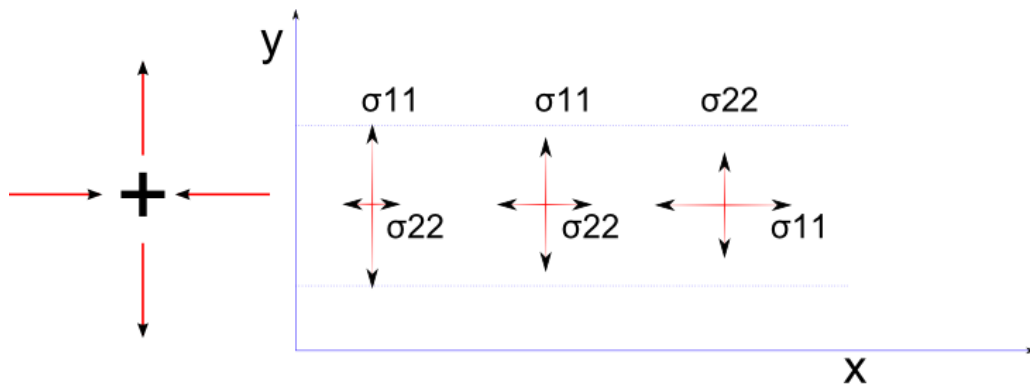
Figure 4.4.6: Principal Stress Reversal Mechanism (a)
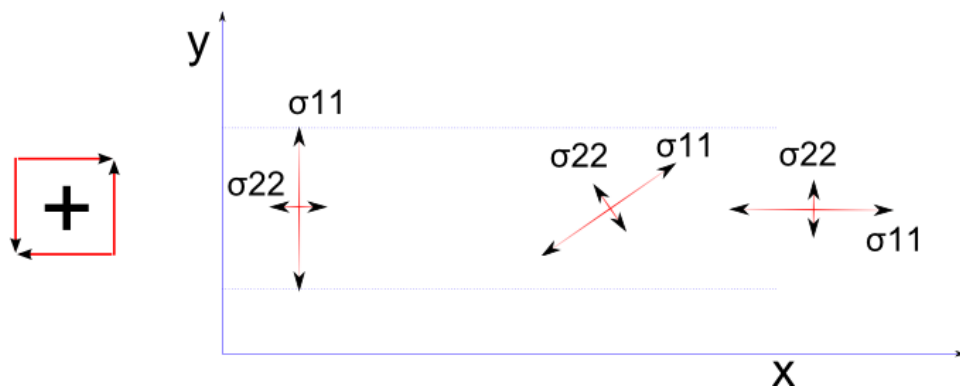
Figure 4.4.7: Principal Stress Reversal Mechanism (b)
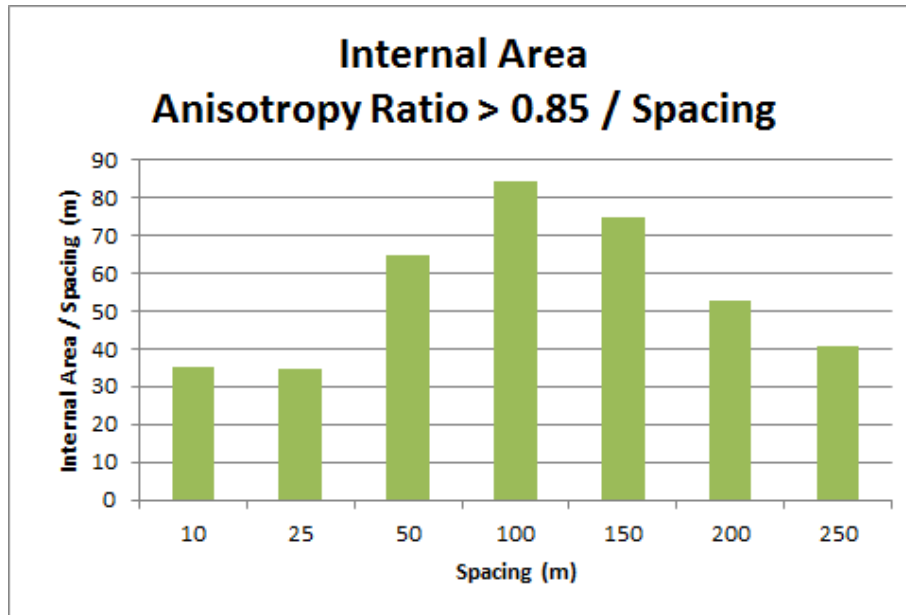
Figure 4.4.5: Total Internal Area with Anisotropy Ratio > 0.85 / Spacing

The superposition of stress states works against an increase in shear stress in the zone between the two fractures for reasons which are clear when τ_{xy} is visualised at the end of pumping the first fracture. Figures 4.4.9 and 4.4.10 plot negative and positive τ_{xy} separately. Shear stress is higher in magnitude surrounding the tips of the fracture, and taking the upper tip as an example, the zone of negative τ_{xy} is largely confined to a zone extending towards the right. Conversely, a zone of positive τ_{xy} extends to the left.

Superimposing a second fracture to the right of Figure 4.4.8 under the same stress conditions would result in the positive τ_{xy} zone to the left of that second fracture's upper tip negatively interfering with the zone of negative τ_{xy} to the right of the first fracture's upper tip. The same applies to the lower tips, and is evident in Figure 4.4.8, as the zone of stress rotation is smaller inside the two fractures than outside. Figure 4.4.11 is a cartoon of this stress cancellation. Chapter 7 examines how these shear interactions might be used to positively reinforce each other, rather than cancel.

Another visualisation technique is employed in Figure 4.4.12, which uses LIC (see section 3.7) to advect a noise image using the principal stress vectors. The plot is of a subsection of the simulation at the end of pumping F_2- a region bounded by (300,300) to (650, 650). The tips of each fracture are highlighted with red dots, and the line joining the start points of each fracture are joined with a straight red line. The third fracture in the sequence for TTSM would start at some point along this line, which represents the well. This region shows little change in stress orientation, consistent with the plot of principal stress angle in Figure 4.4.8.
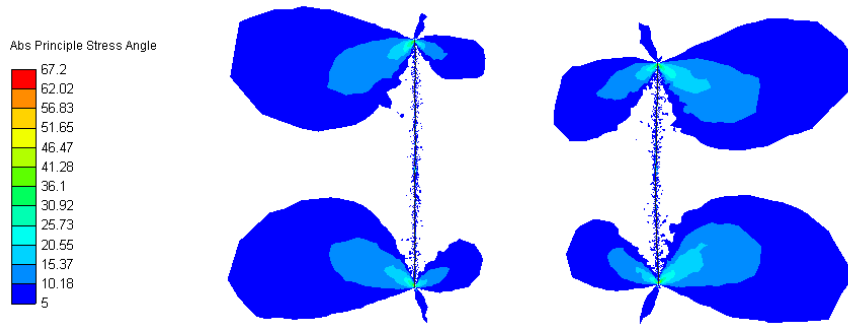
Figure 4.4.8: Absolute Value of Principal Stress Rotation Angle α, $\alpha > 5\breve{r}$
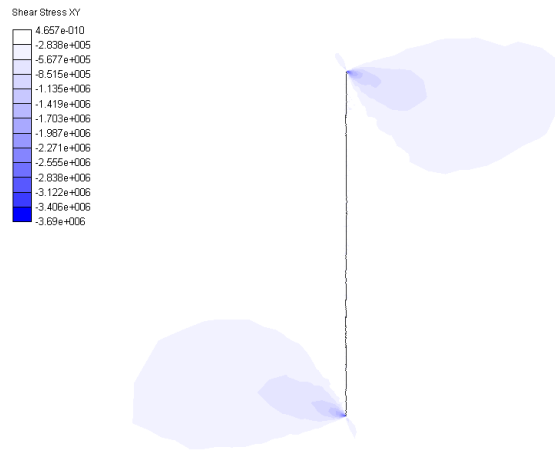
Figure 4.4.9: Single fracture, negative τ_{xy} only

4.4.4 Attractive Fracture Growth

As noted in 4.3.1, the simulations with fractures spaced at 10 and 25m exhibit an unexpected growth towards each other. Figure 4.4.13, from Bunger et al. (2012), distills their work on dimensionless classification of parameters affecting closely spaced fractures into a flow chart. This chart can be used to predict the mechanism driving curvature (if any) of the second fracture. Jo (2012) suggest that this attractive curvature may be due to opening and sliding along the first fracture, or shear stress interactions.

The key parameters required to use the flow chart 4.4.13 are set out in tables 4.3 and 4.4, for one set of laboratory experiments from Bunger et al. (2012) and the simulation values for the 10m spacing numerical simulation, as well as a theoretical case with low friction in the first fracture. The relevant path through the chart is highlighted in red for the zero friction example, and in blue for the low friction case. The low friction case was not simulated numerically, as H1 (F_1) is held open with fluid, rather than a proppant which could provide non-zero friction. Both result in the same outcome, however - "Further
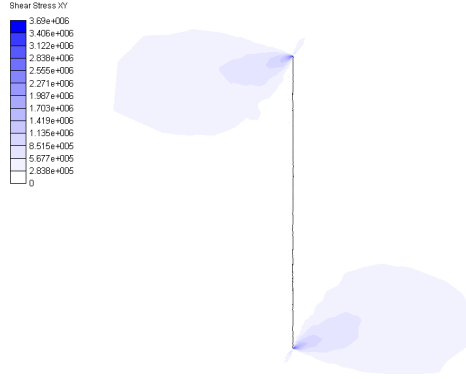
Figure 4.4.10: Single fracture, positive τ_{xy} only
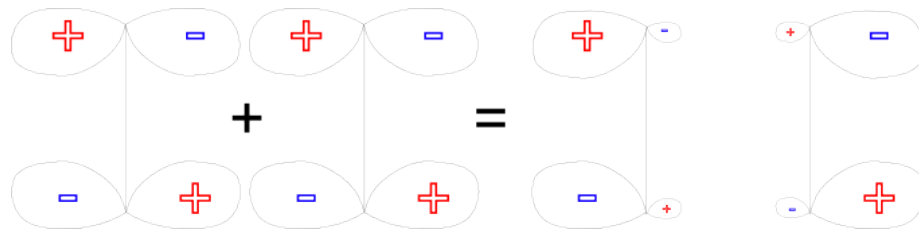
Figure 4.4.11: Shear Stress Summation Cartoon

Analysis". Hence, an examination into the cause of this behaviour is presented.

It is reasonable to assume that the curvature of the second fracture is due to rotation of the stress field ahead of it; it follows that examining the principal stress directions is a logical place to begin. The left of Figure 4.4.14 is a close-up LIC plot of the simulation at time 112s, 12s after pumping begins into F_2 and shortly after it begins to fracture. On the right is the simulation at 120s, and both are using the most compressive principal stress direction as the vector field. A false colouring scheme is used to highlight detail in each image. The colours are scaled according to the following stress intensity σ_I:

$$\sigma_I = \sqrt{\sigma_{11}^2 + \sigma_{22}^2} \tag{4.4.9}$$

Parameter	Description	Unit	ORNL 1-2	B	C
σ_{min}	Min Horizontal Stress	MPa	7.5	5.5	5.5
σ_d	Max Horizontal Stress - σ_{min}	MPa	1	5.63	5.63
E	Young's Modulus	MPa	18000	32000	32000
ν	Poisson's ratio		0.1	0.2	0.2
K_{Ic}	Rock Fracture Toughness	MPa.$\sqrt{\text{m}}$	0.7	1.26	1.26
f	Friction coeff. H1	-	0.03	0	0.03
μ	Fluid dynamic viscosity	MPa.s	3E-09	1.67E-09	1.67E-09
$\bar{Q}$	Injection rate	$\frac{\text{m}^3}{\text{s}}$	1.7E-03	0.1	0.1
Q_0	Injection rate/unit thickness	$\frac{\text{m}^2}{\text{s}}$	3.4E-04	0.01	0.01
H	Initial distance between fractures	m	6.4	10	10
a	Half length H1	m	80	75	75
w_0	Propped width H1	m	9E-03	4E-03	4E-03

Table 4.3: Laboratory and Numerical Simulation Input Parameters.B = 10 m frictionless, C = 10 m low friction
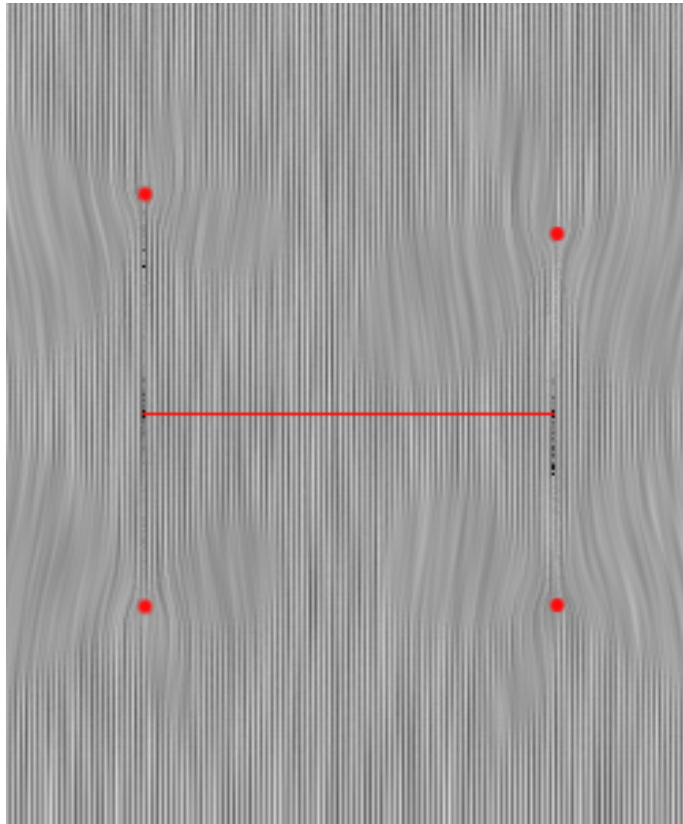
Figure 4.4.12: LIC visualisation of principal stress field
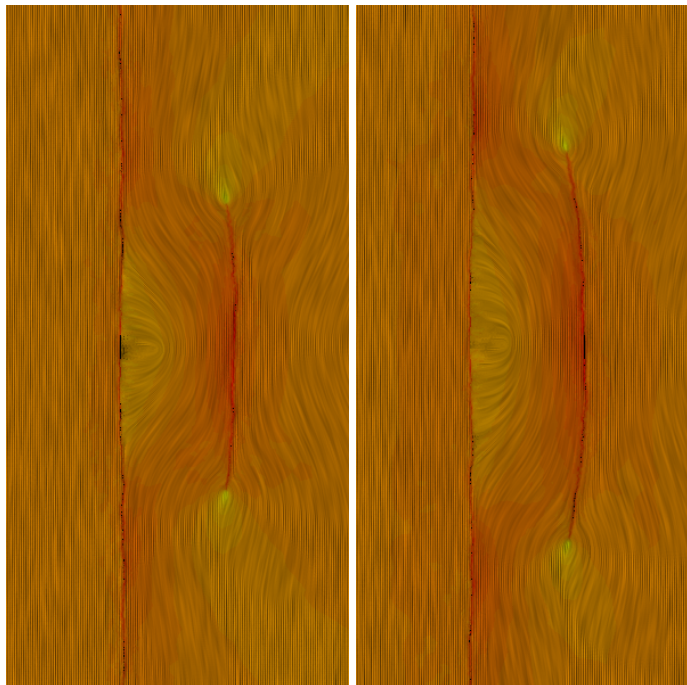
Figure 4.4.14: LIC plot of 10m spacing at 112s (left) and 120s

Parameter	Description	ORNL 1-2	B	C
D	Dimensionless deviatoric stress	3.6140	6.875	6.875
S	Dimensionless minimum far-field stress	2.71E+01	7.50E+01	7.50E+01
M	Dimensionless viscosity	2.95335	27.9443	27.9443
W	Dimensionless H1 width	7.3923	4.4444	3.3333
$SM^{-\frac{1}{4}}$		20.6765	32.6202	59.8038
$DM^{-\frac{1}{4}}$		2.7568	2.9902	1.3592
$\frac{HW}{aD}$		0.1636	0.0862	0.1067
Model Prediction		Neglect Curving	Further Analysis	Further Analysis
Observation		Parallel	Attractive Curvature	N/A

Table 4.4: Laboratory and Numerical Simulation Calculated Parameters.
B = 10 m frictionless, C = 10 m low friction

This is closely related to the von Mises stress, and is used here to aid visualisation of the curvature of the stress field in areas of higher/lower overall principal stress. These renderings show the fracture tips of F_2 surrounded by stress rotation. A zone in yellow at the center, but on the right hand side only, of F_1 shows stress anisotropy reversal- the most compressive stress σ_{Hmax} has become σ_{xx}. The lack of any obvious influence from F_2 on the left hand side of F_1 leads to thoughts regarding the zone of anisotropy reversal, and how it has come about:

- The fluid filled, frictionless F_1 is unable to transfer shear stress to the opposite side. As discussed above, shear stress is analogous to principal stress rotation, so this could explain the anisotropy reversal, as well as the asymmetry of that reversal around F_1.

- The zone of stress rotation due to shear appears to move with the fracture tips, but the zone of anisotropy reversal remains at the center of F_1, extending lengthwise as F_2 grows. This hints that the stresses have not rotated, but the magnitudes have changed. (The first mechanism in 4.4.7).

Plotting the shear stress magnitude together with the orientation of σ_{Hmax} should provide

Figure 4.4.13: Flow chart classifying fracture growth mechanisms (Bunger et al. (2012))

some insight into how the reversal of principal stress directions is enabled. Figure 4.4.15 shows σ_{Hmax} and the absolute shear stress magnitude ($|\tau_{xy}|$) in the lower half of the area between the two fractures. Here, the rotation of principal stress due to higher shear stress values is clear, and the area with the highest stress rotation is in the area of lowest $|\tau_{xy}|$. This suggests that the anisotropy reversal is due to increased lateral stress rather than shear.

Figure 4.4.15: Shear stress and σ_{Hmax}, t=112 s

A look at the displacement in X indicates that the region between the fractures is able to move more in X than the region to the right of F_2. The absolute X displacement is shown in 4.4.16. In this case, the contour colouring is not confined to the interior of the two fractures; the area to the left of F_1 is contoured white, indicating a low displacement, as is the area to the right of F_2. Not shown here are plots confirming that the displacement is towards F_1.

A possible explanation for this additional displacement concerns the bulk modulus of the fluid in F_1 relative to that of the rock. The slickwater used to keep the fracture open has a bulk modulus of 2 GPa, while the shale has a bulk modulus of 15.3 GPa. The fluid is less stiff than the rock, and is allowing the area of rock between the two fractures to move towards F_1 more than the rock to the right of F_2.

Importantly, the tips of F_2 act as pivots for a rotation of the interior region, and an additional asymmetric zone of τ_{xy} on the outside of the tip is created. This causes a rotation of the principal stresses ahead of the fracture tip and consequently alters the fracture path. Figure 4.4.17 illustrates the pivoting direction, overlaid on a plot of the absolute shear stress, which is evidently stronger on the interior of the fracture. The regions of τ_{xy} aligned with the 1 o'clock direction at the top of F_2, and the 5 o'clock direction at the other end are of the same sign as the τ_{xy} on the left of F_2. This is clearer to see in Figure 4.4.20, which plots both absolute and negative values for comparison, albeit in the reverse pivot direc-

tion. It is these zones which are ahead of the opening fracture that appear to influence the propagation direction.
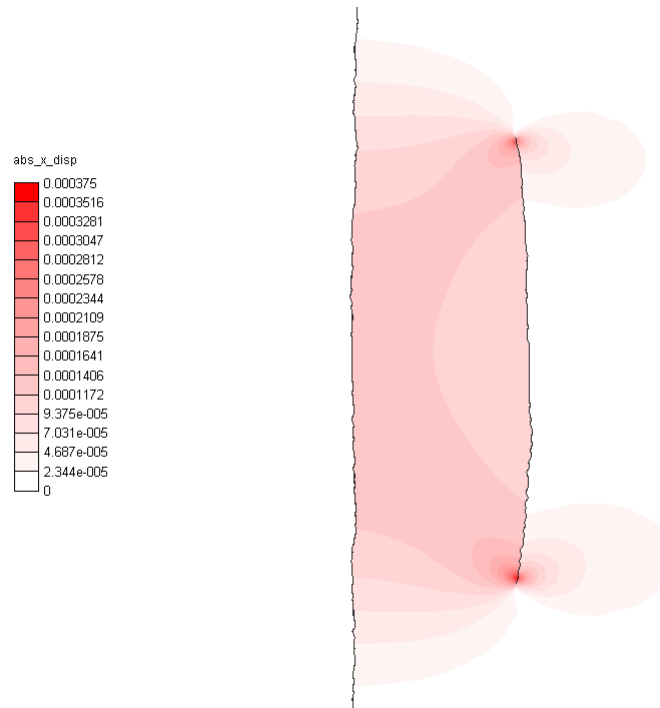
Figure 4.4.16: Absolute displacement in X
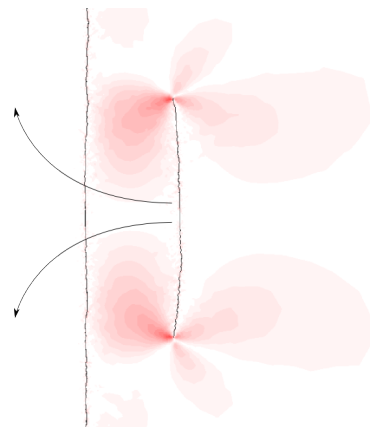
Figure 4.4.17: Pivoting due to lower fluid stiffness

To confirm this explanation for curvature towards F_1, further simulations were carried out to isolate the effect. A fracture was initiated at 10m from the left hand domain boundary of a 1km square block, with a fixity applied in both X and Y directions on the boundary face. The left hand boundary becomes an analogue for F_1 in the previous simulations (denoted $\hat{F}_1$), and removes the possibility of any movement due to sliding on F_1, the shape of the

open fracture, etc. The result is a higher displacement to the right of the opening fracture, the F_2 analogue $\hat{F}_2$. Relative to the fixed $\hat{F}_1$, the domain to the right of $\hat{F}_2$ is less stiff, and there is correspondingly higher displacement in X to the right. The same pivot is seen driving a shear stress increase on the left of $\hat{F}_2$ which in turn rotates the principal stresses ahead of the fracture, causing it to curve away from $\hat{F}_1$. A plot of the absolute accumulated displacement in X is presented in Figure 4.4.18, $|\tau_{xy}|$ in 4.4.20, and areas of negative τ_{xy} in 4.4.20. Comparing figures 4.4.20 and 4.4.20 makes the additional zone of negative τ_{xy} due to the pivoting action. Further plots not presented here confirm rotation of principal stress direction in these zones consistent with the curvature of the fracture.
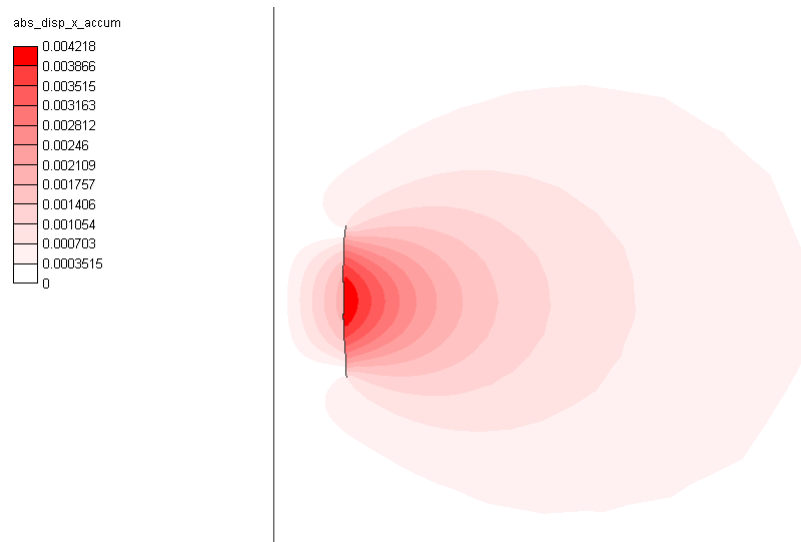
Figure 4.4.18: Accumulated Displacement in X, Fixed Boundary
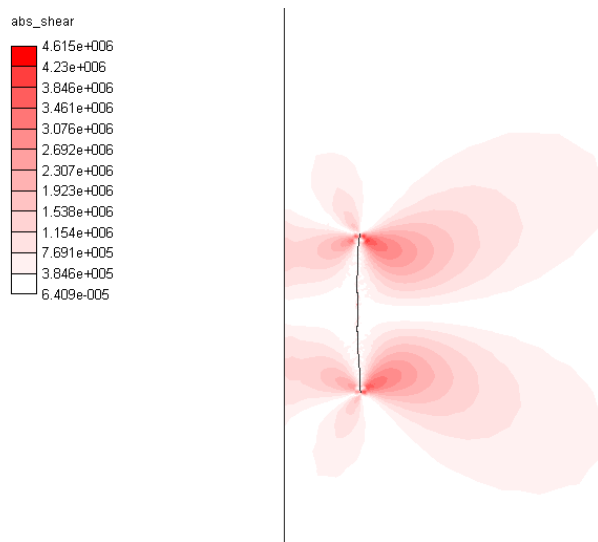
Figure 4.4.19: Shear Stress XY, Fixed Boundary, Absolute Values
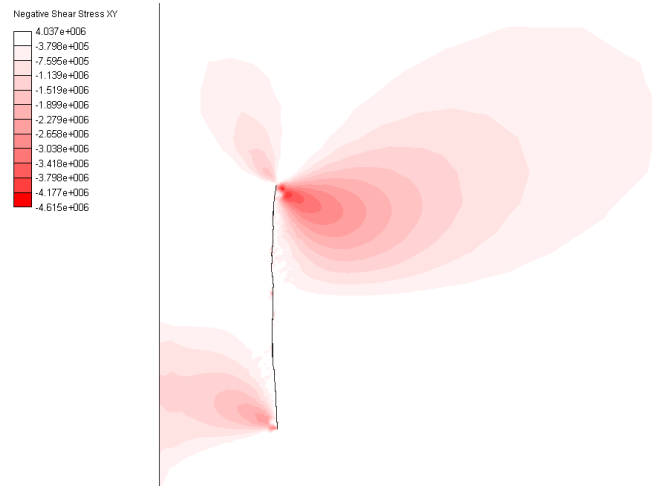
Figure 4.4.20: Shear Stress XY, Fixed Boundary, Negative Values

The simulation above was run with the left hand boundary fixed in displacement and rotation. Similar results were seen when rotation was allowed whilst maintaining the displacement fixities.

A third simulation removed the displacement constraint altogether and replaced it with a face loading equivalent to σ_{Hmin}. This provided an analogue to an open F_1 with zero fluid stiffness. As expected, the fracture curves towards the free boundary using the same mechanism described above. Figure 4.4.21 plots the signed shear stress τ_{xy} at 12s, with the deformation exaggerated by a factor of 300 in both X and Y. This confirms the mechanism for attractive curvature is due to the fluid stiffness being lower than the fracturing medium. The fluid stiffness may also explain the asymmetry in stress anisotropy observed between fractures, see Figure 4.3.12.
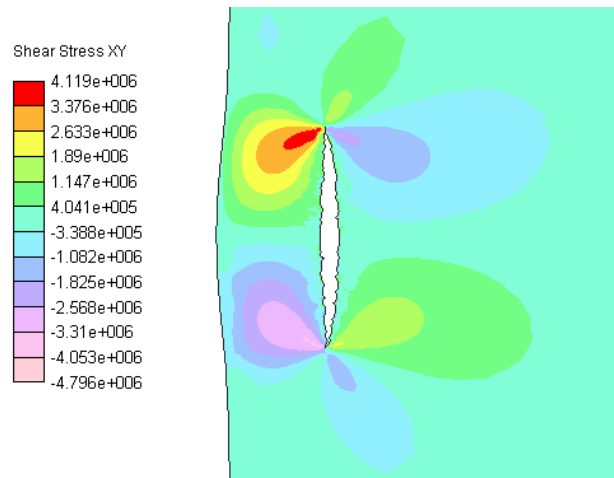
Figure 4.4.21: Shear Stress XY, free boundary with face loading (300x exaggerated deformation)

4.4.5 Summary

This chapter used fully coupled, discrete/finite element modelling to examine the details of fracture growth during the first two steps of the TTSM. Full field representations of stress were examined between the two fractures. Similar results were observed to those in Soliman et al. (2010), with some notable exceptions.

Soliman et al. (2010) anticipated the change in stress at various points in space between the two to approximate the stress interactions between the first two fractures. Using superposition of Sneddon's calculations (Sneddon, 1946), they described the profile of stress anisotropy change along the line between the two fracture initiation points, at different spacings of the first two fractures. Jo (2012) used the boundary element method to predict the path of the second fracture. Generally speaking, as the two fractures were spaced further apart, the effect of stress shadowing diminished, and the associated curvature away from the first fracture similarly fell away with increasing distance. Rather unexpectedly, at closer spacings the second fracture path become increasingly curved towards the first fracture.

The fully coupled nature of the analysis showed additional effects which are not captured by superposition of analytical results. For instance, the continued growth of the first fracture while the second was initiating, due to out of balance pressure locked in the fracture, analogous to a shut in period. Asymmetry in principal stress ratios were observed which are possibly due to fluid stiffness effects. This has implications for the placement of the third fracture, which in Soliman et al. (2010) is recommended to be placed in the middle of the two fractures, owing to the symmetry of the stress anisotropy.

The ability to extract the surface area of the model meeting particular anisotropy conditions was used to evaluate a selection of proposed metrics for appraising the success of each fracture spacing. The final metric arrived at divided the affected area by the fracture spacing, and ranked the 100m spacing ahead of the others. Soliman predicts the 150 m spacing to be optimal based on the anisotropy ratio as measured along the wellbore.

The simulation allowed examination of the full stress field at, within reason, any point in time (limited by the requested output frequency during simulation setup). This allowed detailed analysis of the conditions leading to interesting phenomena, such as the attractive fracture growth observed at close fracture spacings. This analysis has shown that there is another mechanism, unaccounted for in Bunger et al. (2012), which drives this attractive curvature. The observation was explained by the reduced fluid stiffness in the open fracture allowing one side of the second fracture to open preferentially, which in turn caused a principal stress rotation ahead of the fracture tips on one side, altering the path of the fracture towards the open fracture.

Chapter 5

Fracture Reorientation

5.1 Introduction

Chapter 4 examined one method of manipulating the stress field to reduce or reverse stress anisotropy, namely by opening two fractures either side of a zone in which a third fracture would be initiated. The stress field in that zone, depending on the fracture spacing, would experience an alteration in the stress anisotropy. The anisotropy could be reduced to near zero, or possibly reversed, as observed by Soliman et al. (2010). This chapter looks at the behaviour of a single fracture in a similarly affected zone. The stress field can also be influenced by reservoir production, and the following simulations are also pertinent to that situation. The motivation is to understand the behaviour of fractures being stimulated at various orientations to the stress field, which can have applications to the following situations:

- Propagation of a fracture in a zone of stress anisotropy reversal

- Propagation of a fracture in a rotated principal stress zone

- Stimulation of a natural fracture at an arbitrary orientation to the in-situ stresses

- Refracture of a hydraulic fracture or well that is surrounded by a zone of reduced pressure

In an anisotropic stress field, a stimulated starter fracture will re-orient with the in-situ maximum principal stress direction. This has been studied at the wellbore in some detail (Daneshy, 1973, Mogilevskaya et al., 2000). Some works, such as Soliman et al. (2010), predict that a reversed stress field will cause fracture initiation to occur in the reversed maximum principal stress direction. This may well be the case under strong anisotropic

conditions. However, under the near isotropic conditions such as those induced in the TTSM, this may not occur. It is possible that the stresses around the fracture tip created by the opening of the fracture could dominate the in-situ stresses. This may prevent a fracture from initiating in the direction of the maximum principal stress direction. The strength of in-situ anisotropy is likely to affect the propagation pattern, and this chapter examines the effect of varying stress anisotropy on the reorientation rate of fixed length starter fractures.

In addition to stress anisotropy, the length of a starter fracture inclined to the principal stress field is predicted to affect the way it reorients to the stress field. Longer fractures require less pressure to open, which may affect the influence they have on the surrounding stress field.

It is also predicted that the initial orientation of a fracture will be important. A fracture aligned with σ_{Hmin} will take longer or be harder to reorient to σ_{Hmax} than one which is already aligned in that direction. A fracture aligned with σ_{Hmin} is also predicted to require a higher fluid pressure to initiate. Conversely, this higher pressure could act to increase the rate of reorientation.

Simulations to investigate the affect of stress anisotropy, initial length and initial orientation were conducted.

5.2 Methodology

A series of simulations were undertaken using the fully coupled hydro-mechanical analysis technique described in chapter 3. The model is driven by a prescribed fluid flux which generates the required pressure to open a starter fracture. The 2D simulation models a plan view, i.e. at a constant depth, of a relatively thin layer of shale in a 1km square domain. Under these circumstances gravitational effects are ignored, and uniform, axis aligned stresses are used to initialise the model, as well as a uniform pore pressure.

5.2.1 Variation of Stress Anisotropy

In the first set of simulations, the propagation of a fracture initially oriented at 90° to the maximum principal stress direction was examined. Varying degrees of stress anisotropy were used as initial conditions, with the aim of establishing how the stress anisotropy would affect the rate at which the fracture reoriented towards the maximum principal stress direction. Figure 5.2.1 outlines the initial conditions of this set of simulations.

Several exploratory simulations were carried out under varying confining pressures and in-situ pore pressures to establish a robust set of basic parameters. As expected, higher confining pressures[1] were found to require higher pressure to initiate fracturing. Since the fracturing occurred at a higher fluid pressure, the fracture propagated more quickly, requiring a higher coupling frequency between the fluid and mechanical fields to capture the propagation accurately. This was because fracture insertion could only occur after a coupling step, and at lower coupling frequency, the mechanical analysis created large damage zones between fracture insertions. The resulting fracture geometry was less likely to be accurate than many smaller damage zones frequently inserting smaller sections of fracture.
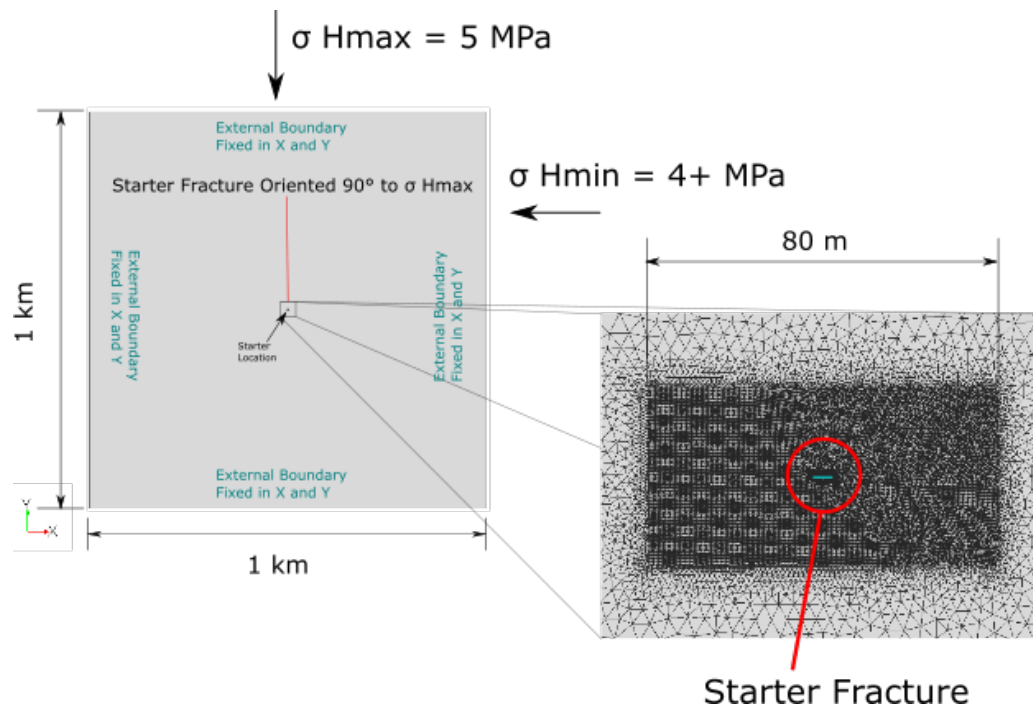
Figure 5.2.1: Simulation Initial Conditions

The higher pressure required to fracture also took longer to achieve in simulation time, resulting in longer realtime runtimes. The results under lower confining pressures were obtained more quickly and matched well with those under higher pressures, so lower confining pressures were used in the final runs to reduce computation time. Similarly, the mechanical effects on rock fluid pressure are ignored during fracturing by default, so rock pore pressure only serves to increase the total stress, resulting in longer computation time. Hence, pore pressure in the shale was removed from these simulations. This is justifiable on a physical basis by considering that the since the pore fluid is a gas, and highly compressible, the pore pressure change due to mechanical stress is likely to be

---

[1]Equiv. to mean effective stresses

insignificant.

The general parameters established are given in Table 5.1. Each simulation used the same initial mesh, with a starter fracture oriented at 90° to the maximum principal stress direction σ_{Hmax}, in this case σ_{yy}. The minimum horizontal stress was varied for each simulation, with the expectation that at high levels of stress anisotropy ($\sigma_{Hmax} \gg \sigma_{Hmin}$) reorientation would occur rapidly, and conversely that there may be some state close to isotropy in which the fracture reoriented slowly if at all.

Parameter	Unit	Value
Young's Modulus	GPa	32
Poisson's Ratio		0.2
Reservoir Pore Pressure	MPa	0
Effective Stress XX	MPa	Varies
Effective Stress YY	MPa	5
Effective Stress ZZ	MPa	5
Porosity		0.01
Fracture Height (Layer thickness)	m	10
Initial Fracture Length	m	0.4
Fluid Volume	m^3	3
Flow Rate	$\frac{\mathrm{m}^3}{\mathrm{s}}$	0.1
Fluid Viscosity	Pa.s	1.67e-3

Table 5.1: Indicative Simulation Parameters

5.2.2 Variation of Initial Fracture Length

A second set of simulations varied the initial fracture length to see if a relationship between this and the fracturing pressure could be established.

The initial fracture length was varied at increasing factors of the fracture length used in the simulations which varied stress anisotropy (section 5.2.1), and Table 5.1 lists the basic parameters used in the study. In addition, these were repeated at two values of σ_{Hmin} to capture any interplay between stress anisotropy and initial fracture length. The simulations were carried out with initial fractures oriented at 90° to the σ_{Hmax} of 5 MPa, with σ_{Hmin} of 4 and 4.9 MPa.

The model setup was identical to that shown in Figure 5.2.1, with the exception of the starter fracture length and minimum horizontal stress magnitude.

5.2.3 Variation of Initial Fracture Orientation

In a third set of simulations, the initial orientation of the starter fracture relative to maximum principal stress direction was varied. The initial stresses were σ_{Hmax}= 5 MPa and σ_{Hmin}= 4 MPa for all simulations. The initial fracture length in these simulations was 4 m, corresponding to a length factor of 10 in the simulations of section 5.2.2. This choice of length factor was made to reduce the opening pressure, based on results in section 5.3.1, and discussed in section 5.4.1.

Figure 5.2.2 outlines the initial conditions of this set of simulations.
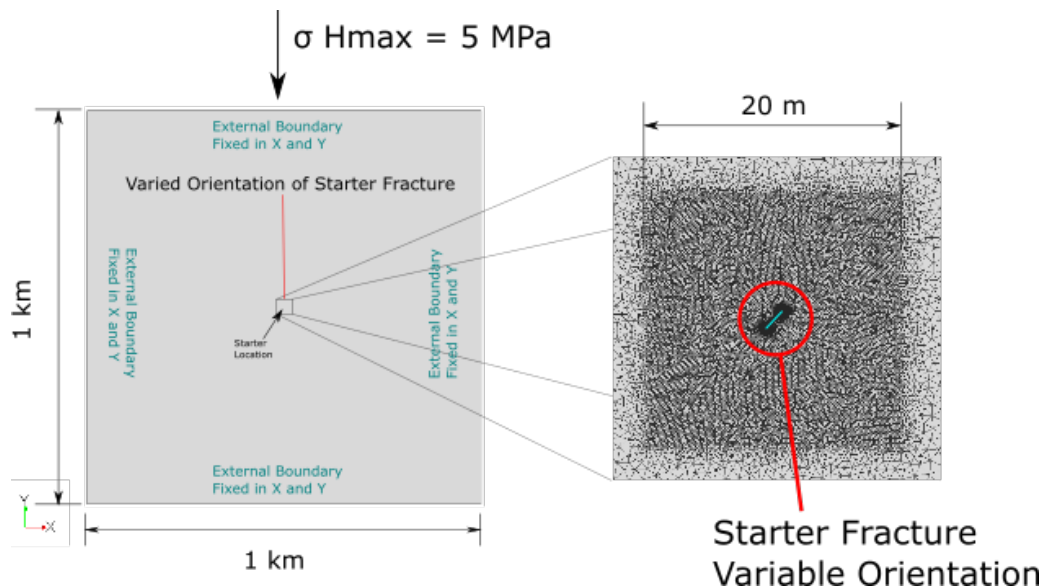
Figure 5.2.2: Simulation Initial Conditions

5.3 Results

5.3.1 Variation of Stress Anisotropy

Several simulations at widely spaced values of σ_{Hmin} were run to establish areas in which to concentrate. The fracture geometry at the end of each simulation for three values of σ_{Hmin} are shown superimposed in Figure 5.3.1. For scale, the blue fracture spans 70 m in the X direction, and the starter fracture in all cases is 0.4 m long. The red fracture has propagated with σ_{Hmin}=2.5 MPa, the green fracture propagated under σ_{Hmin} of 3.5 MPa, and the blue 4.0 MPa. The transition between 3.5 and 4.0 MPa was deemed of more interest than that between 2.5 and 3.5, since both the latter cases reoriented completely. Hence, more simulations were carried out between 3.5 and 4.0 MPa than 2.5 and 3.5. The final values of σ_{Hmin} used in each simulation are presented in Table 5.2.
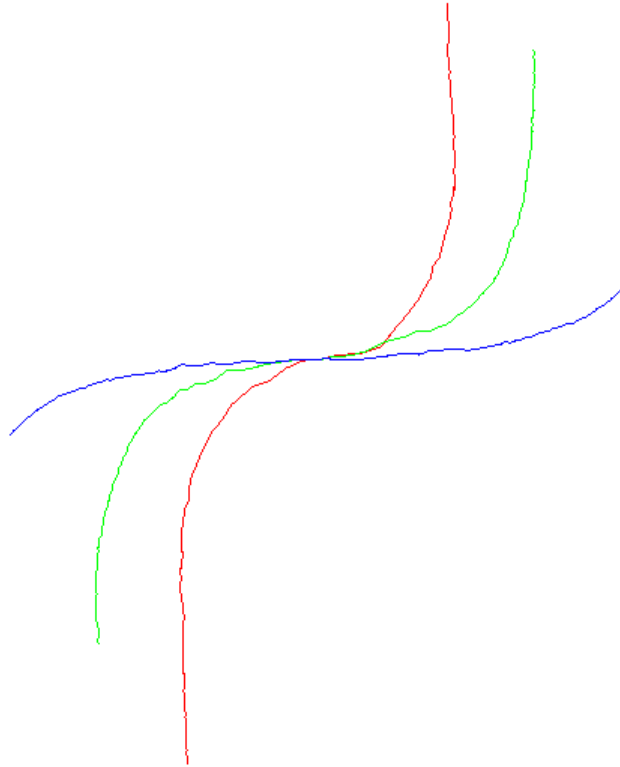
Figure 5.3.1: Reorientation after 30s, σ_{Hmin} =2.5 MPa (red), 3.5 MPa (green), 4 MPa (blue)

σ_{Hmin} =σ_{xx} (MPa)	$\sigma_{Hmax} = \sigma_{yy}$ (MPa)
2.5	5
3.0	5
3.5	5
3.6	5
3.7	5
3.8	5
3.9	5
4.0	5
4.2	5
4.4	5
4.6	5
4.8	5
5	5

Table 5.2: Minimum Horizontal Stress Values

Opening Pressure

The fluid pressure history for simulations with σ_{Hmin} at values between 4.1 and 4.9 MPa are plotted on 5.3.2, and the peak values recorded as the opening pressure in 5.3.3. Note the high pressure in relation to the in-situ stresses.
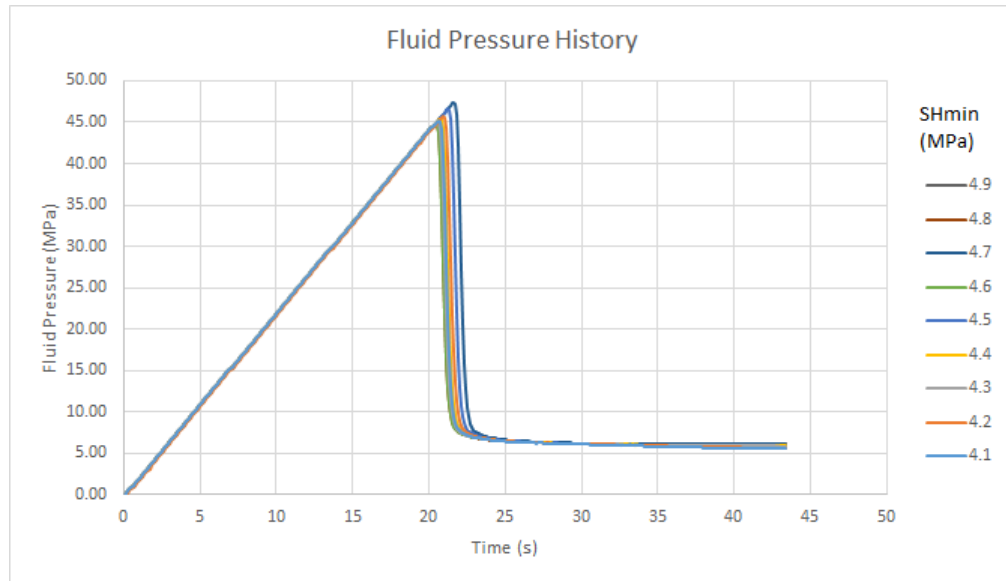
Figure 5.3.2: Fluid Pressure History - Variation of σ_{Hmin}
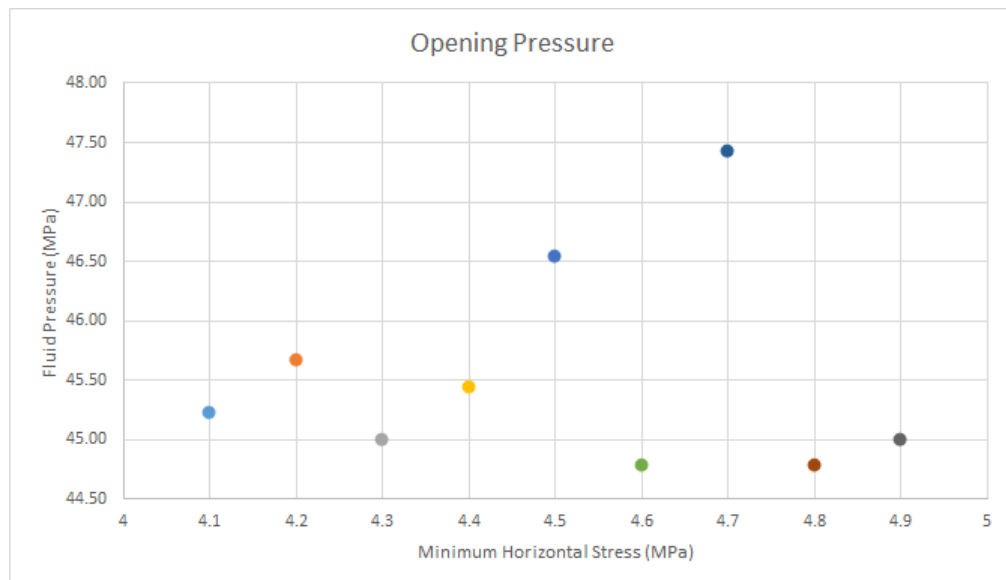
Figure 5.3.3: Fracture Initiation Pressure vs σ_{Hmin}

Reorientation Rate

Given the aim of establishing a rate at which reorientation occurs, it was first necessary to establish a means of measuring the amount of reorientation. The first step was to extract orientation information from the simulation, which was achieved by plotting the orientation of each element along the propagating fracture pipe, as calculated using $atan2(x, y)$ where x and y are the vector components of each segment. These were plotted against the x coordinate of each segment. An example of such a plot is Figure 5.3.4.
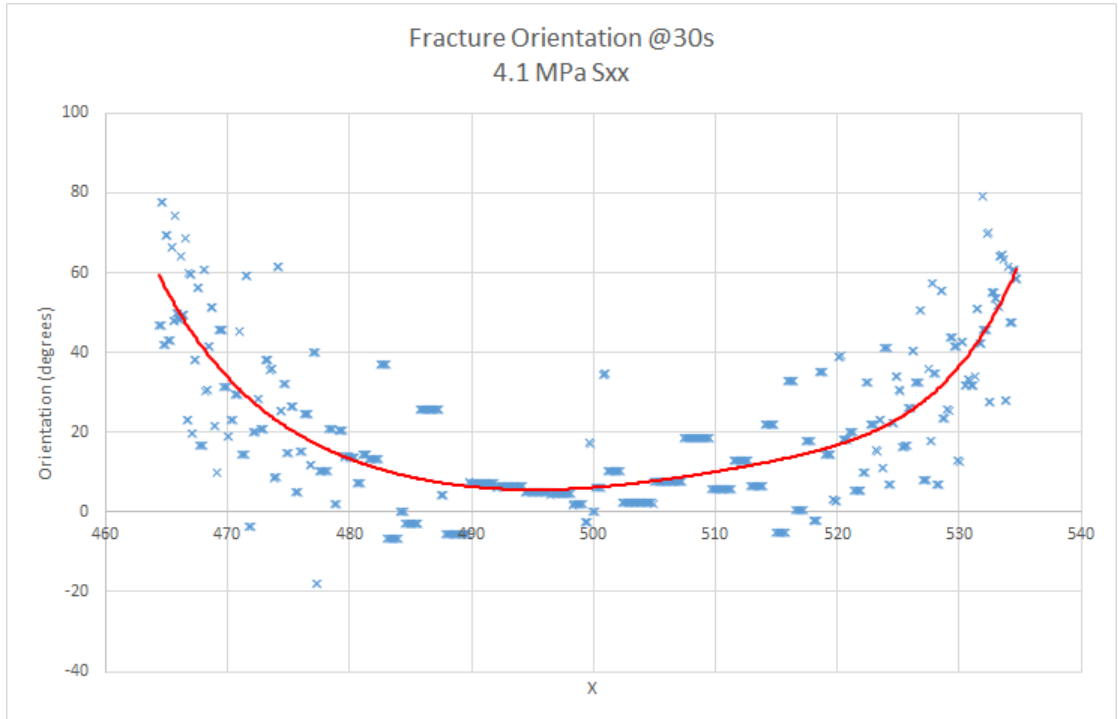
Figure 5.3.4: Fracture Element Orientation Plot σ_{Hmin}= 4.1 MPa

The wide range of orientations for each segment in Figure 5.3.4 is quite pronounced; this is due to the mesh dependence of the fracture insertion scheme, which is discussed further in section 5.4.1. A polynomial fitted through the data points agrees well with the orientation in the center of the fracture as well as the tips, and in this case a value of 60° at the tip was recorded. However, to capture the evolution of fracture tip orientation at a sufficient resolution, this process of fitting was reduced to taking the average of a fixed number of orientations at one end of the fracture. Figure 5.3.5 shows the resulting tip angle measurements through time for a selection of σ_{Hmin} values.
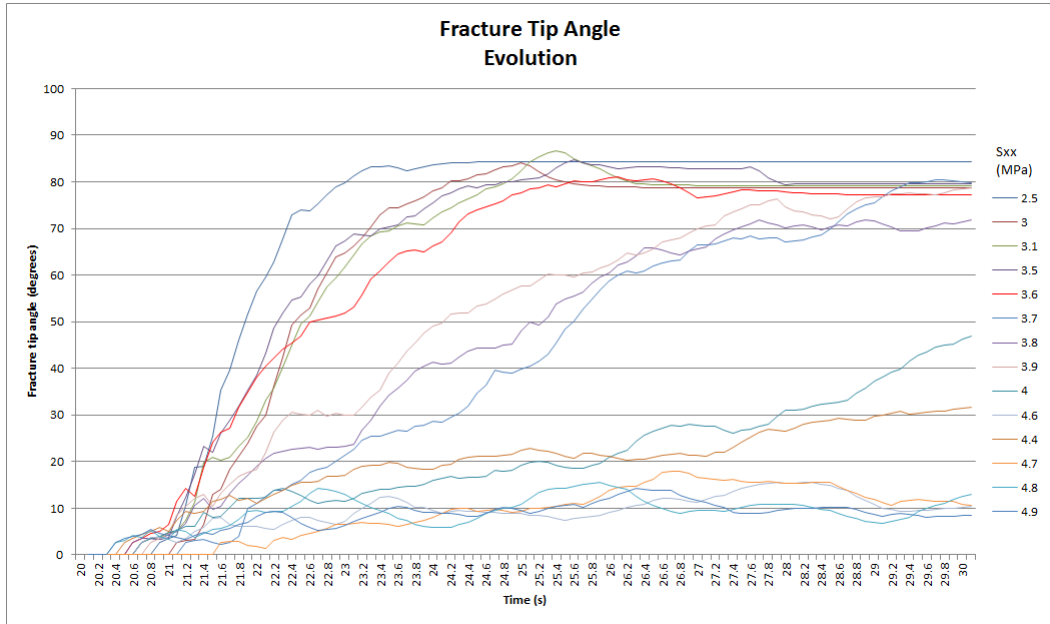
Figure 5.3.5: Fracture Tip Angle Evolution - Variation of Stress Anisotropy

It was unclear from Figure 5.3.5 whether some of the fractures would eventually reorient if given enough time. A selection of longer simulations were run to establish this, with values of σ_{Hmin} between 4 and 4.9 MPa, at 0.1 MPa intervals.

The results of a selection of these simulations (σ_{Hmin}=4, 4.6, 4.9 MPa) are plotted together with simulation results that had completed reorienting in Figure 5.3.6. These are normalised in time, using the start of fracturing and the time at which the fracture tip angle reached a steady value. The fractures with σ_{Hmin} = 4.0 and 4.6 MPa did continue to curve and align more towards the maximum principal stress direction. The shorter run at 4.6 MPa is plotted in a dotted green for comparison with the longer run in solid green. As previously, the results are filtered using exponential smoothing.
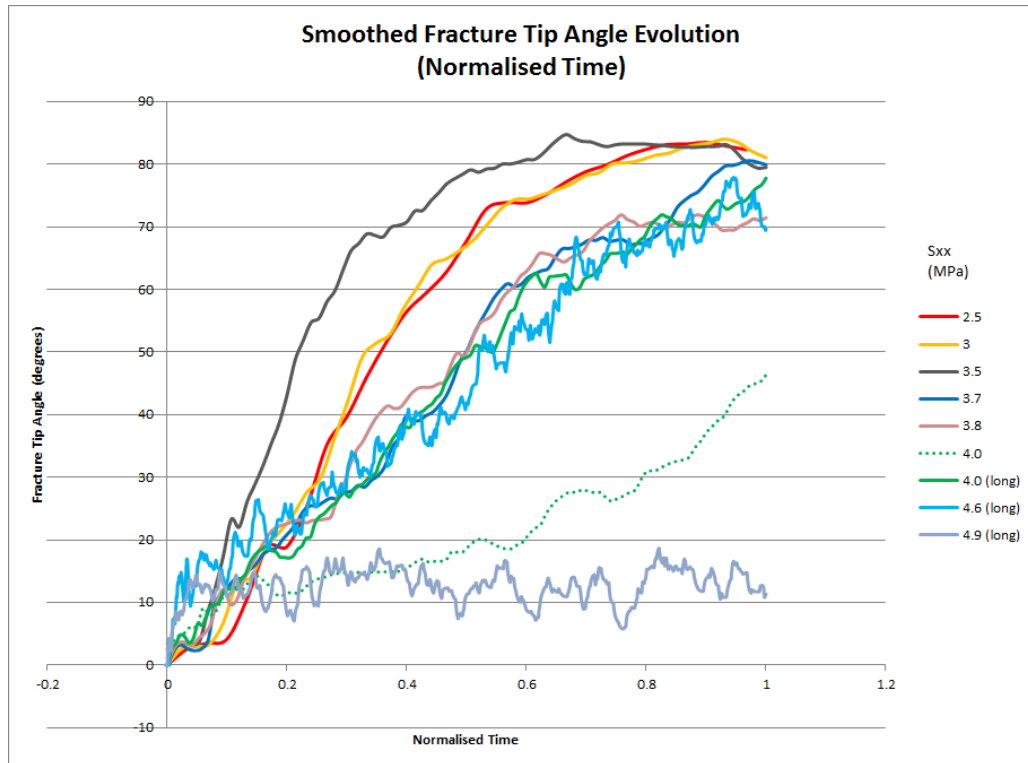
Figure 5.3.6: Smoothed and Normalised Fracture Tip Angle Evolution - Variation of Stress Anisotropy
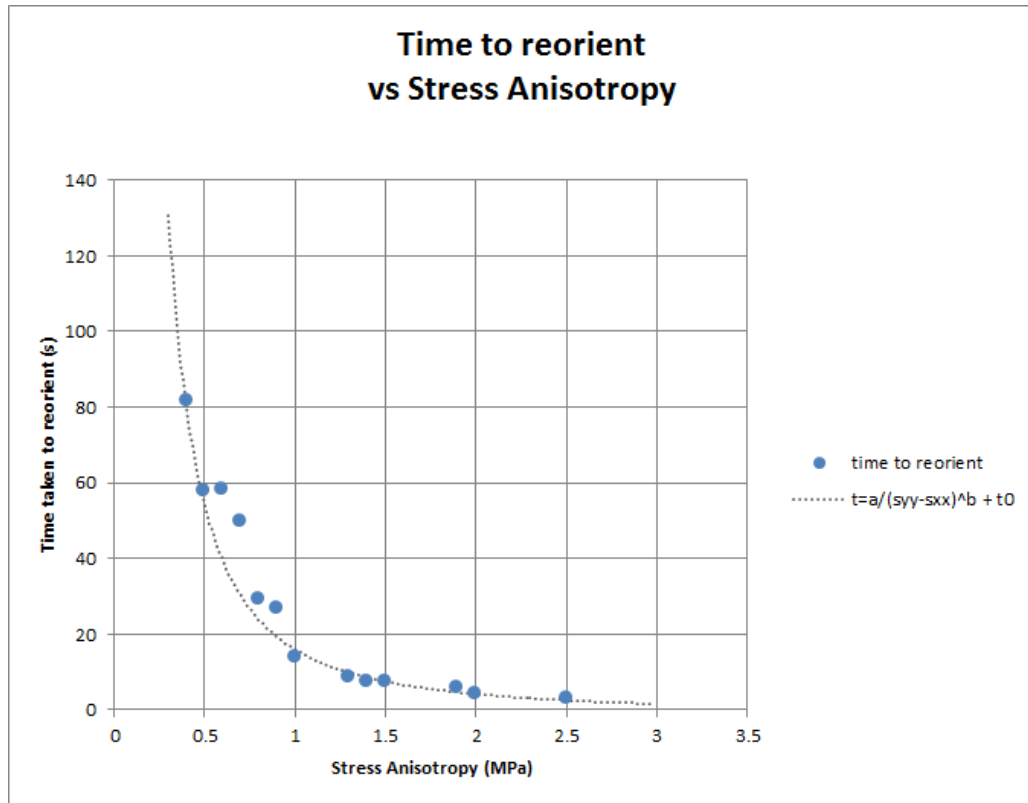
Figure 5.3.7: Time to reorient vs Stress Anisotropy - Variation of Stress Anisotropy

5.3.2 Variation of Initial Fracture Length

Recall from section 5.2.2 that two sets of simulations were run, each varying the initial fracture length. The fluid pressure at fracture initiation (opening pressure) was recorded for 7 factors of the starter fracture length used in the studies in section 5.3.1, and the evolution of the fracture tip angle examined, together with fluid pressure histories and the relationship between fracture length and tip angle.

Geometry

Figure 5.3.8 superimposes the fractures at time 64.6 s for σ_{Hmin}= 4 MPa on the same output. A coloured circle overlaid on the fracture indicates the factor of the reference starter fracture length, that being the length held constant in section 5.3.1, which was 0.4 m. Where they are in similar locations, the indicator is offset to aid identification. This plot shows the pipe elements that transport fluid through the fractures, which have been artificially thickened to aid visibility.
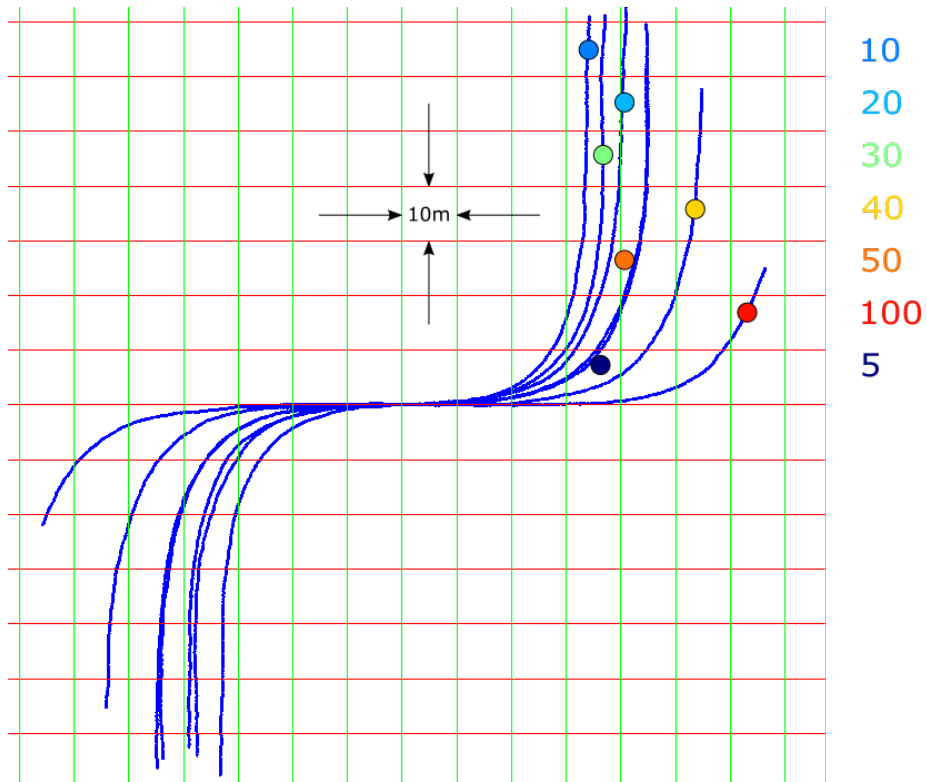
Figure 5.3.8: Fracture geometry at 64.6s

Opening pressure

The fracture initiation pressure for each fracture was recorded for two values of σ_{Hmin}, and is shown in Figure 5.3.9. The opening pressure can also be seen as the peak pressure in Figure 5.3.15, which uses the data from the runs with σ_{Hmin}= 4 MPa.
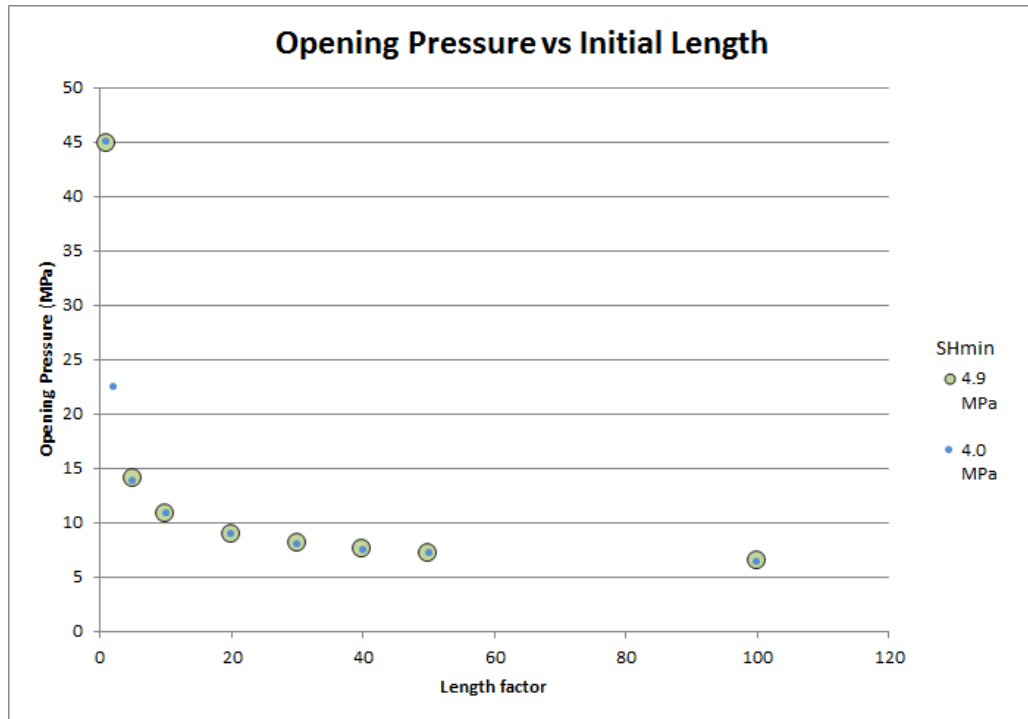
Figure 5.3.9: Opening Pressure vs Initial Length, 90° to σ_{Hmax}

Reorientation Rate

Figure 5.3.10 is a plot of smoothed tip angle evolutions for a selection of initial lengths (as factors of the studies above). The initial stress conditions are $\sigma_{Hmin} = 4.0$ MPa, and $\sigma_{Hmax} = 5.0$ MPa. The reorientation curve is generally more S-shaped in the longer fractures, although a plot of the elapsed time since fracture initiated shows the relative evolution more clearly; this is plotted in Figure 5.3.11. Generally the fracture reorientation time increases with the initial length of the fracture, again illustrated in Figure 5.3.12. These results are not trending as clearly to a particular curve as those in Figure 5.3.9, possibly due to the mesh dependency of the fracture path.

Figure 5.3.13 shows the increase in length of each fracture with time. Figure 5.3.14 plots the tip angle of each fracture against the extension length (the current length - initial length). The fluid pressure at the point of fluid injection was also monitored, and this is shown in 5.3.15.
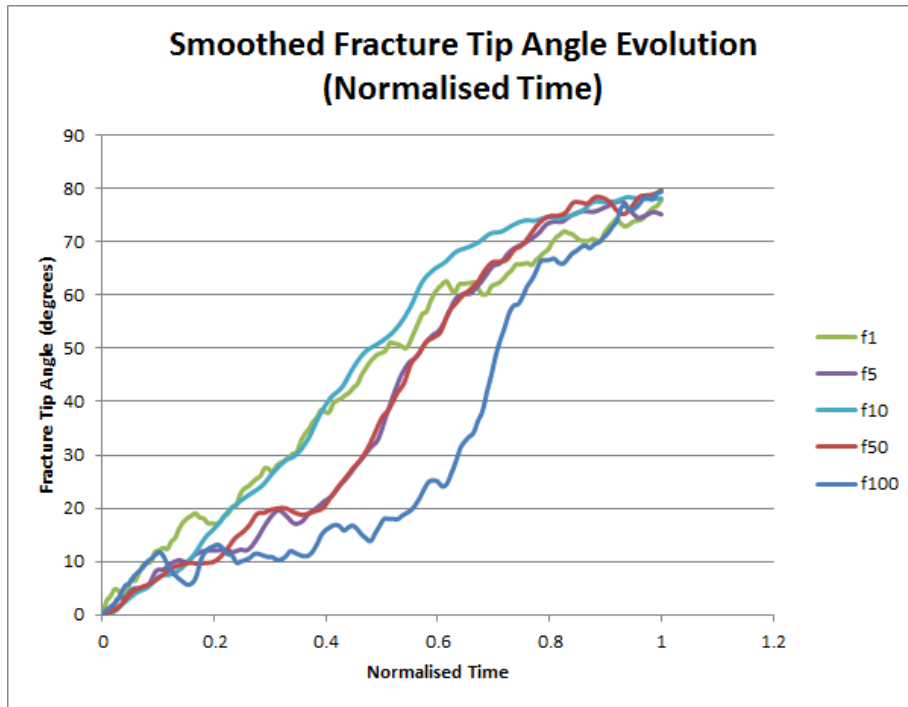
Figure 5.3.10: Fracture Tip Angle Evolution vs Normalised Time - Variation of Initial Length
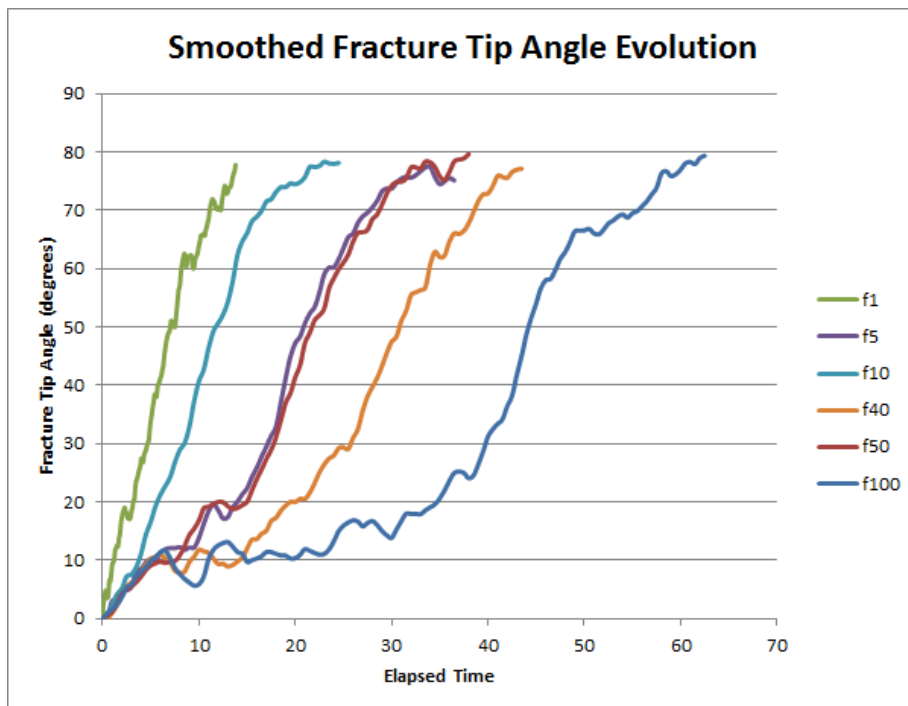
Figure 5.3.11: Fracture Tip Angle Evolution vs Elapsed Time - Variation of Initial Length
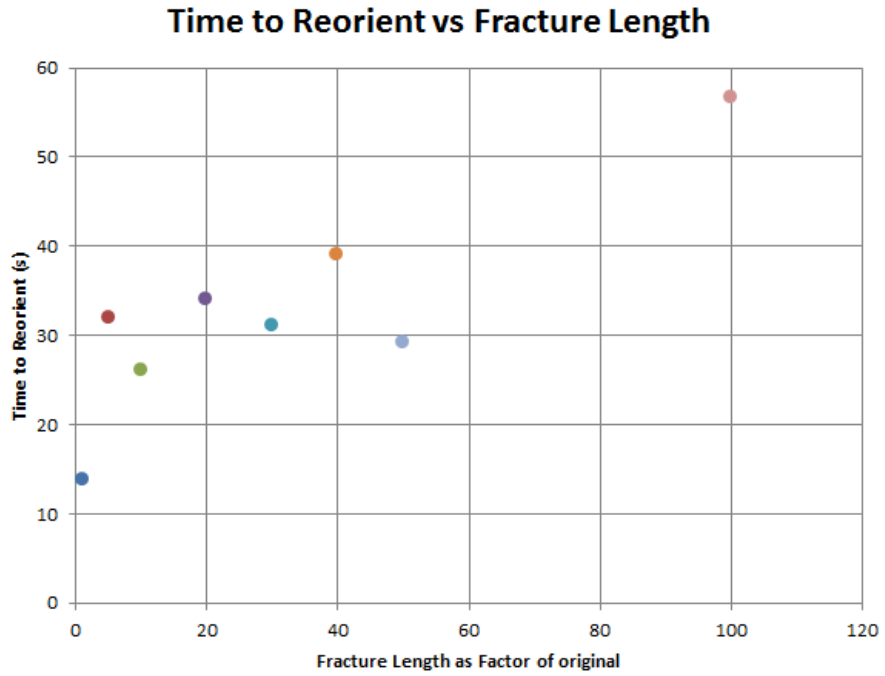
Figure 5.3.12: Time to Reorient vs Fracture Length - Variation of Initial Length
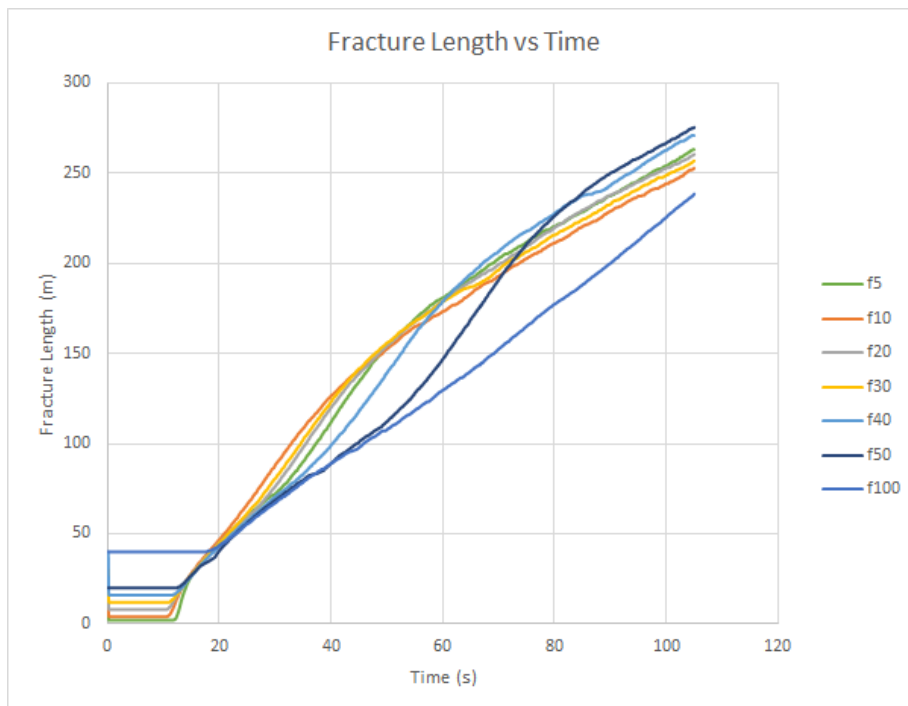
Figure 5.3.13: Fracture Length - Variation of Initial Length
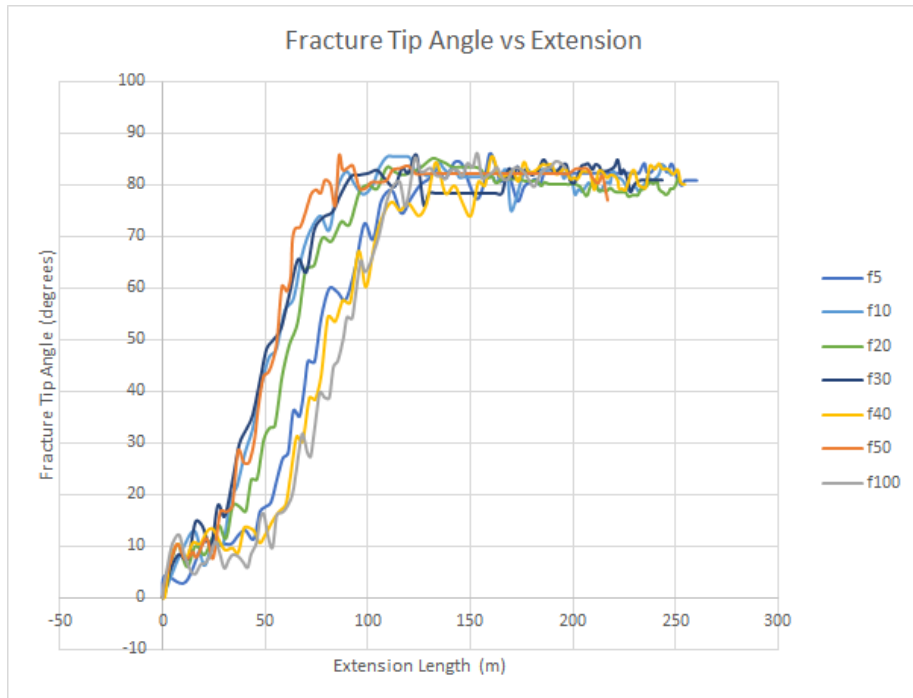
Figure 5.3.14: Fracture Tip Angle vs Extension - Variation of Initial Length
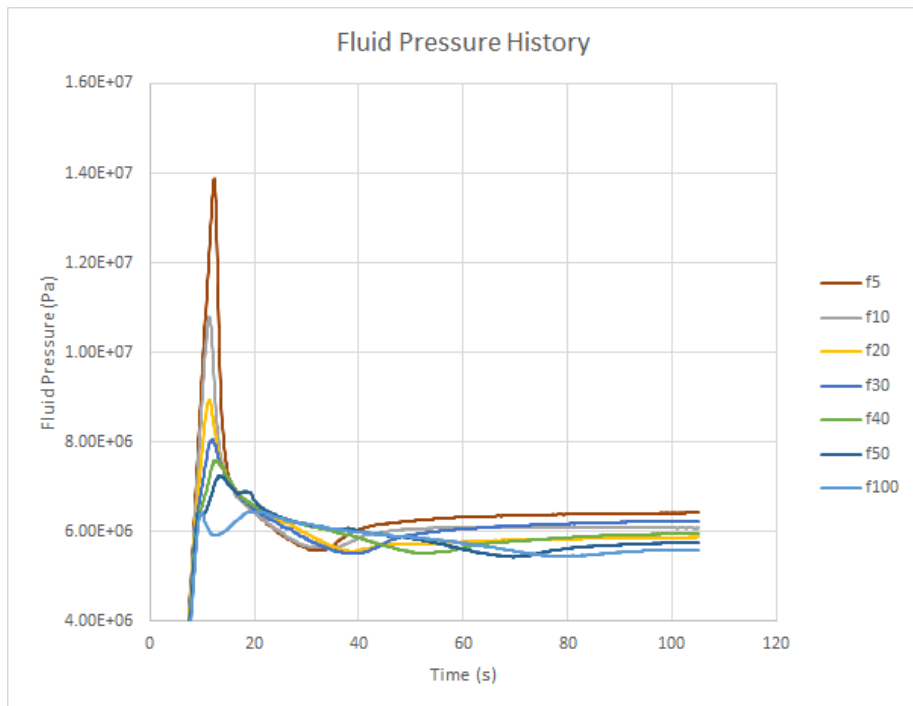
Figure 5.3.15: Fluid Pressure History - Variation of Initial Length

5.3.3 Variation of Initial Fracture Orientation

Geometry

Figure 5.3.16 superimposes the fractures at time 36 s on the same output. The legend uses a coloured circle overlaid on the fracture to indicate the initial fracture orientation relative to the minimum horizontal stress (in degrees). This plot shows the pipe elements which transport fluid through the fractures, and have been artificially thickened to aid visibility.

Figure 5.3.16: Fracture geometry at 36 s - Variation of Initial Orientation

Opening Pressure

The fracture initiation pressure was recorded for each simulation, presented in 5.3.17. The values are the peaks seen in 5.3.18, which shows the fluid pressure at the point of injection during the simulations.
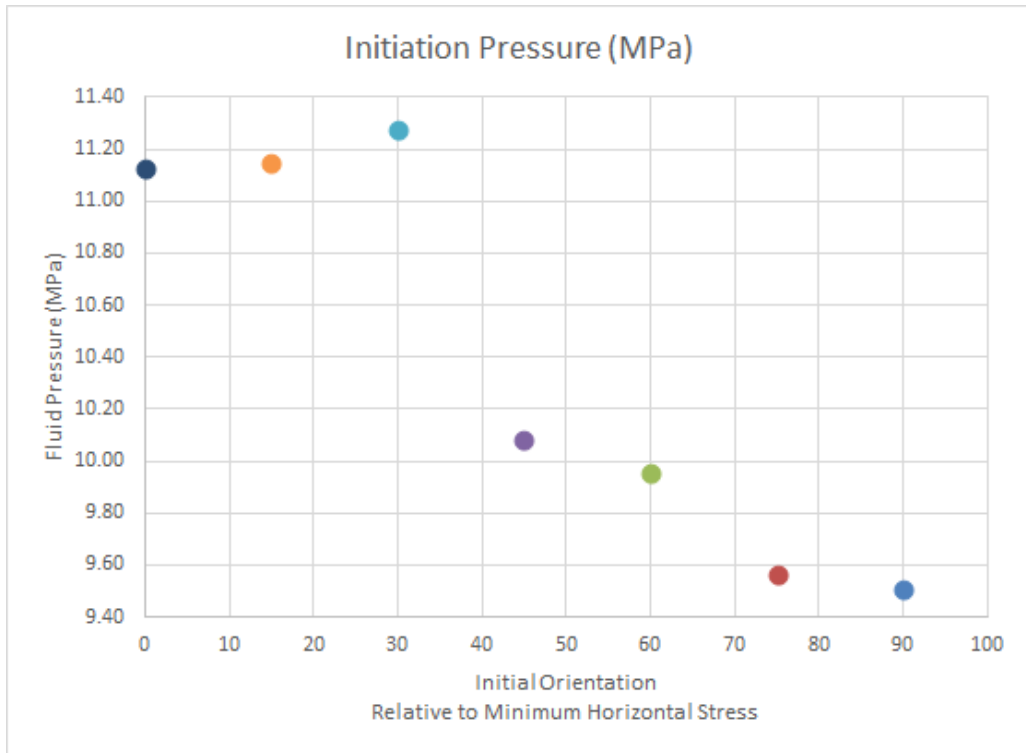
Figure 5.3.17: Opening Pressure - Variation of Initial Orientation
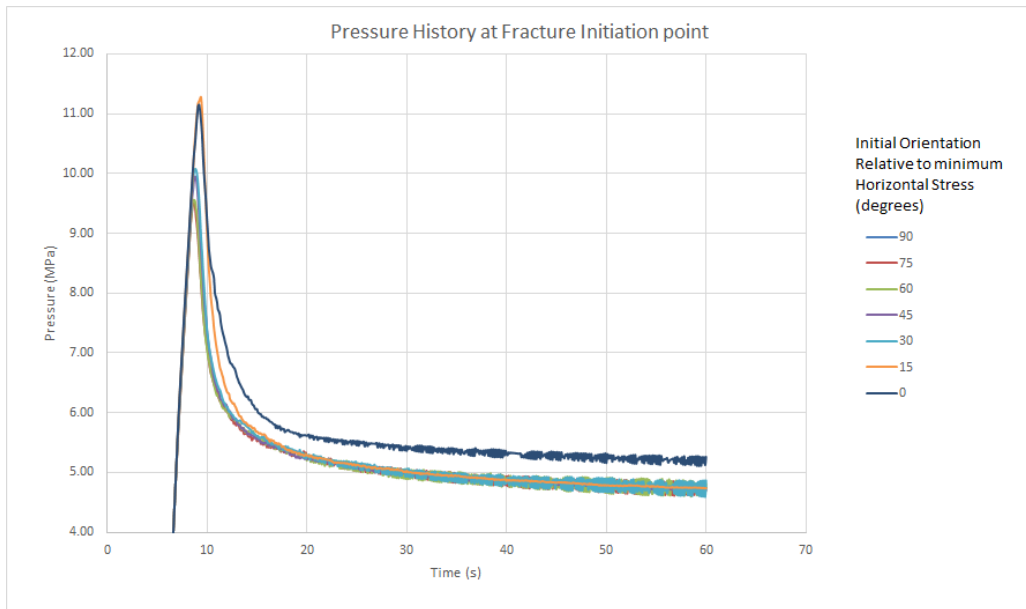
Figure 5.3.18: Pressure Evolution - Variation of Initial Orientation

Reorientation Rate

The fracture tip angle was extracted as described in 5.3.1, and the smoothed evolution of the fracture tip angle is plotted in 5.3.19, and normalised in time in 5.3.20. In both cases the legend refers to the angle from the minimum horizontal stress direction.
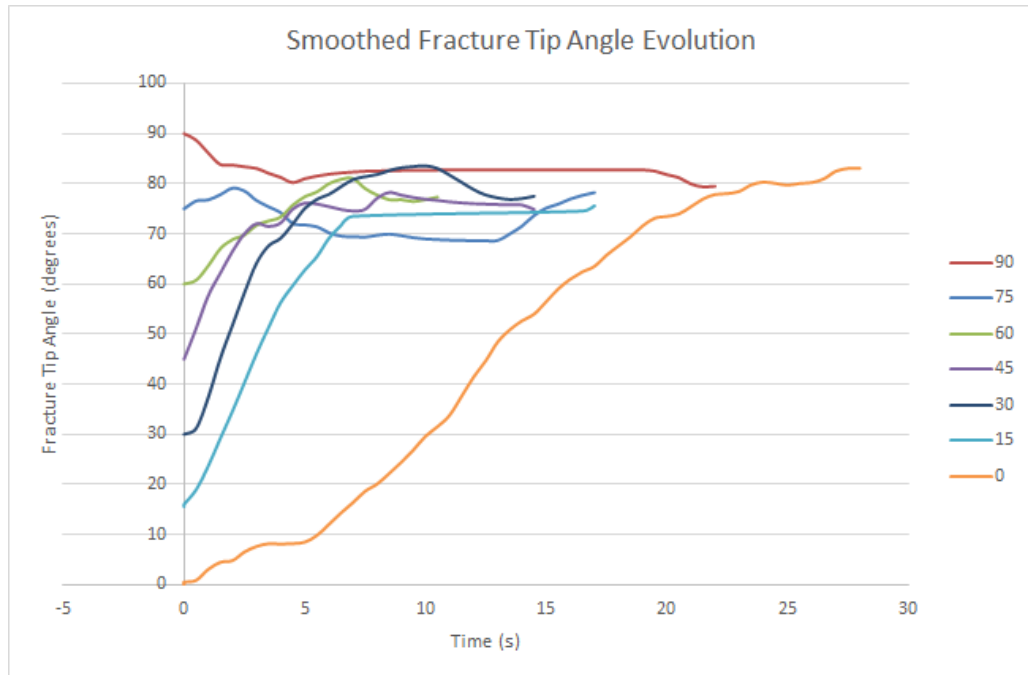
Figure 5.3.19: Tip Angle Evolution - Variation of Initial Orientation
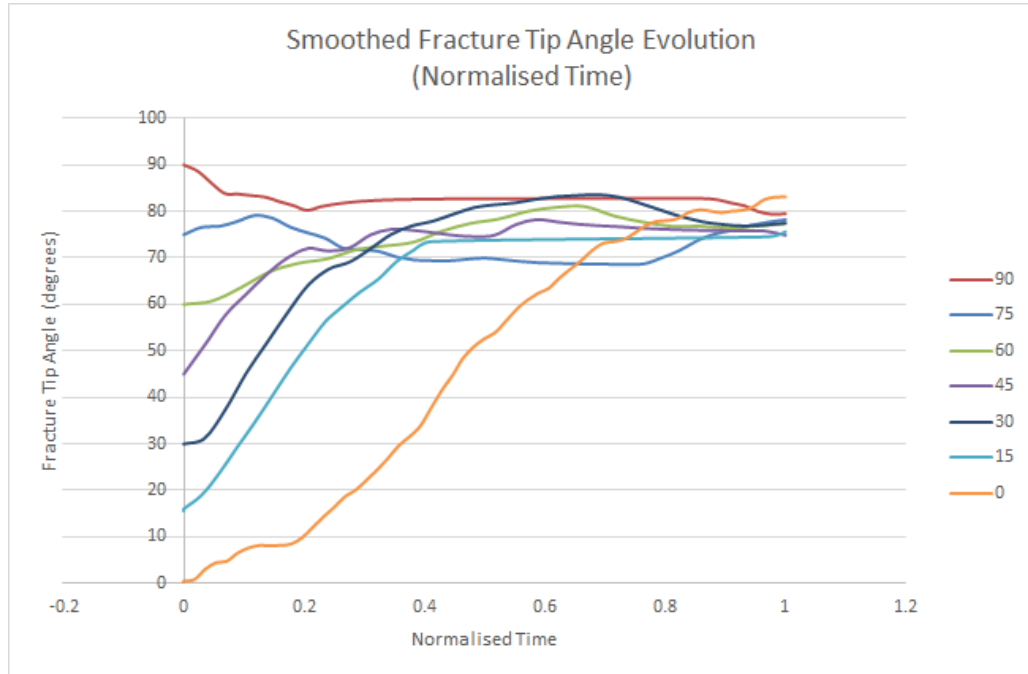
Figure 5.3.20: Normalised Tip Angle Evolution - Variation of Initial Orientation

5.4 Discussion

5.4.1 Variation of Stress Anisotropy

Mogilevskaya et al. (2000) examined the dependence of fracture orientation on near-wellbore fracture paths. Their model used a starter crack of varying orientation and length. They found that in terms of stress, the dependency could be reduced to a normalised version of the stress anisotropy. A dimensionless parameter β was defined:

$$\beta = \frac{\sigma_{Hmax} - \sigma_{Hmin}}{K_{1C}/\sqrt{R}} \tag{5.4.1}$$

Where R = wellbore radius and K_{1C} is the fracture toughness (unit $\frac{\mathrm{MPa}}{\sqrt{\mathrm{m}}}$). Their results of varying β are shown in Figure 5.4.1. While not directly comparable with the following results, their results show a smooth reorientation from the initial crack, and faster reorientation in higher stress anisotropy.
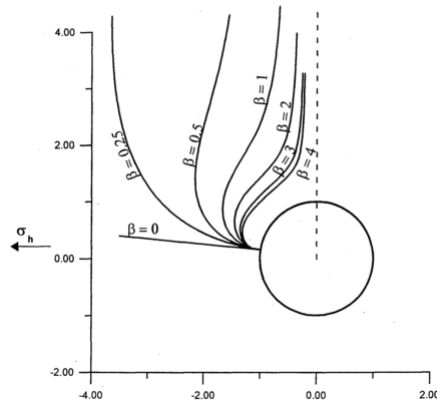
Figure 5.4.1: Reorientation dependence on β, Mogilevskaya et al. (2000)

Geometry

It was readily apparent on extraction of the element orientations that while at a macro level the fractures propagate fairly smoothly, the tip angle was actually quite noisy when considered on a per-element basis. Figure 5.3.4 exemplifies this, showing orientation perturbations of 20° or more between adjacent sections from a polynomial fit of the same data. This is an effect of the fracture insertion method. The mechanical simulation looks for elements that have reached a damage threshold based on the material failure properties of each element - in these examples, this is when the tensile strength of the rock has been exceeded by one of the principal stresses.

Once a required number of elements at the current fracture tip have been damaged beyond the threshold value, the fracture geometry is modified by inserting a new section of fracture based on the geometry of the damaged elements. An illustrative example is presented in Figure 5.4.2, which shows the current fracture tip location as a thick black line - representing the pipe elements used in the fluid analysis. The current elements that have reached the threshold damage value are red, and a dashed blue line is indicative of the direction in which a new segment of geometry will be added. This will not extend past the last damaged element, and the direction is determined by the geometric mean of the damaged elements. Local remeshing of the area around the inserted line ensures that the direction is maintained - further details of this process are given in section 3.6. Since the threshold number of elements required to trigger fracture insertion is quite low (around 3), and the elements are small in relation to the main fracture, the stresses around the fracture tip are not unduly affected by the inserted geometry. This means that the stresses due to the fracture being propagated continue to produce inserted geometry which is representative of that stress field, yet at fine scale show the perturbations seen in Figure 5.4.2, and the noise in temporal plots such as Figure 5.3.6.

125
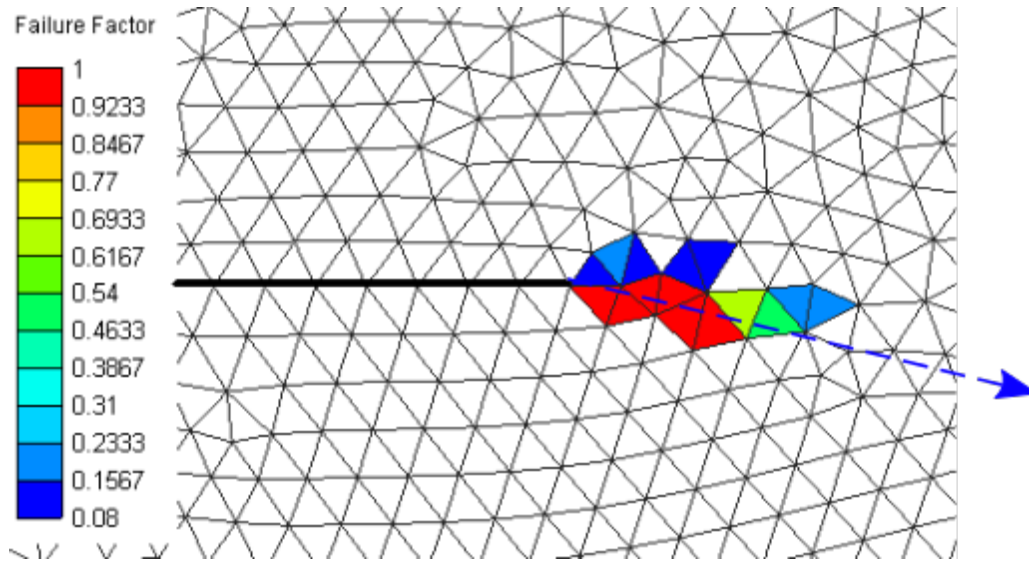
Figure 5.4.2: Fracture direction prediction

It is possible, however, that when the fracture is small or of similar scale to the in compar-
ison to the element size, that fractures are artificially difficult to initiate. For this reason it
is important that the ratio of in-situ fracture length to minimum element size is considered
when setting up the simulations.

Opening Pressure

The opening pressure of this set of simulations is very high - much higher than that pre-
dicted by wellbore tensile failure pressures, for example. Hossain et al. (2000) derive the
fracturing pressure P_{wf} for a horizontal well parallel to σ_{Hmax}, in a normal faulting regime:

$$P_{wf} = 3\sigma_{Hmin} - \sigma_V - P_p - \sigma_t \tag{5.4.2}$$

A normal faulting regime is one in which both σ_{Hmin} and σ_{Hmax} are of lower magnitude
than σ_V, which is the case in these simulations. They are run with pore pressure $P_p = 0$.
The rock tensile strength is denoted as σ_t, which for the simulations in this chapter is 1
MPa. This is frequently assumed to be near zero due to the presence of natural fractures
(Zoback (2007), Hossain et al. (2000)) . Nevertheless, according to equation 5.4.2, the
predicted fracturing pressure in MPa for the most isotropic case above is:

$$P_{wf} = 3 * 4.9 - 5 - 0 - 1 = 8.7 \tag{5.4.3}$$

Clearly this is nowhere near the pressures of around 45-48 MPa seen in the simulations,

126

and the reason is quite obvious - the derivations used to arrive at equation 5.4.2 use the wellbore geometry to predict the stresses around the wellbore at a given a fluid pressure. The simulations here are without the internal surface of the wellbore, and are likely to be dependent on the fracture length - which is explored in more detail in section 5.4.2.

Figures 5.3.2 and 5.3.3 do not make it clear whether there is a consistent effect due to changing σ_{Hmin}. Three extra simulations were run to provide a greater range of σ_{Hmin}, and these added to the opening pressure chart, updated in Figure 5.4.3. From this data it would appear that if there is a change in initiation pressure due to the stress anisotropy changing, that it is being masked by numeric or algorithmic issues. One potential source of contamination of the data is discussed further in section 5.4.2, and given the results presented there, these results may have been more useful (in terms of fracture initiation pressure) had the initial fracture been longer.
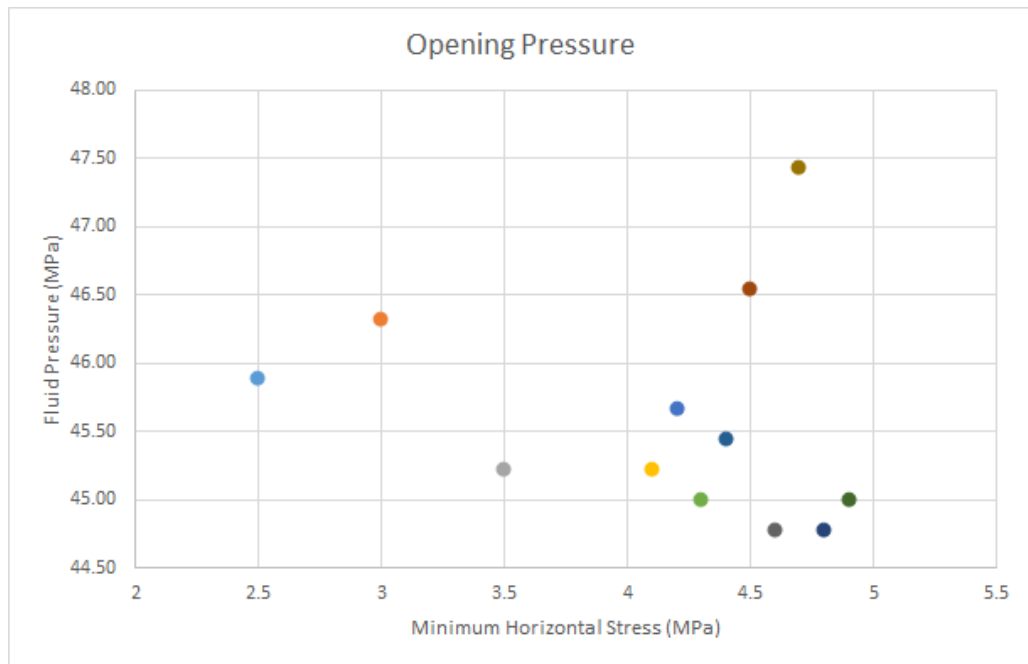
Figure 5.4.3: Fracture Initiation Pressure vs σ_{Hmin} - extended results

In contrast to the fracture initiation pressure, propagation pressures in Figure 5.3.2 appear to be closer to those predicted by fracture mechanics for linear propagation of a long fracture in a normal faulting regime, i.e. just above one of the horizontal principal stresses.. However, from the scale of the chart it is difficult to determine whether it the minimum or maximum horizontal stress is influencing the propagation pressure. A detail of the pressure history is presented in Figure 5.4.4. This plot is especially interesting when considering the time taken for the fracture to reorient, which will be discussed in 5.4.1. Of particular interest are the dips in pressure for the more anisotropic examples.

The propagation pressure for each case was taken as the final pressure of each history plot; in Figure 5.4.4 many of the histories have already reached a steady pressure, and this is the case eventually for all of the simulations. This steady pressure P_p was measured at the point of fluid injection, and is compared to a propagation pressure calculated using both σ_{Hmax} and σ_{Hmin}, i.e. the following vales are plotted for each variation of σ_{Hmin} simulation, in Figure 5.4.5:

- $P_p - \sigma_{Hmax}$

- $P_p - \sigma_{Hmin}$

For most cases the propagation fluid pressure is within 0.5 to 1 MPa of the *maximum* principal stress value, consistent with the pressure required to hold open the starter fracture walls, which are oriented perpendicular to the maximum horizontal stress direction. However, that same pressure is not required to hold the fracture open once it has reoriented, and the fluid pressure drops significantly in the reoriented areas of the fracture, as can be seen in Figure 5.4.6. Similarly in Figure 5.4.7, which shows propagation with $\sigma_{Hmin} = 4.5$ MPa the fluid pressure in the reoriented area is lower than at the injection point, but at a generally higher pressure, because of the higher σ_{Hmin}. In both cases at the end of the reoriented zone the fluid pressure is approximately 0.5 MPa above σ_{Hmin}.

Mogilevskaya et al. (2000) calculated similar behavior for small initial fracture length, describing the process as unstable, due to pressure oscillations.
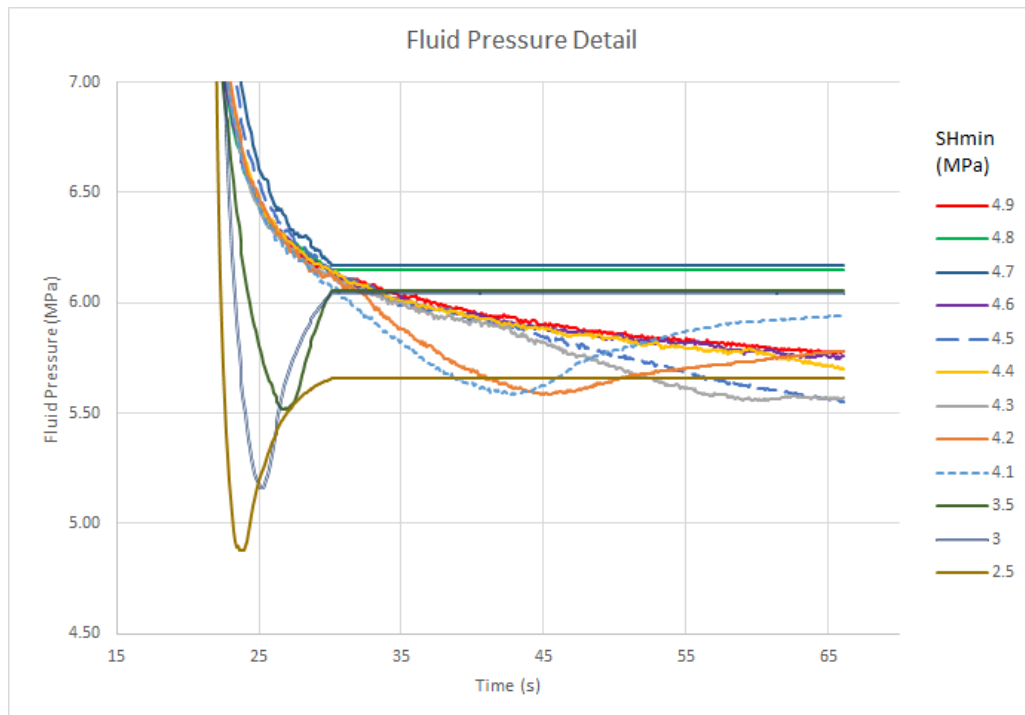
Figure 5.4.4: Fluid Pressure Detail
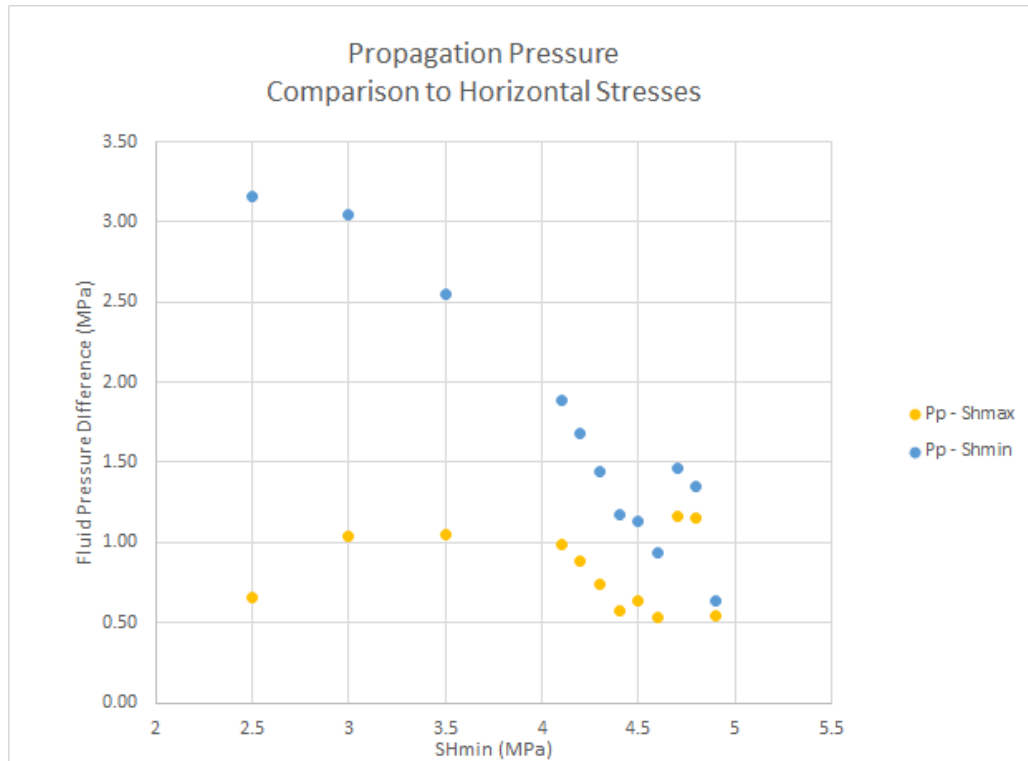
Figure 5.4.5: Propagation Pressure comparison to σ_{Hmax} and σ_{Hmin}
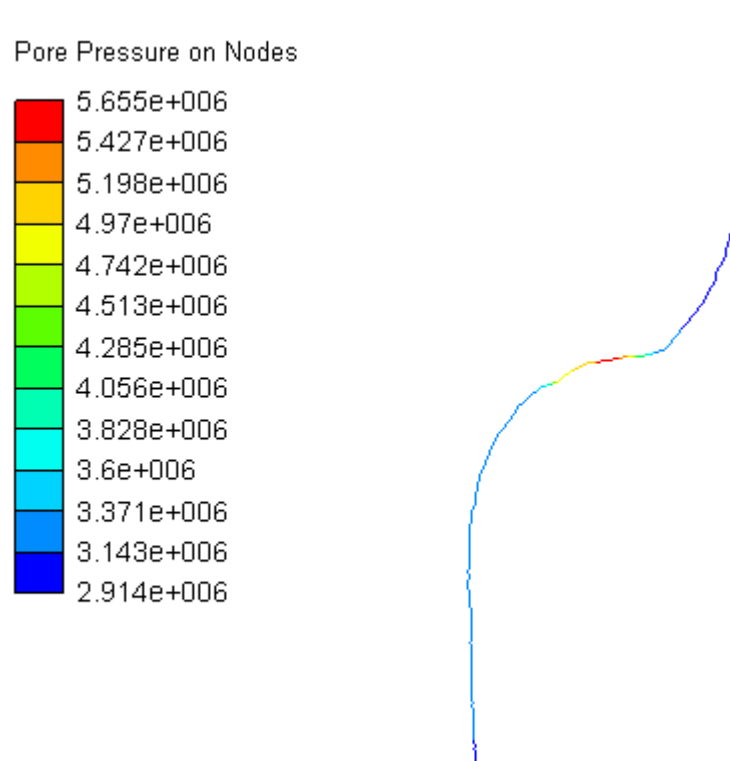
Figure 5.4.6: Fluid Pressure in Fracture, $\sigma_{Hmin} = 2.5$ MPa
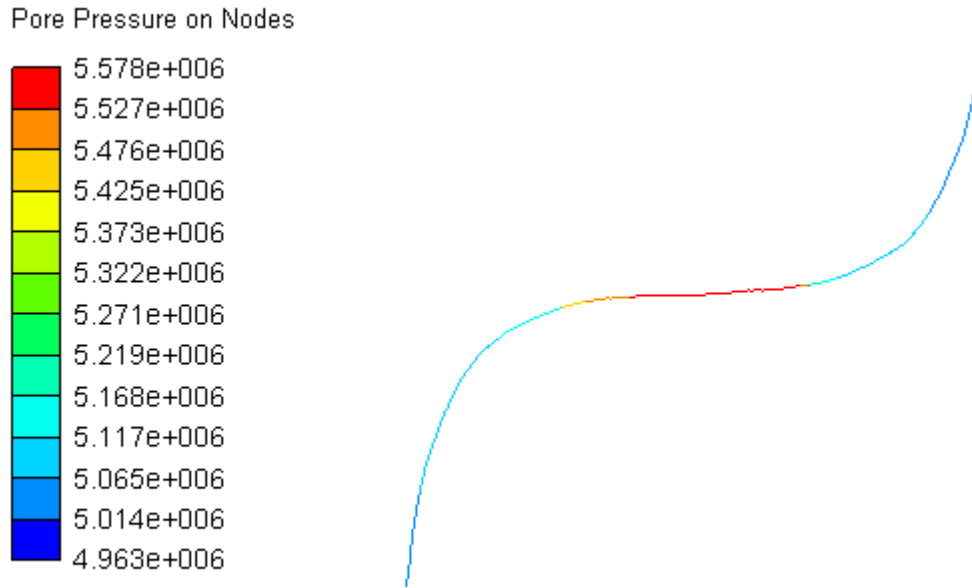
Figure 5.4.7: Fluid Pressure in Fracture, $\sigma_{Hmin} = 4.5$ MPa

Reorientation Rate

Figure 5.3.5 shows the history of the fracture tip orientation for varying values of σ_{Hmin}, which was varied at 0.1 MPa intervals. The data is smoothed using exponential smoothing[2] with a smoothing factor $\alpha_s = 0.3$. This acts as a low-pass filter, reducing the noise of rapid tip orientation changes due to mesh dependence. Higher stress anisotropy resulted in a more rapid transition to the maximum principal stress direction. Conversely, at near-isotropic stress values the tip angle changes very little, if at all in time. Single moving average trend lines are plotted for some representative values of σ_{Hmin}, which help to identify three broad categories of curve:

- Rapid reorientation for $\sigma_{Hmin} \lesssim 3.9$ MPa

- Constant, low tip angle for $\sigma_{Hmin} \gtrsim 4.7$ MPa

- Steady increase in tip angle

It was unclear whether some of the simulations in the third category would eventually reorient given more time, so these were re-run for a longer duration. The time normalised tip orientation plot 5.3.6 includes these longer simulation runs. The fractures with σ_{Hmin}

---

[2] $s_t = \alpha_s x_t + (1 - \alpha_s) s_{t-1}$
s_t= smoothed sample at time t, x_t= unsmoothed sample at time t, α_s = smoothing factor.

= 4.0 and 4.6 MPa did continue to curve and align more towards the maximum principal stress direction. In this plot, the gradient of the lowest three values of σ_{Hmin} are similar, and curve to become more shallow as the tip angle approaches the final value. The curve is shallower and more linear for higher values of σ_{Hmin}. It is worth noting that at even at high anisotropy, the fracture tip angle does not reach 90°. It is not possible to tell whether the range of final orientations is due to mesh dependent effects or a trend related to the anisotropy.

Figure 5.3.7 plots the time taken for the fracture to align with the maximum horizontal stress against the amount of stress anisotropy. This data appears to show an inverse power relationship, illustrated by a trend line plotted on the same chart. An inverse power relationship makes sense in that an asymptote on the y axis is expected, as this corresponds to a fracture propagating under isotropic conditions, where no reorientation is expected. At the upper limit of x, namely $\sigma_{Hmin} = 0$, a low or zero reorientation time is expected. To allow for an intercept of the horizontal axis, an offset of t_0 can be introduced.

$$t = \frac{\alpha_f}{(\sigma_{Hmax} - \sigma_{Hmin})^\beta} + t_0 \qquad (5.4.4)$$

For the trend line plotted in 5.3.7, α_f=17, β =1.7 and $t_0 = 1.102$, which allows instant reorientation under maximum anisotropy (σ_{Hmin}=0).

Figure 5.4.4 gives a detailed view of the fluid pressure at the injection point as many of the fractures were reorienting. For the first set of shorter simulations, the final pressures are extrapolated as horizontal lines, to provide a reference for the additional longer runs. Figures 5.4.8 and 5.4.9 examine this chart for the case of $\sigma_{Hmin} = 2.5$ MPa, with the addition of tip angle and fracture aperture data. Figure 5.4.8 shows that the reorientation occurred during the rapid drop in pressure that began when the fracture initiated. The fluid pressure drops below 5 MPa, which is required to hold the fracture open at that point. According to Figure 5.4.9,the fracture remains open at this point. A third chart, Figure 5.4.10 shows a spike in flow rate during the rapid drop in fluid pressure.
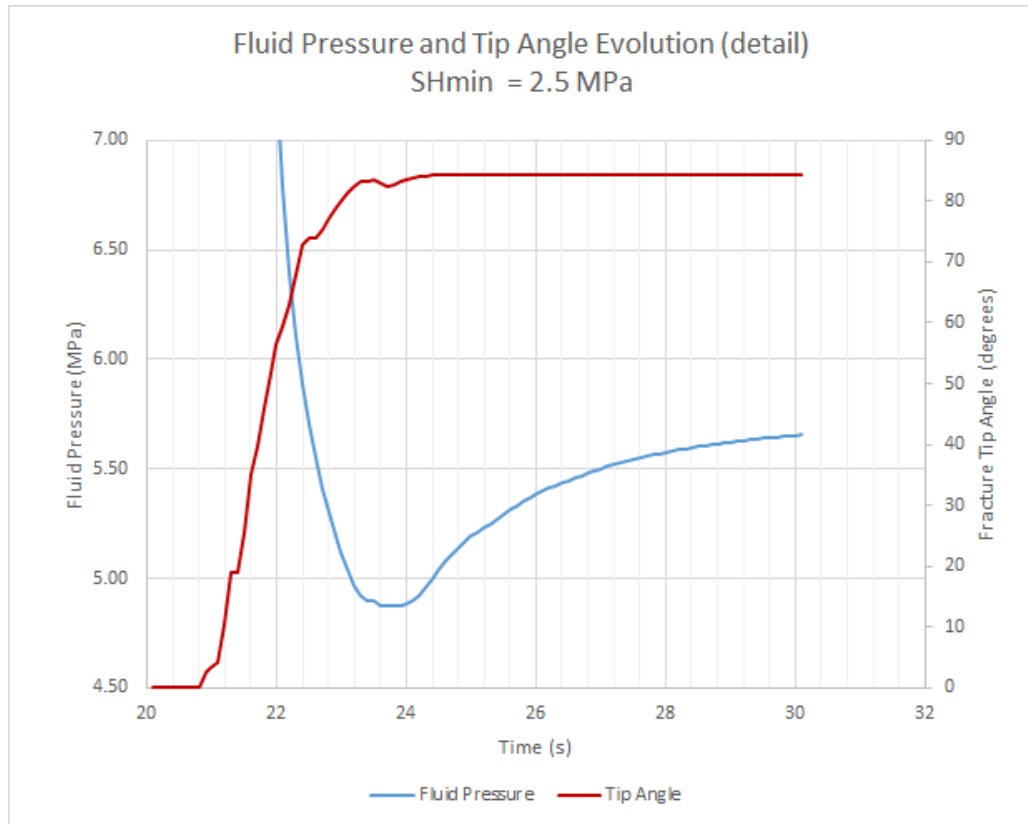
Figure 5.4.8: Fluid Pressure and Tip Angle Evolution, $\sigma_{Hmin} = 2.5$ MPa
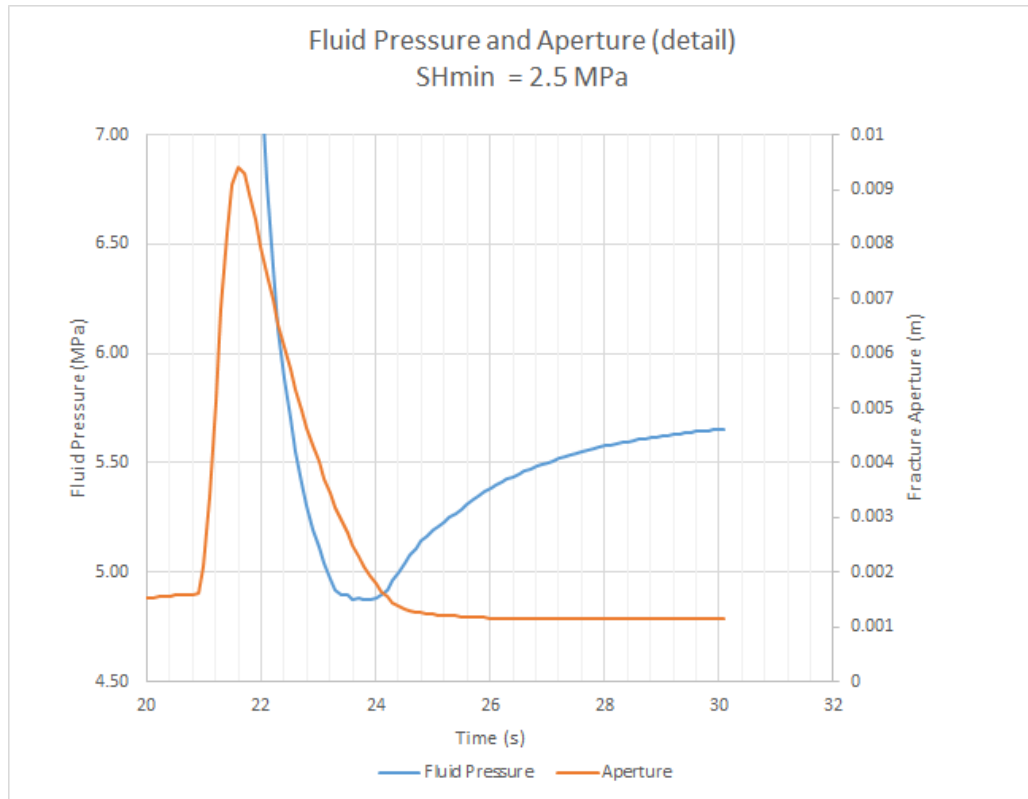
Figure 5.4.9: Fluid Pressure and Aperture Evolution, $\sigma_{Hmin} = 2.5$ MPa
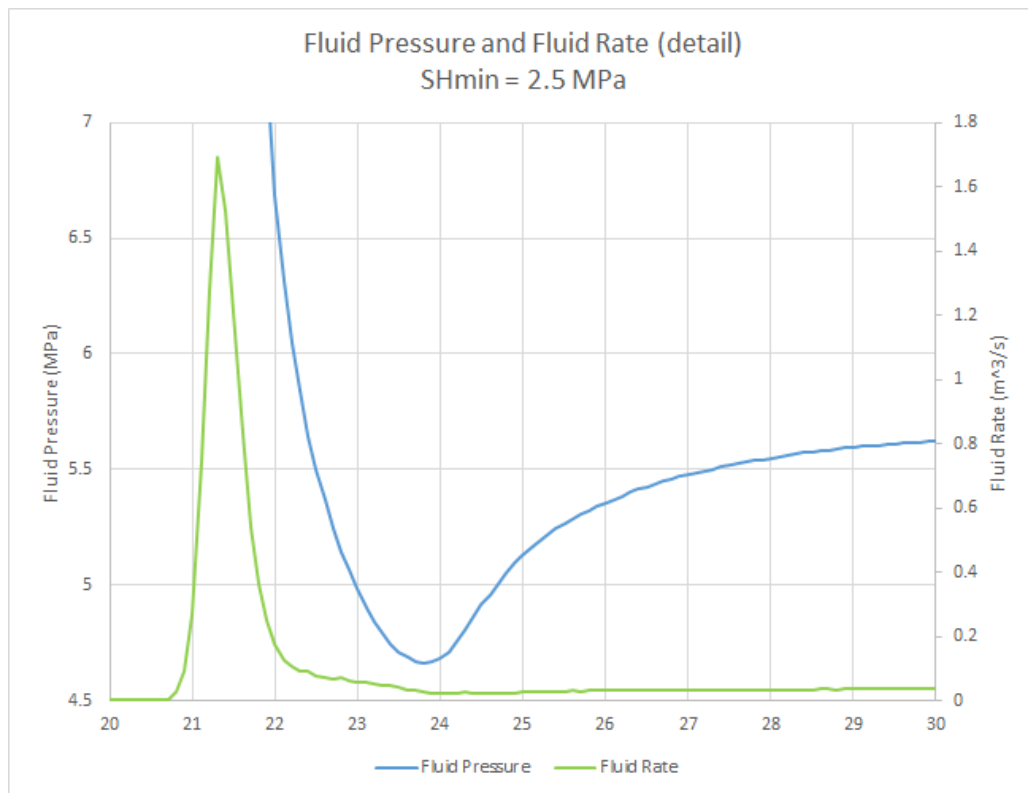
Figure 5.4.10: Fluid Pressure and Fluid Rate, σ_{Hmin}= 2.5 MPa
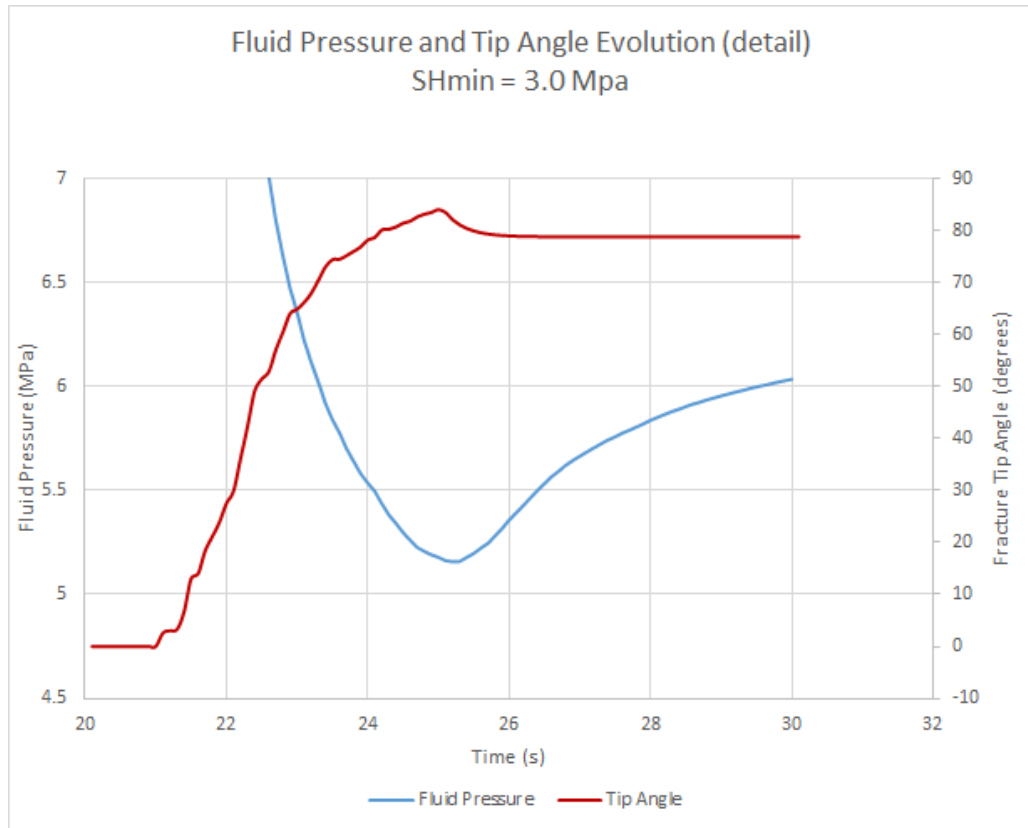
Figure 5.4.11: Fluid Pressure and Tip Angle Evolution, $\sigma_{Hmin} = 3$ MPa

The flow rate spike in Figure 5.4.10 peaks some time before the pressure reaches its minimum value, whereas in Figure 5.4.8 the tip angle is most closely aligned with σ_{Hmax} at close to the minimum pressure. This suggests that the pressure drop is due to the realignment itself, and Figure 5.4.4 appears to support this, in that the drop below σ_{Hmax} is less for the less anisotropic cases. In more detail, Figure 5.4.11 shows a fluid pressure and tip angle evolution chart for the case σ_{Hmin}= 3 MPa, with the same time and fluid pressure axis ranges as Figure 5.4.8. The fluid pressure minimum occurs later in the 3 MPa case, and correspondingly, so does the maximum tip angle.

The fact that the fracture remains open at this position as the pressure drops below σ_{Hmax} suggests that it is being held open mechanically at another position (i.e. it has closed at that other position), or that the fluid pressure drop is a transient effect, with the surrounding fluid able to provide the pressure to support the fracture as a wave of low pressure passes.

An examination of the mechanical simulation makes it clear that the fracture has closed at isolated positions, and no evidence of a pressure wave moving through the fracture could be found. Where the fracture has closed, the simulation enforces a minimum permeability value, equivalent to an aperture of 0.45mm. This will allow some fluid to flow, possibly enough to maintain fracture growth. It is also possible that the closure has stopped

significant flow, and that fracture growth is simply due to residual pressure in the fracture.

Considering the fluid pressure required to open the fracture in the reoriented area is half that at the initiation point, the closure may simply be a function of the difference in those pressures. The Newtonian, low viscosity fluid is nearly completely incompressible, and a pressure differential along the pipe is difficult to justify. It is also possible that the fracture closure is an artifact of the mesh and/or fracture insertion. For example, the oscillations in fracture direction seen in section 5.4.1 could produce a mesh which results in penetration if any relative lateral movement of the two sides of the fracture occurs. A nodal penetration would close the fracture. However, a reduction in fluid pressure is seen consistently in Figure 5.4.4, to a lesser effect at lower levels of stress anisotropy. This suggests that this is a real phenomenon which is anisotropy dependent. Further studies with much finer meshes could prove useful to confirm this.

The result of the closure is a reduction of permeability which is not symmetrical, and running the simulation again for longer demonstrates the effect; one wing grows preferentially due to having the higher permeability. Figure 5.4.12 shows the fracture pipe elements at 7 5s overlaid on a grid of 10 m squares for scale. The upper arm has grown nearly 30 m further than the lower. The contour of flow rate highlights the difference between the two wings.
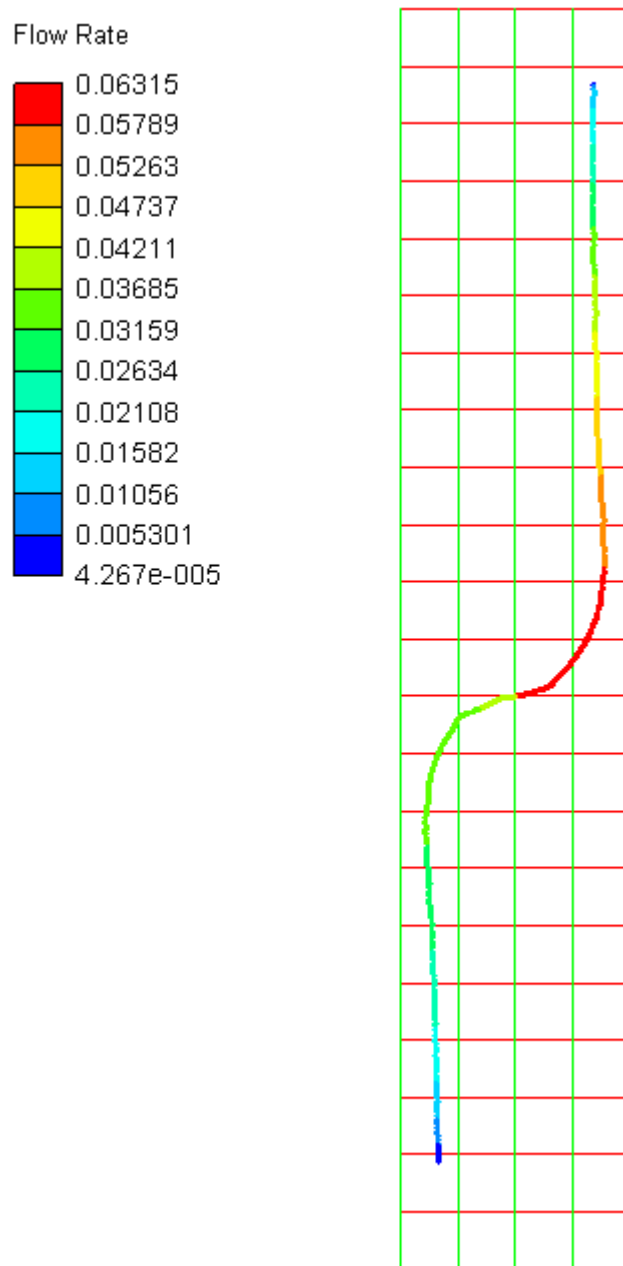
Figure 5.4.12: Asymmetric fracture growth with flow rate, σ_{Hmin}=2.5 MPa

5.4.2 Variation of Initial Fracture Length

Geometry

Figure 5.3.13 plots the length growth of each fracture in time. It was expected that eventually the rate of growth of each fracture would become the same; the fluid pressures in each fracture should converge as the lengths increase. This behaviour is observed, and

the longest fracture has a fairly constant gradient. Others transition from their higher rate of growth, which is consistent with a higher opening pressure, to the lower rate. Examining the fluid pressure history - which is measured at the point of fluid injection and presented in 5.3.15 shows a marked difference in the evolution of the fluid pressure, quite different from the profile seen in linear fracture growth. This is typically a linear ramp in pressure as the fluid pressure builds in the starter fracture with little volume change, followed by a rapid drop in pressure as the volume of the fracture increases, levelling out at a pressure that is just above the minimum horizontal stress + the tensile strength of the rock. 5.3.18 plots the pressure history for a smaller starter length at different initial orientations, which are a good example of this behaviour.

Figure 5.3.14 plots the tip angle of each fracture against the extension length (the current length - initial length).

An interesting observation is the similarity of the fracture reorientation rates of the f5 and f50 fractures - in Figure 5.3.11 these are almost identical. Figure 5.3.15 shows markedly different pressure histories, indicating that the reorientation rate is not simply dependent on the opening pressure.

Opening Pressure

It seems intuitive that the length of a pre-existing fracture being opened should affect the fluid pressure required to cause it to propagate further, since a longer wall length provides a longer lever with which to open the fracture. How this reduced opening pressure and/or the length of open fracture affects the rate of reorientation is less clear.

Figure 5.3.9 plots the opening pressure for the various fracture lengths at the two values of σ_{Hmin} (4 and 4.9 MPa, with $\sigma_{Hmax} = 5.0$ MPa), with the fracture oriented parallel to the minimum horizontal stress.

The relationship between length and opening pressure appears to follow an inverse power rule, similar to the reorientation rate in Figure 5.2.3. Little difference can be distinguished between the two sets of runs, indicating that the opening pressure is not sensitive to σ_{Hmin}. There appears to be a horizontal asymptote of the relationship between opening pressure and initial fracture length around 1 MPa (the tensile strength of the shale) above the *maximum* horizontal stress σ_{Hmax}.

This is of interest given that a tensile fracture opening without a starter fracture direction (e.g. from a wellbore leak off test) is expected to propagate at the tensile strength of the rock $T_0 + \sigma_{Hmin}$ once it is $\gtrsim$ 1m long (Zoback, 2007).

The dependency on σ_{Hmax} is understandable when the results in section 5.3.1 are considered, namely that all the fractures initiated in the direction of σ_{Hmin}, and therefore had

to overcome σ_{Hmax} to open as a mode I fracture.

This is of particular interest when considering a propagating hydraulic fracture encountering a natural fracture in this orientation. This will be examined further in 6, but the implied consequence is that a natural fracture oriented perpendicular to the maximum principal stress direction could significantly affect the propagation pressure of the hydraulic fracture, dependent on the level of stress anisotropy, and any resistance to opening in the natural fracture, such as cementation.

Once the fracture has reoriented, the lower limit on the propagation pressure should be $\sigma_{Hmin} + T_0$, and Figure 5.3.15 supports this somewhat, with some fractures propagating at less than $\sigma_{Hmax} + T_0$.

Reorientation Rate

Figure 5.3.10 is a plot of smoothed tip angle evolutions for the various initial lengths, normalised in time. The reorientation curve is generally more S-shaped in the longer fractures, and a plot of the actual elapsed time since fracture initiated shows the relative evolution more clearly; this is plotted in Figure 5.3.11. Generally, the fracture reorientation time increases with the initial length of the fracture, again illustrated in Figure 5.3.12. These results are not trending as clearly to a particular curve as those in Figure 5.3.9.

Despite being smoothed, the amount of noise in the tip angle data could contribute towards some runs lying outside a clear trend. As mentioned in subsection 5.4.1, the results can be affected by the geometry of the finite element mesh. Asymmetry of the growth in the Y direction could also account for the lack of consistency - see Figure 5.3.8. The tip angles used in the data above are always taken from the lower tip.

Of particular interest is the fact that the f50 and f5 cases take very similar paths in time. This would warrant further study.

5.4.3   Variation of Initial Fracture Orientation

Geometry

The final geometry of each fracture (see Figure 5.3.16) shows a non uniform relationship between the initial orientation and reorientation rate. This is inferred from the larger "gaps" between the final fracture paths as the initial orientation is reduced. All curves appear to follow a tangential curve, and further investigation could confirm this, and possibly determine coefficients to a function of the type:

$$Y = A + B\tan(C(x - d))$$

Mogilevskaya et al. (2000) also examined the dependence of fracture orientation on near-wellbore fracture paths. Figure 5.4.13 shows the fracture paths they calculated for a fixed value of the stress anisotropy normalisation parameter β, and variations of initial orientation α. Their results are clearly highly influenced by the well geometry, and less comparable to the results here than the stress anisotropy variations.
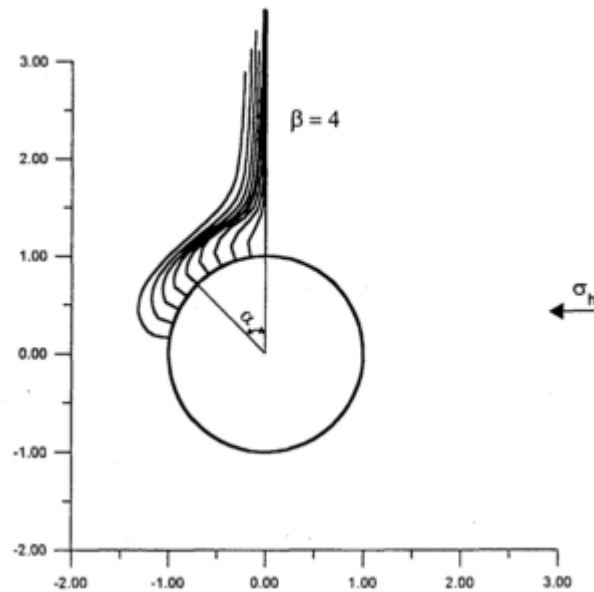
Figure 5.4.13: Fracture path dependence on orientation, Mogilevskaya et al. (2000)

Opening Pressure

Opening pressures follow a decreasing trend as the starter fracture approaches the direction of maximum horizontal stress. This is as expected, as when it is oriented parallel to the minimum horizontal stress (0° in Figure 5.3.17) the fracture will be trying to open against the maximum horizontal stress rather than the minimum. The trend in Figure 5.3.17 appears to be linear, with the 30° case slightly out of range. The curve may also be S-shaped, something which further simulations could establish.

Reorientation Rate

The non-uniform behaviour suggested by the fracture geometry can be considered more likely after examining the normalised reorientation rate data in Figure 5.3.20. This shows a shallow s-curve for the 0° case, a straight line for the 90° case, and between the two, curves which vary to some degree. These simulation runs had less frequent output than some of those in previous chapters, which made the fracture tip noise more troublesome.

The simulations at orientations near 90° were more difficult to prescribe a reorientation time, again in part due to the tip angle noise. Without some further analysis, and possibly more frequent output, no clear conclusions about the relationship between initial orientation and rate of reorientation can be made.

5.4.4 Summary

A key finding of all simulations was that all fractures initiated in the direction of the starter fracture. Some literature (e.g. Soliman et al., 2010) assume that the stress field will dictate the orientation of a fracture. The three factors studied here are all shown to influence the way in which the fracture realigns with σ_{Hmax}, in agreement with Mogilevskaya et al. (2000).

During fracture reorientation, a drop in pore pressure was detected which appeared to be dependent on the stress anisotropy. At high levels of stress anisotropy, some simulations exhibited fracture closure in one wing. It is not clear if this is a real world effect of curvature, the pressure drop, or an artifact of the mesh.

When varying the starter fracture length, two length factors were observed to reorient in a very similar manner, not only when normalised in time, but in actual time. There was an order of magnitude difference in length between the two cases, and an explanation for this behaviour is not clear at this time.

Difficulties involved in this study were dominated by two factors. The first was the noise around the fracture tip orientation, which made evaluation of the final time taken to reorient challenging. This could be improved by running simulations with finer meshing parameters and better smoothing algorithms. The influence of stress anisotropy on initiation pressure was difficult to quantify owing to very high initiation pressures, which in turn were the result of small starter fractures. Revisiting these simulations with longer starter fractures could be of benefit.

Fracture closure which appeared to be due to the curvature of the fracture was identified in some cases, resulting in asymmetric fracture growth. Examining this in detail would be useful, as it is not currently clear whether this is an artifact of the fracturing algorithm, a real effect due to reduction in of pressure, or a geometric/mechanical effect.

Further studies could apply a variation of flow rate, which would result in fluid pressure differences that were independent of the stress anisotropy. Finer graduations of initial fracture orientation would enable determination of the trend for opening pressure to vary with starter fracture orientation. In general, all studies were limited to finding qualitative relationships between parameters, and work to quantify these may provide equations that could be used to actively influence fracture paths.

The apparent anomaly in behaviours when varying fracture length is of interest. Two cases, at factors 5 and 50 of the reference length, showed remarkably similar reorientation rates. This is not predicted by the model in Mogilevskaya et al. (2000), nor observed.

All studies assumed a homogeneous fracturing medium. Additional simulations in the presence of natural fractures near or around the starter fractures would be of interest. The finding that all fractures initiated parallel to the starter fracture could be challenged by natural fractures of varying interface properties and orientations intersecting the starter fractures.

Chapter 6

Interaction with Natural Fractures

6.1 Introduction

Previous chapters have considered the propagation of a hydraulic fracture through a homogeneous system. Fracturing treatments such as the TTSM aim to increase fracture complexity through reduced stress anisotropy, which in turn requires some form of heterogeneity in the fractured medium to be exploited. In this chapter, the effect of natural fractures on a propagating fracture are examined using the numerical simulation technique described in Chapter 3.

The assortment of fracturing mechanisms, and resulting fracture properties, result in a system that is very difficult to characterise in the field, and for this reason natural fracture modelling will often take some form of stochastic approach based on core or wire-line log observations, or simplify the problem to regular sets of fractures oriented in a small number of orientations. Section 2.6 presents a review of the current literature regarding natural fractures in shales. The following studies begin by using a single set in a single orientation, moving on to using stochastically generated sets to examine the effect on fracture reorientation. Finally, a study of the effect shear stresses can have on unconnected natural fractures is presented.

6.1.1 Shear Stress and Tensile Fracturing

A tensile fracture opens due to tensile forces acting at its tip, which pull apart the medium it is propagating through. This occurs in hydraulic fractures because fluid pressure is providing a compressive force on the fracture walls, acting to create tensile forces at the fracture tip. As a free surface, the fracture walls support no shear stress, and the principal stresses are perpendicular and parallel to them. The transition between compressional

stresses on the fracture walls and tensile stresses at the tip must occur via either a region of stress rotation or a pure magnitude change. The mechanism for the former is shear stress - it is equivalent to the rotation of the principal stresses, and it must occur outside the fracture walls, i.e. in the fracturing medium. It follows that in the absence of stress discontinuities, the fracturing medium must support shear stress to allow the fracture to propagate. Hence, the following simulations focus on the effects of varying that ability via natural fractures, and the effect this has on the propagation of the fracture.

6.1.2 Propagation Through Natural Fractures

As a hydraulic fracture propagates in a matrix containing sets of natural fractures, it will eventually encounter a natural fracture unless it is propagating parallel to them. Gu et al. (2011) summarise the possible interactions which may occur between the hydraulic fracture (HF) and natural fracture (NF). The hydraulic fracture can be arrested due to slippage along the NF. This is the loss of shear strength discussed in section 6.1.1, resulting in dilation of the NF and continued propagation along its length. If the HF crosses the NF, it may either continue propagating while the NF stays closed, or dilate the NF and continue along its length. Figure 6.1.1 summarises these interactions.
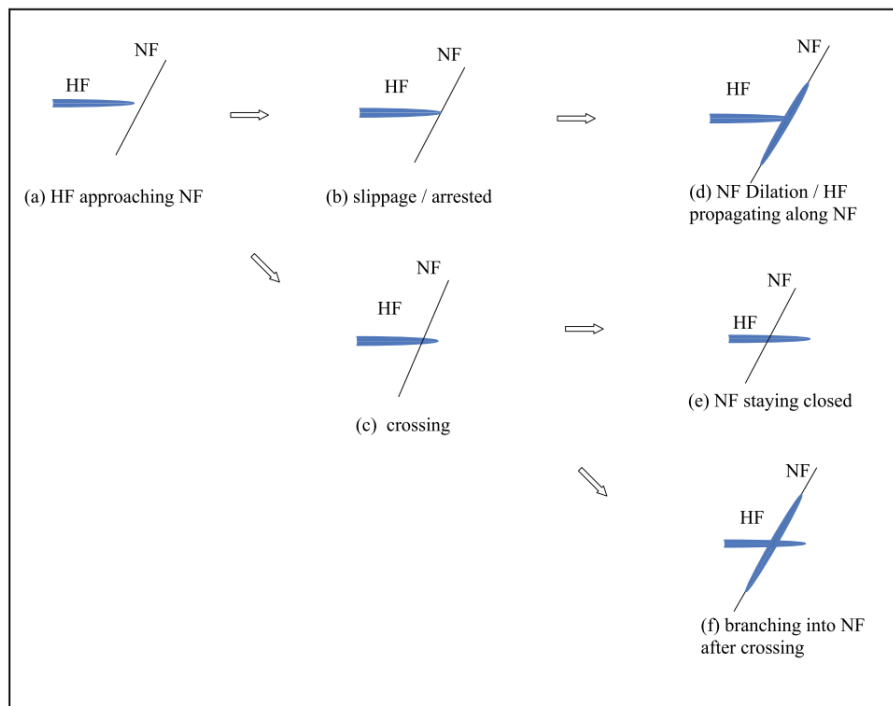
Figure 6.1.1: Possible Hydraulic Fracture/Natural Fracture Interactions (taken from Gu et al. (2011))

The above outcomes consider the entry of the hydraulic fracture into the natural fracture and behaviour shortly afterwards. In addition, should the hydraulic fracture travel along the NF, the following may occur (Figure 6.1.2) ; the HF may exit part way along the NF, or the HF may exit from the ends of the NF.
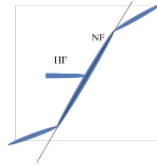
(g) Branching part way along HF
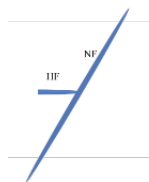
(h) HF exits end of NF

Figure 6.1.2: Possible HF exit conditions

Gu et al. (2011) describe a criterion for the hydraulic fracture crossing the natural fracture, based on the requirement that no slip occurs on the natural fracture boundary. While this can be expressed explicitly for an orthogonal interaction, this is not the case for non-orthogonal cases. Figure 6.1.3 is their chart showing the criterion for a selection of various interaction angles. The friction coefficient of the interface required for the fracture to cross is to the right of the chart and higher. For instance, under isotropic stress conditions the friction coefficient required for a fracture to cross a natural fracture at 90° is just above 0.4. The high sensitivity of the criterion to the interface angle is clear from the wide spacing of each of the criterion limiting curves.

Chuprakov et al. (2010) quantify the activation of a natural fault interacting with the propagating hydraulic fracture.

The studies below begin by analysing sets of natural fractures, which are oriented perpendicular to the main hydraulic fracture. The interaction between the hydraulic fracture and the natural fractures is examined in a qualitative manner. The effect of varying stress anisotropy on the more complex geometries is then investigated.

6.1.3 Moment Tensors

This chapter makes use of a capability of Elfen TGR to generate microseismic moment tensors. In practice, a series of geophones are employed either in the subsurface, or more
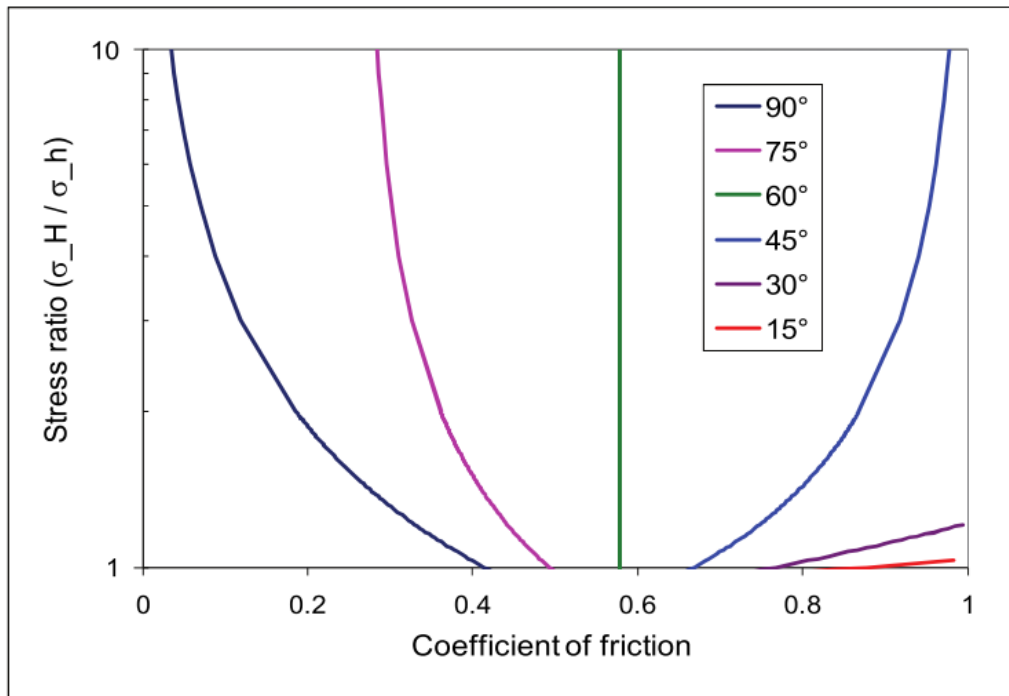
Figure 6.1.3: Crossing Criterion for Anisotropic Stresses, Cohesionless, Zero Tensile Strength (Gu et al., 2011)

typically on the surface in large 2D arrays. These record compressional (P) and secondary shear (S) wave arrival times and initial polarization direction, from microseismic events created during hydraulic fracturing. As P waves are compressional, when experienced by a point in space they appear as a compression followed by dilation. These data are then inverted to arrive at an estimate of the origin of the microseismic event, as well as a stress moment tensor, which can be visualised in a number of ways. A common visualisation technique is the "beachball" plot. Figure 6.1.5 shows a series of moment tensors, each with a corresponding beachball plot.

The simplest form of the beachball plot retains two orthogonal axes, and can be seen in the second row of 6.1.5. The beachball plot can be explained by considering a sliding event between two surfaces. A down/up sliding motion is represented in Figure 6.1.4 (left). The relative movement along the central vertical axis of each side of this square is represented by a red arrow on each side of the axis. Pressure waves will exit this rectangular region in all directions, but at points above and to the right hand side, the compression will be seen first. At points below and to the right hand side, a dilation will be seen first. The upper right of this event descriptor is labelled + for compression, and likewise the lower left the same. Shading the positive areas give a beachball such as the second from the top on the left hand side of Figure 6.1.5. The two orthogonal axes represent the two *possible* fault planes, as the up/down sliding illustrated on the left of Figure 6.1.4 will give

the same beachball plot as a left/right sliding as per the right hand image. Of particular interest in the 2D examples in this work are the isotropic compressional and dilational representations, which are solid colours.

Elfen TGR calculates the stress state as slip or failure occurs, and can generate the microseismic representations directly. In Elfen dilational events are coloured blue while compressional are white.
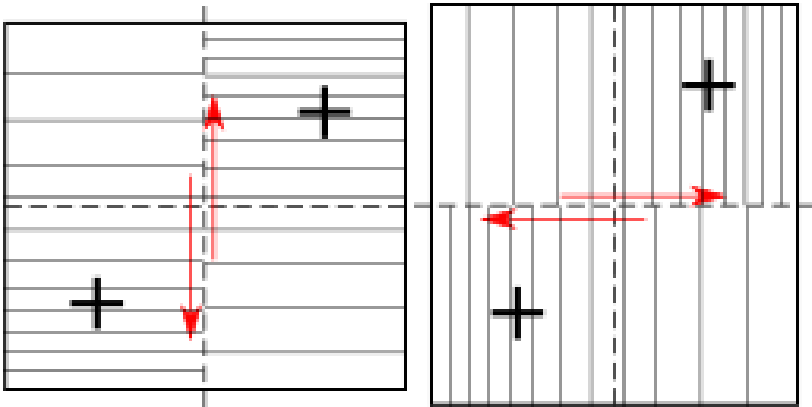
Figure 6.1.4: Beachball Schematic

Moment tensor	Beachball	Moment tensor	Beachball
$\frac{1}{\sqrt{3}}\begin{pmatrix}1&0&0\\0&1&0\\0&0&1\end{pmatrix}$		$-\frac{1}{\sqrt{3}}\begin{pmatrix}1&0&0\\0&1&0\\0&0&1\end{pmatrix}$	
$-\frac{1}{\sqrt{2}}\begin{pmatrix}0&1&0\\1&0&0\\0&0&0\end{pmatrix}$		$\frac{1}{\sqrt{2}}\begin{pmatrix}1&0&0\\0&-1&0\\0&0&0\end{pmatrix}$	
$\frac{1}{\sqrt{2}}\begin{pmatrix}0&0&-1\\0&0&0\\-1&0&0\end{pmatrix}$		$\frac{1}{\sqrt{2}}\begin{pmatrix}0&0&0\\0&0&-1\\0&-1&0\end{pmatrix}$	
$\frac{1}{\sqrt{2}}\begin{pmatrix}-1&0&0\\0&0&0\\0&0&1\end{pmatrix}$		$\frac{1}{\sqrt{2}}\begin{pmatrix}0&0&0\\0&-1&0\\0&0&1\end{pmatrix}$	
$\frac{1}{\sqrt{6}}\begin{pmatrix}1&0&0\\0&-2&0\\0&0&1\end{pmatrix}$		$\frac{1}{\sqrt{6}}\begin{pmatrix}-2&0&0\\0&1&0\\0&0&1\end{pmatrix}$	
$\frac{1}{\sqrt{6}}\begin{pmatrix}1&0&0\\0&1&0\\0&0&-2\end{pmatrix}$		$-\frac{1}{\sqrt{6}}\begin{pmatrix}1&0&0\\0&1&0\\0&0&-2\end{pmatrix}$	

Figure 6.1.5: Microseismic Moment Tensors and Beachball Renderings

6.2 Methodology

The reference setup for an initial set of simulations was chosen to be a set of uniformly spaced horizontal natural fractures, with a hydraulic fracture propagating vertically through them. It was expected that the natural fracture permeability would play a large part in controlling the path of the hydraulic fracture. Assuming that the natural fractures had high frictional properties or cohesive cementation, two end case scenarios were predicted. A very high permeability natural fracture would arrest the hydraulic fracture by allowing fracturing fluid to fill it and stop the transferral of tensile stress to the opposite side. This could occur through reduction in frictional properties via lubrication or dilation of the fracture. Similarly, given natural fracture interface properties which reduced the chance of sliding, a very low permeability natural fracture should appear almost invisible to the hydraulic fracture, and the hydraulic fracture should continue propagating vertically. It was predicted that at an "intermediate" value of permeability, the effects of frictional properties within the natural fracture would come into play and could be studied in closer detail. A set of simulations

was conducted to identify a suitable intermediate permeability which could be used for such closer studies. This permeability value was used in further simulations which varied the contact properties and stress anisotropy during propagation through horizontal fractures.

Further simulations were carried out to ascertain the influence natural fractures may have on the results from chapter 5. Two of the simulations are presented; both using stochastic natural fracture generation to create natural fracture sets at a non-orthogonal angle to the principal stress directions. A hydraulic fracture was initiated in the horizontal direction, where σ_{Hmax} was vertical and reorientation in a homogeneous medium occurred smoothly. The first simulation used a single natural fracture set which was oriented around 60° to the vertical. A second simulation with an additional set placed around 30° was also performed.

Finally, the impact of shear stress on natural fractures was investigated, with one simulation presented here. Since significant shear stresses can develop around a propagating fracture, the simulation was designed to assess the impact these may have, without the influence of fracturing fluid on the interface properties becoming a factor.

6.2.1 Fracture interface properties

The behaviour of the natural fractures in the following simulations was modified by altering the contact properties of fractures in the system. These govern the strength of the bond between two surfaces using a Mohr-Coulomb failure criterion, illustrated in Figure 6.2.1. The two parameters cohesion - c and friction angle ϕ dictate the shear stress (or difference in principal stresses) at which the bond between the two surfaces is broken. In terms of simulation input parameters, the coefficient of friction $\alpha = tan(\phi)$

For a given normal stress σ, the failure shear stress $\tau_f = c + \sigma tan(\phi)$, or $\tau_f = c + \alpha\sigma$.
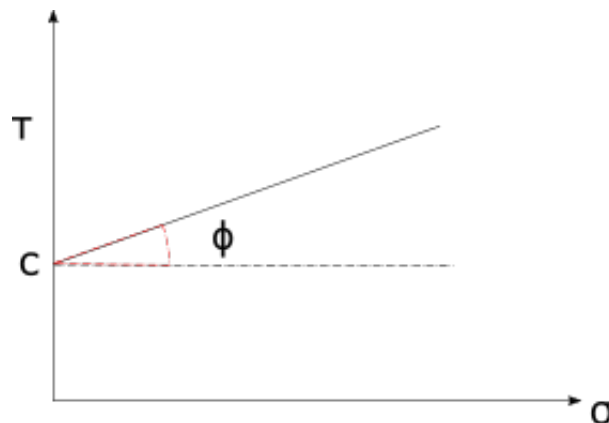
Figure 6.2.1: Mohr-Coulomb failure envelope

6.2.2 Propagation Through Natural Fractures

One set of simulations used a simple set of natural fractures oriented at 90° to the anticipated hydraulic fracture propagation direction, i.e. horizontally. These were 40m long and spaced 2m apart vertically. These long fractures could be interpreted as inter-bedded strata, planes of weakness within the fracturing medium, as well as in-situ natural fractures.

Three parameters were varied. First, the permeability of the natural fractures. This was to establish a permeability that would allow the natural fractures to take on fluid without arresting the hydraulic fracture. Following the establishment of a suitable natural fracture permeability, the frictional properties of cohesion and friction angle were permuted between high and low values. The simulations were initially run under near-isotropic conditions. The basic parameters are shown in Table 6.1, and a detail of the fracture area in Figure 6.2.2. This shows the region with natural fractures, which is at the centre of a 1km square block. The denser region near the very centre of this image is the initiation point of the hydraulic fracture. This model is not entirely symmetrical. While the starter fracture is centered in the model, the region of natural fractures is slightly offset, and there is one more natural fracture on the lower part of the model than the upper. The consequences of this asymmetry will be discussed when they become pertinent.

Parameter	Value	Unit
Young's Modulus	32	GPa
Poisson's Ratio	0.2	
Reservoir Pore Pressure	0	MPa
Effective Stress XX	4.9	MPa
Effective Stress YY	5	MPa
Effective Stress ZZ	5	MPa
Porosity	0.01	
Fracture Height (Layer thickness)	10	m
Initial Fracture Length	0.4	m
Fluid Volume	10	m^3
Flow Rate	0.1	$\frac{m^3}{s}$
Fluid Viscosity	1.67e-3	Pa.
Natural Fracture Length	40	m
Natural Fracture Spacing	2	m

Table 6.1: Indicative Simulation Parameters
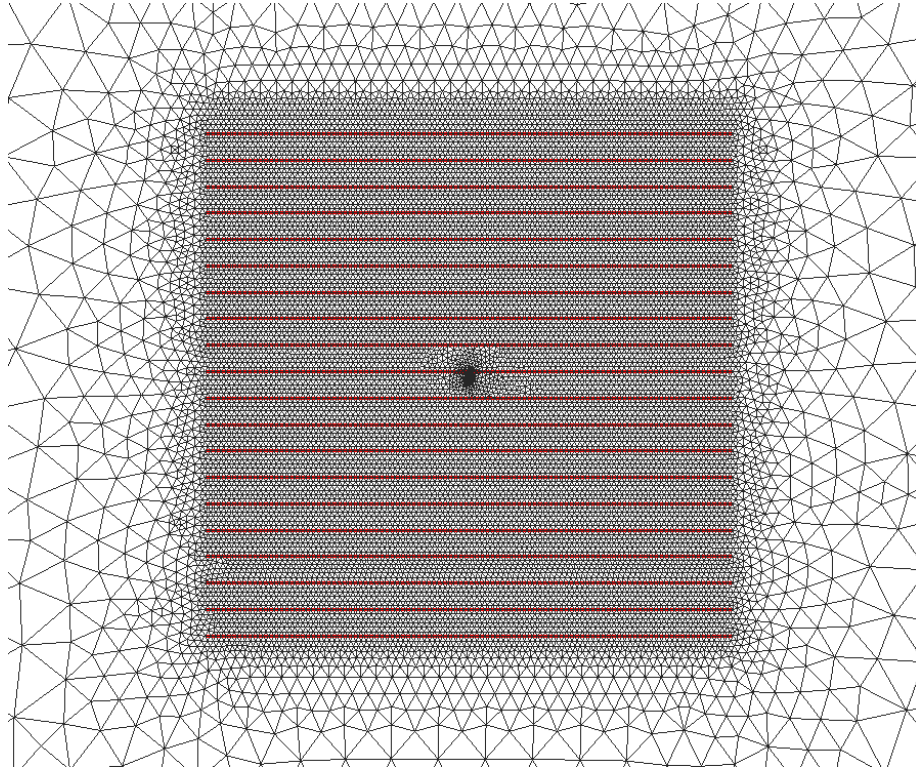
Figure 6.2.2: Model setup: Propagation Through Natural Fractures
This figure shows the refinement region which is 40m square. This region sits in a block
1km square. A region of further mesh refinement in the centre of the image shows the
position of the starter fracture.

Permeability

The basic case for these simulations used very high friction and cohesion parameters for
the natural fractures, so that their permeability alone determined the propagation of the
hydraulic fracture. Friction was set to 0.95 and cohesion to 20 MPa, which put the failure
envelope outside the stresses anticipated. For comparison, the cohesion value of intact
shale was 25 MPa.

This involved running a series of simulations, modifying the permeability of the natural
fractures by around one order of magnitude at a time. Although many simulations were
carried out, the most relevant examples are presented. Permeability values examined in
section 6.3.1 are tabulated with the corresponding hydraulic conductivity and apertures in
Table 6.2:

Reference	Permeability (m^2)	Hydraulic Conductivity ($\frac{\mathrm{m}}{\mathrm{s}}$)	Aperture (m)
A	$1.7\,\mathrm{E}^{-8}$	0.1	$4.52\,\mathrm{E}^{-4}$
B	$1.7\,\mathrm{E}^{-10}$	0.001	$4.52\,\mathrm{E}^{-5}$
C	$8.51\,\mathrm{E}^{-10}$	0.005	$1.01\,\mathrm{E}^{-4}$
D	$3.47\,\mathrm{E}^{-11}$	$2.04\mathrm{E}^{-4}$	$1.7\mathrm{E}^{-6}$

Table 6.2: Permeability Values of Natural Fractures

Natural Fracture Interface Properties

On attaining "intermediate" permeability values from section 6.2.2, the two main contact property parameters - friction coefficient and cohesion- were alternately switched off in isolation and together. Friction was set to zero while retaining a high cohesion value, and cohesion was reduced to zero while retaining a high coefficient of friction.

The first three simulations presented in the results section are given in Table 6.3.

Description	ID	Friction	Cohesion (Pa)	Permeability (case ID)
High Friction Cohesionless	1	0.95	0	B
High Cohesion Frictionless	2	0	20e6	B
Frictionless Cohesionless	3	0	0	B

Table 6.3: Natural Fracture Contact Properties

Stress Anisotropy

To briefly examine the influence of increased stress anisotropy on propagation through natural fractures, two simulations were performed with permeability case B in Table 6.2, reducing the minimum horizontal stress to 4 MPa and 3 MPa respectively. These simulations were intended to augment the previous simulations examining propagation through perpendicular fractures.

6.2.3 Fracture Reorientation

The impact of natural fractures on a selected fracture reorientation case was examined. Two simulations were run under the conditions in Table 6.4. The results from chapter 5 were used to select the key parameters. The level of stress anisotropy used previously gave a clear reorientation from the minimum horizontal stress direction, and the fracture

length of 4m resulted in a lower, more stable initiation pore pressure. With the exception of these parameters and additional natural fractures, the simulations were identical to the simulations in chapter 5. Both simulations used the same contact and permeability properties for the natural fractures, shown in Table 6.5.

The first simulation introduced a single, stochastically generated set of fractures aligned at a mean 60° to the vertical. The mean fracture length was 10m, with a standard deviation of 8, providing a wide range of fracture lengths. Other parameters used, and their descriptions are given in Table 6.6 for this first set of natural fractures.

A second set of natural fractures was introduced in the second simulation. The only difference in parameters of that set was the mean orientation, set to 30° for the second set.

Parameter	Value	Unit
Young's Modulus	32	GPa
Poisson's Ratio	0.2	
Reservoir Pore Pressure	0	MPa
Effective Stress XX	4	MPa
Effective Stress YY	5	MPa
Effective Stress ZZ	5	MPa
Porosity	0.01	
Fracture Height (Layer thickness)	10	m
Initial Fracture Length	4	m
Fluid Volume	3	m^3
Flow Rate	0.1	$\frac{m^3}{s}$
Fluid Viscosity	1.67e-3	Pa.s
Initial Orientation to σ_{Hmin}	0	°

Table 6.4: Indicative Simulation Parameters

Parameter	Value	Unit
Friction Coefficient	0.95	
Cohesion	20e6	MPa
Initial Aperture	4.53e-5	m
Permeability	1.7e-10	m^2

Table 6.5: Natural Fracture Sets Common Properties

Parameter	Description (unit)	Mean S1	Std Deviation S1
Orientation	Rotation from Vertical (°)	60	2
Spacing	Perpendicular distance between fractures (m)	5	3
Fracture Length	(m)	10	8
Persistence	Longitudinal Distance between fracture tips (m)	3	1

Table 6.6: Natural Fracture Set 1 - Parameters

6.2.4 Impact of Shear Stress

The shear zone around the tip of a propagating fracture is of some interest, and in particular the interaction of this with natural fractures. A simulation was seat up with the intention of examining the effect of a propagating hydraulic fracture on surrounding natural fractures, without coming into direct communication (i.e. via fracturing fluid). The pertinent geometry of the initial project is shown in Figure 6.2.3. The stress field is anisotropic, with horizontal effective stresses of $\sigma_{Hmax} = 5$ MPa, $\sigma_{Hmin} = 3$ MPa, and a pore pressure of 20 MPa. Two separate natural fracture systems are set up on either side of the predicted fracture path, both oriented in the same (45°) direction. The natural fracture region is a 100m square sitting in a domain 1km square. The fracture was stimulated in the same manner as the other simulations in this work; with a proppantless slickwater, pumped at 0.1 $\frac{m^3}{s}$. Microseismic event simulation was used to produce output at positions where displacements occurred, mimicking the results obtained by microseismic data processing.

Although fluid interaction with the natural fractures was not expected, the permeability of the natural fractures was reduced to 1.02e-11 m^2(10.33 Darcy).

6.3 Results

6.3.1 Propagation Through Natural Fractures

Permeability

Selected results from a high permeability (reference A in Table 6.2) simulation are below.

High Permeability   Pore pressure at the end of the simulation is shown in Figure 6.3.1, and the flow rate at the same time in Figure 6.3.2. Details of the mechanical simulation are presented in figures 6.3.3 and 6.3.4. Those show the most tensile principal stress magnitude σ_{11} before and after insertion of the fracture propagating slightly through the
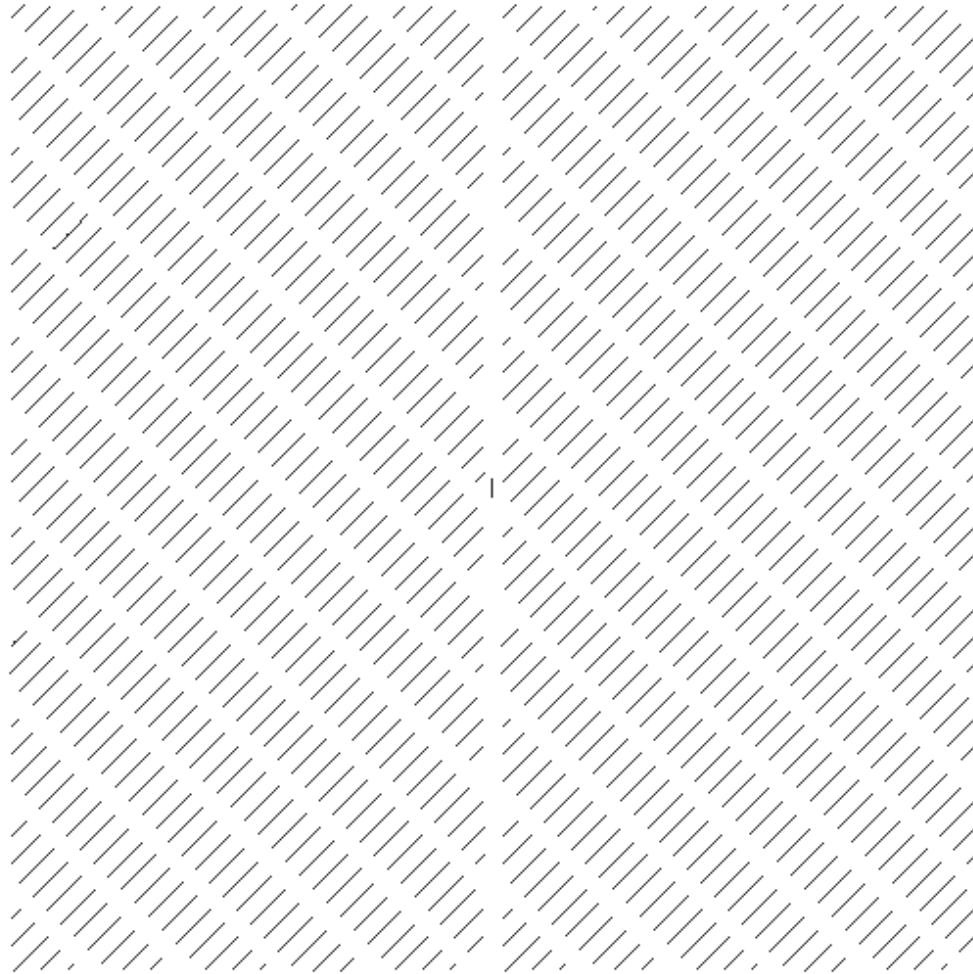
Figure 6.2.3: Initial geometry, shear stress influence on natural fractures
This figure shows a region of in-situ fractures 100m square, which sit in a block 1km square. The starter hydraulic fracture can be seen in the centre of the image.

natural fractures. The former is restricted to show only tensile stress (positive values), while the latter shows the lack of any tensile stress after the fracture is inserted. Shear stress τ_{xy} is shown in Figure 6.3.5 prior to fracture insertion.
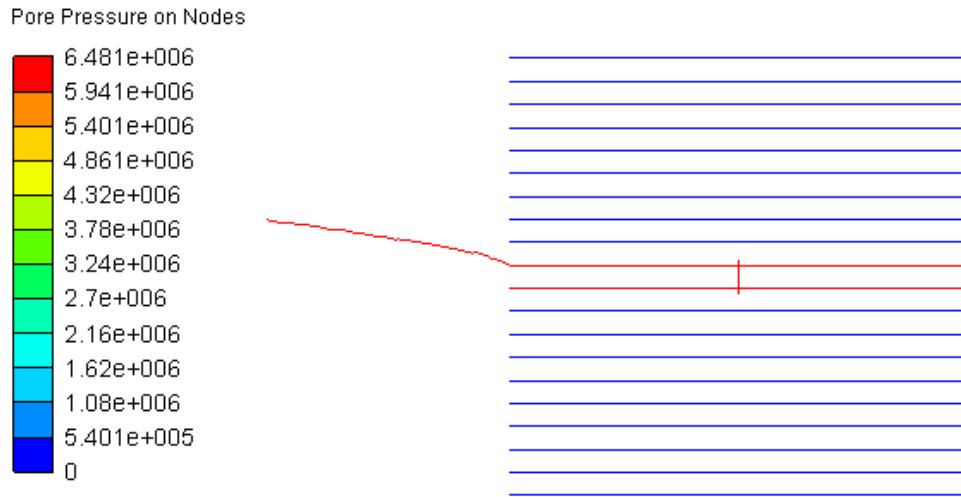
Figure 6.3.1: Pore Pressure - High Permeability Fractures
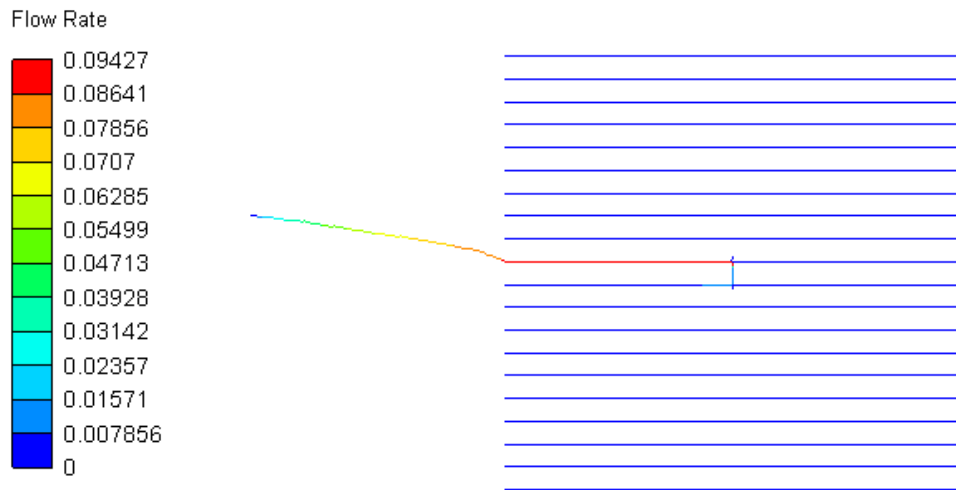
Figure 6.3.2: Flow Rate - High Permeability Fracture
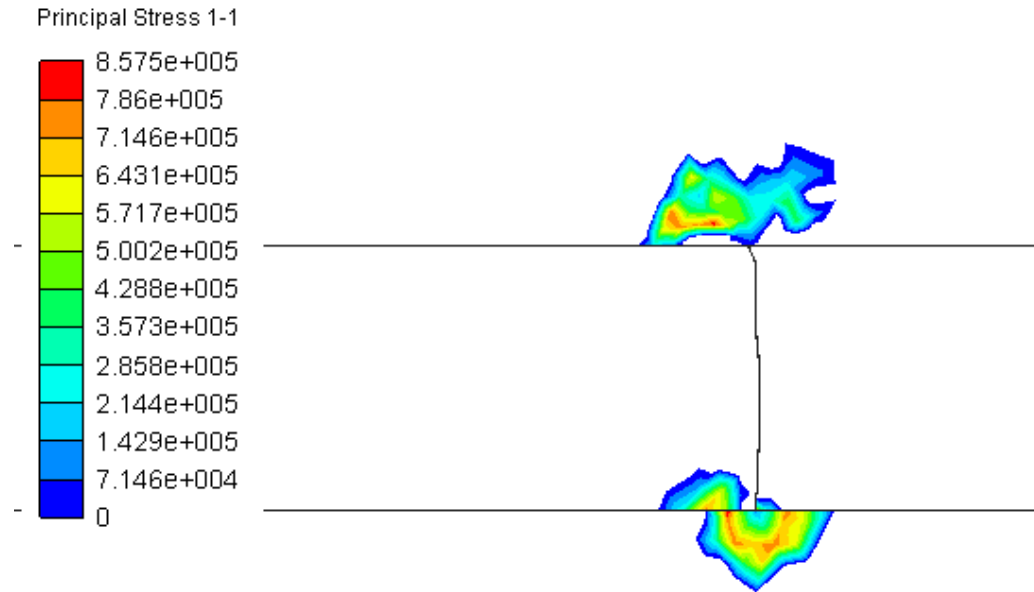
Figure 6.3.3: Tensile Principal Stress at 13.9s - High Permeability Fractures
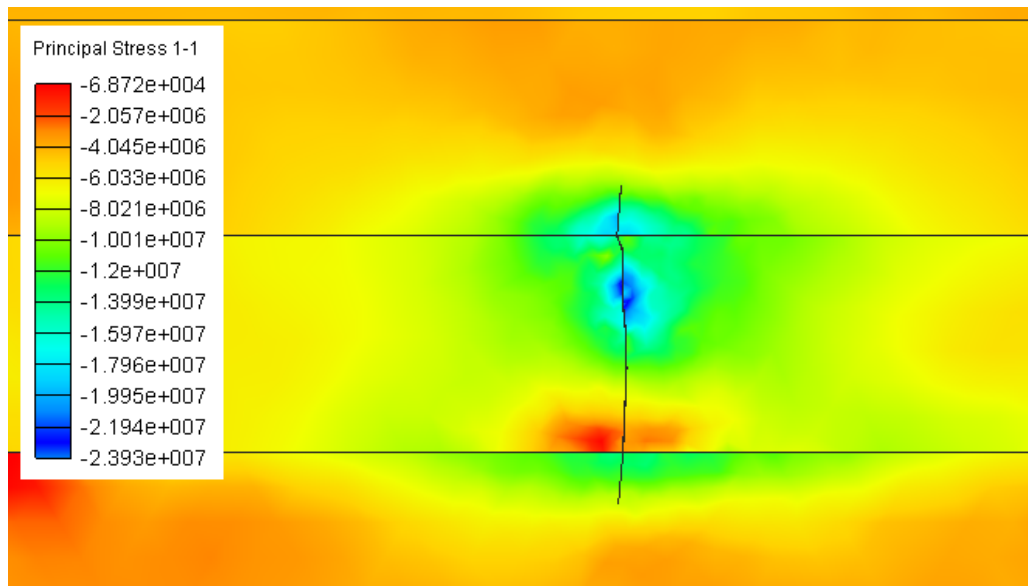
Figure 6.3.4: Most Tensile Principal Stress at 14s - High Permeability Fractures
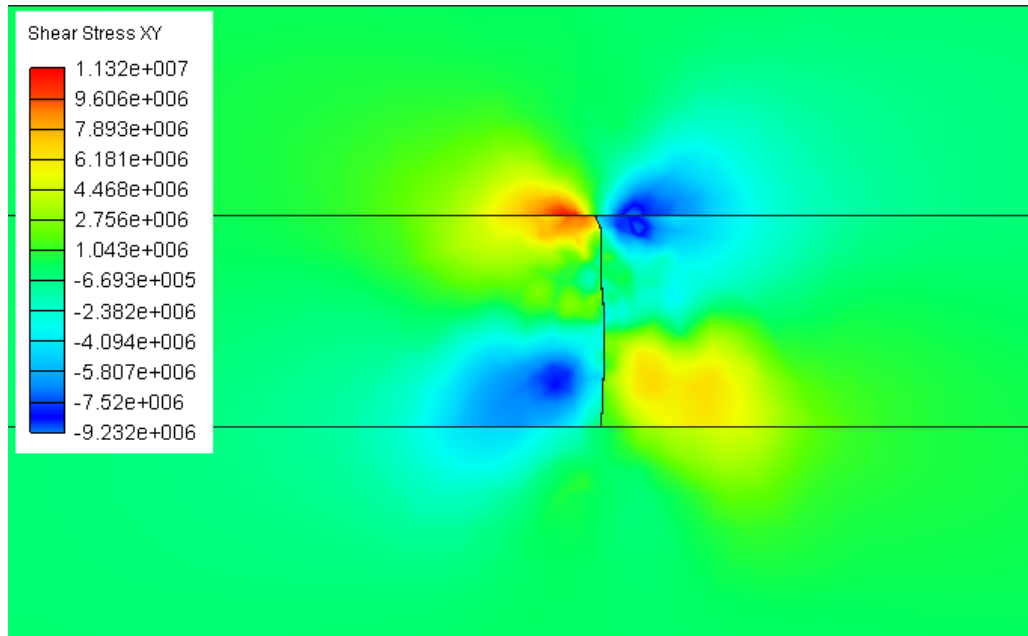
Figure 6.3.5: Shear Stress XY at 13.9s - High Permeability Fractures

Low Permeability   At the other end of the permeability range, case D in 6.2 has a very low permeability of 3.4 E^{-11}m^2. Figure 6.3.6 is a plot of fluid pressure after 24s.
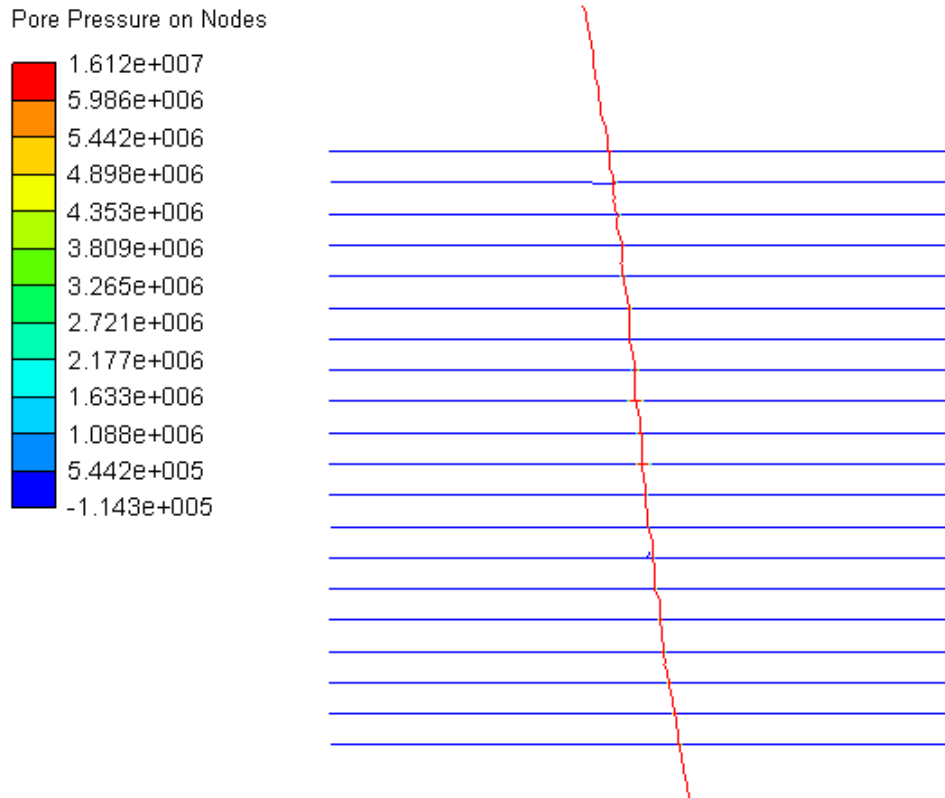
Figure 6.3.6: Pore Pressure - Low Permeability Fractures

Intermediate Permeability   Selected results from intermediate permeability simulations include the pore pressure plot at the end of the simulation for case B in Table 6.2. Figure 6.3.7 shows the results of a run with natural fracture permeability of 1.7 $E^{-10}m^2$. This value was selected with one other to use for later studies on the effects of natural fracture interface properties. The end of the fracture outside the natural fracture area has been truncated in this image.
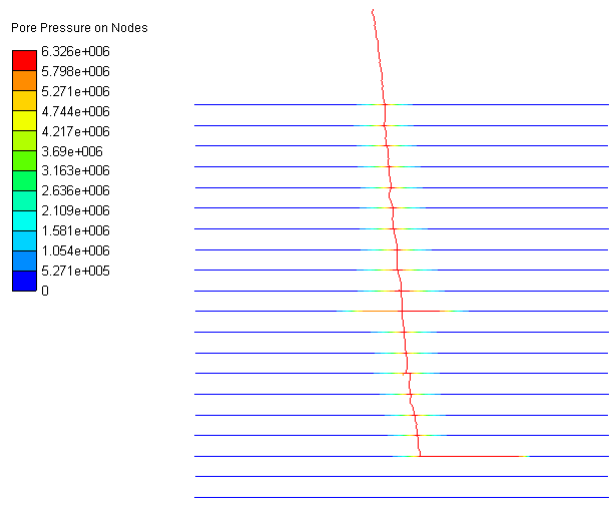
Figure 6.3.7: Pore Pressure - Intermediate Permeability Fractures (case B)

Higher permeabilities took more fluid into the natural fractures and allow fracturing through several natural fractures, ultimately propagating from the end one of the first natural fractures encountered. Figure 6.3.8 shows the pore pressure at the end of one of those simulations; this permeability value was selected as case C in Table 6.2.
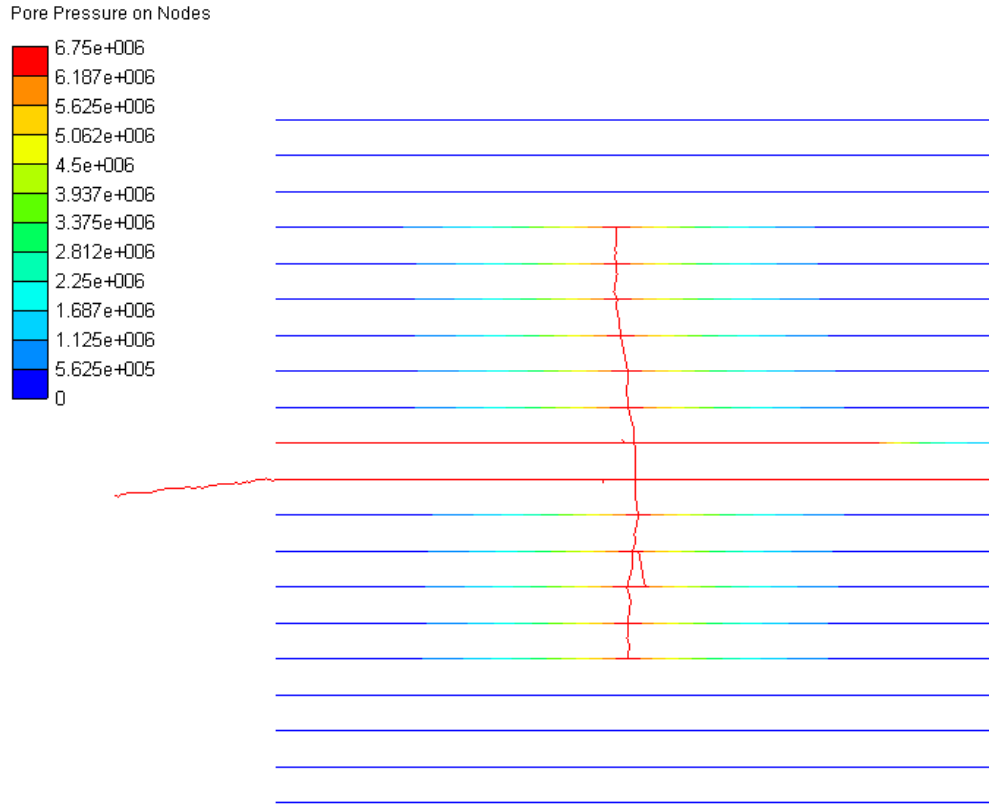
Figure 6.3.8: Pore Pressure - Intermediate Permeability Fractures (case C)

Natural Fracture Interface Properties

Fluid Pressure History   Two fluid pressure charts are presented in figures 6.3.9 and 6.3.10, which show the fluid pressure at the point of injection for the three simulations discussed in this section, as well as the corresponding high friction, high cohesion (obtained in section 6.3.1) example. The first highlights the fracture initiation pressure for the four simulations, and the second focuses on the propagation pressure.
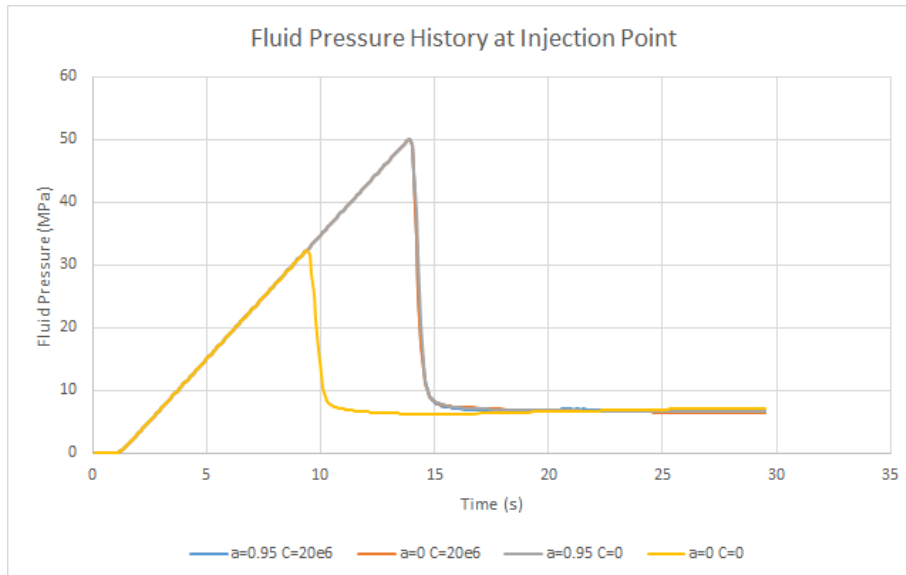
Figure 6.3.9: Fluid Pressure History, Variation of Contact Parameters
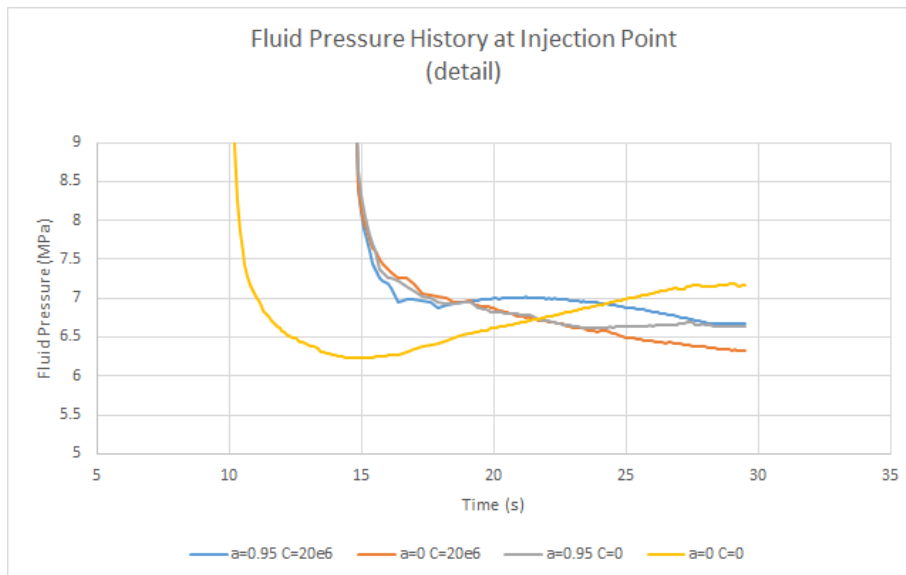
Figure 6.3.10: Fluid Pressure History, Variation of Contact Parameters Detail

High Friction-Cohesionless Removing the cohesion from the contact surface properties results in Y shaped branching in one wing of the hydraulic fracture. Figure 6.3.11 shows the pore pressure in the system at 19.2s, and Figure 6.3.12 the flow rate through the fractures at the same time.
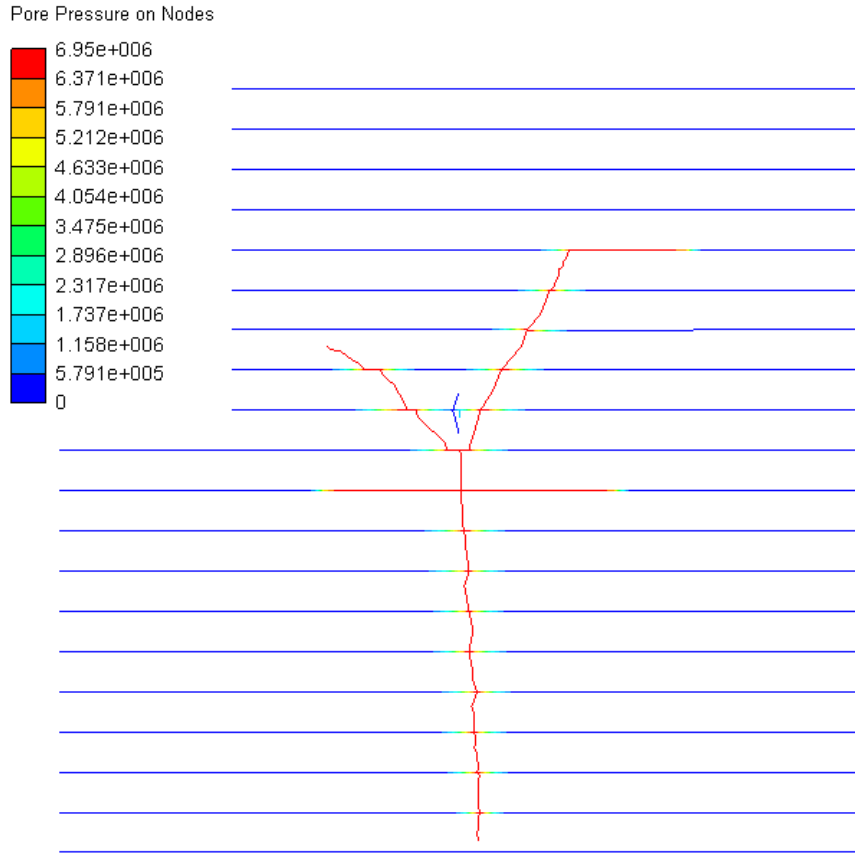
Figure 6.3.11: Pore Pressure - High Friction, Cohesionless, Permeability B
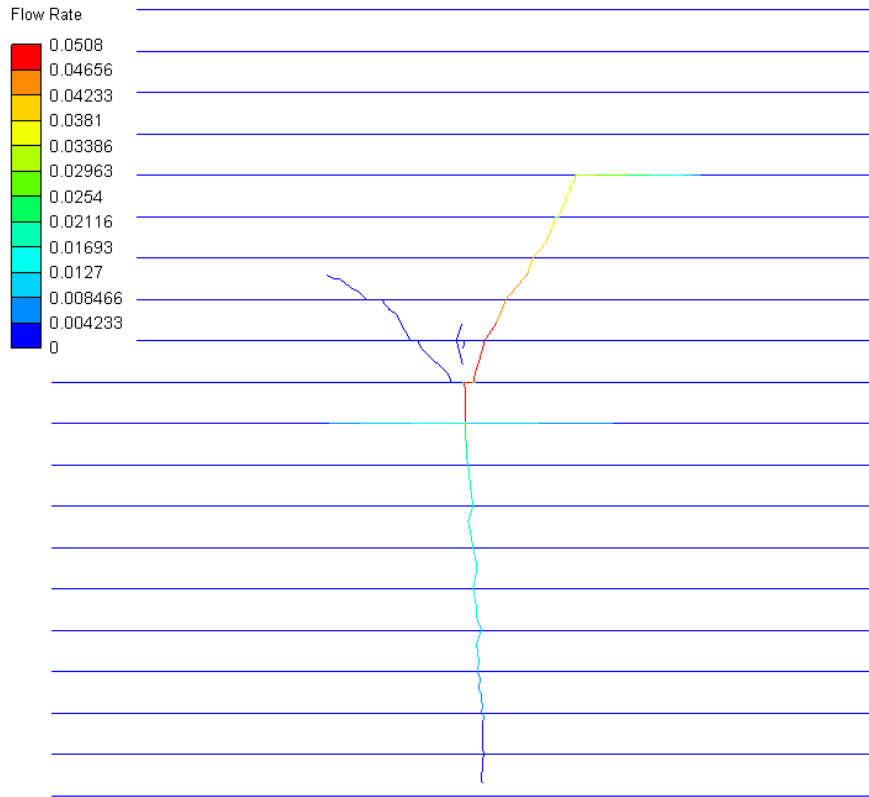
Figure 6.3.12: Flow Rate - High Friction, Cohesionless, Permeability B

High Cohesion-Frictionless   The results of this simulation were similar to those with high friction and cohesion, although not identical. Figure 6.3.13 shows the pore pressure at the end of the simulation ID 2 in Table 6.3.
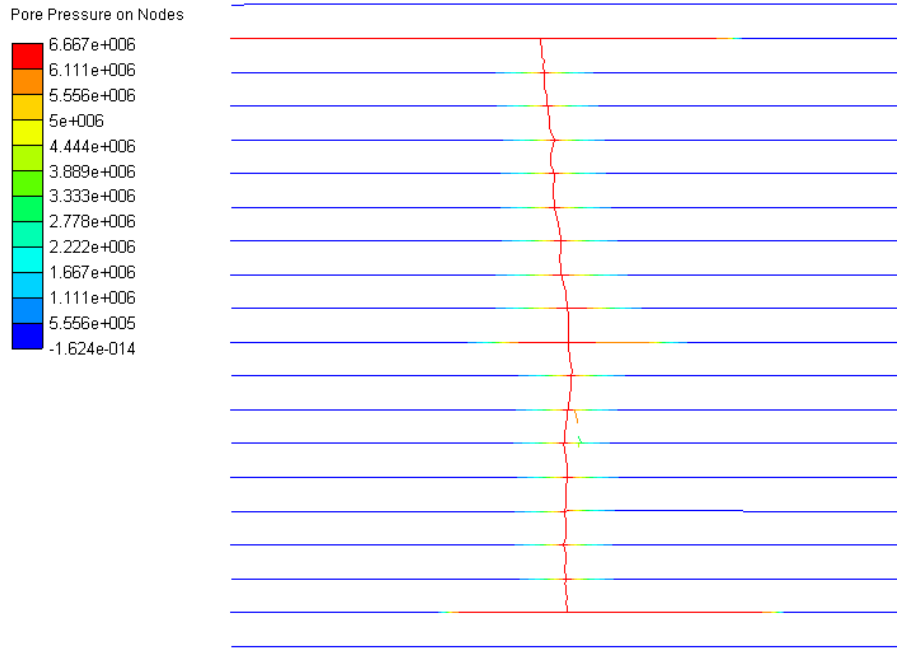
Figure 6.3.13: Pore Pressure - High Cohesion, Frictionless Permeability B

Frictionless and Cohesionless This simulation demonstrates the effect of removing all strength and friction properties of the natural fractures. Figure 6.3.14 shows the fluid pressure in the natural fractures at the end of the simulation. The vertical fracture propagation was arrested, pore fluid filling the natural fractures until propagating from the end of one natural fracture.
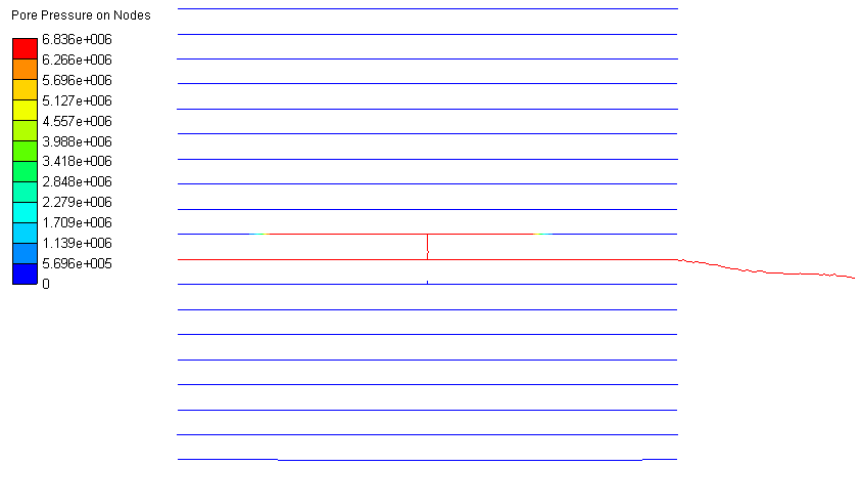
Figure 6.3.14: Pore Pressure - Frictionless, Cohesionless Permeability B

Stress Anisotropy

Two simulations were performed with the same parameters as those described in section 6.2.2, i.e. $\alpha = 0.95$, C=20e6 MPa. The minimum principal stresses were reduced to 4 MPa and 3 MPa, for comparison with the earlier simulation that had σ_{Hmin}= 4.9 MPa.

Plots of fluid pressure in the network elements of the two simulations are shown in Figures 6.3.16 and 6.3.15. A plot of the hydraulic fracture length and volume for all three simulations is presented in Figure 6.3.17. The data are plotted against elapsed fracturing time, removing the offset of fracturing start time which is due to the higher pressure needed to fracture as σ_{Hmin} increases. Note that the reference simulation ran for a shorter period, so is not directly comparable beyond 16s fracturing time.

Figure 6.3.18 shows the fluid pressure history for the three simulations.
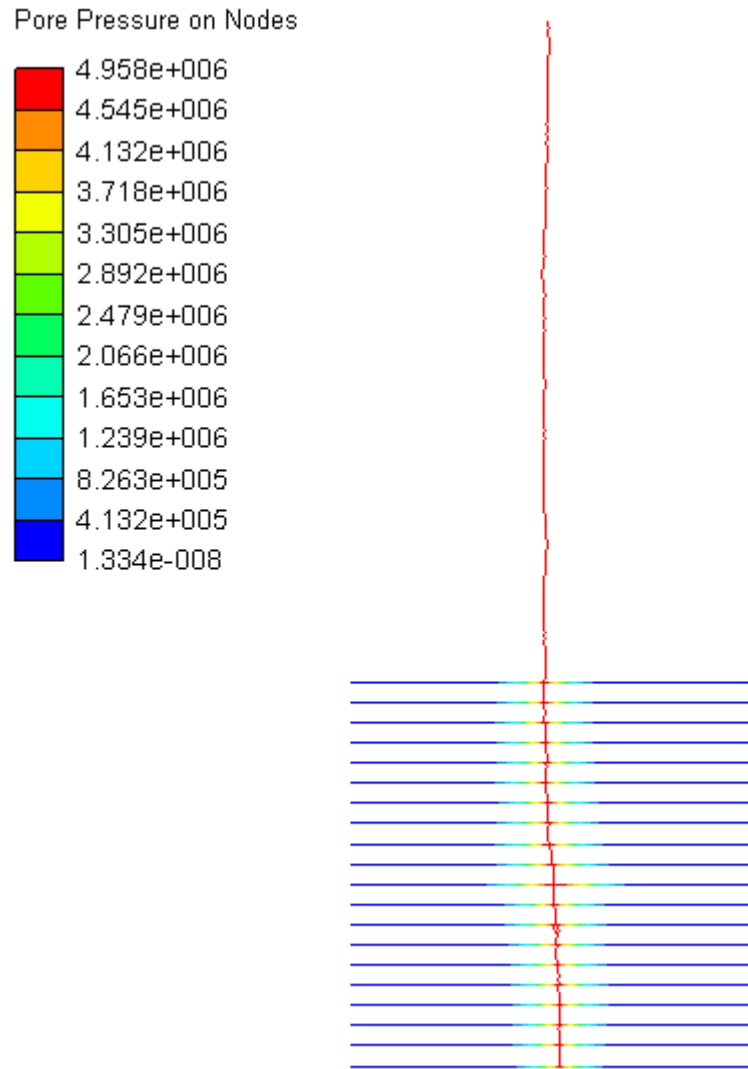
Figure 6.3.15: Fluid Pressure $\sigma_{Hmin} = 4$ MPa
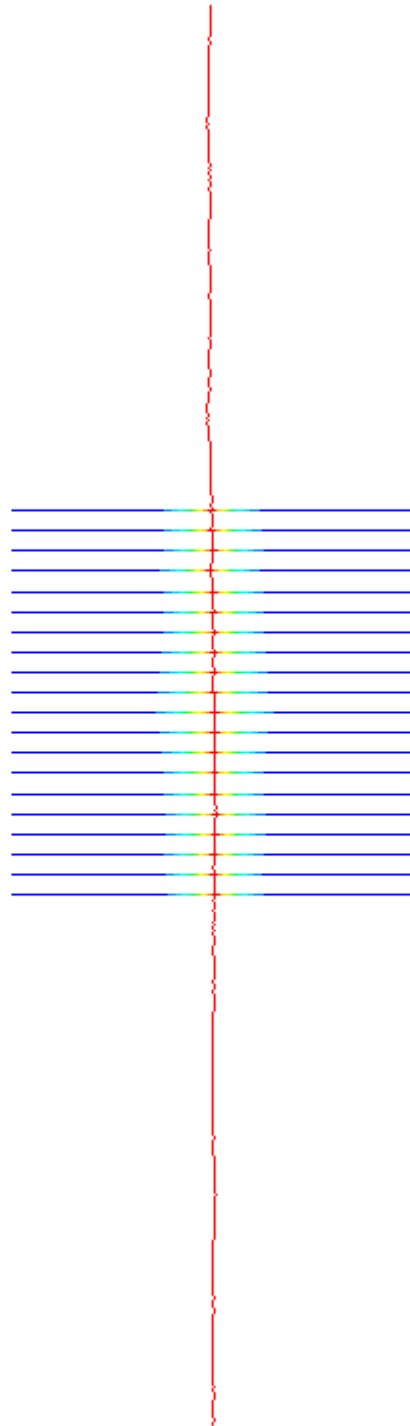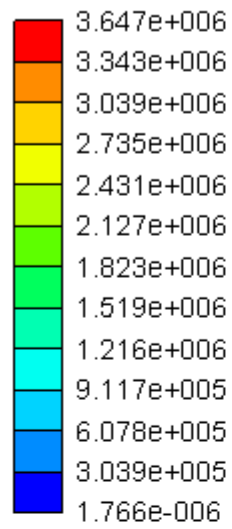
Figure 6.3.16: Fluid Pressure $\sigma_{Hmin} = 3$ MPa
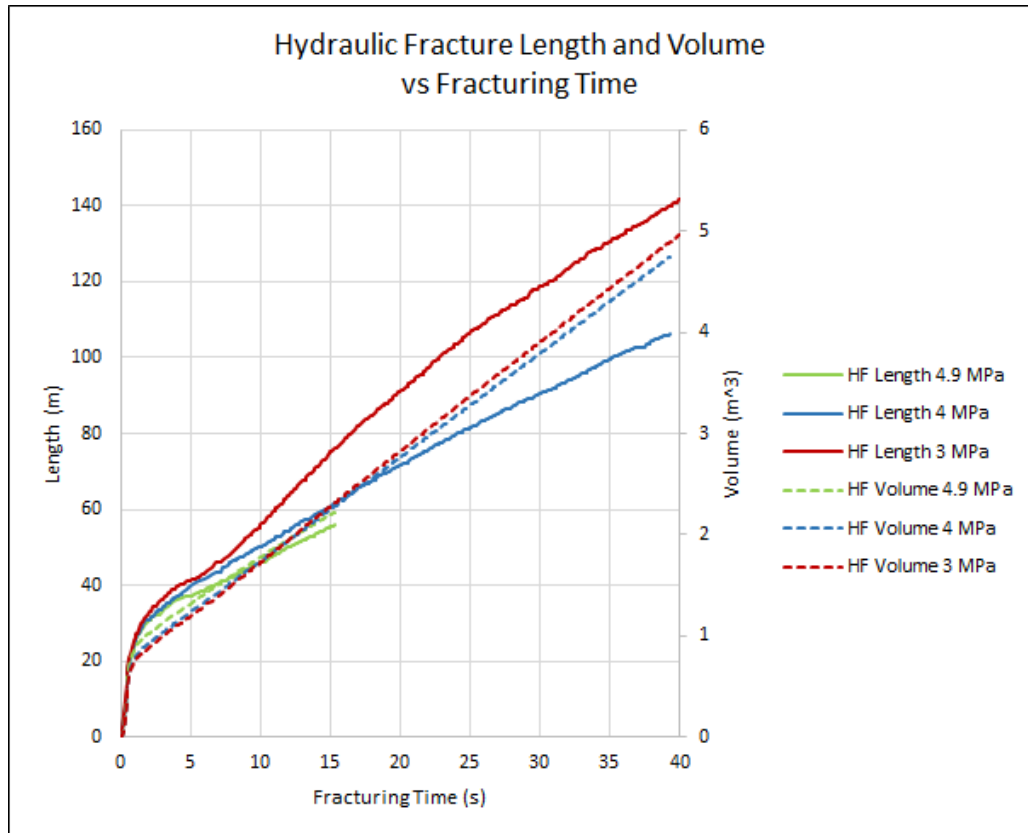
Figure 6.3.17: Length and Volume of Hydraulic Fracture through Natural Fractures, varying Anisotropy
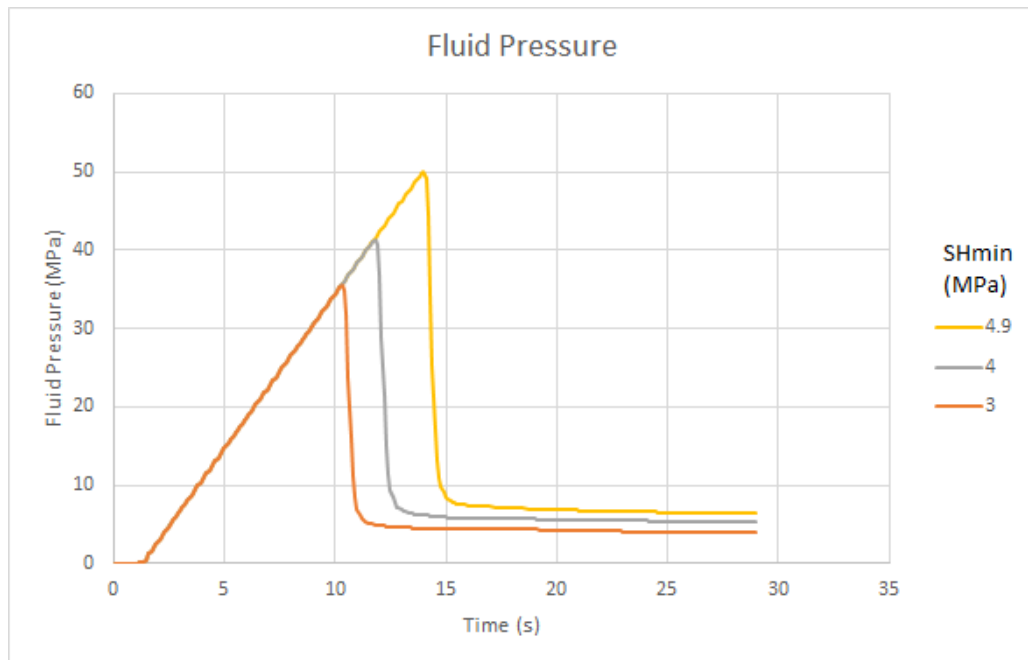
Figure 6.3.18: Fluid Pressure, varying stress anisotropy

6.3.2 Fracture Reorientation

Plots of the final pore pressure in the natural and hydraulic fractures are shown for the single and two set simulations in figures 6.3.19 and 6.3.20 respectively. The two set simulation failed to complete owing to a software fault, and is shown at 76s. The first simulation completed and is at time 100s. The fluid pressure histories of both simulations up to 76s are shown in Figure 6.3.21.
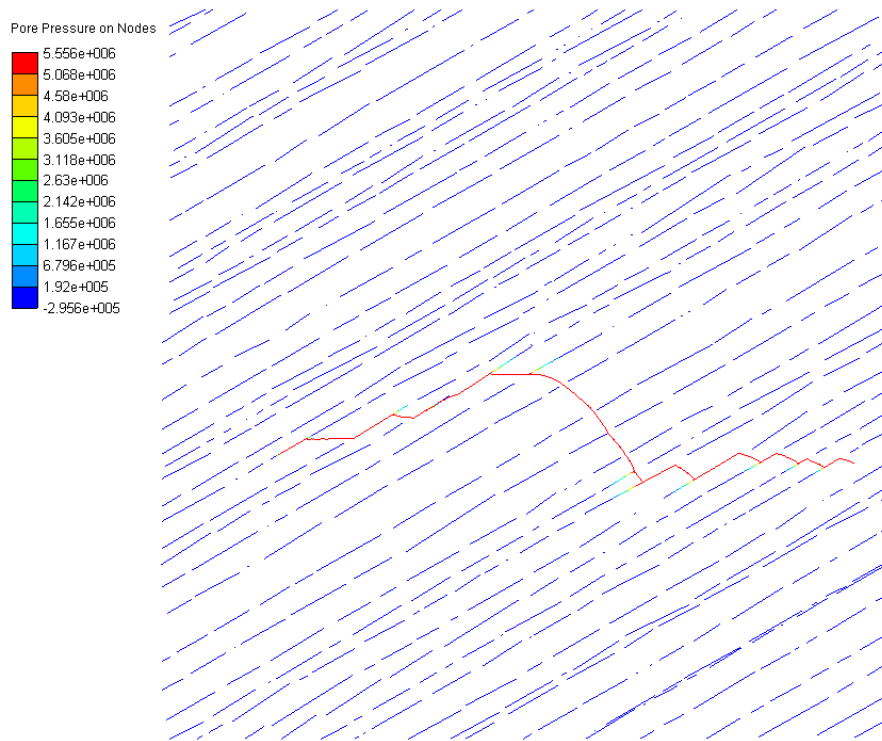
Figure 6.3.19: Fracture Reorientation, single Natural Fracture set
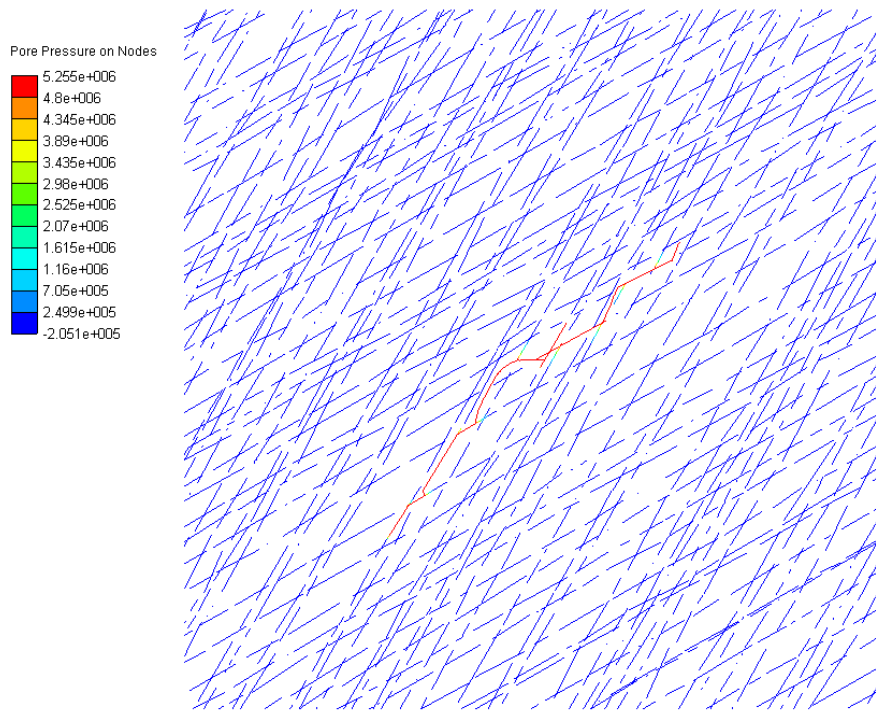
Figure 6.3.20: Fracture Reorientation, two Natural Fracture Sets
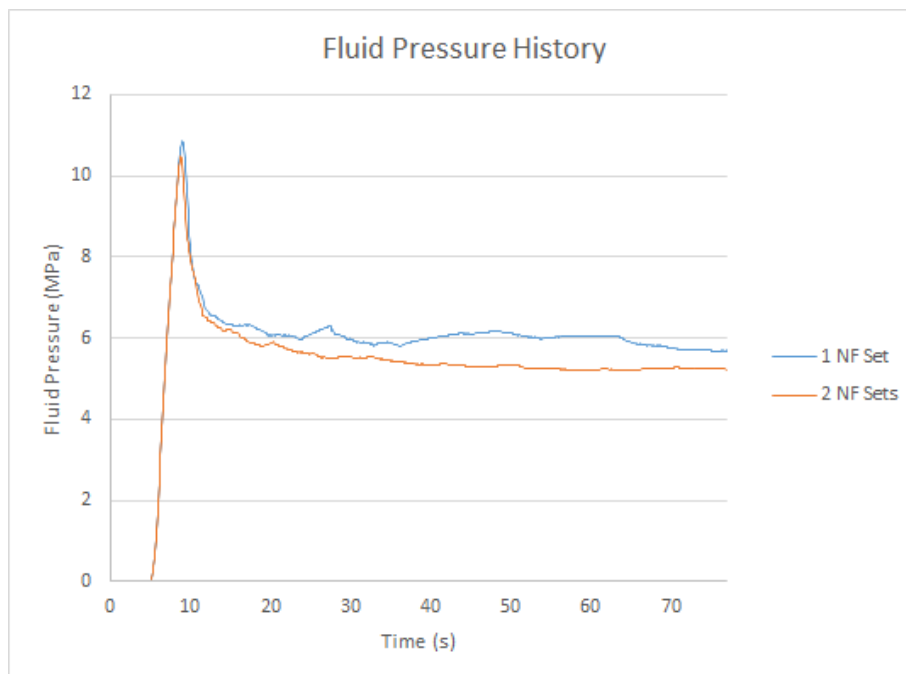
Figure 6.3.21: Fluid Pressure History - Reorientation with Natural Fractures

170

6.3.3 Impact of Shear Stress

Figure 6.3.22 shows the pore pressure at the end of the simulation.
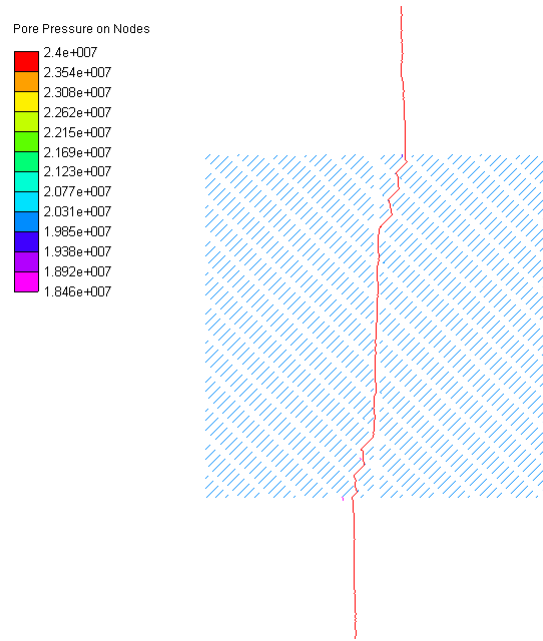
Figure 6.3.22: Pore Pressure - Shear Stress Influence

Figure 6.3.23 plots the value of the damage state indicator on a per-element basis. This value indicates that the material has begun to fail, and due to tensile damage, the material has begun soften and travel the downward slope in Figure 3.5.3. The plot is taken at 31 s, just before the hydraulic fracture first makes contact with a natural fracture.

The absolute shear stress in XY is plotted at the same time in Figure 6.3.24, while Figure 6.3.25 shows elements of the two previous plots superimposed. These are the absolute shear stress in XY, τ_{xy}, for values between 1 MPa and the maximum 3.73 MPa, which are contoured blue to red. The peak values occur in only a few elements, so most of the visible part of this contour is a shade of blue. On top of this is overlaid the data from Figure 6.3.23, with all damaged elements coloured red.
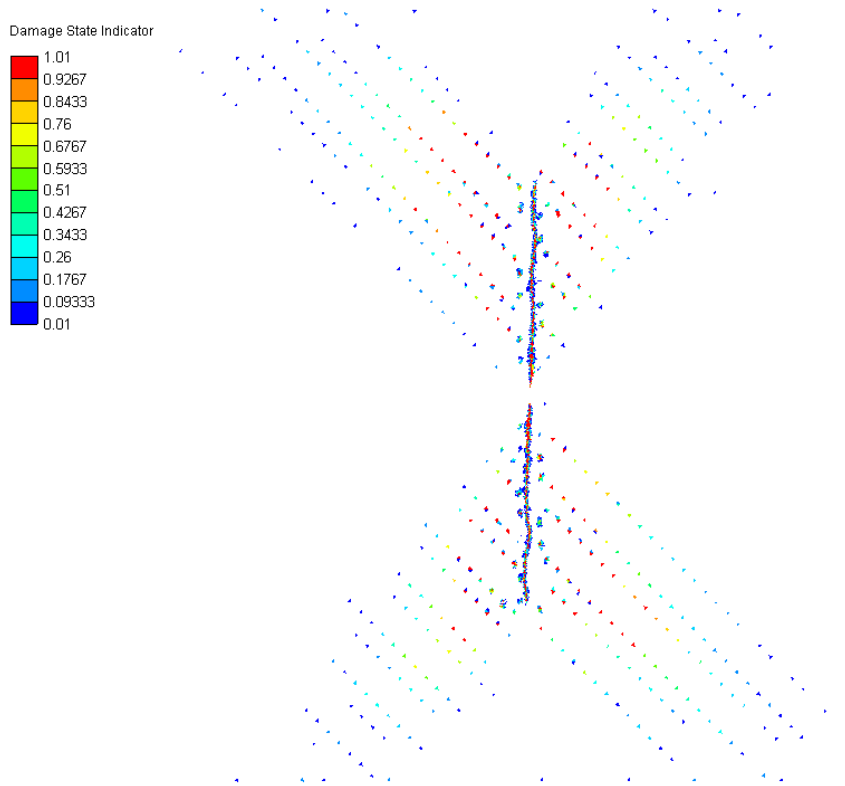
Figure 6.3.23: Damage State Indicator - Shear Stress Influence, 32s
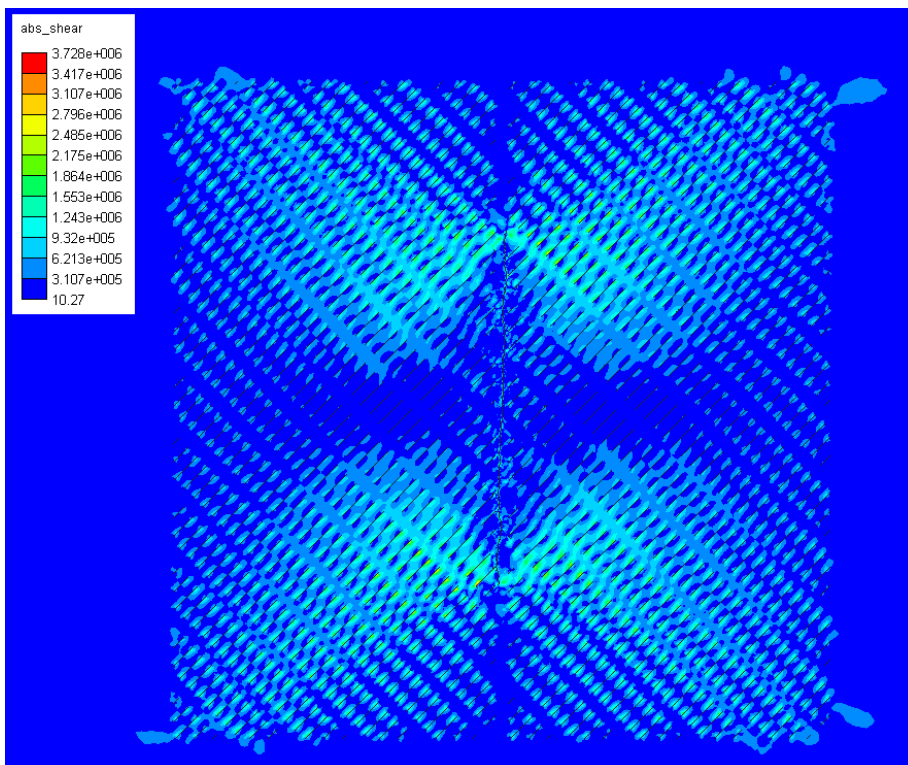
Figure 6.3.24: Absolute value of τ_{xy}
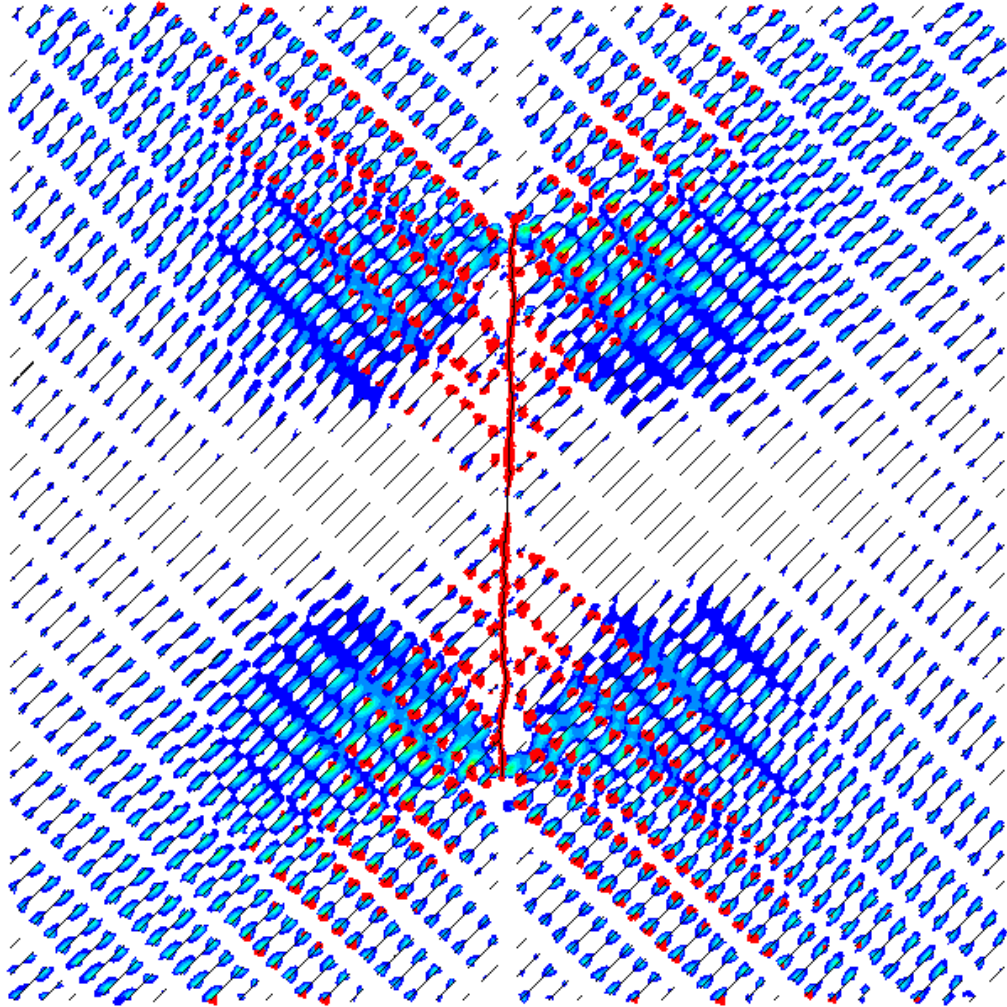
Figure 6.3.25: Absolute τ_{xy} and Damage State Indicator

An LIC plot of the stress field prior to hydraulic fracture interaction with the natural fractures is shown in 6.3.26.
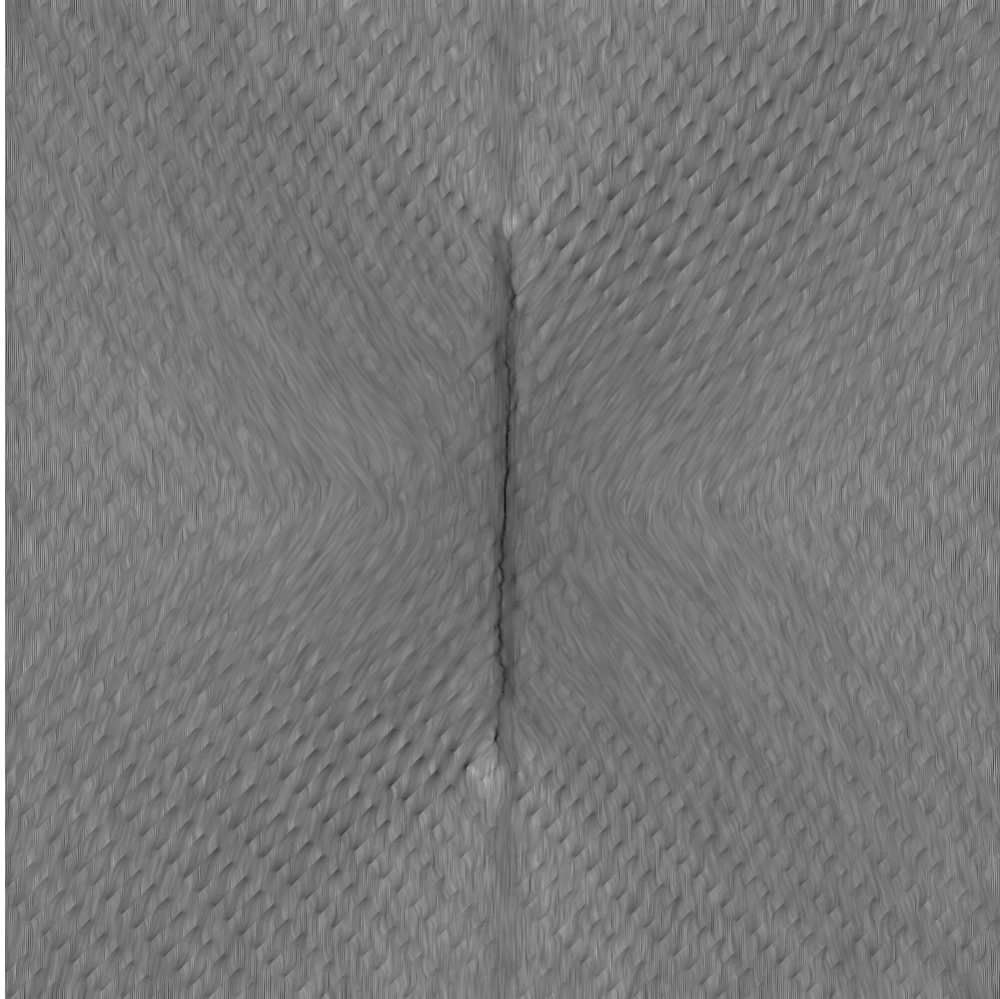
Figure 6.3.26: LIC plot of Principal Stress Field, 31 s

Microseismic event output is visualised in two plots below. The first, Figure 6.3.27 is at the time 31 s, before the hydraulic fracture contacts any natural fractures. Figure 6.3.28 shows the microseismic data output until time 71 s, which is the time the hydraulic fracture exits the region of natural fractures.

Beachball plots are used to represent the moment tensor. All events up to the current time are overlaid on the same plot, with the most tensile principal stress contoured. The beach-balls are coloured blue in the tensional quadrants, with solid blue markers representing isotropic dilation, or tensile failure events.

The pore or fluid pressure in the fractures is contoured in Figure 6.3.28. This is primarily to show the fracture has not affected pore pressure outside of the simple path it takes between nearby natural fractures, once it has begun travelling through them.
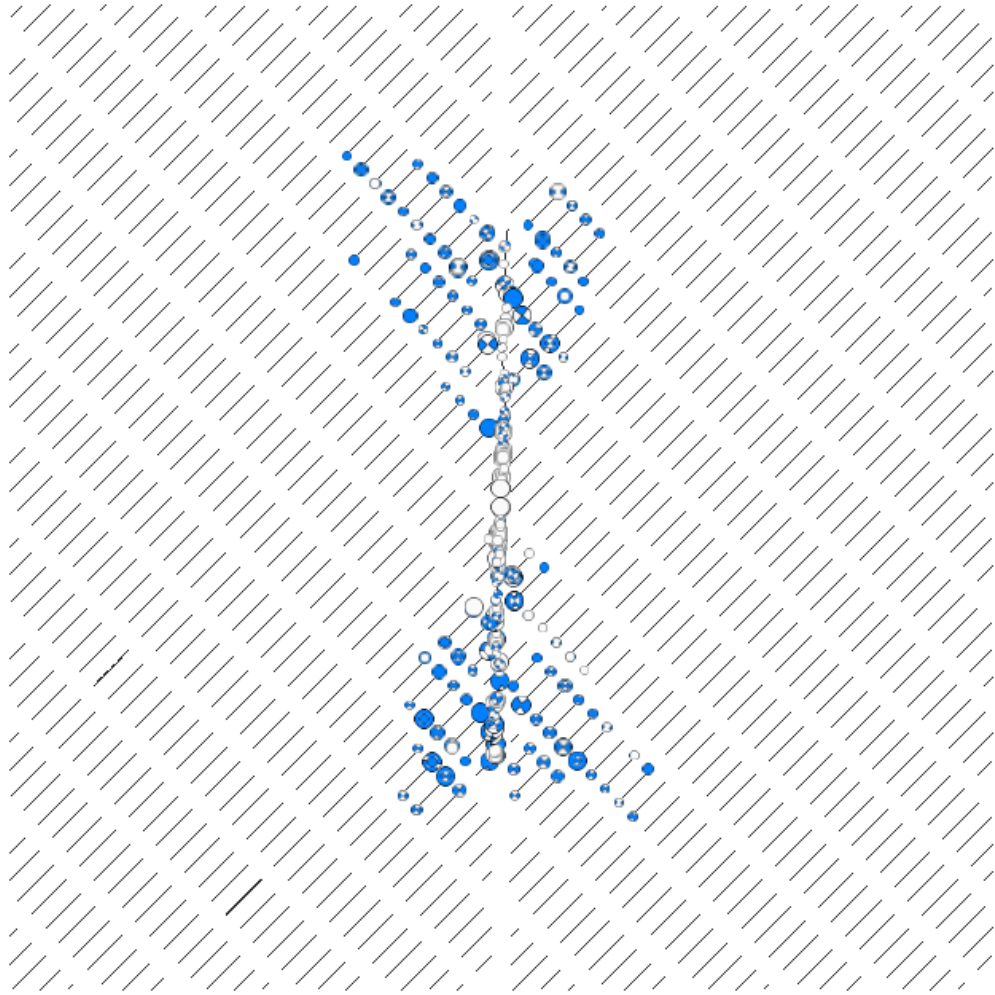
Figure 6.3.27: Microseismic Events, 31 s
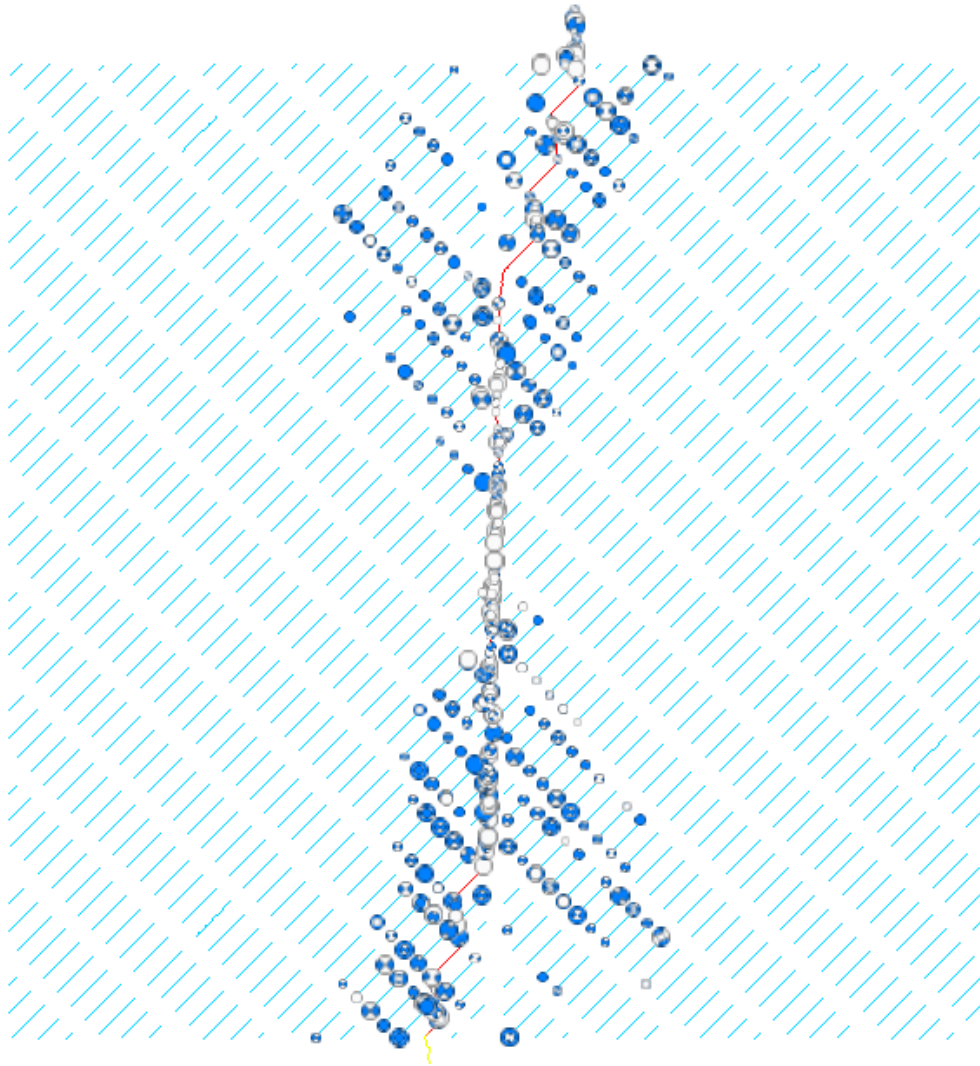
Figure 6.3.28: Microseismic Events and Pore Pressure, 71 s

6.4 Discussion

6.4.1 Propagation Through Natural Fractures

Permeability

High Permeability Figure 6.3.1 illustrates the effect of a hydraulic fracture coming into contact with a high permeability natural fracture set. The contact properties allow transmission of the mechanical forces required to continue propagating the hydraulic fracture. This is shown by the continuation of the fracture through the first fracture each wing sees. However, it is easier for the fluid to flow into the natural fracture than to continue opening

the hydraulic fracture, and pore pressure in the natural fractures begins to build. By the time the pressure has increased along the length of the natural fracture, its length makes it easier to open than the original hydraulic fracture. One side of the natural fracture begins to propagate, which then takes the rest of the pumped fluid. The flow rate contour plot Figure 6.3.2 shows that although three other wings are pressurised, fluid is propagating in one direction only. Unless some impediment is encountered by the propagating fracture, the other wings are unlikely to grow, nor the original hydraulic fracture to propagate further.

An examination of a detail of the mechanical analysis shows that despite the high permeability of the natural fractures, the hydraulic fracture does continue to propagate briefly. Figure 6.3.3 shows the magnitude of σ_{11} prior to fracture insertion - and importantly the contact properties within the natural fracture have allowed the tensile stress area to cross the natural fracture. Similarly a plot of τ_{xy} (Figure 6.3.5) confirms that shear stress has been transmitted through the fracture. These go hand in hand, as the shear stress zones allow the transition from compressional forces at the fracture walls to tensile stress at the tip (see section 6.1.1).

Low Permeability   The low permeability case serves to confirm the expected behaviour - the hydraulic fracture continued to propagate through the natural fractures. Figure 6.3.6 shows this clearly. However, the fracture behaviour is not completely unchanged in comparison to a fracture propagating in a homogeneous rock. The fracture is diverted from the vertical in small amounts between each natural fracture, to the left in the upper wing and to the right in the lower. The hydraulic fracture exited the region of natural fractures at both ends, despite there being fewer natural fractures to cross at the top of the model.

Intermediate Permeability   The two intermediate permeability cases each exhibit behaviour similar to either the high or low permeability examples. Figure 6.3.7 shows the lower of the two permeabilities. In this example the pore pressure has increased in the natural fractures, but in contrast to the low permeability example, one wing of the hydraulic fracture exits the area of natural fractures before the other. One contributing factor to this (aside from the asymmetry of the model) could be one of the natural fractures taking on more fluid than the others. The nearest fracture to the initiation point on the lower half of the model can be seen in Figure 6.3.7 to have a longer region of higher pore pressure than many of the other fractures. Closer examination of this area reveals some interesting points.

Figure 6.4.1 plots markers indicating contact pressures on top of the natural and hydraulic fracture geometry. The fracture initiation point is indicated by a blue arrow on this image.

177

At this point in the simulation, several of the natural fractures have opened, indicated by the lack of contact markers near the hydraulic fracture. This is due to the high propagation pressure at the beginning of the simulation, in turn a factor of the starter fracture length. Charts such as 5.3.9 illustrate the length dependence of opening pressure on starter fracture length (albeit under a different stress regime). The pressure in the propagating fracture - 17.2 MPa - is more than enough to overcome the maximum horizontal stress σ_{Hmax} (5 MPa), and open the natural fractures which reached a similar pressure. The higher permeability of the opened fractures allowed them to take a larger volume of fluid than those which encountered a lower fluid pressure later in the simulation.
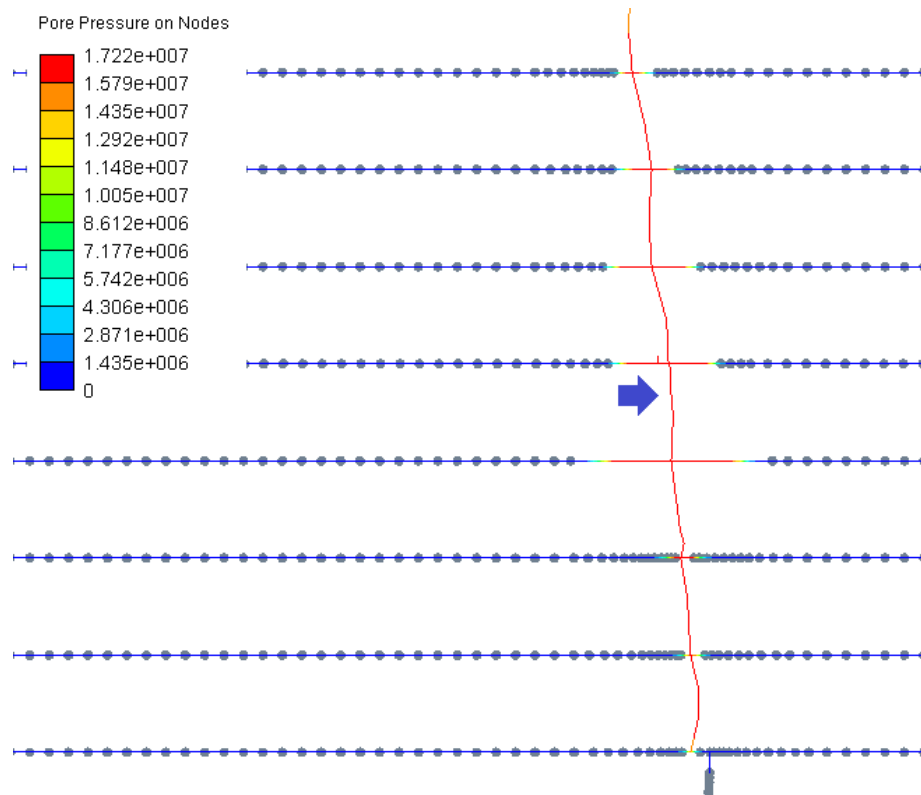
Figure 6.4.1: Open Natural Fractures - case B at 14.4s

Figure 6.4.2 shows the same area later in the simulation. At this point the fluid pressure in the hydraulic fracture had reduced to 7.1 MPa, which was still higher than σ_{Hmax}. Contact markers at the ends of the previously open natural fractures indicate that the fractures have closed, isolating the fluid in the natural fracture from the hydraulic fracture. The reason for this closure, when the natural fractures are under enough pressure to remain open, is intriguing. Two possible mechanisms are:

- Stress shadowing effects - the pressurised neighbouring natural fractures acting to close each other

- Pinching of the natural fracture openings due to the opening of the hydraulic fracture

Further simulations to investigate this effect in more detail would be of benefit, including behaviour as the fluid pressure is reduced, and in particular in the presence of proppant. It may be the case that this is an illustration of fluid leak-off occurring. If the fluid was isolated for the latter reason above, a propped fracture may maintain the contact points, and continue to isolate the fluid in the natural fracture. Conversely, the natural fractures may allow the fluid to escape when the pressure is reduced.
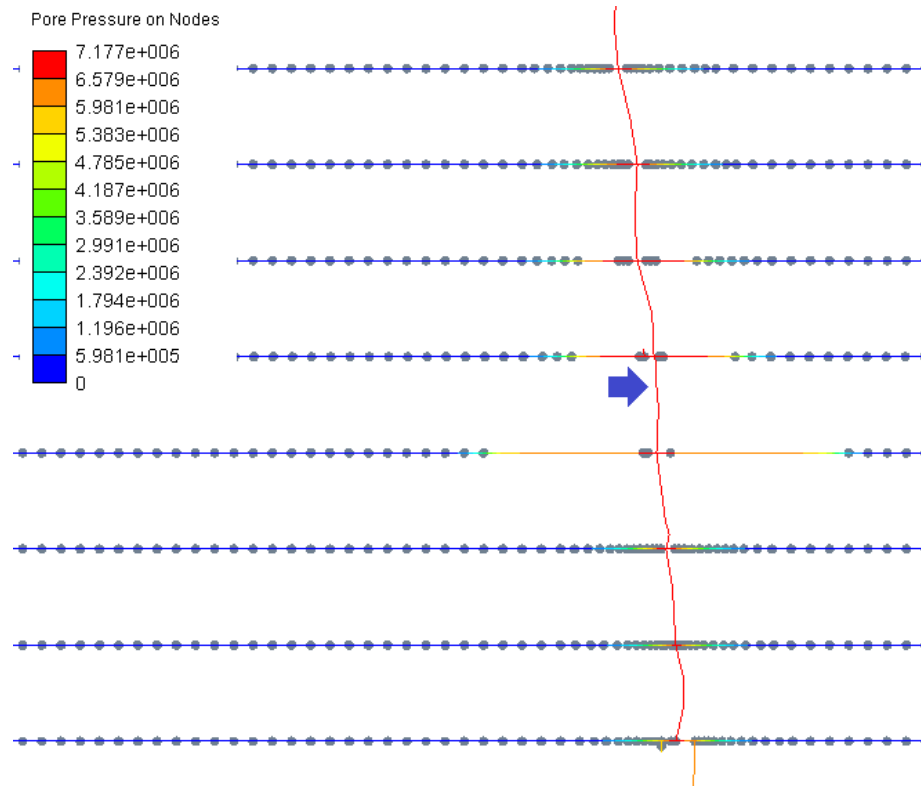
Figure 6.4.2: Isolated Fluid in Natural Fractures - case B at 17.1s

Figure 6.3.8 shows the fluid pressure at the end of simulation for the higher permeability of the two intermediate cases - case C (permeability 8.51 E$^{-10}m^2$). This exhibits similar behaviour to the high permeability example in terms of the final outcome - the fluid fills the natural fractures nearest the initiation point and propagates from the end of one of them. It differs to that example in that while the natural fractures near the initiation point open, the hydraulic fracture continues to propagate vertically.
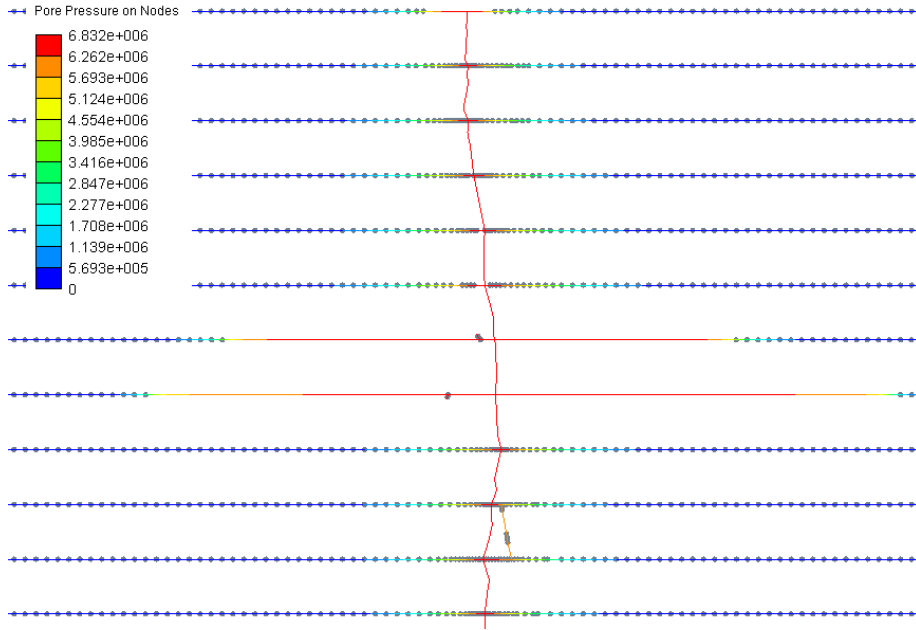
Figure 6.4.3: Open Natural Fractures - case C at 17.2s

Figure 6.4.3 shows a plot similar to Figure 6.4.1 for this permeability. Again, the lack of contact markers indicate natural fractures that have been opened by the fluid pressure of the hydraulic fracture. At the top of the image an open fracture can be seen, and this is mirrored at the lower region of the model (the image has been cropped). At previous times in the simulation, some of the other natural fractures showed the same behaviour, opening when first coming into contact with the propagating fracture, but closing some time later.

This example also shows one instance of branch creation in the lower half of the model. This simulation was not run with a high enough output resolution to determine the exact cause of this branch. It can be seen that the right hand branch is inserted first, followed by the left, which then becomes the preferred route for the fluid, closing the right hand side as it is filled.

The intermediate permeability cases were selected to use as base cases for variation of contact properties, since they both displayed effects which are due to the natural fracture permeability, yet allowed vertical continued propagation of the hydraulic fracture to varied extents.

Natural Fracture Interface Properties

High Friction-Cohesionless   The immediately obvious departure from the high friction, high cohesion examples (6.3.1) is the branching behaviour of the upper wing. Recon-

sidering Figure 6.2.1, this can be drawn as Figure 6.4.4 for the cohesionless case and $\alpha = 0.95$:
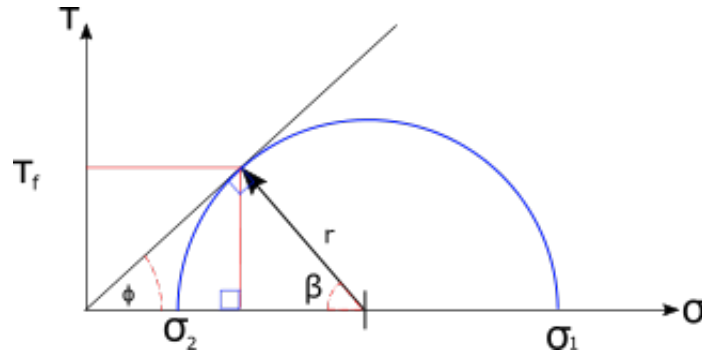
Figure 6.4.4: Mohr-Coulomb Failure Envelope - Cohesionless

To determine whether the shear zones around the propagating fracture are triggering sliding, τ_f can be determined from the magnitudes of the principal shear stresses σ_1 and σ_2 (which are our σ_{Hmax} and σ_{Hmin}, respectively) and the angle β.

$$\beta = \frac{\pi}{2} - \phi \tag{6.4.1}$$

$$r = \frac{\sigma_1 - \sigma_2}{2} \tag{6.4.2}$$

$$\sin(\beta) = \frac{\tau_f}{r} \tag{6.4.3}$$

$$\tau_f = \frac{\sigma_1 - \sigma_2}{2} \sin(\beta) \tag{6.4.4}$$

Because the natural fractures are aligned with the X axis, this value τ_f can be compared against the shear stress τ_{xy} to indicate fractures which may have slipped. Figure 6.4.5 plots positive values of $\tau_{nf} = \tau_f - |\tau_{xy}|$ as NF_STRS. Where these positive values cross natural fractures (in light blue), the natural fracture is able to slip - whether or not this happens may depend on the surrounding mechanics. This plot shows that while the hydraulic fracture (in purple) has propagated towards the lower part of the model, the upper part has not yet inserted a fracture.
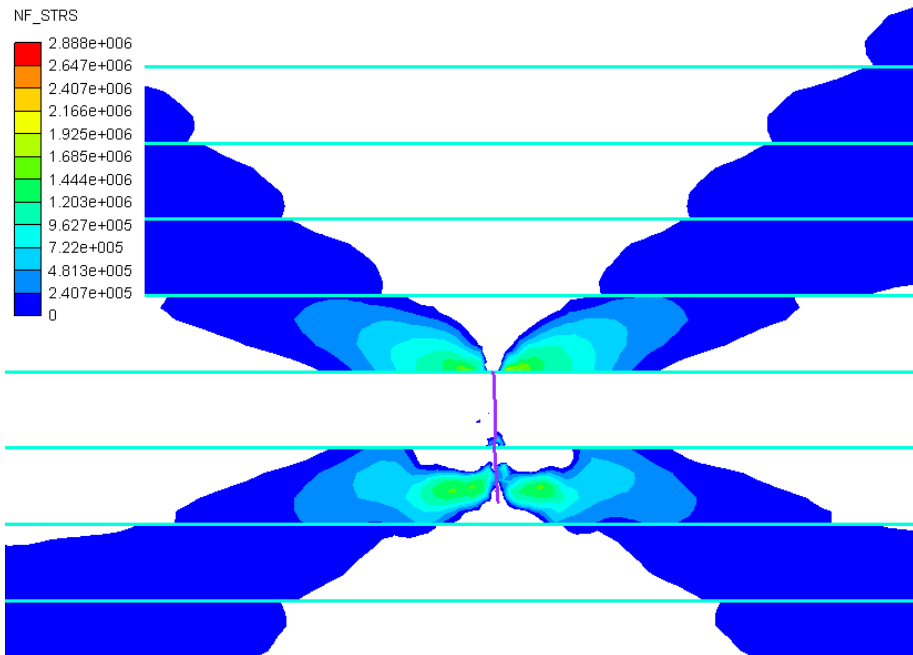
Figure 6.4.5: Slip Inducing Stress Prior to Branching - 14.01s
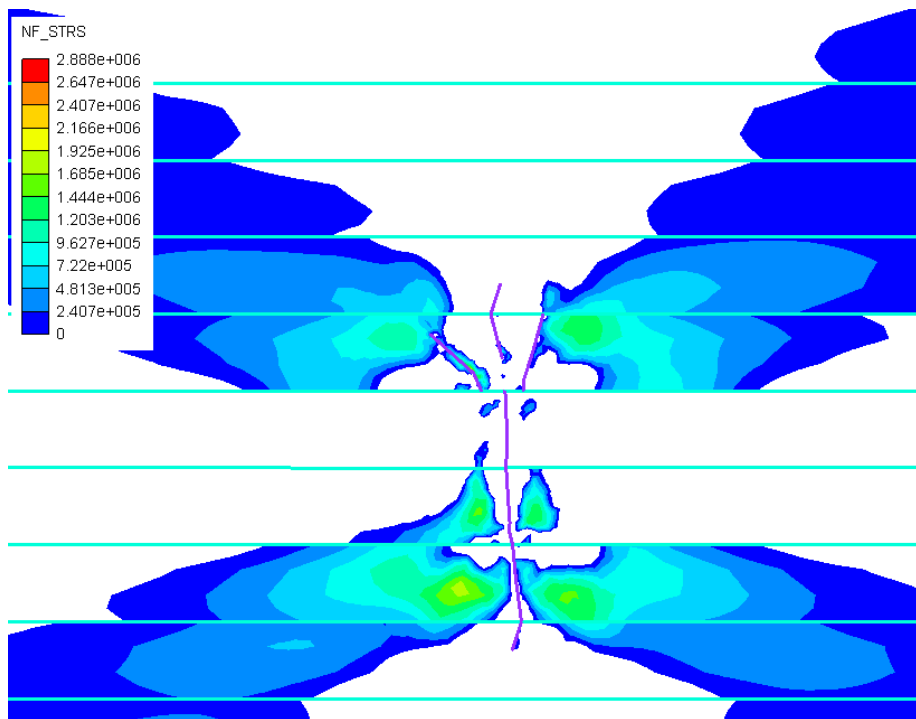
Figure 6.4.6: Slip Inducing Stress after Branching - 14.21s

Comparing Figure 6.4.5 with Figure 6.4.6, which shows the same area after the branch fractures are inserted, the boundary of areas of positive τ_{nf} appear closely related to the insertion location of the branch fractures. Figures 6.4.7 and 6.4.8 are LIC visualisations

of the principal stress field, contoured by stress intensity factor σ_I (equation 4.4.9), and make clear a discontinuity in stress intensity that is more pronounced in the upper part of the model prior to branching. The principal stress directions also make a "V" shape in the upper part of the model, differing from a smoothly curved transition to the vertical that is expected in a homogeneous medium, and is demonstrated to a lesser extent in the lower part of the model. Note that the range of σ_I varies in the first image between 1.67 MPa and 34.7 MPa, and in the second from 2.95 MPa to 41.1 MPa.
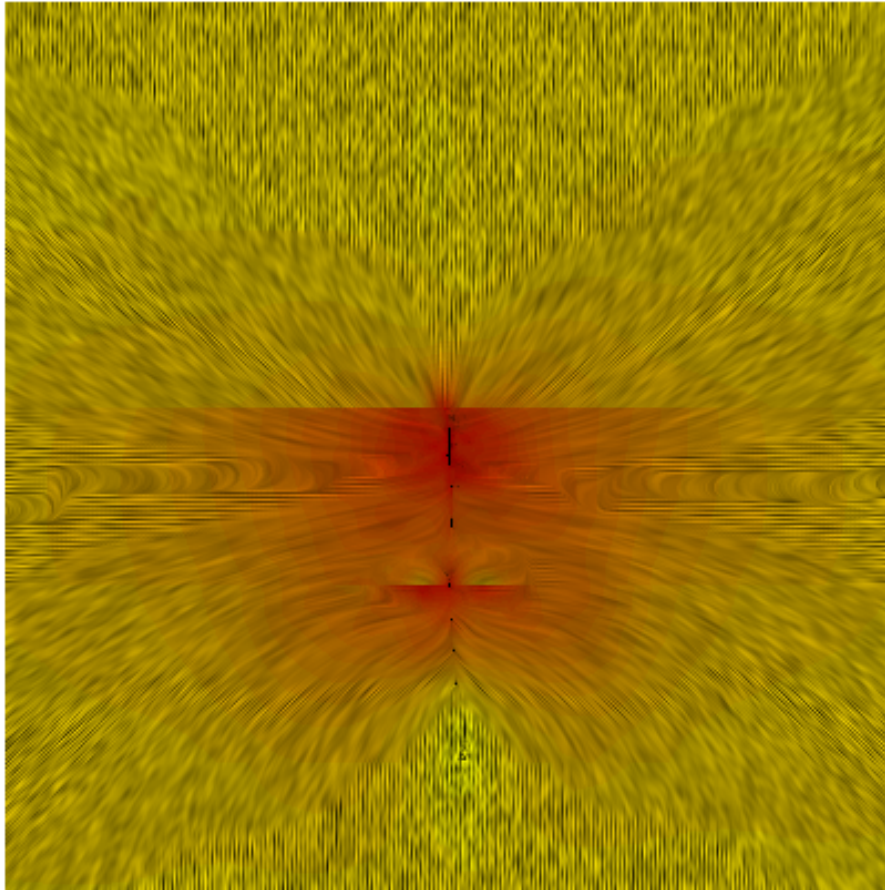
Figure 6.4.7: Principal Stress Field prior to Branching

The output of this simulation was not at high enough frequency to examine the mechanics of the fracture insertion in minute detail, and would warrant further study. In comparison to the high friction, high cohesion simulations run in section 6.4.1, the effect of removing cohesion is to put the natural fractures within the range of being affected by shear stress, allowing slip.

High Cohesion-Frictionless   It was expected that the results for these simulations would be identical to those with both high friction and cohesion. The cohesion value was ex-
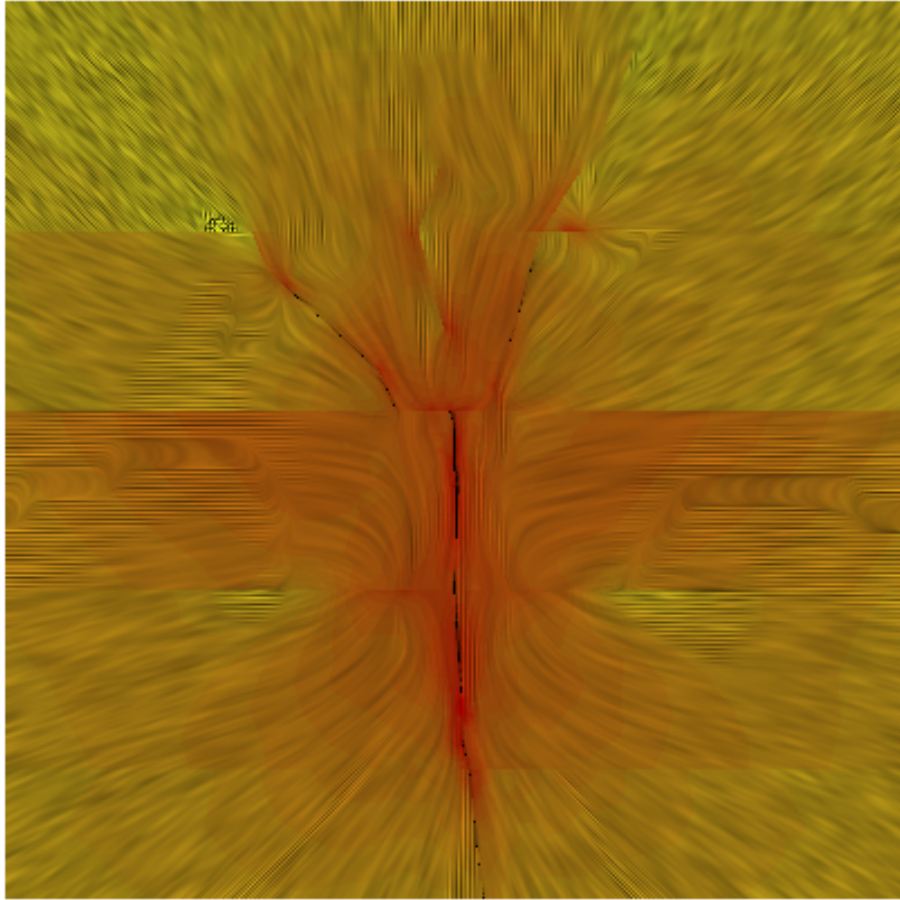
Figure 6.4.8: Principal Stress Field after Branching

pected to be high enough to prevent movement of the fracture even in the absence of friction. When $\alpha = 0$, the failure envelope becomes a horizontal line at the selected cohesion value, as illustrated in Figure 6.4.9. Movement on natural fractures becomes possible if the shear stress exceeds τ_f, which is equal to the cohesion value C, 20 MPa in this case. To exceed this value, the principal stress magnitudes would need to differ by twice this value, or 40 MPa.
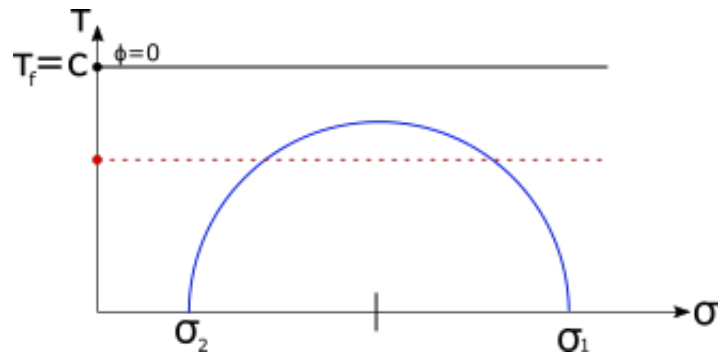
Figure 6.4.9: Mohr-Coulomb Failure Envelope - Frictionless

However, comparing Figures 6.3.7 and 6.3.13, which differ only in the value of the friction coefficient α, there are differences. The fracture propagates through the top of the natural fracture region in Figure 6.3.7, but is arrested in Figure 6.3.13. The chance of the principal stresses differing by more than 40 MPa seemed unlikely given the in-situ stresses of 4 and 5 MPa. However, the high fracturing pressure brought about by the small initial fracture size did create large stress differences. The simulation was run with outputs at every coupling (every 0.1s), which is low frequency in relation to the explicit timestep size. Of the those low frequency outputs, the maximum difference in principal stresses magnitudes was 34.7 MPa. It is quite possible that a difference of 40 MPa was exceeded in between coupling steps.

Comparing the indicator of contact slip flag in the output, this reaches a maximum of 0.96 in the zero friction case, but only 0.66 in the high friction example. If the cohesion value was exceeded between coupling steps, this flag could have reached 1, indicating slip. Unfortunately the output for slip magnitude is reset between outputs.

Given that the friction parameter is the only difference between this and the high friction, high cohesion examples in section 6.4.1, the difference between the two sets of results will be attributed to exceeding the cohesion value during early fracturing. This could have resulted in a minor permeability or mechanical difference that affected whether fracture propagation. A further set of simulations with a larger starter fracture, and therefore lower initial propagation pressure, may be less likely to show differences between high and low friction values. The sensitivity of these simulations, and quite possibly field scale fracturing, to minor changes in parameters is clear to see.

Frictionless and Cohesionless   In this simulation, the natural fractures have no resistance to sliding, and are unable to *directly* support shear stress along their length. That is; they are unable to transfer stress between their two walls tangentially. However, they continue to exert a normal force, and the bending of a fracture wall is able to cause a shear

stress on its opposite side. Similarly, the fracture opening under fluid pressure will bend a fracture wall and bring about shear stress in the material behind it. Also, the fractures are of finite length, so there may be some shear transfer through the rock continuum beyond the ends of the fractures.

In this simulation, none of the above mechanisms of shear transfer appeared to have a significant effect, and the propagating hydraulic fracture was arrested. Figure 6.3.14 shows the first natural fractures encountered by the hydraulic fracture have filled with fluid, and the fracture has propagated out of the end of one fracture at a direction normal to the maximum principal stress. This is very similar to the high permeability simulations in section 6.4.1.

Shear stress can be seen on the opposite side of these fractures in Figure 6.4.10, which shows the displacement vectors at each mesh node as well as the shear stress τ_{xy} contour at 9.8 s. This is during the drop in pressure from initiation to propagation - in Figure 6.3.10 the minimum pressure can be seen at around 15 s. If this is considered to show three layers, the primary displacement of the central layer is horizontal, due to the hydraulic fracture opening in that direction. The displacement of the layers above and below is consistent with the natural fractures opening; this is confirmed by the examination of the apertures.
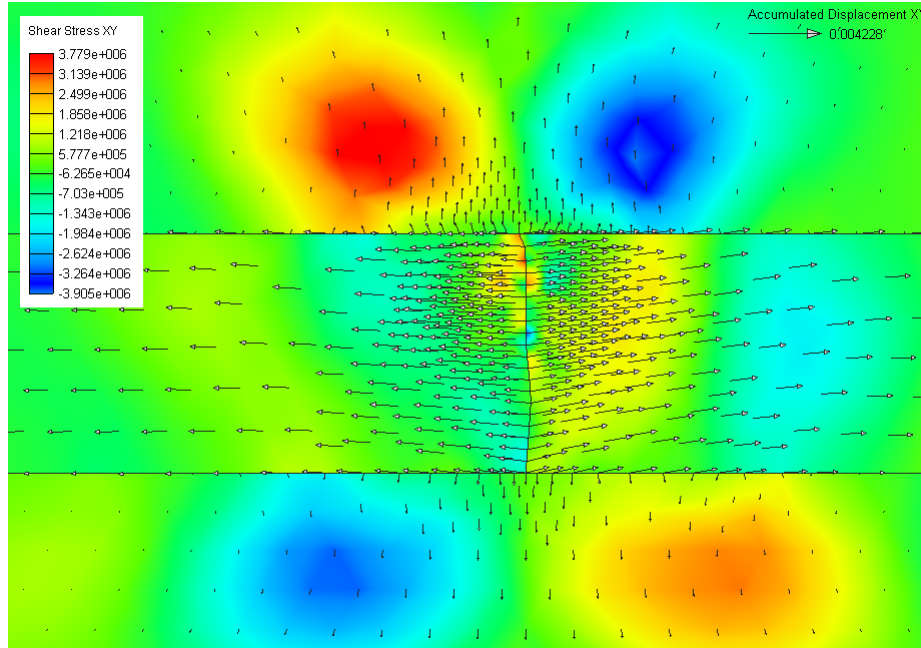
Figure 6.4.10: Shear XY and Displacement Vectors - Cohesionless Permeability B

The removal of friction and cohesion has an effect on the initiation pressure of the hydraulic fracture - Figure 6.3.9 shows this very clearly. The initiation pressure is reduced

from 50.1 MPa in all the simulations with either high friction, cohesion or both, to 32.3 MPa. This can be explained in one way by considering the effect of the natural fractures on the stiffness of the formation (Li et al. (2013)) - on a large scale, the natural fractures act to reduce the effective Young's modulus of the formation, and the orientation of the fractures will effectively create an anisotropic Young's modulus.

On a local scale, considering the 'layer' containing the starter fracture; it has zero stiffness in the X direction at the natural fracture boundaries. It is easier to open in that direction, because it is not necessary to move the material on the other side of the fracture. This is illustrated by examining a similar plot to 6.4.10 for the high friction, high cohesion case, at a similar stage in fracturing. Figure 6.4.11 shows the material above and below the natural fractures has moved with the central layer, due to the cohesion of the fracture. In contrast, the frictionless example shows horizontal displacement only in the central layer, and the vertical movement in the layers above and below has already been attributed to the natural fractures opening under fluid pressure.
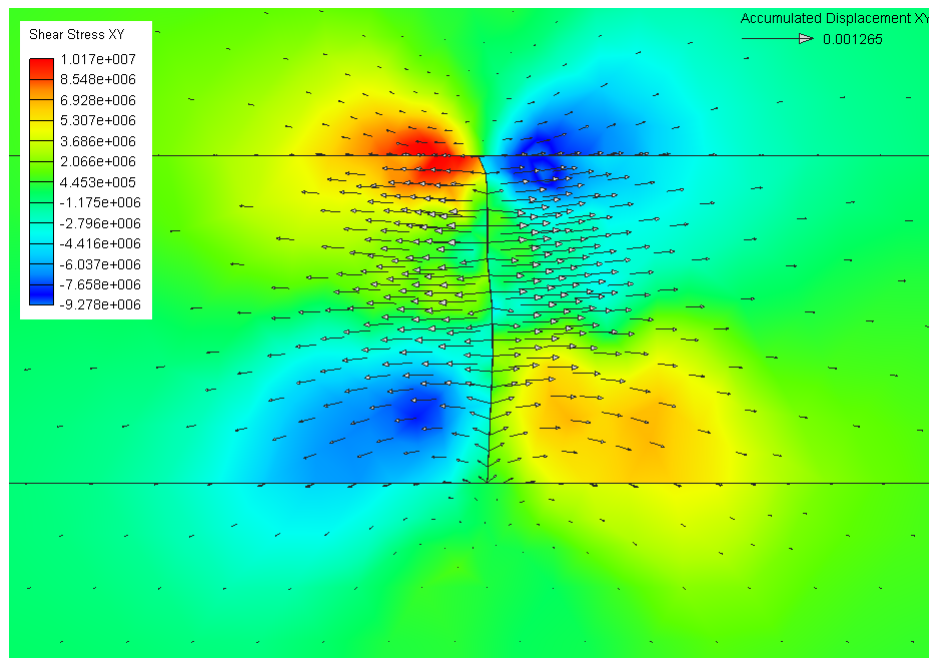
Figure 6.4.11: Shear XY and Displacement Vectors - High Cohesion Permeability B

The outcome of this simulation and the high permeability example of 6.4.1 are similar in terms of fracture propagation direction, although examining the fluid pressure required to both initiate and continue propagating the fractures highlights some important differences. Figure 6.4.12 shows this frictionless, cohesionless simulation with a high friction, high cohesion example at the same permeability, and a high permeability (case A in Table 6.2) with the same contact properties. For the sake of brevity, these three examples will be

enumerated as follows:

Identifier	α	C (MPa)	k (case identifier in Table 6.2)
1	0	0	B
2	0.95	20e6	A
3	0.95	20e6	B

Table 6.7: Simulation Identifiers

Case 2 shows the same high initiation pressure as the other examples in these simulations with strong contact properties, for example case 3, which is provided to enable this comparison. It would be unexpected if the initiation pressure were dependent on the natural fracture permeability, since the hydraulic fracture is not in communication with the natural fractures until it begins propagating. Figure 6.4.13 shows a detail of Figure 6.4.12, comparing cases 1 and 2 in Table 6.7.
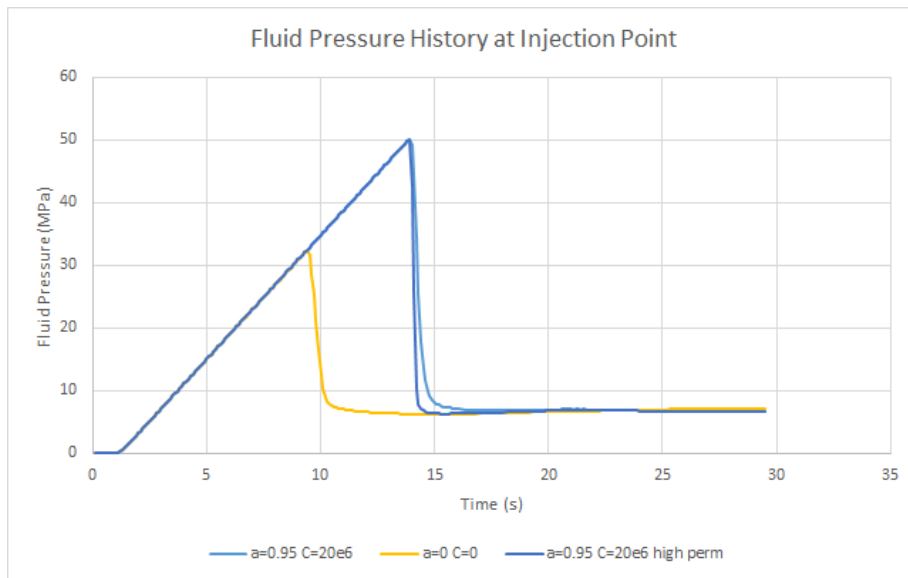
Figure 6.4.12: Fluid Pressure Comparison - High Permeability
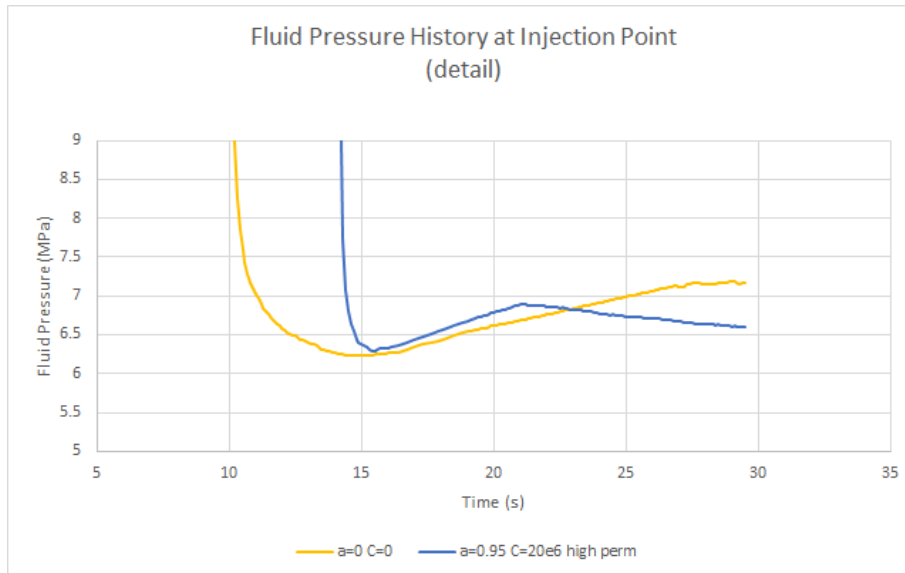
Figure 6.4.13: Fluid Pressure Comparison - High Permeability

Comparing cases 1 and 2, both hydraulic fractures see a pressure drop as the fracture first extends, both dropping to a similar pressures. For case 2 - the high permeability example - during the initial pressure drop, the hydraulic fracture connects with the natural fractures. These then dilate and increase in permeability while also building pore pressure. The pressure drops again when the fracture begins to propagate from the end of the natural fractures at around 21 s. The same process occurs in case 1. This fracture begins to extend from 27 s, at a slightly higher pressure than case 2. The difference in fracture permeability between the two examples explains the difference in rate of pressure increase, since neither natural fracture sees an aperture increase along its entire length until just before the fracture extends. This shows that the permeability of the unopened natural fracture affects the rate at which fluid can fill the fracture and increase the pressure.

Stress Anisotropy

These simulations were performed to assess the impact of increasing the differential in-situ stress on scenarios such as those discussed in section 6.4.1, by reducing the minimum horizontal stress. It was expected that propagation pressure would initially be lower, but that vertical propagation could be affected because of the same reduced pressure in the propagating fracture. Of particular interest was whether the expected lower propagation pressure in a higher anisotropy setting would provide enough stress to continue propagating vertically.

Figure 6.3.18 confirms the expected effect on propagation pressure; both cases initiated and propagated at lower pressures than the reference case with σ_{Hmin} =4.9 MPa. A

linear relationship between initiation pressure and σ_{Hmin} is confirmed by colinear slopes of the three pressure history curves.

The difference between the two end of simulation images - Figures 6.3.16 and 6.3.15 - were not expected. The fracture propagating under higher fluid pressure was arrested at the lower boundary of the natural fracture set, while in the lower fluid pressure example, the fracture continued to propagate both wings through all layers. The cause of the single wing result of the 4 MPa simulation can be found by looking in detail at the path taken by the lower wing. Figure 6.4.14 shows the offset fracture inserted at 12.1s. This is followed by another fracture connected directly to the upper fracture soon afterwards, but the offset becomes part of the main fracture path (Figure 6.4.15). This offset acts as a choke on the lower wing, lowering flow rates and isolating the fluid pressure. Figure 6.4.16 shows the fluid pressure isolation - the fracture continues to propagate in this direction. Once the upper wing is clear of the natural fracture region, flow rates to the lower wing drop off substantially and propagation downwards ceases.
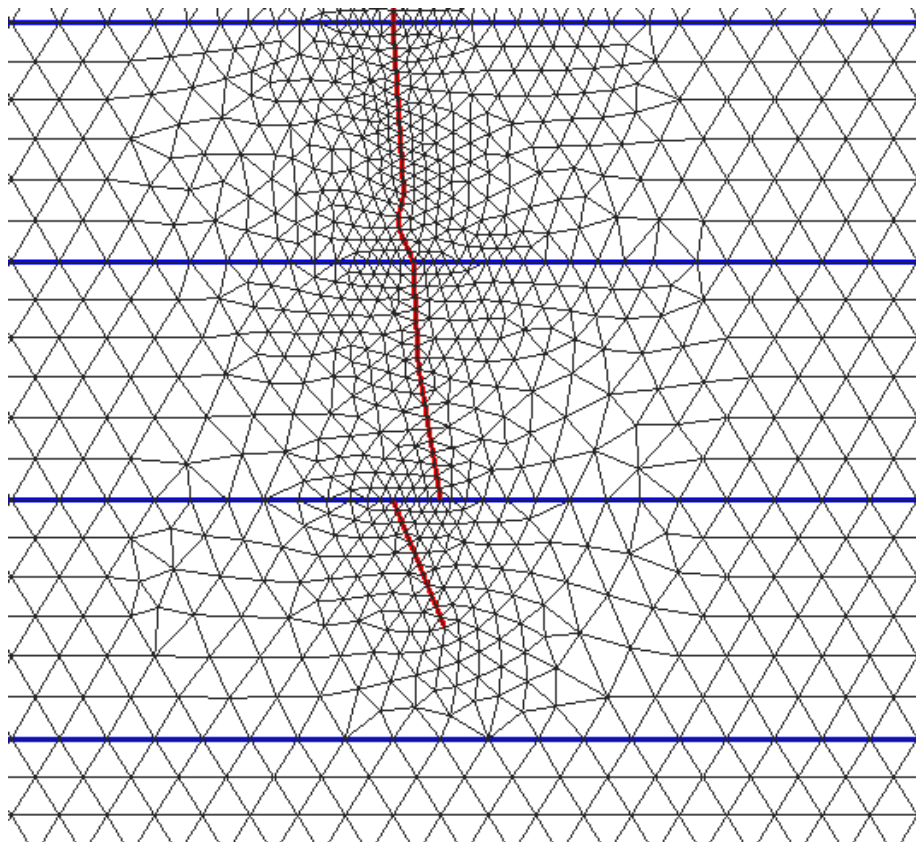
Figure 6.4.14: Branch 4 MPa case, 12.1s
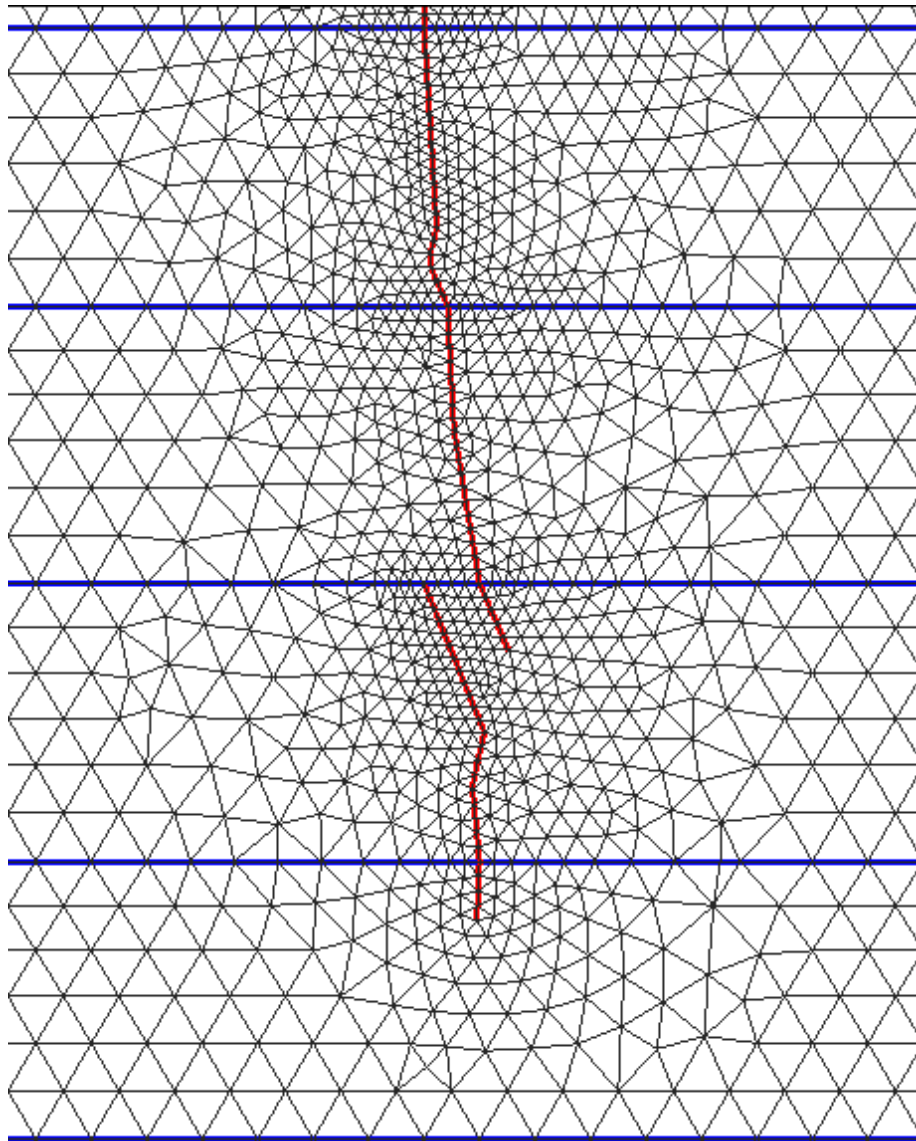
Figure 6.4.15: Branch 4 MPa case, 12.2s
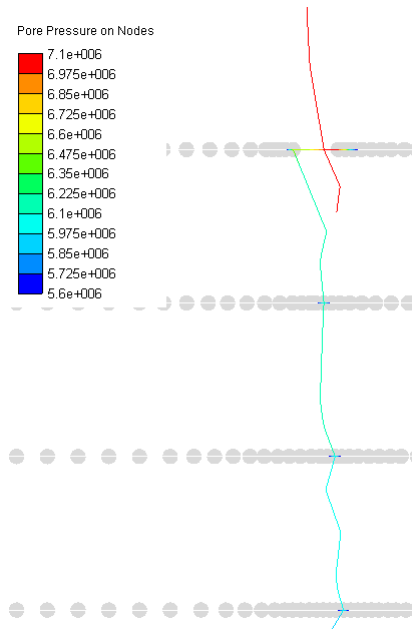
Figure 6.4.16: Branch 4 MPa case Fluid Pressure, 12.8 s

6.4.2 Fracture Reorientation

The principal aim of these simulations were to assess the impact of introducing natural fractures to the fracture reorientation examples in chapter 5. These simulations can only be expected to provide a representation of what may occur under some very specific natural fracture conditions. Chapter 2 describes the varied conditions that can lead to natural fractures, showing that the potential variation of parameters describing each natural fracture set is enormous, and a comprehensive study is beyond the scope of this work. Nevertheless, the interaction of a reorienting fracture with a natural fracture set of some description is of interest.

The permeability assigned to the natural fractures is the same value used for "intermediate" permeability in other simulations in this chapter - case B in Table 6.2. In simulations propagating a hydraulic fracture perpendicular to natural fractures (e.g. see 6.4.1), this value was found to allow the fractures to take on fluid without arresting the hydraulic fracture flow. In these examples, this was still the case, although the natural fractures significantly affected the fracture path. A key difference between these simulations and the vertical fracture propagation examples in 6.4.1 is the minimum horizontal stress, which was 4 MPa in these simulations and 4.9 MPa in 6.4.1. The maximum horizontal stress was 5 MPa in both cases.

Single Natural Fracture Set Figure 6.3.19 shows that the fracture path has not reoriented to the vertical orientation expected. Observing the propagation of the hydraulic fracture through the field of natural fractures yields some interesting discussion points. One such point of interest occurs when the right hand wing begins an arc towards the maximum principal stress direction, and encounters a natural fracture whilst oriented perpendicular to it. A detail from this simulation at time 36 s shows this about to occur in an LIC plot (Figure 7.3.6). The position and orientation of the natural fracture is marked in red, and it can be observed that the principal stresses are orthogonal to the natural fracture when the hydraulic fracture approaches.
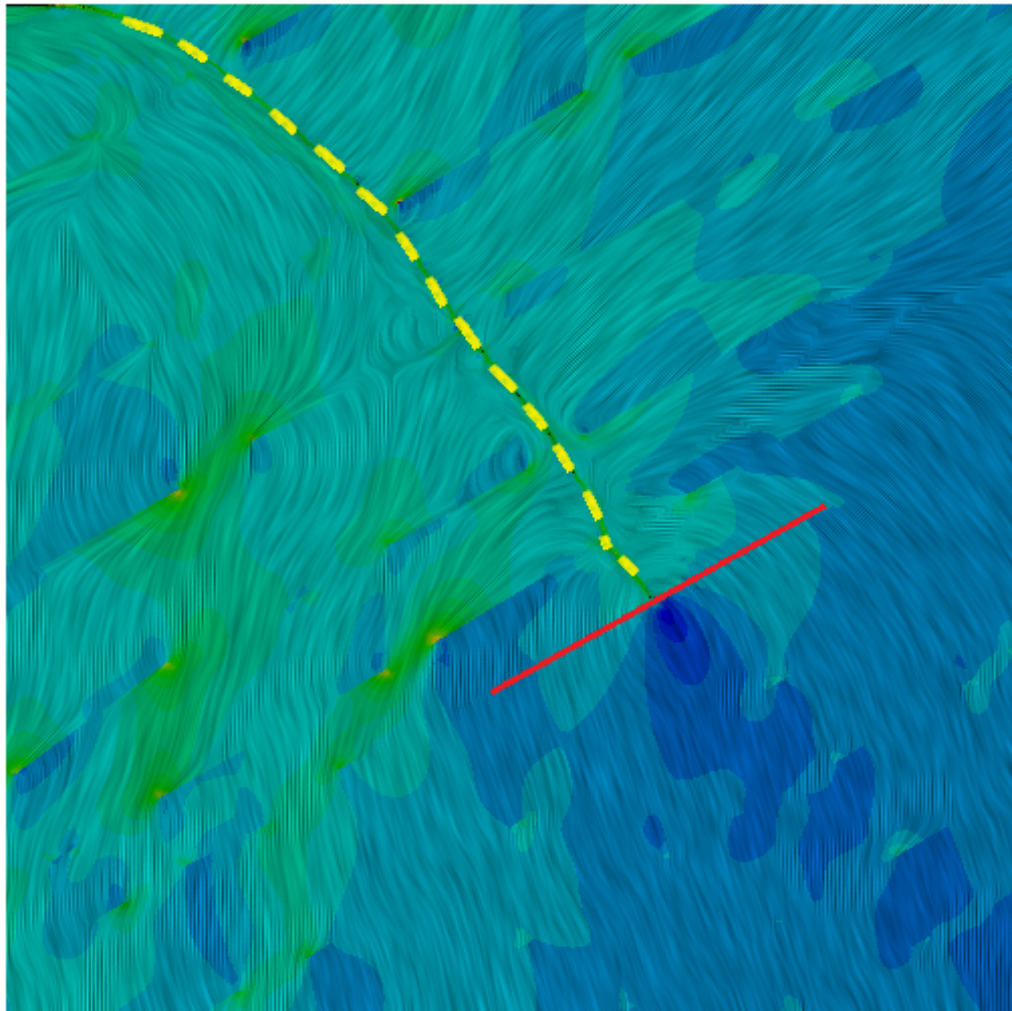
Figure 6.4.17: LIC plot- Hydraulic Fracture Arrest
The hydraulic fracture path is indicated with dotted yellow lines, and the natural fracture with a solid red line.

The hydraulic fracture does not cross the natural fracture, although it is approaching at 90° and the natural fracture has the same high friction and cohesion parameters to prevent slip

as the vertical propagation simulations in 6.4.1. Examination of contact markers on the interface confirm that the natural fracture fills with fluid and opens, rather than slipping due to frictional forces being overcome. Figure 6.3.21 plots the fluid pressure at the injection point through time, which at the time of contact with the natural fracture is 5.8 MPa. The detail of fluid pressure history in the vertical propagation examples 6.3.10 shows that those fractures were growing at a higher pressure, which is consistent with the lower horizontal stress in this simulation.

This suggests that the propagation pressure was unable to create a high enough tensile stress on the opposite side of the natural fracture to fracture it before fluid pressure could open the natural fracture. Examination of the failure factor variable shows that an element did fail on the opposite side of the natural fracture, however this is not a large enough number of elements to trigger fracture insertion (see section 3.6.2). This is an interesting result when considered in the context of chapter 4, in which the treatment method focused on reducing stress anisotropy by *increasing* the minimum horizontal stress σ_{Hmin}. The higher propagation pressure brought about by a higher σ_{Hmin}, whilst reducing anisotropy, can increase the likelyhood of natural fracture crossing.

Once the natural fracture has opened, it is flooded with fluid quickly and fracture propagation continues, providing another point of interest when it exits the natural fracture. Being filled with fluid, the interface parameters are irrelevant, and the fracture will support no shear stress along its length. Figure 6.4.18 is the same area as Figure 6.4.17 at a later point in time. It shows the stress state immediately prior to the hydraulic fracture exiting the natural fracture.
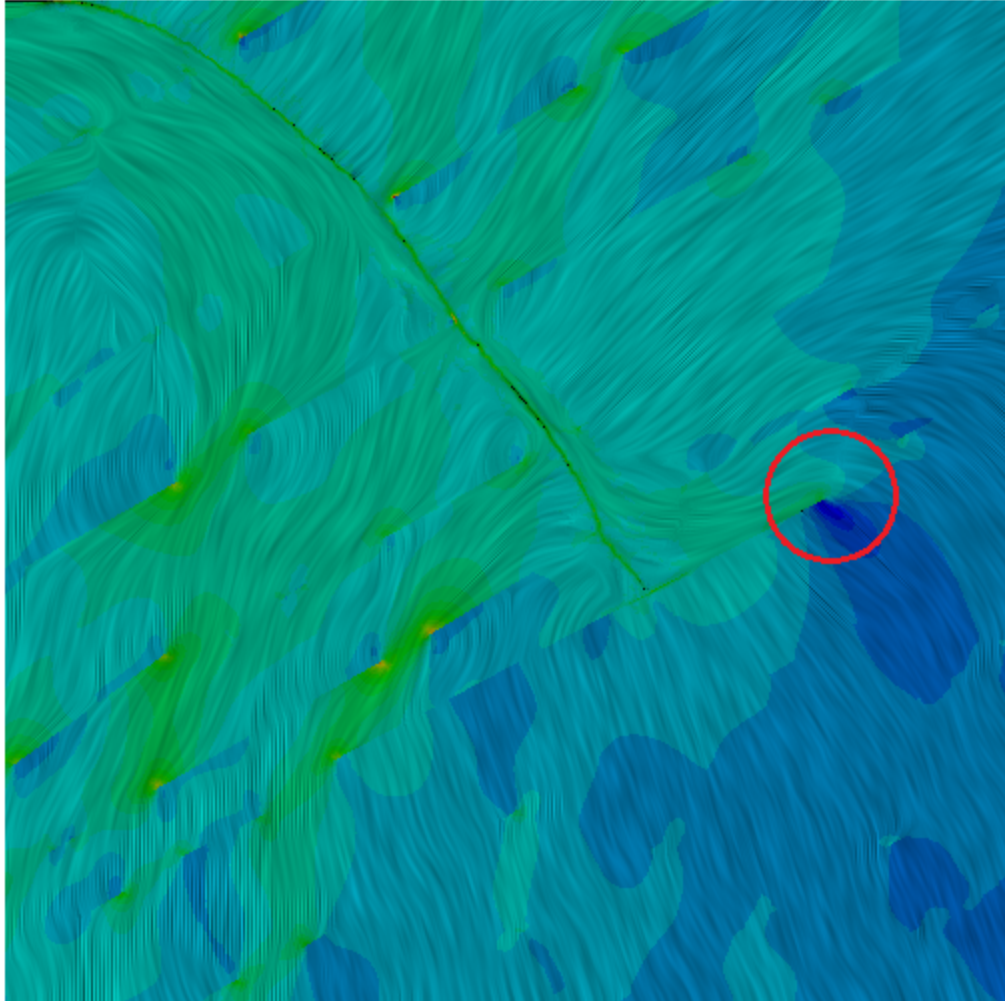
Figure 6.4.18: LIC plot- Hydraulic Fracture Exit

The tip of the natural fracture is circled, and the stress discontinuity that the natural fracture creates once filled is apparent. The difference in stress states on either side of the natural fracture gives rise to a tensile force which is acting on one side of the natural fracture only. The result is that the hydraulic fracture exits the natural fracture at a sharp angle, without the gradual reorientation simulations in chapter 5. This process of being arrested by the next natural fracture encountered, filling it and propagating at a sharp angle continues. The combination of downward exits and travelling up the slope of the natural fractures results in a net horizontal propagation of the right hand wing. The left hand wing exits the natural fractures horizontally, and travels down the slope of the natural fractures. Overall, the expected reorientation to vertical propagation does not occur.

Two Natural Fracture Sets   The net path taken by the hydraulic fracture in this example approaches the vertical orientation suggested by the in-situ stress field more closely than

the single set case (see Figure 6.3.20).

A point of interest in this simulation is the propagation direction of the new fracture segments, which do not appear to "try" to curve towards the vertical after exiting the natural fractures used as conduits (which are opened). This appears to be due to intersection angle of the hydraulic fracture with the natural fracture. Figure 6.4.19 shows a detail of the right hand wing of the fracture path, with a section of new hydraulic fracture geometry marked with a blue ellipse.
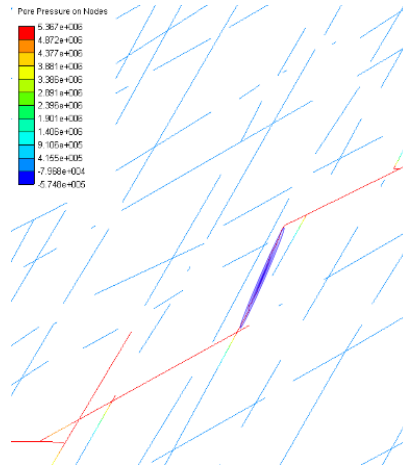
Figure 6.4.19: Fluid Pressure - Two NF Sets

Two figures illustrate the process that has occurred. In Figures 6.4.20 and 6.4.21, principal stress tensors are overlaid on the fracture geometry. Note that the tensors are coloured according to Elfen convention, which is that the most compressive stress direction is coloured blue. In Figure 6.4.20, the direction of σ_{Hmax} is quite varied. On the central natural fracture itself the stress is normal to the fracture, while to the left it is oriented diagonally left, and on the right is for the most part vertical. Also of interest, in the region between two natural fractures, marked in a blue circle, σ_{Hmax} is aligned tangentially to those fractures. The mechanics behind this stress state require closer investigation. The fracture central to the green circle is opened after fluid propagates through the connected fracture.
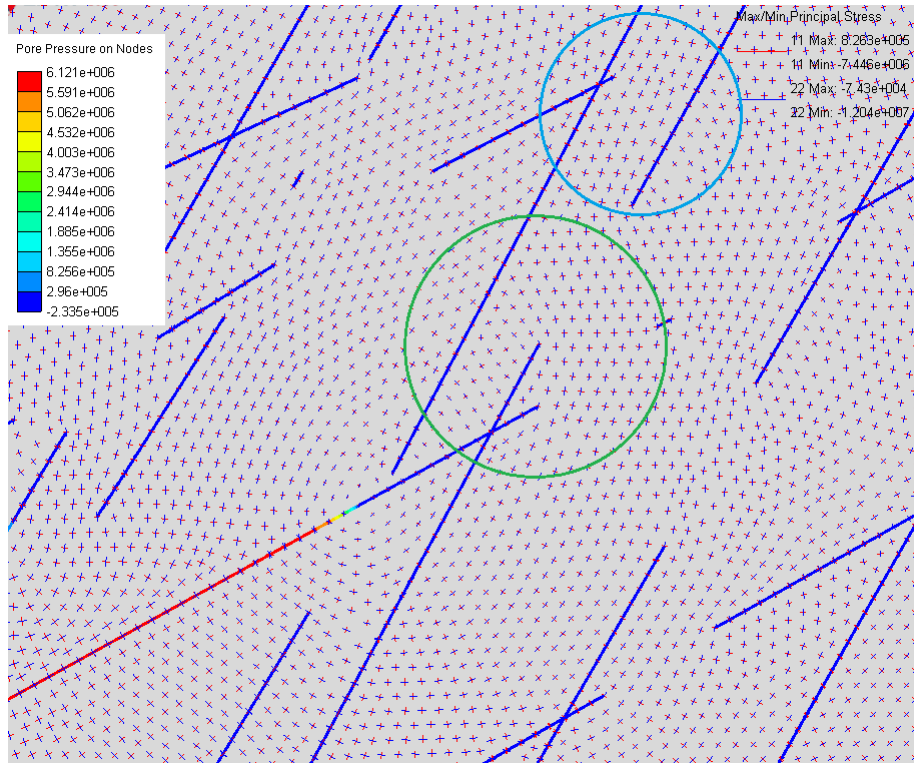
Figure 6.4.20: Fracture Insertion, Two NF Sets, 16s
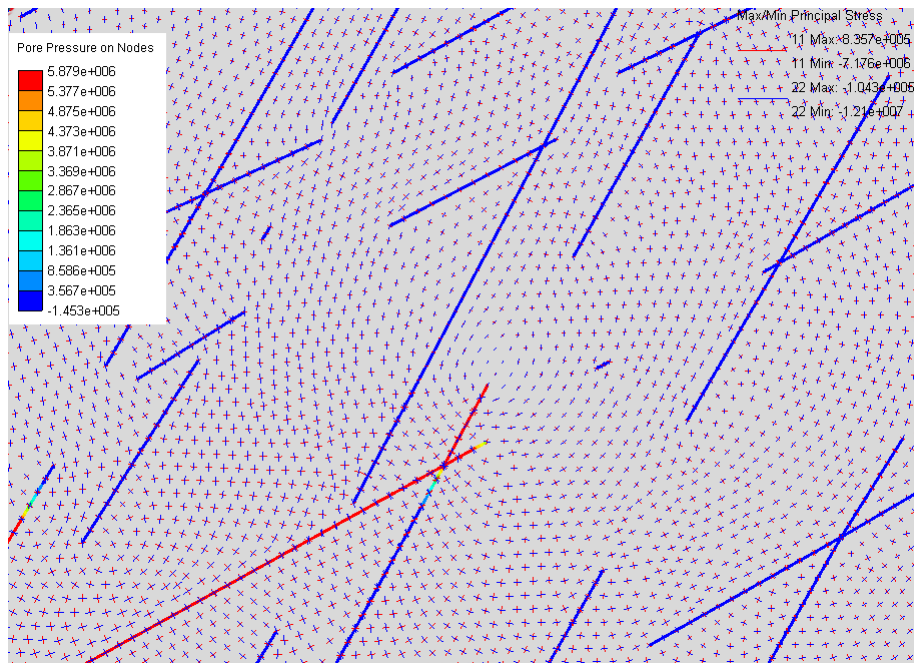
Figure 6.4.21: Fracture Insertion, Two NF Sets, 20s

Figure 6.4.21 shows the stress state after this fracture has opened; a recognisable, rela-

tively symmetric pattern about the tip can be seen. This is due to the fracture being able to open more symmetrically on both sides of the opened tip. Figure 6.4.22 compares a T shape intersection at 90° case A (such as that examined in the single fracture set above) with an inclined intersection case B. In the first case, the lower material on the lower side of the horizontal fracture is unconstrained by pressure from the vertical fracture, but the upper half is being compressed by fluid pressure in the vertical fracture. In case B, the material on the upper right hand side of the horizontal fracture is less constrained by the pressure from the inclined fracture, and will be easier to open than the left hand side. This results in a stress pattern around the horizontal fracture which is similar to a horizontal fracture opening in isolation, which in turn orients the principal stresses ahead of it towards the horizontal. This mechanism appears to be the cause of the stress rotations apparent in Figure 6.4.21, which result in the fracture travelling parallel to the natural fracture set.
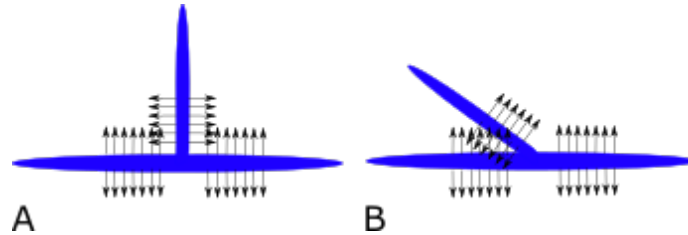
Figure 6.4.22: Intersection Angle Impact on Opening Preference

It is also worth noting that failure of the bond between fractures outside the stimulated fracture (due to shear stress) was observed, and that this will have further altered the stress field.

Figure 6.3.21 shows the fluid pressure required to propagate the fracture in both cases. It is apparent that more energy was required to propagate through the single fracture set than the two set case. This is probably due to a combination of factors. The first is that the second fracture set was more closely aligned with the in-situ σ_{Hmax}, so less fluid pressure would be required to open those fractures if contacted by the hydraulic fracture. The second is that the variety of intersections available to the hydraulic fracture is higher in the two set case, which increases the chance of one of those intersections being preferable. In both cases, the propagation pressure was less smooth than seen in single fracture examples. This is presumed to be due to fluid travelling through a natural fracture until coming to an impediment, which requires higher fluid pressure to continue propagation. Impediments could be a smaller fracture at an obtuse angle to the current principal stress direction, and/or unfavourable stress magnitudes or directions ahead of the fracture tip.

6.4.3 Impact of Shear Stress

Immediately obvious in Figure 6.3.22 is that the hydraulic fracture made contact with the natural fracture sets, and used them as conduits owing to their high permeability. The horizontal stress anisotropy was relatively unchanged in the space between the natural fractures, and the fracture continued vertically on exiting each natural fracture. Figure 6.3.26, an LIC plot of the stress field at 31s, shows the vertical sections between the natural fractures ahead of each fracture tip. While it has already been seen that a snapshot of the stress state is not necessarily indicative of the future path of a fracture (e.g. in chapter 4), in this case the fracture did travel in the vertical direction.

The hydraulic fracture contacted the natural fractures on the top right and bottom left of the model, which appears to be related to the way the shear stress interacts with the natural fractures. Considering the upper part of the fracture prior to contact with the natural fractures, on the right hand side the maximum principal stress aligns tangentially to the natural fractures. Conversely, on the left hand side, the stresses have rotated to be normal to the natural fractures. Figure 6.4.23 is an LIC plot of the principal stress field at 31s demonstrating this. This shows the area between coordinates 488-511m in X, and 507-530 in Y (the origin being the bottom left corner of the model). Since the sign of the shear stress is reversed on each side of the hydraulic fracture, it follows that the rotation of principal stresses will be towards the alignment of the natural fractures on one side, and away from them on the other. The effect is also visible in an LIC plot of a larger area, in 6.3.26.
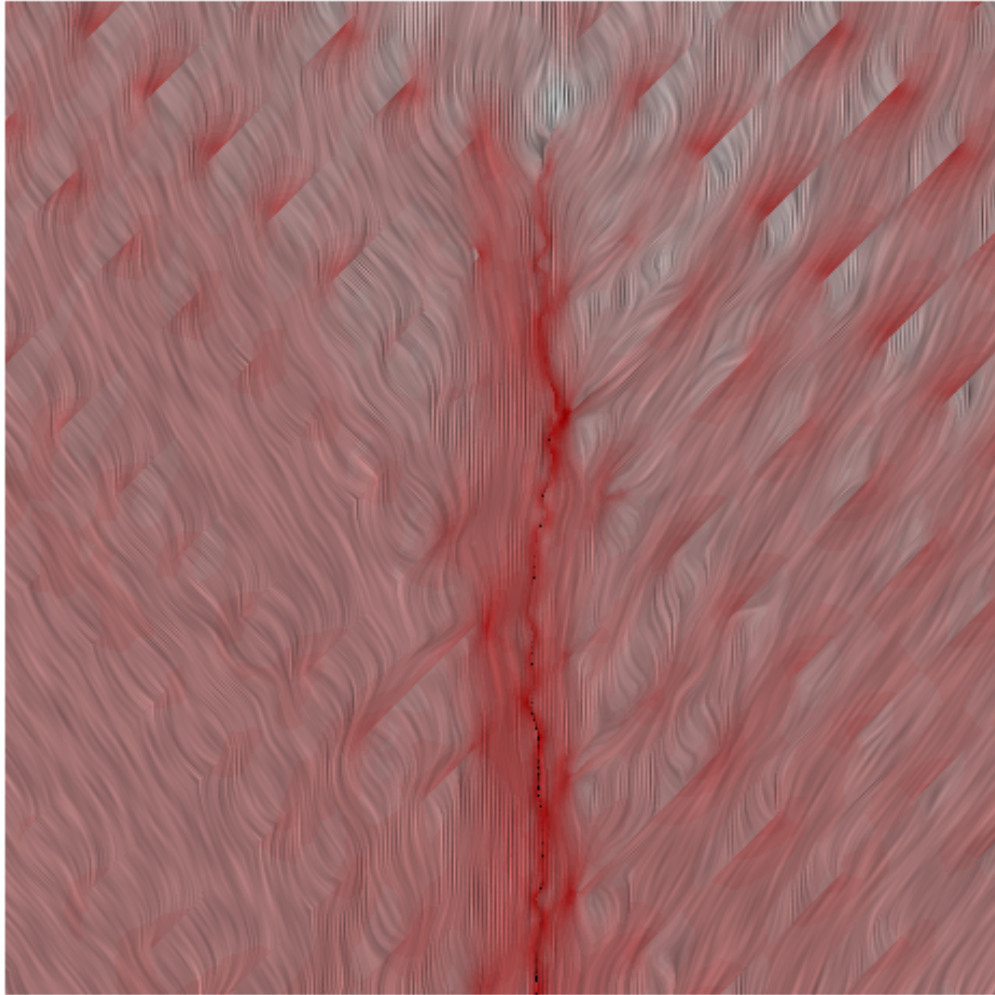
Figure 6.4.23: Principal stress field at 31 s

As noted above, and seen elsewhere in this chapter, once contacted by the hydraulic fracture, the alignment of the natural fractures can have a large influence on the fracture path. In relation to interface friction, the prospect of the fracture crossing a natural fracture is very low due to the angle the hydraulic fracture makes with the natural fracture. Using Figure 6.1.3 as a guide, this example has an effective principal stress ratio of 1.667, requiring a frictional coefficient above 0.8 to cross.

Figures 6.3.27 and 6.3.28 are of interest because they point out potential difficulties in interpreting microseismic data from the field. Considering Figure 6.3.27, at this point the hydraulic fracture has had no direct interaction with the natural fractures. Microseismic events triggered by the shear stress zone indicate tensile failure at the tips of several natural fractures extending some distance from the hydraulic fracture - up to 17m in the zones of positive τ_{xy} (top left and lower right), and 10m in the zones of negative τ_{xy}. A detail of some microseismic data is shown in Figure 6.4.24, with the microseismic event

representations generated up until that point in time displayed concurrently.
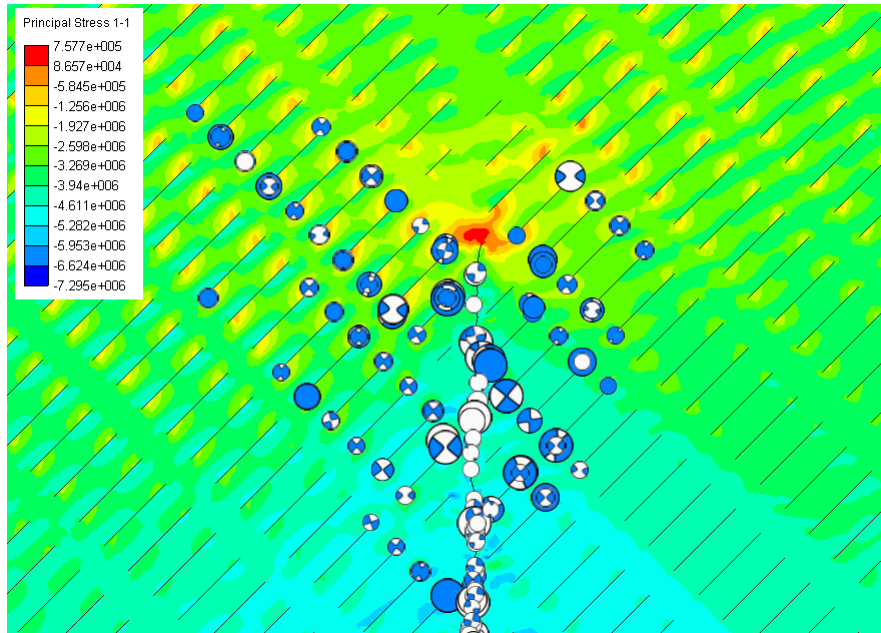
Figure 6.4.24: Microseismic Events and Most Tensile Principal Stress

It is possible that the microseismic data captured would give the impression that a complex, connected fracture network has been created in the example above, in contrast to the single planar fracture that is the reality. A similar phenomenon was observed in Taleghani and Olson (2013); they show reactivation of natural fractures which are close to but not in communication with the hydraulic fracture. They observe that this reactivation would generate microseismic events, and that shearing could increase the natural fracture permeability. These simulations have shown that an addition to shearing, the shear stresses can induce tensile failure in the natural fractures.

6.4.4 Summary

Natural fractures are likely to be present in most shales in the field, and are critical to the development of complex fracture networks. This chapter set out to examine the effects of natural fractures on hydraulic fracture propagation, beginning with very structured simulations. The impact of natural fracture permeability and interface properties were studied. Fracture reorientation within arbitrary natural fracture sets was compared with earlier examples in a homogeneous medium. The potential effect of shear stress zones around a propagating fracture on nearby natural fractures was found to be significant.

Permeability variation simulations were run to establish a suitable intermediate permeability to use in subsequent simulations. Two values were selected, each of which showed some characteristics of the high and low permeability cases. The value used for the majority of later simulations was 1.7 E^{-10}m^2.

Fracture interface properties using the intermediate permeability were able to show hydraulic fracture branching by removing cohesion but retaining a high friction coefficient. Frictionless interfaces without cohesion arrested the hydraulic fracture as expected. A comparison between this result and a strong but highly permeable interface showed that the frictionless example initiated at a lower fluid pressure due to a reduced lateral stiffness. The permeability of the interfaces affected the time taken and pressure required to exit the natural fracture.

The isolation of fracturing fluid was observed, and could provide a mechanism for fracturing fluid leakoff. Further simulations to investigate whether this fluid returns to the hydraulic fracture when the pumped fluid pressure is reduced would be of some interest.

Limited investigations into the effect of stress anisotropy showed the expected behaviour in terms of initiation and propagation fluid pressure, although the creation of an offset fracture resulted in an unsymmetric fracture in the medium anisotropy case. Similarly to the example showing branched fracturing in section 6.4.1, the exact cause of the offset fracture requires more detailed analysis, with higher frequency output. In both simulations, the hydraulic fracture continued propagating vertically through the natural fractures.

Fracture reorientation simulation results suggest that permeability should be taken into account in defining a crossing criterion, such as that in Gu et al. (2011). Fluid filling a high permeability natural fracture can dilate it and remove the impact of interface properties before they are able to transfer stress across the interface.

A consequence of reducing stress anisotropy via treatments such as described in Soliman et al. (2010) was shown to be an increase in propagation pressure. This can in turn increase the likelihood of a hydraulic fracture crossing a natural fracture, working against the stated aim of increasing fracture complexity. The importance of being able to model dynamic interaction between fluid and mechanics was demonstrated, in particular in showing the importance of the interaction angle between hydraulic fracture and natural fracture. This was observed to affect the way in which the natural fracture dilated, and the subsequent effect on the propagation direction on exiting the natural fracture. A comparison of the two simulations found that propagation pressure was lower in the two set example, primarily due to the second fracture set being more aligned with σ_{Hmax}.

Chapter 5 showed that in single fracture experiments, stress reorientation was dominated by the amount of stress anisotropy, and the length and orientation of the fracture. Smooth

fracture paths which began in the direction of the original fracture invariably resulted, with sharp reorientations predicted only under very high stress differentials (Figure 5.3.7 and equation 5.4.4). These simulations highlighted that the complexity introduced to the stress field by natural fractures can result in outcomes radically different than the predictions made by single fracture models. In particular, sharp exits from the ends of natural fractures were observed.

Future work could include detailed studies of fracture fluid isolation. In particular, whether the fluid remains sealed after the well pressure is reduced. A better understanding of branching could be obtained by setting up targeted simulations. The interface angle between hydraulic and natural fractures was shown on a qualitative basis to influence the dilation of the natural fracture, and quantification of the mechanism would be of benefit. The interface property simulations used extremes of each parameter; more moderate values could provide further insight into natural fracture reactivation behaviour.

Chapter 7

Shear Stress Reinforcement

7.1 Introduction

Chapter 6 highlighted in 6.4.3 the influence that shear stresses can have on unconnected natural fractures, including inducing tensile failure. Other works have noted that shear stress produced by an advancing hydraulic fracture can be favourable for enhancing fracture complexity, as it can debond natural fracture cementation, or induce permeability enhancing slip (Taleghani and Olson, 2013, Cheng, 2012).

Chapter 4 examined one method of influencing the stress state between fractures - direct modification of the relative magnitudes of the principal stresses directly. This chapter examines altering the stress state between fractures by using shear stresses to rotate the principal stresses.

The areas of strongest shear stress in a single propagating hydraulic fracture, in a homogeneous medium as examined throughout this work, are near and either side of the fracture tips. These can extend some distance from the fracture. As illustrated in 4.4.11, the propagation of fractures in treatment designs such as those in chapter 4 is such that these zones of shear stress act to cancel each other out if they are within range of each other.

By placing fractures so that their zones of shear stress can reinforce rather than mitigate each other, it may be possible to introduce larger changes in the stress state between fractures than methods such as the TTSM. This could be measured by principal stress rotation, or change in anisotropy ratio.

7.2 Methodology

Horizontal Well A single well was simulated, with 5 perforations being simultaneously exposed to the pumped fluid. Table 7.1 shows the parameters used for the initial simulation - these were broadly identical to those used in chapter 5, although more fluid was pumped to account for the larger number of fractures.

Inclined Well The well was inclined at 45° to the principal stress directions, with the dual aim of reducing stress shadowing effects, and allowing zones of similarly signed shear stresses to reinforce each other. The starter fractures were aligned with the maximum principal stress direction, so that any direction change of the fractures could be attributed to the stress change brought about by their propagation, rather than realignment to the in-situ stresses (as examined in Chapter 5). Aside from the well orientation, the simulation parameters were identical to the horizontal well. The perforations remained the same distance from each other along the well, making them closer to each other in the horizontal direction.

Parameter	Value	Unit
Young's Modulus	32	GPa
Poisson's Ratio	0.2	
Reservoir Pore Pressure	0	MPa
Effective Stress XX	4	MPa
Effective Stress YY	5	MPa
Effective Stress ZZ	5	MPa
Porosity	0.01	
Fracture Height (Layer thickness)	10	m
Initial Fracture Length	4	m
Fluid Volume	50	m^3
Flow Rate	0.1	$\frac{\mathrm{m}^3}{\mathrm{s}}$
Fluid Viscosity	1.67e-3	Pa.s
Perforation Spacing along wellbore	20	m

Table 7.1: Indicative Simulation Parameters

7.3 Results

Geometry   The geometry of the resulting fractures at 100 s are shown in figures 7.3.1 and 7.3.2 for the horizontal and inclined wells respectively. On each plot, a 10 m grid is shown for comparison of scale.
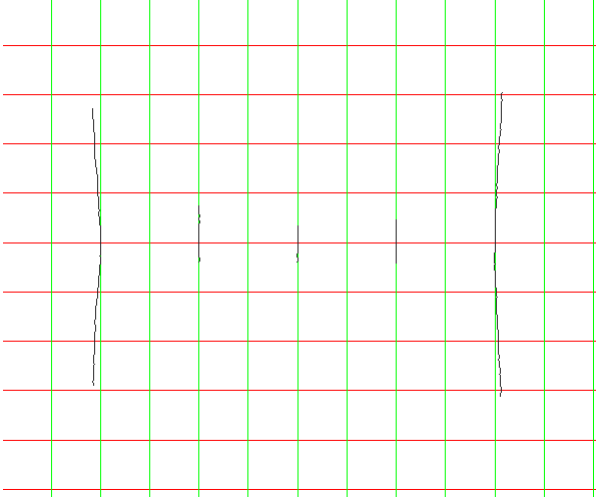
Figure 7.3.1: Horizontal Well, 100s
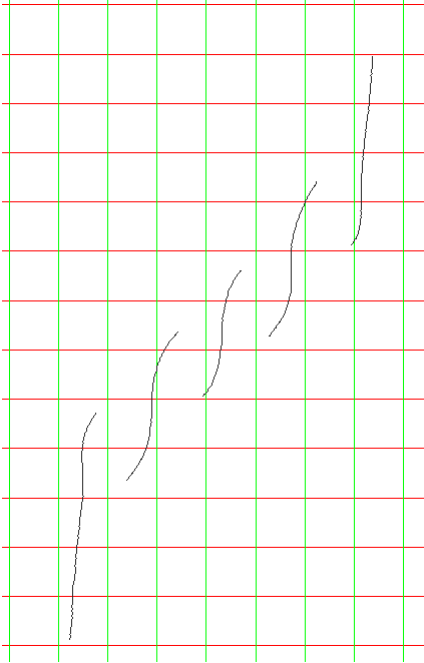
Figure 7.3.2: Inclined Well, 100s

Propagation Pressure   A comparison of the fluid pressure during the first 200s of both simulations is shown in Figure 7.3.3.
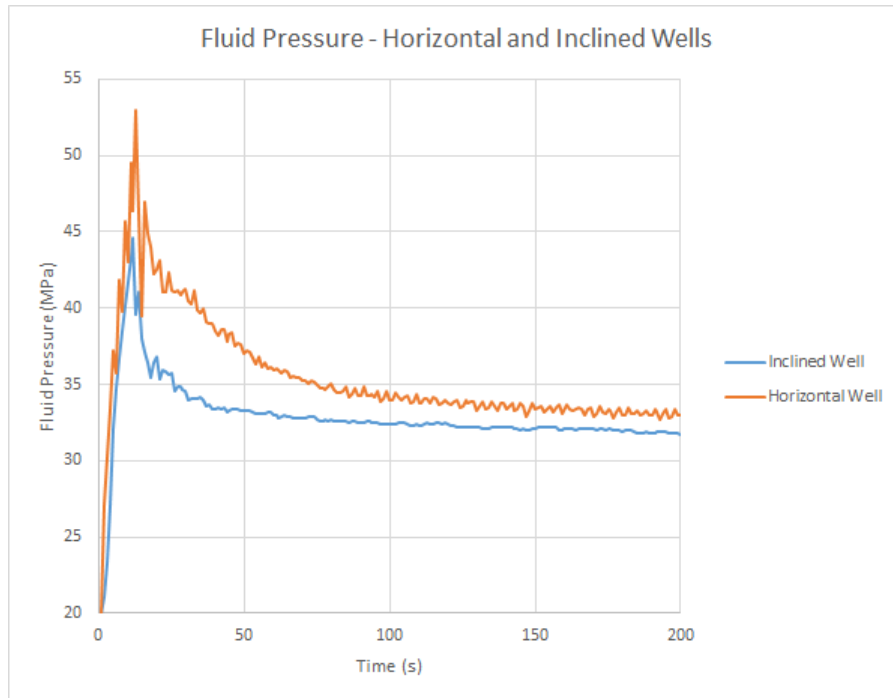
Figure 7.3.3: Fluid Pressure - Horizontal and Inclined Wells

Total Fracture Length   The length of hydraulic fracture over the entire simulation is shown (500s) in Figure 7.3.4.
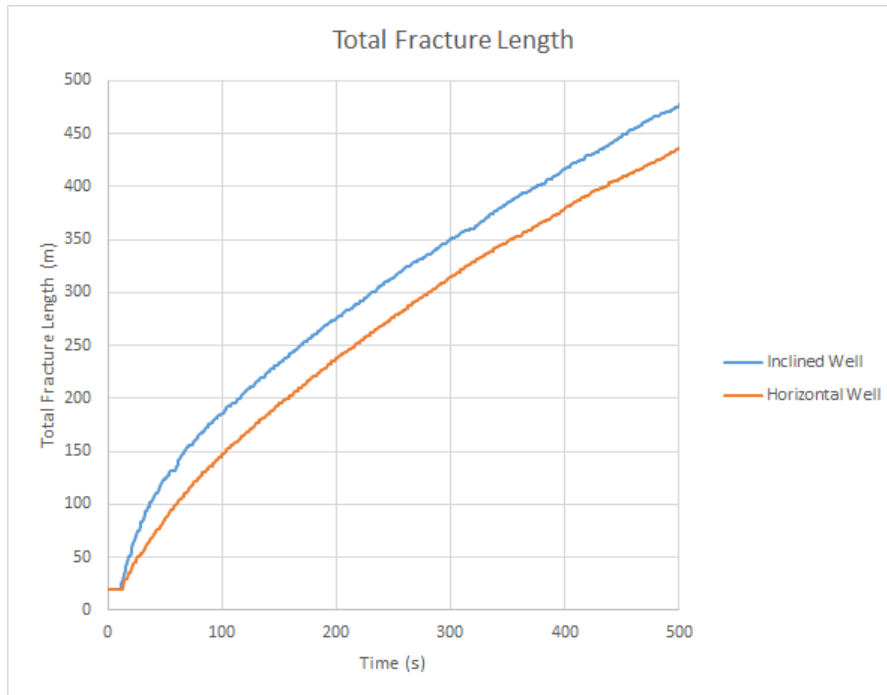
Figure 7.3.4: Total Fracture Length (m)

Stresses Figures 7.3.5 and 7.3.6 are LIC plots of the principal stress field for the inclined and horizontal wells, respectively. Both images are coloured according to the stress intensity σ_I (eqn 4.4.9).
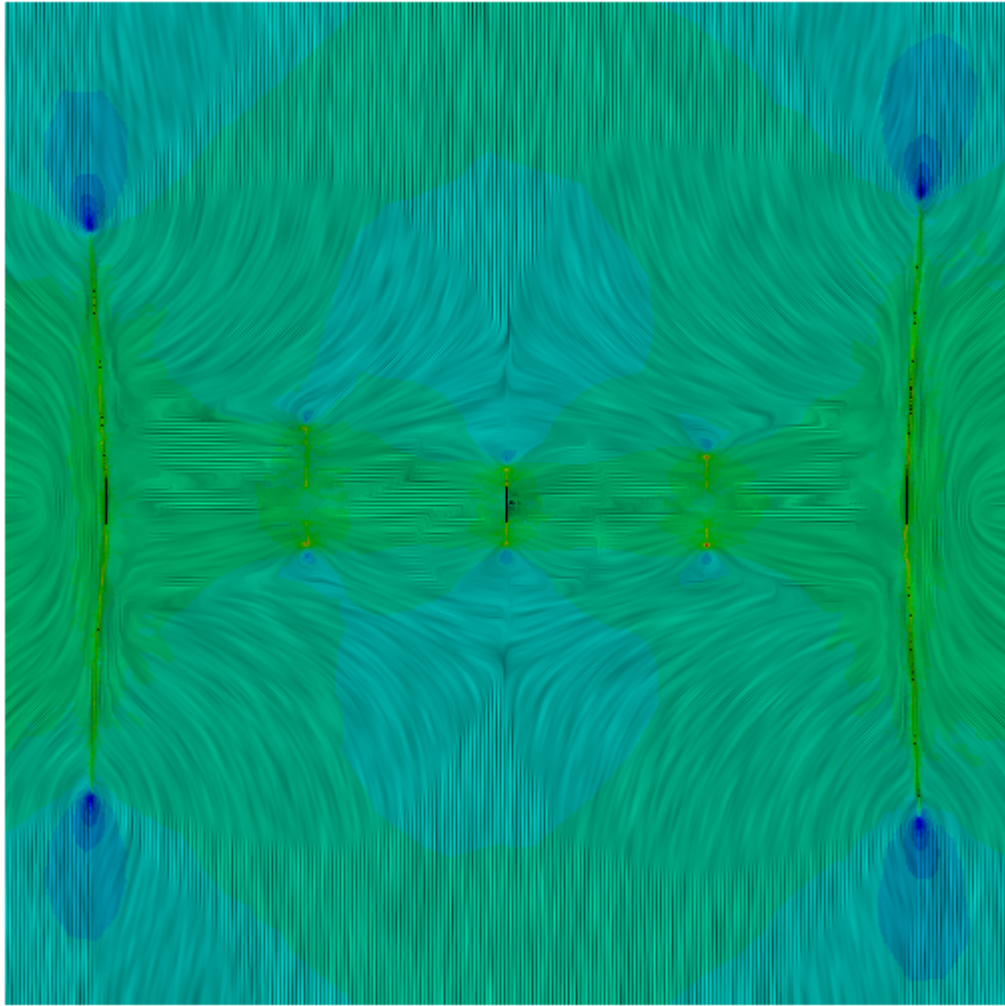
Figure 7.3.6: LIC plot - horizontal well

The stress anisotropy ratio $\frac{\sigma_{Hmin}}{\sigma_{Hmax}}$ is plotted for both wells in Figures 7.3.7 and 7.3.8.
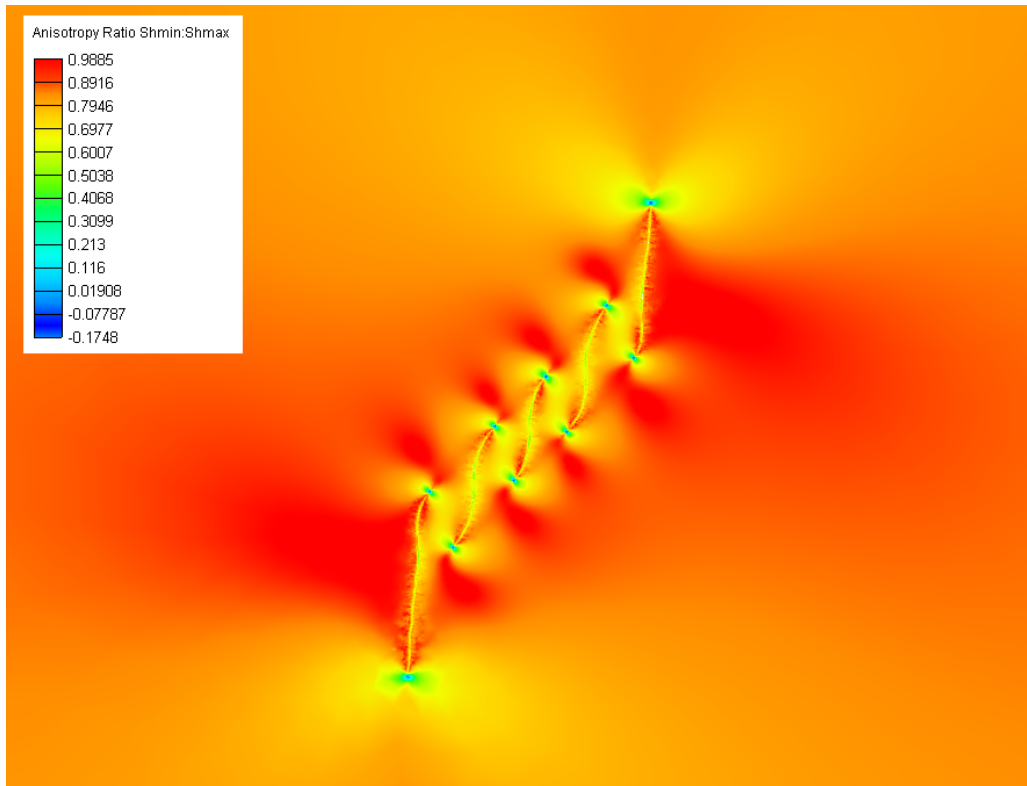
Figure 7.3.7: Stress Anisotropy, Inclined Well
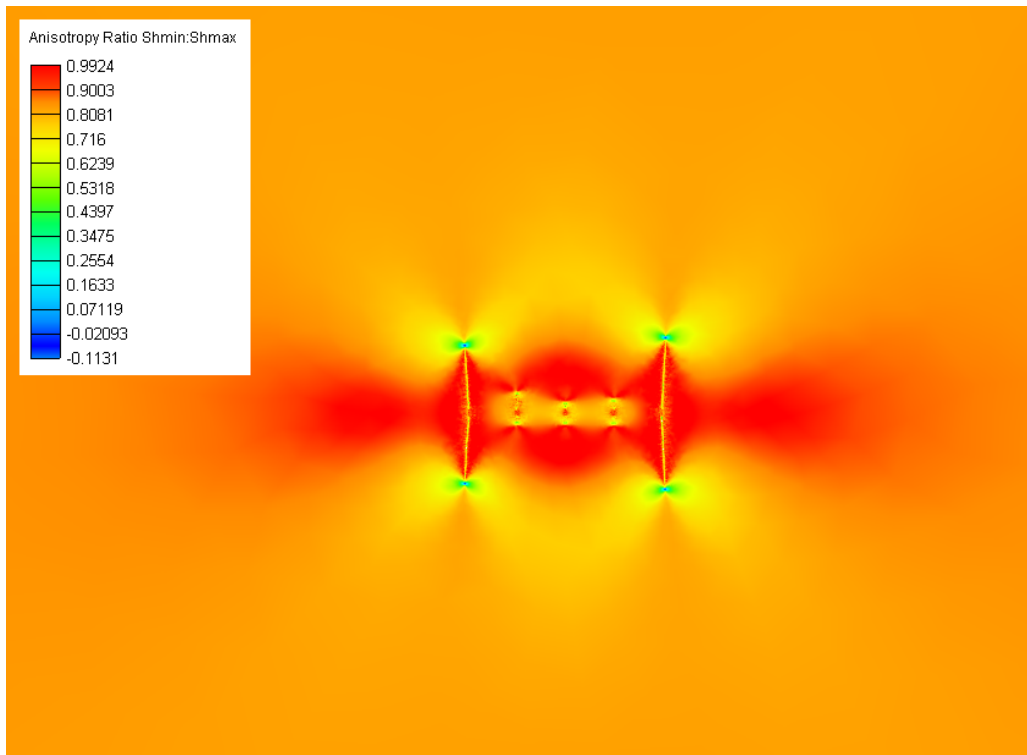
Figure 7.3.8: Stress Anisotropy, Horizontal Well

All of the above plots are at time=100 s.

7.4 Discussion

7.4.1 Geometry

The horizontal well geometry shows the classic signs of stress shadowing, which were expected in this simulation. As each starter fracture began to grow, the outer fractures were less constrained laterally on one side than the three interior fractures. The outer fractures grew preferentially from both wings, in turn further stunting the growth of the interior fractures. This pattern is clearly seen in Figure 7.3.1. Some curvature away from the interior can also be seen, although this is not particularly pronounced.

In contrast, at fracture initiation, the starter fractures of the inclined well were relatively unconstrained laterally. As they grew in length, the predicted shear reinforcement caused the interior fractures to curve towards each other.

That is not to say that the inclined well's interior fractures did not experience stress shadowing; they were effectively arrested once the tips became aligned vertically, and the outside fractures continued to grow one wing each preferentially. Figure 7.4.1 shows the geometry after 50 0s. It could be argued that from the geometric perspective an ideal treatment of this type would pump enough volume to take the interior fractures to the point of arrest, and stop there.

It is also worth noting that in these simulations, there was no fracture closure associated with the curvature of the fractures originating in the inclined well. This phenomenon was observed during fracture reorientation simulations, discussed in section 5.4.

These simulations were restricted to fracture growth only, and it follows that any predictions about impact on production are only able to be made qualitatively. A generalisation regarding Darcy flow from low permeability reservoirs into hydraulic fractures can be made, based on some previous simulations that are not presented elsewhere in this work. Figure 7.4.2 shows the pore pressure measured along lines at three positions in relation to a vertical fracture. The fracture was in a reservoir with 31 MPa pore pressure and a permeability of 5 nD. The production pressure was just above 8 MPa. Considering, for example, a region at which the pore pressure had dropped to 30 MPa, this formed a type of ellipse around the fracture, with the widest point at its midpoint, and its narrowest vertically above the upper tip. Figure 7.4.3 shows the pore pressure in the reservoir around the fracture after 4.5 years. For the most part the "ellipse" had straight sides, narrowing and becoming round at the tips.
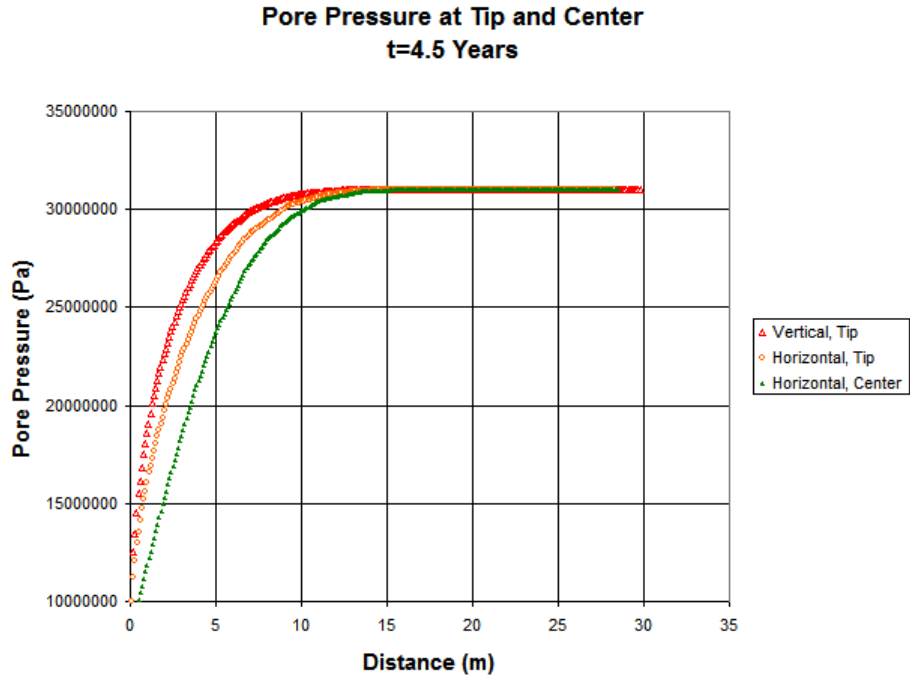
Figure 7.4.2: Darcy Flow into Vertical Fracture: Numerical solution at tip and center (5nD)

Allowing for some minor fluctuations in the elliptical region size (for curvature), the generalisation of this shape forming around each fracture can aid in discussing the merits of the inclined well for production. A fracture pattern such as that in Figure 7.3.2 could on the one hand provide a means of extracting more gas near the wellbore - at a distance dictated by the fracture curvature - in comparison to the horizontal well. On the other hand, this could be considered a constraint on the "reach" of the well into the reservoir.

Fracture length increased in the inclined example more quickly than the horizontal, continuing at the same rate once both sets of interior fractures had been arrested - see Figure 7.3.4. This is consistent with the interior fractures initially growing concurrently in the inclined example, while the horizontal well sees the interior fracture growth stunted early. Once the interior fractures in the inclined example are arrested, the rate of growth of the exterior wings is close in both examples.

Figure 7.4.1: Inclined Well Geometry at 500s

7.4.2 Propagation Pressure

Figure 7.3.3 demonstrates that a significantly higher pressure
was required to initiate fractures in the horizontal well than the
inclined well. This is due to stress shadowing - each starter fracture has to overcome
the additional lateral stress of the others to remain open. Similarly, the decline from initiation to propagation pressure was considerably slower for the horizontal well, and the
propagation pressure remained slightly higher throughout the simulation.

7.4.3 Stresses

The LIC plots in figures 7.3.5 and 7.3.6 show very clearly the difference in stress orientation between the two examples. The stress field of the horizontal well is typical of a stress
shadowed example; between the fractures the dominant principal stress direction has become horizontal, and ahead of the stunted interior fractures, there are areas of rotation
which are due to the shear stress around the tips of the outer fractures. As discussed in
Chapter 4, this mode of stress magnitude change occurs via the lateral stresses directly
increasing σ_{xx} until it becomes σ_{Hmax}.

The interior fractures originating from the inclined well have caused the stress field to
rotate significantly between them. Along the direction of the well, the principal stresses
are aligned with the well direction. This is nothing to do with interaction with a physical
well; the pipe elements representing the well are not part of the mechanical simulation.
Whether this is a positive outcome is debatable, since this stress field manipulation may
encourage any future fractures from the well to propagate parallel to the well. It could also
be argued that since this treatment allows closer initial spacing than the horizontal case,
additional fracturing may between the initial fractures may not be required. Also, once the
fractures are propped, the stress field changes may be mitigated by reduced apertures.

Shear stresses have probably been introduced around the well, which would warrant further investigation with wellbore scale modelling. On the other hand, bearing in mind the
results from Chapter 6, the higher level of shear stress experienced in those zones could
have increased connectivity of natural fractures, or caused the unbonding of cementation
in sealed fractures, both potentially permeability enhancing effects.

Both figures 7.3.7 and 7.3.8 show the stress anisotropy ratio, $\frac{\sigma_{Hmin}}{\sigma_{Hmax}}$. The far field value
is of 0.833. The results highlight the unsuitability of the metrics discussed in 4 for this
application. In that chapter, the metrics rank anisotropy values nearer to 1.0 above others
- in fact ignoring values below the far-field value. This is due in part to an isotropic stress
state being considered favourable to a highly anisotropic in the TTSM (Soliman et al.

(2010)). Also, the mechanism through which the TTSM modifies the stresses can only act in one direction - to increase the minimum horizontal stress. Increasing this past the previous maximum horizontal stress by a large enough value to reduce the stress anisotropy ratio appears to be difficult, at least under the conditions simulated in this work. A more useful metric to compare these two cases would probably use the change in stress anisotropy.

The anisotropy change is plotted for both simulations in figures 7.4.4 and 7.4.5. The values shown are simply

$$\delta\sigma_\triangle = \left| \frac{\sigma_{11,0}}{\sigma_{22,0}} - \frac{\sigma_{11,t}}{\sigma_{22,t}} \right| \tag{7.4.1}$$

where the change in stress anisotropy, $\delta\sigma_\triangle$ is plotted for values 0.1 and above. This does show larger regions between the fractures, near the wellbore, in the inclined case. These plots are interesting to compare to the LIC information, since the value is indicative of the relative stress magnitude change rather than the orientation.
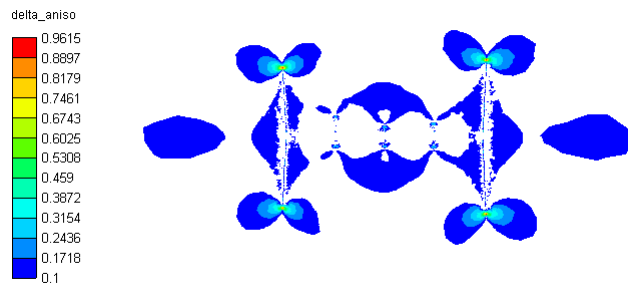
Figure 7.4.4: Change in Stress Anisotropy, Horizontal Well
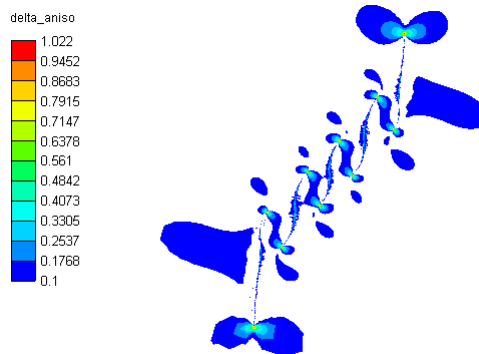
Figure 7.4.5: Change in Stress Anisotropy, Inclined Well

The LIC plots highlight a failing of this metric; it can be seen in Figure 7.3.6 that the principal stress directions have reversed along the direction of the horizontal well, yet this

area is not represented in Figure 7.4.4. This shows that although the directions have reversed, the ratio between them remains close to the original value of 0.833. A better method of measuring the change in stress state should probably consider orientation as well as magnitude. One visual method of doing this would be to contour the LIC plots according to anisotropy ratio change.

7.4.4   Other Alternative Treatments

Alternative fracture treatments such as the TTSM aim to use the mechanical interactions between fractures to ultimately enhance production, or increase operator efficiency. Waters et al. (2009) proposed one such treatment, known as the zipper-frac method. This involves the stimulation of multiple lateral wells, in sequential but alternate stages, as illustrated in Figure 7.4.6. Sequential stimulation would fracture Well1 heel to toe, followed by Well2. In zipper fracturing, while one well is being prepared for fracturing by setting a plug and perforating the wellbore, the other lateral is being stimulated. This operation can be conducted efficiently from one drilling pad.

Rafiee et al. (2012) proposed a modification to the zipper-frac method, by staggering the stages in each of the lateral wells so that each fracture propagating from one well is between two fracture from the other, in a similar manner to the TTSM, but without the operational issues involved in repeatedly moving the stimulation cluster.
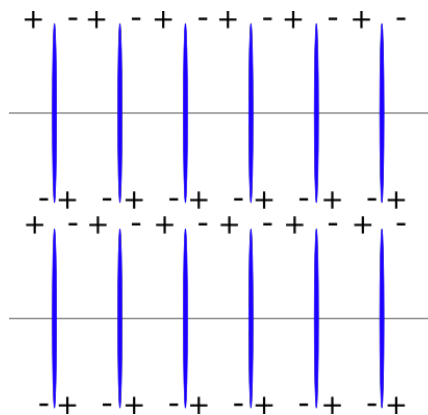
Figure 7.4.7: Shear Stress Cartoon, Zipper Fracturing
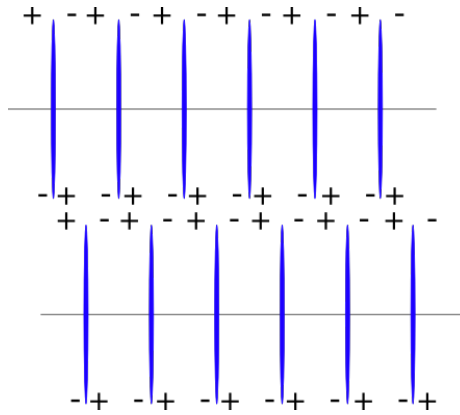
Figure 7.4.8: Shear Stress Cartoon, Alternate Zipper Fracturing

The zipper method places the shear zones of each fracture such that they act to mitigate each other, as illustrated in Figure 7.4.7. Alternate zipper fracturing, on the other hand, should allow shear stresses from the each lateral to reinforce the fracture from the other, illustrated in Figure 7.4.8. However, in both treatments, within each lateral the shear stresses of the adjacent fractures are working against each other, and if stimulated simultaneously as proposed in Rafiee et al. (2012), subject to constraints on spacing due to stress shadowing. Qiu et al. (2015) point out the difficulty that stress shadowing effects can act to reduce stress anisotropy, and thus supposedly enhance fracture complexity, whilst also acting to stabilise natural fractures - which acts against fracture complexity. Studying the behaviour of these and other alternative treatments with Elfen TGR, and in particular in the presence of natural fracture systems could provide insight into the particular strengths and weaknesses of these treatments.

7.4.5 Summary

The simultaneous stimulation of a well inclined at an angle of 45° to the maximum principal stress direction was compared to that of a horizontal well. Fracture spacing was such that in the horizontal well, significant stress shadowing was observed, resulting in a region between the two outer fractures which was relatively inaccessible to the hydraulic fractures. The fractures originating in the inclined well did not experience the negative effects of stress shadowing until later in the simulation. During that time, the fractures propagated evenly, and owing to the reinforcement of the shear stress zones ahead of each fracture tip, curved significantly until lateral to the wellbore. Once the fracture tips were aligned vertically, stress shadowing effects dominated the interior fractures, and the exterior fractures propagated preferentially. It was proposed that future evaluations of the treatment design would pump enough fluid to reach this point, providing a region of

uniformly stimulated reservoir around the wellbore. In comparison to the horizontal well, the stress shadowing effect was reduced, and the fractures initiated and propagated at a lower fluid pressure.

The interaction of the shear stresses was by design, and as well as altering the fracture directions, is likely to have caused significant damage to cemented natural fractures nearby, based on results from the previous chapter, in section 6.4.3. Including natural fractures in future simulations would be of particular interest. Utilising the shear reinforcement as a pre-treatment to reactivate or debond natural fractures before a further treatment for production could be of benefit. Simulation of production from the generated fracture geometry would allow quantitative evaluation of the production benefits (or otherwise) of such a treatment.
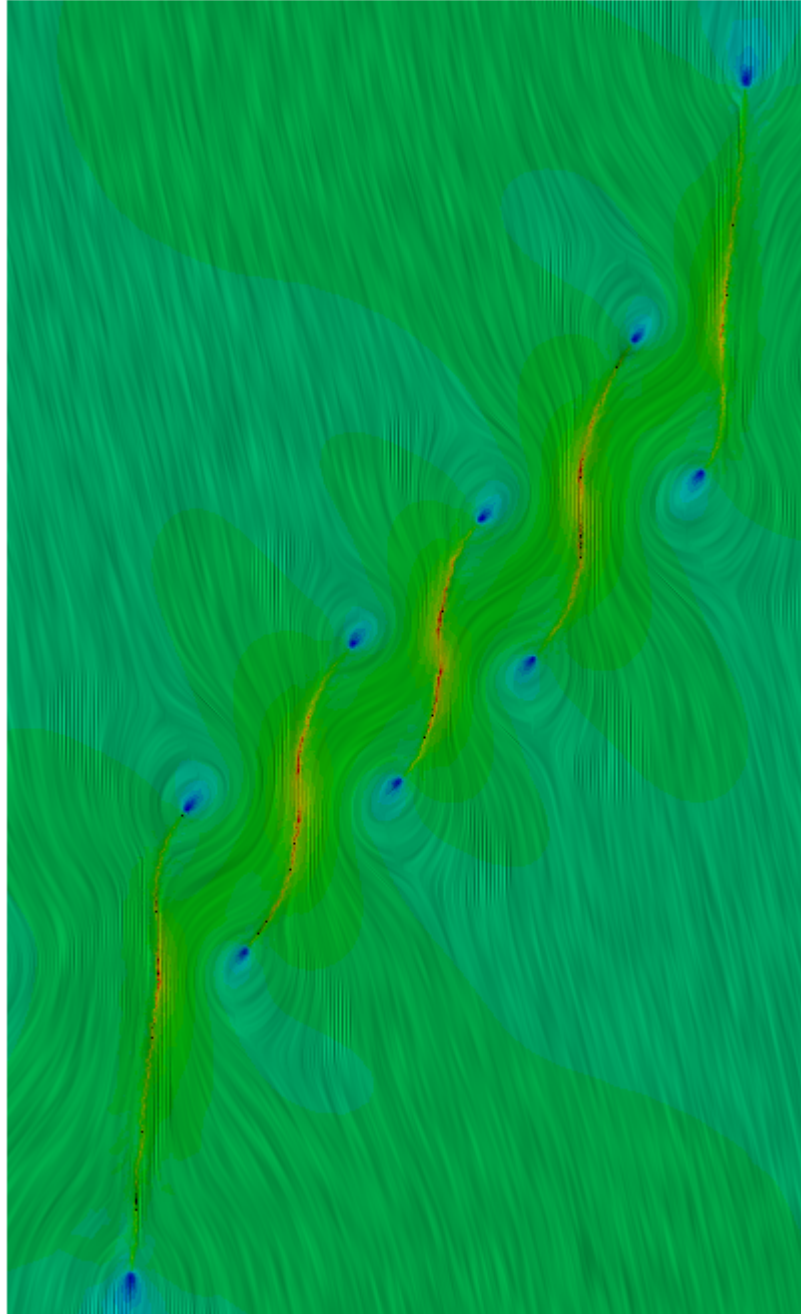
Figure 7.3.5: LIC plot - inclined well
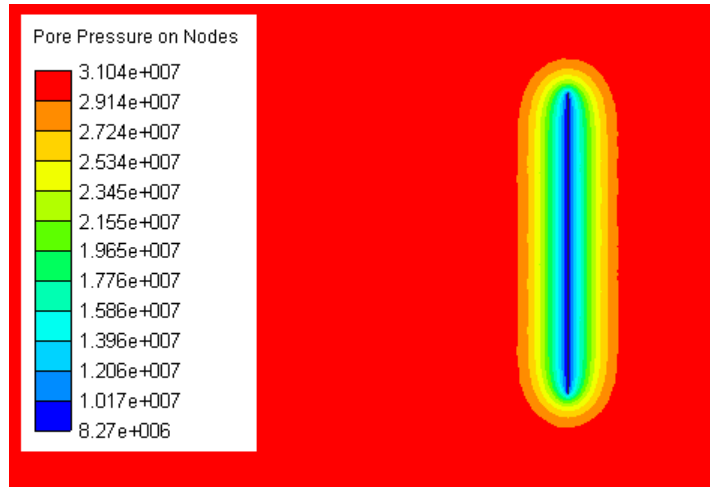
Figure 7.4.3: Darcy Flow into a Vertical Fracture - 5 nD reservoir, 4.5s
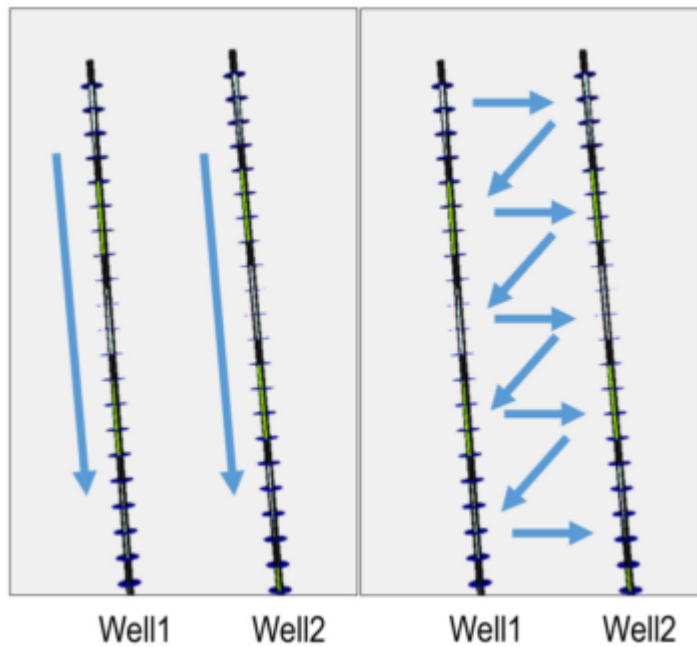
Figure 7.4.6: Sequential vs Zipper Fracturing

Chapter 8

Conclusions

This study focused on utilising an advanced numerical simulation framework to examine particular aspects of hydraulic fracture stimulation in tight gas shales. Their ultra low permeability requires the application of advanced stimulation techniques to become economically recoverable. Although not a new concept, production from tight shales has become big business in recent years, and literature regarding many facets of their properties, has become available. A review of studies on shale mechanical properties, mineral makeup, and properties related to fluid flow was presented.

The presence of natural fractures in brittle shales in particular is commonplace, and several studies on natural fracture scale, abundance and orientation provide useful background information which is reviewed in Chapter 2. Most studies seem to agree that there is no single rule for natural fracture properties in shales, and that modelling specific to the particular play is essential. Several difficulties associated with characterisation of natural fractures were discussed, and by extension the introduction of stochastic methods to modelling natural fractures. A particularly interesting result of the literature review was a study by Landry et al. (2014), which suggests that calcite filled natural fractures are permeable enough to be considered fracturing fluid conduits in these extremely tight shales.

An overview of numerical modelling of this field was presented, with a summary of numerous studies related to the many varied methods employed to simulate parts of this complex system. The issue of scale is present throughout attempts to model this process; from LBM simulations within pore space, to simulation of microseismic event generation in reservoir scale field simulations.

The modelling framework employed by Elfen TGR, the commercial software employed to undertake the simulations within this work, was presented in Chapter 3. The fundamental governing equations in the mechanical and fluid sides of the coupled simulations, and aspects key to managing the issue of scale, were described. In particular the localised

adaptive remeshing makes fracture insertion possible without relying on element boundaries. It enables the finite element mesh to be as fine as possible where required - at fracture tips and intersections- while being large enough to give realistic numbers of elements even in domains many kilometres in extent. Furthermore, a coarsening algorithm is able to de-refine regions which once encompassed the fracture tip, but become fracture boundaries later in the simulation.

The simulation work in this study began in Chapter 3 with the simulation of a treatment designed to enhance fracture complexity, the Texas Two-Step Method (TTSM).

Key Outcomes of the work around TTSM included:

- The observation of fracture geometries consistent with numerical results in literature.

- The observation of unintuitive attractive fracture growth close range.

    - This growth was predicted in previous literature, but not explained.

    - The mechanism for this growth pattern was found and explained in detail.

- The introduction of basic metrics to evaluate the area of affected stress anisotropy.

Central to the improvement of fracture complexity is the reduction of stress anisotropy, which is achieved by reinforcing the lateral stresses that each hydraulic fracture introduces into the formation. This is proportionally larger than the increased longitudinal stress, which results in the minimum horizontal stress increasing, reducing the stress anisotropy. Several simulations were conducted to compare with literature on the effect of opening two fractures at different spacings along the same well in sequence. The simulations matched literature well.

Of particular interest was the phenomenon of attractive fracture curvature, which appears to be in contradiction to familiar stress shadowing behaviour. The ability of the simulation package to view the whole domain at any point in time allowed the cause of this attractive fracturing to be identified: although described as incompressible, the Newtonian fracturing fluid does have a stiffness parameter, which is lower than the fracturing medium. This enabled preferential opening towards an open fracture, in turn affecting the stress rotation ahead of the fracture tip and causing the fracture to curve towards the open fracture. This effect was mitigated by distance from the open fracture, where the increased lateral stresses promoted curvature away from the open fracture. The effect was not accounted for in the literature, although some authors did postulate that it was due to shear stress effects.

The chapter also set out to identify a metric based on analysis of the full simulation field, to describe the impact the combined lateral stresses had on the anisotropy between the two fractures. The metric arrived at took into account the area affected per length of well and arrived at a different spacing than the literature example being used for comparison. Other differences, notably asymmetry in the stress anisotropy induced were noted. These were attributed to the more realistic modelling capabilities of Elfen TGR, which was able to account for the first fracture continuing to propagate due to residual pressure, and the compressibility of the fracturing fluid. It was observed that the aim of reducing or reversing the stress anisotropy could be achieved in two ways; by direct manipulation of the principal stress magnitudes, or by rotating them. The TTSM was shown to use direct magnitude manipulation, while the superposition of opposite signed shear stresses were noted to act to reduce shear stress in the area between fractures.

Subsequent chapters addressed various issues associated with the key aim of the TTSM - enhancing fracture complexity. Firstly, the behaviour of a fracture propagating in an altered stress field was considered. The manner in which a fracture reacts to a field rotated in relation to its own orientation was investigated in Chapter 5. Fracture complexity is associated with interaction with natural fractures, the topic of Chapter 6. A short final chapter proposed the second mechanism identified in Chapter 4 which could modify the stress anisotropy - rotation via shear stress.

Chapter 5 aimed to answer the following questions:

- How does a fracture grow within a region of reversed stress anisotropy?

  - Reorientation from the starter fracture orientation towards the maximum principal stress direction is expected.

- How do the following factors influence reorientation:

  - Amount of initial stress anisotropy

  - Initial fracture length

  - Initial orientation relative to the stress field

Key findings of this chapter included:

- In all cases, fractures initiated tangentially to their own fracture walls

  - This is in contradiction to the literature describing the TTSM

  - Reorientation towards the maximum principal stress direction occurred smoothly

- A drop in propagation pressure was observed during reorientation

- Under strong stress anisotropy, fracture choking could be observed in one wing

    - It is currently unclear whether this is due to the fracture curvature, the observed pressure drop, mesh artifacts, or another explanation

    - Examination of the choking mechanism would be a good area for further study

- While varying initial fracture length, two particular lengths an order of magnitude apart exhibited very similar curvature

    - This is also unexplained, and would make an interesting topic for further investigation

Reorientation to align with the maximum in-situ principal stress direction occurred at different rates. As well as the fracture path and reorientation rate, the effect on opening pressure was evaluated for all simulations. Measurement of the fracture orientation was achieved by extracting the geometry of the fracture from the results, and measuring the tip angle at every timestep in the simulation. This highlighted some significant noise in the tip angle, a consequence of a slight mesh dependency in the fracture insertion algorithm. The noise made it difficult to determine for certain when a fracture had reached its final orientation. Smoothing of the data via a low pass filter helped somewhat.

Some examples of fracture closure in one wing were observed, and the effect was to choke one wing, resulting in asymmetric growth of the fracture. It is unclear whether this is a real effect or an artifact of the tip angle noise noted earlier; further study would be warranted.

Simulations altering the stress anisotropy used quite a short starter fracture, which resulted in high initiation pressures. The high initiation pressures made it difficult to establish a trend as the anisotropy was altered, and future work could include setting those simulations up with longer starter fractures.

When varying the starter fracture length, two simulations an order of magnitude apart in length both showed very close behaviours. Further investigation of this aspect would be of benefit. The effect of the fracture orientation relative to the stress field was also examined, again all cases began to propagate tangentially to the fracture orientation, realigning smoothly with the principal stress field. Trends in reorientation rate were not as clear in these simulations as others.

The need to consider reorientation in the presence of natural fractures was identified as a prime candidate for future study.

Chapter 6   aimed to evaluate the effect of natural fractures on the propagation of a hydraulic fracture. The impact of natural fracture permeability and interface properties were studied.

Findings of particular interest included:

- Natural fractures (NF) were observed taking fracturing fluid from the hydraulic fracture (HF), and closing as HF propagation pressure dropped, retaining fluid.

    - This is a possible mechanism for fluid leakoff, and further study could indicate whether the fluid is retained when flowback fluid is removed from the system, particularly when the HF is propped.

- The stress field within the NF set was observed to influence the propagation direction of the HF. For instance, sharp exits from natural fractures were seen; in contrast to the results obtained in the previous chapter, in which reorientation of a single fracture was studied without the influence of any natural fractures.

- It was shown that reducing stress anisotropy by increasing the minimum horizontal stress (as per the TTSM) could act to *reduce* fracture complexity, by increasing the likelyhood of a propagating hydraulic fracture crossing a given natural fracture.

- Shear stress around a propagating hydraulic fracture was shown to cause tensile failure in adjacent, but unconnected, natural fractures.

    - This has potential implications in the interpretation of microseismic data. Simulation of the microseismic events generated by the observed failures could be misinterpreted as a highly stimulated region, whereas in fact no fracturing fluid has reached the areas indicated. Discussions with experts in microseismology would be of benefit, in order to discuss whether the simulated events would be in fact interpreted this way.

    - This result, in particular with the aforementioned input from microseismologists, has been identified as a candidate for publication.

- Interesting branching behaviour was observed, which further studies could model in more detail with targeted simulations. For instance, quantification of the fracture dilation/interface angle relationship, could be of benefit.

- The simulations used extreme settings for natural fracture interface properties; more moderate values could be used to provide further insight into fracture reactivation behaviour.

- Overall, the difference between results with natural fractures present, and those without, highlighted the importance of taking natural fractures into account when attempting to predict hydraulic fracture propagation.

Initial simulations were in a highly structured model; hydraulic fracturing perpendicular to a set of natural fractures of uniform length. Suitable values for high and low natural fracture permeabilities, and their influence on the hydraulic fracture propagation, were identified. Intermediate permeability values were then identified which displayed some aspects of each behaviour, and were used in subsequent studies of the natural fracture interface properties.

Stochastically generated fracture sets were then added to a model used in Chapter 5, to examine the effect of natural fractures on the reorientation rate. This was by no means exhaustive, and as noted earlier, an in depth examination of reorientation rates in the presence of natural fractures would be valuable work.

The examples considered in this work both resulted in heavily modified fracture paths. The modifications that dilated natural fractures can make to the stress field were observed and significant; hydraulic fractures were observed to exit natural fractures at sharp angles brought about by tensile stresses induced on one side of the natural fracture.

The angle the hydraulic fracture had first contacted the natural fracture at was observed to have an important effect on the exit direction from the natural fracture.

Finally, the chapter examined the impact that shear stresses induced by a propagating hydraulic fracture could have on a set of natural fractures without coming into direct contact. Simulations of microseismic events confirmed that that tensile failures, as well as shear slippage could be brought about by those shear stresses. A possible implication of this is that microseismic data could be interpreted as creating a complex fracture network of hydraulically stimulated natural fractures due to the tensile events; whereas it can be shown that the fractures are not in communication with the fracturing fluid at all. On the other hand, the shear stresses can be considered a useful tool in weakening cemented natural fractures and potentially opening new ones. The final, short, chapter conducted a simulation designed to magnify such shear stresses.

Chapter 7   demonstrated an alternative treatment design based on observations from simulations in previous chapters. It aimed to utilise the shear stresses which form around a propagating fracture to improve the behaviour of simultaneous stimulation treatment.

In particular, a well inclined at an angle of $45°$ to the maximum principal stress direction enabled the propagating fracture tips to interact in a way which is not possible using the standard TTSM.

The results were compared to that of a horizontal (stress-aligned) well. Some key findings of this chapter include:

- The inclination of the well to the in-situ stresses was shown to result in reinforcement of the shear stresses of adjacent fractures.

- The stress field was rotated by the reinforced shear stresses, resulting in fractures propagating towards each other.

    - This in contrast to TTSM, which directly affects the magnitudes of principal stresses without modifying their direction significantly.

- The onset of stress shadowing effects were delayed significantly.

- Lower work was required to propagate the fractures to a given length.

- It was observed that given the results from Chapter 6, the increased shear stresses could produce significant damage to existing natural fractures

    - The treatment could potentially be utilised in industry as a pre-treatment, to enhance conductivity of natural fractures prior to further stimulation

- Results from this chapter were identified as being suitable for publication.

Fracture spacing was designed so that in the horizontal well, significant stress shadowing was observed, resulting in a region between the two outer fractures which was relatively inaccessible to the hydraulic fractures. The fractures originating in the inclined well did not experience the negative effects of stress shadowing until later in the simulation. During that time, the fractures propagated evenly, and owing to the reinforcement of the shear stress zones ahead of each fracture tip, curved significantly until lateral to the wellbore. Once the fracture tips were aligned vertically, stress shadowing effects dominated the interior fractures, and the exterior fractures propagated preferentially. It was proposed that future evaluations of the treatment design would pump enough fluid to reach this point, providing a region of uniformly stimulated reservoir around the wellbore.

The interaction of the shear stresses was by design, and as well as altering the fracture directions, is likely to have caused significant damage to natural fractures nearby, as the results in section 6.4.3 demonstrate. Including natural fractures in future simulations would be of particular interest, as would investigation into employing the technique as a precursor to more linear fracturing; utilising the shear reinforcement as a pre-treatment to reactivate or debond natural fractures before a further treatment for production.

This proposed treatment design has potential for both improving fracture density during simultaneous fracturing, and acting as a pre-treatment to improve conductivity of natural fractures. Further study would be warranted, in particular:

- Evaluation of gas recovery, using a production model with propped fractures.

- Simulation of interaction with natural fracture sets, quantifying conductivity changes.

Bibliography

Abousleiman, Y., Tran, M., Hoang, S., Bobko, C., and Ulm, F.-J. Geomechanics Field and Laboratory Characterization of Woodford Shale : The Next Gas Play. In *SPE Annual Technical Conference and Exhibition*. 2007.

Baghbanan, a. and Jing, L. Stress effects on permeability in a fractured rock mass with correlated fracture length and aperture. *International Journal of Rock Mechanics and Mining Sciences*, 45(8):1320–1334, 2008. ISSN 13651609.

Bahorich, B., Olson, J., and Holder, J. Examining the Effect of Cemented Natural Fractures on Hydraulic Fracture Propagation in Hydrostone Block Experiments. *SPE Annual Technical Conference and Exhibition*, 2012.

Baihly, J., Altman, R., Malpani, R., and Luo, F. Shale Gas Production Decline Trend Comparison Over Time and Basins. In *SPE Annual Technical Conference and Exhibition*, September. 2010.

Barree, R. D., Gilbert, J. V., and Conway, M. W. Stress and Rock Property Profiling for Unconventional Reservoir Stimulation. In *SPE Hydraulic Fracturing Technology Conference*, January. Society of Petroleum Engineers, 2009.

Britt, L. and Schoeffler, J. The Geomechanics of a Shale Play: What Makes a Shale Prospective! In *Proceedings of SPE Eastern Regional Meeting*. Society of Petroleum Engineers, 2009.

Bunger, A. P., Zhang, X., and Jeffrey, R. G. Parameters Effecting the Interaction among Closely Spaced Hydraulic Fractures. *SPE Journal*, (March):1–18, 2012.

Cabral, B. and Leedom, L. C. Imaging vector fields using line integral convolution. *Proc. SIGGRAPH*, pages 263–270, 1993. ISSN 0097-8930.

Chen, Y., Zhou, C., and Sheng, Y. Formulation of strain-dependent hydraulic conductivity for a fractured rock mass. *International Journal of Rock Mechanics and Mining Sciences*, 44(7):981–996, 2007. ISSN 13651609.

Cheng, Y. Mechanical Interaction of Multiple Fractures-Exploring Impacts of the Selection of the Spacing/Number of Perforation Clusters on Horizontal Shale-Gas Wells. *Spe Journal*, 17(4):992–1001, 2012. ISSN 1086-055X.

Cho, T., Plesha, M., and Haimson, B. Continuum modelling of jointed porous rock. *International Journal for Numerical and Analytical Methods in Geomechanics*, (15):333–353, 1991.

Chuprakov, D. A., Akulich, A. V., Siebrits, E., and Thiercelin, M. SPE 128715 Hydraulic Fracture Propagation in a Naturally Fractured Reservoir. In *Oil and Gas India Conference and*, pages 1–12. 2010.

Daneshy, A. A Study of Inclined Hydraulic Fractures. *Society of Petroleum Engineers Journal*, 13(2), 1973. ISSN 0197-7520.

Detournay, E. Mechanics of Hydraulic Fractures. *Annual Review of Fluid Mechanics*, 48(1):311–339, 2016. ISSN 0066-4189.

Duarte Azevedo, I. C., Vaz, L. E., and Vargas, E. A. A numerical procedure for the analysis of the hydromechanical coupling in fractured rock masses. *International Journal for Numerical and Analytical Methods in Geomechanics*, 901(January 1997):867–901, 1998.

Economides, M. J. and Martin, T. *Modern Fracturing - Enhancing Natural Gas Production*. Energy Tribune Publishing Inc, Houston, 2007.

Engelder, T., Lash, G. G., and Uzcátegui, R. S. Joint sets that enhance production from Middle and Upper Devonian gas shales of the Appalachian Basin. *AAPG Bulletin*, 93(7):857–889, 2009. ISSN 0149-1423.

Fisher, M., Heinze, J., and Harris, C. Optimizing Horizontal Completion Techniques in the Barnett Shale Using Microseismic Fracture Mapping. SPE paper 90051 presented at the SPE Annual. 2004.

Fossum, A. F. Effective Elastic Properties for a Randomly Jointed Rock Mass. *International Journal of Rock Mechanics and Mining Sciences & Geomechanics Abstracts*, 22(6):467–470, 1985.

Fu, P., Johnson, S. M., and Carrigan, C. An explicitly coupled hydro-geomechanical model for simulating hydraulic fracturing in complex discrete fracture networks. *International Journal for Numerical and Analytical Methods in Geomechanics*, online, 2012.

Gale, J. F. W. and Holder, J. Natural fractures in the Barnett Shale : constraints on spatial organization and tensile strength with implications for hydraulic fracture treatment in

shale-gas reservoirs. In *The 42nd U.S. Rock Mechanics Symposium (USRMS)*. American Rock Mechanics Association, 2008.

Gale, J. F. W., Laubach, S. E., Olson, J. E., Eichhubl, P., and Fall, A. Natural fractures in shale: A review and new observations. *AAPG Bulletin*, 98(11):2165–2216, 2014. ISSN 01491423.

Gale, J. F. W., Reed, R. M., and Holder, J. Natural fractures in the Barnett Shale and their importance for hydraulic fracture treatments. *AAPG Bulletin*, 91(4):603–622, 2007. ISSN 0149-1423.

Gerrard, C. M. Elastic Models of Rock Masses Having One , Two and Three Sets of Joints. *International Journal of Rock Mechanics and Mining Sciences & Geomechanics Abstracts*, 19, 1982.

Grieser, B. and Bray, J. Identification of Production Potential in Unconventional Reservoirs. In *Carbon Production and Operations Symposium*. Society of Petroleum Engineers, 2007.

Grün, G. U., Wallner, H., and Neugebauer, H. J. Porous rock deformation and fluid flow - numerical FE -simulation of the coupled system. *Geologische Rundschau*, 78(1):171–182, 1989. ISSN 0016-7853.

Gu, H., Weng, X., Lund, J., Mack, M., Ganguly, U., and Suarez-Rivera, R. Hydraulic Fracture Crossing Natural Fracture at Non-orthogonal Angles, A Criterion, Its Validation and Applications. *Proceedings of SPE Hydraulic Fracturing Technology Conference*, 2011.

Gutierrez, M., Øino, L. E., and Nygård, R. Stress-dependent permeability of a de-mineralised fracture in shale. *Marine and Petroleum Geology*, 17(8):895–907, 2000. ISSN 02648172.

Han, G. Description of fluid flow around a wellbore with stress-dependent porosity and permeability. *Journal of Petroleum Science and Engineering*, 40(1-2):1–16, 2003. ISSN 09204105.

Hao, H., Wu, C., and Zhou, Y. Numerical Analysis of Blast-Induced Stress Waves in a Rock Mass with Anisotropic Continuum Damage Models Part 1: Equivalent Material Property Approach. *Rock Mechanics and Rock Engineering*, 35(2):79–94, 2002. ISSN 0723-2632.

Holder, J., Olson, J., and Philip, Z. Experimental determination of subcritical crack growth parameters in sedimentary rock. *Geophysical Research Letters*, 28(4):599–602, 2001a.

Holder, J., Olson, J. E., and Philip, Z. Experimental determination of subcritical crack growth parameters in sedimentary rock. *GEOPHYSICAL RESEARCH LETTERS*, 28(4):599–602, 2001b.

Horsrud, P., Sonstebo, E. F., and Boe, R. Mechanical and Petrophysical Properties of North Sea Shales. *International Journal of Rock Mechanics and Mining Sciences*, 35(8), 1998.

Hossain, M. M., Rahman, M. K., and Rahman, S. S. Hydraulic fracture initiation and propagation: Roles of wellbore trajectory, perforation and stress regimes. *Journal of Petroleum Science and Engineering*, 27(3-4):129–149, 2000. ISSN 09204105.

Huang, T. H., Chang, C. S., and Yang, Z. Y. Elastic moduli for fractured rock mass. *Rock Mechanics and Rock Engineering*, 28(3):135–144, 1995. ISSN 07232632.

Jacot, R. H., Resources, A. E., Bazan, L. W., and Meyer, B. R. Technology Integration - A Methodology to Enhance Production and Maximize Economics in Horizontal Marcellus Shale Wells. In *SPE Annual Technical Conference and Exhibition*. Society of Petroleum Engineers, 2010.

Javadpour, F., Fisher, D., and Unsworth, M. Nanoscale gas flow in shale gas sediments. *Journal of Canadian Petroleum Technology*, 46(10), 2007.

Jiang, X., Wan, L., Wang, X., Liang, S., and Hu, B. Estimation of fracture normal stiffness using a transmissivity-depth correlation. *International Journal of Rock Mechanics and Mining Sciences*, 46(1):51–58, 2009. ISSN 13651609.

Jin, M. and Somerville, J. Coupled Reservoir Simulation Applied to the Management of Production Induced Stress-Sensitivity. In *International Oil and Gas Conference and Exhibition in China*. 2000.

Jo, H. Optimizing Fracture Spacing to Induce Complex Fractures in a Hydraulically Fractured Horizontal Wellbore. In *Americas Unconventional Resources Conference*. Society of Petroleum Engineers This, 2012.

Karimi-Fard, M. and Firoozabadi, A. Numerical Simulation of Water Injection In 2D Fractured Media Using Discrete-Fracture Model. In *SPE Annual Technical Conference and Exhibition, 30 September-3 October 2001, New Orleans, Louisiana*. 2001.

Kassis, S. and Sondergeld, C. H. Fracture Permeability of Gas Shale : Effects of Roughness , Fracture Offset , Proppant , and Effective Stress. In *CPS/SPE International Oil & Gas Conference and Exhibition*, 1, pages 1–17. 2010.

Killops, S. D. and Killops, V. J. *Introduction to organic geochemistry*. John Wiley and Sons, 2, revised edition, 2004. ISBN 9780632065042.

King, G. E. SPE 133456 Thirty Years of Gas Shale Fracturing : What Have We Learned ? *Technology*, (September):19–22, 2010.

Kulhawy, F. H. Geomechanicalmodel for rock foundation settlement. *International Journal of Rock Mechanics and Mining Sciences & Geomechanics Abstracts*, 104:211–227, 1978.

Lander, R. H. and Laubach, S. E. Insights into rates of fracture growth and sealing from a model for quartz cementation in fractured sandstones. *Bulletin of the Geological Society of America*, 127(3-4):516–538, 2014. ISSN 19432674.

Landry, C. J., Eichhubl, P., Prodanovic, M., and Tokan-Lawal, A. Permeability of calcite-cemented fractures in mudrocks: Flow highway or hindrance? *AGU Fall Meeting Abstracts*, 2014.

Lash, G. G. and Engelder, T. An analysis of horizontal microcracking during catagenesis: Example from the Catskill delta complex. *AAPG Bulletin*, 89(11):1433–1449, 2005. ISSN 0149-1423.

Laubach, S. E., Marrett, R. A., Olson, I. E., and Scott, A. R. Characteristics and origins of coal cleat: a review. *International Journal of Coal Geology*, 35(1-4):175–207, 1998. ISSN 01665162.

Li, Y., Wei, C., Qi, G., Li, M., and Luo, K. Numerical Simulation of Hydraulically Induced Fracture Network Propagation in Shale Formation. *IPTC 2013: International Petroleum Technology Conference*, 2013. ISSN 2214-4609.

Liu, J., Elsworth, D., and Brady, B. H. Linking stress-dependent effective porosity and hydraulic conductivity fields to RMR. *International Journal of Rock Mechanics and Mining Sciences*, 36:581–596, 1999.

Lorenz, J. C., Teufel, L. W., and Warpinski, N. R. Regional Fractures I: A mechanism for the Formation of Regional Fractures at Depth in Flat-Lying Reservoirs. *The American Association of Petroleum Geologists Bulletin*, 75(11):1714–1737, 1991.

Lothe, a. E., Borge, H., and Gabrielsen, R. H. Modelling of hydraulic leakage by pressure and stress simulations and implications for Biot's constant: an example from the Halten Terrace, offshore Mid-Norway. *Petroleum Geoscience*, 10(3):199–213, 2004. ISSN 1354-0793.

Mas Ivars, D. Water inflow into excavations in fractured rock - a three-dimensional hydro-mechanical numerical study. *International Journal of Rock Mechanics and Mining Sciences*, 43(5):705–725, 2006. ISSN 13651609.

Mayerhofer, M. J., Lolon, E. P., Warpinski, N. R., Cipolla, C. L., Walser, D., and Rightmire, C. M. What Is Stimulated Reservoir Volume ? *SPE Production & Operations*, 25:89–98, 2010.

Min, K. Numerical determination of the equivalent elastic compliance tensor for fractured rock masses using the distinct element method. *International Journal of Rock Mechanics and Mining Sciences*, 40(6):795–816, 2003. ISSN 13651609.

Min, K., Rutqvist, J., Tsang, C., and Jing, L. Stress-dependent permeability of fractured rock masses: a numerical study. *International Journal of Rock Mechanics and Mining Sciences*, 41(7):1191–1210, 2004. ISSN 13651609.

Miskimins, J. L., Ramirez, B. A., and Graves, R. M. The Economic Value of Information and Biots' Constant : How Important Are Accurate Measurements? 2004.

Mogilevskaya, S. G., Rothenburg, L., and Dusseault, M. B. Growth of pressure-induced fractures in the vicinity of a wellbore. *International Journal of Fracture*, (104):23–30, 2000.

Morales, R. and Marcinew, R. Fracturing of High-Permeability Formations: Mechanical Properties Correlations. *Proceedings of SPE Annual Technical Conference and Exhibition*, pages 467–475, 1993.

Morrill, J. C. and Miskimins, J. L. Optimizing Hydraulic Fracture Spacing in Unconventional Shales. In *SPE Hydraulic Fracturing Technology Conference*, February, pages 6–8. Society of Petroleum Engineers, 2012. ISBN 9781613991787.

Mukhopadhyay, P. K. Petrographic and Molecular Characterization and Its Applications to Basin Modeling. In *Vitrinite Reflectance as a Maturity Parameter*, volume 10, chapter 1, pages 1–24. 1994.

Mullen, M., Roundtree, R., and Barree, B. A Composite Determination of Mechanical Rock Properties for Stimulation Design. In *Rocky Mountain Oil & Gas Technology Symposium*. Society of Petroleum Engineers, 2007.

Ohman, J., Niemi, a., and Tsang, C. Probabilistic estimation of fracture transmissivity from Wellbore hydraulic data accounting for depth-dependent anisotropic rock stress. *International Journal of Rock Mechanics and Mining Sciences*, 42(5-6):793–804, 2005. ISSN 13651609.

Olson, J., Holder, J., and Rijken, P. Quantifying the Fracture Mechanics Properties of Rock for Fractured Reservoir Characterization. In *Proceedings of SPE/ISRM Rock Mechanics Conference*. Society of Petroleum Engineers, 2002.

Olson, J. E. Predicting fracture swarms – the influence of subcritical crack growth and the crack-tip process zone on joint spacing in rock. *Geological Society, London, Special Publications*, 231(1):73–88, 2004. ISSN 0305-8719.

Olson, J. E., Laubach, S. E., and Lander, R. H. Natural fracture characterization in tight gas sandstones: Integrating mechanics and diagenesis. *AAPG Bulletin*, 93(11):1535–1549, 2009. ISSN 01491423.

Osorio, J. G., Chen, H.-y., and Teufel, L. W. Numerical Simulation of the Impact of Flow-Induced Geomechanical Response on the Productivity of Stress-Sensitive Reservoirs. In *SPE Reservoir Simulation Symposium*. 1999.

Prioul, R., Karpfinger, F., Deenadayalu, C., and Suarez-rivera, R. Improving Fracture Initiation Predictions on Arbitrarily Oriented Wells in Anisotropic Shales. In *Canadian Unconventional Resources Conference*. Society of Petroleum Engineers, 2011.

Qiu, F., Porcu, M. M., Xu, J., Malpani, R., Pankaj, P., and Pope, T. L. Simulation Study of Zipper Fracturing Using an Unconventional Fracture. In *SPE/CSUR Unconventional Resources Conference*. Society of Petroleum Engineers, 2015. ISBN 9781613994184.

Rafiee, M., Soliman, M. Y., and Pirayesh, E. Hydraulic Fracturing Design and Optimization : A Modification to Zipper Frac x z. In *SPE Annual Technical Conference and Exhibition*. 2012.

Rickman, R., Mullen, M., Petre, E., Grieser, B., and Kundert, D. A Practical Use of Shale Petrophysics for Stimulation Design Optimization : All Shale Plays Are Not Clones of the Barnett Shale. In *SPE Annual Technical Conference and Exhibition*, Wang. Society of Petroleum Engineers, 2008.

Rijken, M. C. M. *MODELING NATURALLY FRACTURED RESERVOIRS : FROM EXPERIMENTAL ROCK MECHANICS TO FLOW SIMULATION*. Ph.d., The University of Texas at Austin, 2005.

Rutqvist, J. and Stephansson, O. The role of hydromechanical coupling in fractured rock engineering. *Hydrogeology Journal*, 11(1):7–40, 2003. ISSN 1431-2174.

Schieber, J. Common Themes in the Formation and Preservation of Intrinsic Porosity in Shales and Mudstones - Illustrated With Examples Across the Phanerozoic. *Proceedings of SPE Unconventional Gas Conference*, 2010.

Segall, P. and Fitzgerald, S. D. A note on induced stress changes in hydrocarbon and geothermal reservoirs. *Tectonophysics*, 289:117–128, 1998.

Segura, J. M., Fisher, Q. J., Crook, a. J. L., Dutko, M., Yu, J. G., Skachkov, S., Angus, D. a., Verdon, J. P., and Kendall, J.-M. Reservoir stress path characterization and its implications for fluid-flow production simulations. *Petroleum Geoscience*, 17(4):335–344, 2011. ISSN 1354-0793.

Sheng, Y., Sousani, M., Ingham, D., and Pourkashanian, M. Recent Developments in Multiscale and Multiphase Modelling of the Hydraulic Fracturing Process. *Mathematical Problems in Engineering*, 2015, 2015. ISSN 15635147.

Singh, B. Continuum Characterization Of Jointed Rock Masses. *International Journal of Rock Mechanics and Mining Sciences & Geomechanics Abstracts*, 10, 1973.

Sneddon, I. N. The Distribution of Stress in the Neighbourhood of a Crack in an Elastic Solid. *Proceedings of the Royal Society A: Mathematical, Physical and Engineering Sciences*, 187(1009):229–260, 1946. ISSN 1364-5021.

Soliman, M. Y., East, L., Adams, D., and Services, H. E. Geomechanics Aspects of Multiple Fracturing of Horizontal and Vertical Wells. (September):16–18, 2008.

Soliman, M. Y., East, L., and Augustine, J. SPE 130043 Fracturing Design Aimed at Enhancing Fracture Complexity. *Society,* (June):14–17, 2010.

Sondergeld, C. H., Newsham, K. E., Comisky, J. T., Rice, M. C., and Rai, C. SPE 131768 Petrophysical Considerations in Evaluating and Producing Shale Gas Resources. 2010.

Sone, H. and Zoback, M. Visco-plastic properties of shale gas reservoir rocks. *American Rock Mechanics Association*, 2011.

Sridevi, J. and Sitharam, T. Analysis of strength and moduli of jointed rocks. *Geotechnical and Geological Engineering*, 18:3–21, 2000.

Taleghani, A. D. and Olson, J. E. How Natural Fractures Could Affect Hydraulic-Fracture Geometry. *SPE Journal*, 19(01):161–171, 2013. ISSN 1086-055X.

Taleghani, D. Fracture Re-Initiation as a Possible Branching Mechanism during Hydraulic fracturing. In *44th U.S. Rock Mechanics Symposium and 5th U.S.-Canada Rock Mechanics Symposium*. American Rock Mechanics Association, 2010.

Tran, D. T., Roegiers, J.-c., and Thiercelin, M. Thermally-Induced Tensile Fractures in the Barnett Shale and Their Implications to Gas Shale Fracability. In *44th US Rock Mechanics Symposium and 5th U.S.-Canada Rock Mechanics Symposium*. American Rock Mechanics Association, 2010.

Vincke, O., Longuemare, P., Bouteca, M., and Deflandre, J. Investigation of the Porome-chanical Behavior of Shales in the Elastic Domain. *Proceedings of SPE/ISRM Rock Mechanics in Petroleum Engineering*, 1998.

Walsh, J. Effect of pore pressure and confining pressure on fracture permeability. Int. J. Rock Mech. Min. Sci & Geochem. Abstr., 18, 429-435. 18:429–435, 1981.

Warpinski, N. R., Kramm, R. C., Heinze, J. R., and Corp, D. E. Comparison of Single-and Dual-Array Microseismic Mapping Techniques in the Barnett Shale. In *SPE Annual Technical Conference and Exhibition*. 2005.

Warpinski, N. R., Mayerhofer, M. J., Cipolla, C. L., Vincent, M. C., and Lolon, E. P. Stimu-lating Unconventional Reservoirs : Maximizing Network Growth While Optimizing Frac-ture Conductivity. *Journal of Canadian Petroleum Technology*, 48:39–51, 2009.

Waters, G., Dean, B., Downie, R., Kerrihard, K., Austbo, L., and McPherson, B. Simulta-neous Hydraulic Fracturing of Adjacent Horizontal Wells in the Woodford Shale. *SPE Paper 119635-MS*, 2009.

Wu, Y.-s., Moridis, G., Bai, B., and Zhang, K. A Multi-Continuum Model for Gas Production in Tight Fractured Reservoirs. In *SPE Hydraulic Fracturing Technology Conference*, 1, pages 1–16. 2009.

Yang, Y. and Aplin, A. C. Permeability and petrophysical properties of 30 natural mud-stones. *Journal of Geophysical Research*, 112, 2007.

Yuan, S. and Harrison, J. Development of a hydro-mechanical local degradation approach and its application to modelling fluid flow during progressive fracturing of heterogeneous rocks. *International Journal of Rock Mechanics and Mining Sciences*, 42(7-8):961–984, 2005. ISSN 13651609.

Zhang, L. Using RQD to estimate the deformation modulus of rock masses. *Interna-tional Journal of Rock Mechanics and Mining Sciences*, 41(2):337–341, 2004. ISSN 13651609.

Zhang, X., Sanderson, D., Harkness, R. M., and Last, N. Evaluation of the 2-D Permeabilit Y Tensor for Fractured Rock Masses. *International Journal of Rock Mechanics and Mining Sciences & Geomechanics Abstracts*, 33(1):17–37, 1996.

Zhang, Y., Sayers, C. M., and Adachi, J. I. The use of effective medium theories for seismic wave propagation and fluid flow in fractured reservoirs under applied stress. *Geophysical Journal International*, 177(1):205–221, 2009. ISSN 0956540X.

Zienkiewicz, O. C. and Pande, G. N. Time-dependent multilaminate model of rocks, a numerical study of deformation and failure of rock masses. *International Journal for Numerical and Analytical Methods in Geomechanics*, 1(3):219–247, 1977.

Zoback, M. D. *Reservoir geomechanics*. Cambridge University Press, 2007. ISBN 0521770696.